



BOOK OF ABSTRACTS

8th International Conference on Unsolved Problems on Noise

GDAŃSK
JULY 9-13 2018

UPoN

GDAŃSK 2018

Random fluctuations, and their effect on systems, have always been an interdisciplinary subject that has attracted some of the best scientists. The aim of the UPoN conference is to provide a forum for researchers working on different fields of noise, fluctuations and variability, where they can present their scientific problems which do resist solutions and discuss together in a fruitful atmosphere.

KEYNOTE SPEAKERS

Sergey Bezrukov, National Institutes of Health (USA)

Unsolved problems of ion channel dynamics

François Danneville, Institute of Electronics, Microelectronics and Nanotechnology (France)

Open problems in brain-emulating hardware

Pertti Hakonen, Aalto University School of Science (Finland)

Quantum vacuum, noise, and entanglement

Michael Levinshtein, Ioffe Institute (Russia)

Lorentzians vs global warming hysteresis

BANQUET SPEAKER

Michael Shlesinger, Office of Naval Research (USA)

Pitfalls and Paradoxes in the History of Probability Theory

INVITED SPEAKERS

Bruno Andò, University of Catania (Italy)

Open problems of utilizing noise in energy harvesting systems

Eli Barkai, Bar Ilan University (Israel)

1/f noise on the nanoscale

Wolfgang Belzig, University of Konstanz (Germany)

Noisy quantum measurements: just a nuisance or fundamental physics?

Dante R. Chialvo, CEMSC3 - UNSAM (Argentina)

Life at the edge, complexity and criticality in biological function

Carmine Ciofi, University of Messina (Italy)

Unsolved problems in instrumentation for noise measurements

Niels Lörch, University of Basel (Switzerland)

Fluctuations and time-translation symmetry breaking in vibrational Floquet systems

Mikhail Feigel'man, L.D.Landau Institute for Theoretical Physics; Skoltech, Moscow (Russia)

Non-equilibrium noise in a simple model of ageing in glassy dynamics

Igor Goychuk, University of Potsdam (Germany)

Molecular motors operating in a highly dissipative, noisy and subdiffusive interior of living cells: How a highly efficient operation is possible, lessons from the fluctuation-dissipation theorem.

Grzegorz Jung, Ben-Gurion University of the Negev (Israel)

Macroscopic random telegraph noise

Jerzy Łuczka, University of Silesia (Poland)

On the principle of equipartition of kinetic energy: classical versus quantum

Aneta Stefanovska, Lancaster University (UK)

Noise generated from a small network of time-varying phase oscillators

Sponsored by

Office of Naval Research - Washington
Office of Naval Research - London
Ministry of Science and Higher
Education allocated for activities which
disseminate the science, contract
840/P-DUN/2018



UPoN 2018 Patrons



BOOK OF ABSTRACTS

UPoN 2018
Gdańsk, 9-13 July 2018

CONTENT

Program of UPoN 2018 conference	5
ORAL PRESENTATIONS	
L. B. Kish – Is there thermal noise in thermal equilibrium at zero temperature? (<i>opening talk</i>)	11
S. M. Bezrukov – Unsolved problems in ion channel dynamics (<i>keynote talk</i>)	12
P. Hakonen – Quantum vacuum, noise, and entanglement (<i>keynote talk</i>)	13
I. Goychuk – Molecular motors operating in a highly dissipative, noisy and subdiffusive interior of living cells: How a highly efficient operation is possible, lessons from the fluctuation-dissipation theorem (<i>invited talk</i>)	15
G. Gonnella, F. Cagnetta, F. Corberi, A. Suma – Large fluctuations and dynamic phase transition in active Brownian particle systems	17
M. Lechelon, M. Gori, M. Pettini, Y. Meriguet, J. Torres, L. Varani – Can noise and diffusion help to solve the puzzle of biomolecules interactions?	19
D. Makowiec, D. Wejer, B. Graff, Z. R. Struzik – Multiscale approach in discovering cardiovascular couplings from cardiovascular time series	21
G. Jung – Macroscopic random telegraph noise (<i>invited talk</i>)	23
J. Müller – Origin of $1/f$ - noise of strongly-correlated electrons in low-dimensional molecular metals	25
R. Pedurand, G. Hansali, V. Dolique, G. Cagnoli, L. Bellon – The CryoQPDI: a new research instrument for mechanical thermal noise investigation	27
S. Pralgauskaitė, M. Tretjak, J. Matukas, J. Macutkevič, J. Banys – Low-frequency fluctuations in composite materials with carbon nanoparticles	29
D. R. Chialvo – Life at the edge, complexity and criticality in biological function (<i>invited talk</i>)	31
L. B. Kish – Information storage and channel capacity of brain; an unsolved problem of noise	32
M. Barabash, W. A. T. Gibby, D. G. Luchinsky, C. Guardiani, I. A. Khovanov, P. V. E. McClintock – Combining molecular dynamics and the Chapman-Kolmogorov theory of ion transport in biological channels	33
Y. Kutovyi, I. Zadorozhnyi, V. Handziuk, H. Hlukhova, M. Petrychuk, S. Vitusevich – The impact of biomolecules binding on low-frequency noise in Si NW FET biosensors	35
Y. F. Suprunenko, A. Stefanovska – Noise generated from a small network of time-varying phase oscillators (<i>invited talk</i>)	37
E. A. Miranda, A. Mehonic, W. H. Ng, J. Suñé, A. J. Kenyon – Correlated fluctuation and variability in SiO _x -based memristors: a simplified approach for circuit simulation environments	39
G. Cywiński, J. Przybytek, D. But, I. Yahniuk, P. Kruszewski, M. Grabowski, K. Nowakowski-Szkudlarek, P. Prystawko, P. Sai, W. Knap, G. S. Simin, S. L. Rumyantsev – Low frequency noise in wire-channel GaN/AlGaIn transistors	41
J. Przybytek, G. Jung – Noise features of metastable resistivity states in La _{0.86} Ca _{0.14} MnO ₃ manganite	43
F. Danneville, I. Sourikopoulos, S. Hedayat, C. Loyez, V. Hoel, A. Cappy – Open problems in brain emulating-hardware (<i>keynote talk</i>)	45
E. Barkai – $1/f$ noise on the nanoscale (<i>invited talk</i>)	47
M. V. Feigel'man – Non-equilibrium noise in a simple model of ageing in glassy dynamics (<i>invited talk</i>)	48
E. Colomés, X. Oriols, J. Mateos, T. González – Is the nanoscale scaling of electron devices ultimately limited by noise?	49

E. Colomés, Z. Zhan, D. Pandey, X. Oriols – Can linear or parabolic band dispersions in 2D materials be tested by noise?	51
M. Petrychuk, I. Zadorozhnyi, Y. Kutovyi, S. Karg, H. Riel, S. Vitusevich – 1D electron transport in InAs nanowires	53
M. Seif, F. Pascal, B. Sagnes, J. El-Beyrouthy, A. Hoffmann, S. Haendler, P. Chevalier, G. Gloria – Localization of 1/f noise sources in Si/SiGe:C HBTs	55
W. Belzig, J. Bülte, A. Bednorz, B. Reulet, C. Bruder – Noisy quantum measurements: just a nuisance or fundamental physics? (<i>invited talk</i>)	57
A. Fontana, R. Pedurand, L. Bellon – Fluctuations in a NESS: is there any universal behavior?	59
B. Dybiec, E. Gudowska-Nowak, I. M. Sokolov – Damped underdamped non-equilibrium stochastic harmonic oscillator	61
I. A. Khovanov – What is a form of the escape rate for white non-Gaussian noise?	63
W. A. T. Gibby, D. G. Luchinsky, M. L. Barabash, C. Guardiani, O. F. Fedorenko, S. K. Roberts, P. V. E. McClintock – Towards a resolution of the conductivity-selectivity paradox in the NaChBac ion channel	65
G. Muñoz-Gil, M. A. Garcia-March, C. Manzo, A. Celi, M. Lewenstein – Anomalous diffusion in structured environments	67
R. Shinagawa, K. Sasaki – Enhanced diffusion in a model of molecular motors with potential switching	69
M. A. Farahani, M. Takagi, K. Akehi, K. Mito, T. Mizuno, N. Itakura – The analyze of conducting waves of lower leg muscle using Multichannel Surface EMG	71
J. Łuczka, P. Bialas – On the principle of equipartition of kinetic energy: classical versus quantum (<i>invited talk</i>)	73
M. Kapfer, P. Roulleau, I. Farrer, D. A. Ritchie, D. C. Glatli – Measuring the Josephson frequency of fractional charges with shot noise	74
K. Ptaszyński – First-passage times in single-reset and multiple-reset discrete Markovian systems	76
H. Zhan, G. Rastelli, W. Belzig– Light emission from noise in ac-driven contact	78
S. Yuvan, M. Bier – Characterizing deviations from Poissonian and IID statistics with compressed exponentials	80
G. Vadai, A. Antal, Z. Gingl – Spectral analysis of fluctuations in humans’ daily motion using location data	82
J. Song, L. B. Kish – Standalone cold virtual resistor? Can we cool by a linear amplifier without non-linearity, switches, or phase transition?	84
V. Handziuk, F. Gasparyan, L. Vandamme, M. Coppola, V. Sydoruk, M. Petrychuk, D. Mayer, S. Vitusevich – Transport regimes in tunable gold nanoconstrictions: proposed solution by low-frequency noise spectroscopy	85
S. Galla, Ł. Lentka, A. Szewczyk – Supercapacitor’s temperature fluctuations during charging/discharging processes	87
I. V. Tyulkina, L. S. Klimenko, D. S. Goldobin, A. Pikovsky – Effect of intrinsic noise on Chimera states in coupled Kuramoto ensembles: Towards constructing the perturbation theory for the Ott-Antonsen theory	89
A. Dubkov, O. Chichigina, A. Krasnova – White noise as a model of harmonic input for billiard-like systems	91

G. Nadzinski, M. Dobrevski, C. Anderson, P. V. E. McClintock, A. Stefanovska, M. Stankovski, T. Stankovski – Noise robustness analysis and experimental implementation of the coupling function secure communications protocol	93
M. Melhem, L. B. Kish – How to defend against loop current attacks in the KLJN secure key exchange scheme?	95
Y. Tadokoro, H. Tanaka, M. I. Dykman – Signal detection with a noisy nanomechanical bifurcation amplifier	96
M. Levinshtein, V. Dergachev, A. Dmitriev, P. Shmakov – Lorentzians vs global warming hysteria (<i>keynote talk</i>)	98
B. Andò, S. Baglio, A. R. Bulsara, V. Marletta – Open problems of utilizing noise in energy harvesting systems (<i>invited talk</i>)	100
N. Lörch, Y. Zhang, C. Bruder, M. I. Dykman – Fluctuations and time-translation symmetry breaking in vibrational Floquet systems (<i>invited talk</i>)	102
C. Ciofi, G. Scandurra, G. Giusi – Unsolved problems in instrumentation for noise measurements (<i>invited talk</i>)	104
T. Kosztolowicz – How fluctuations of membrane permeability parameter influence on subdiffusion in a membrane system	106
G. Scandurra, S. Beyne, G. Cannatà, G. Giusi, C. Ciofi – On the design of an automated system for the characterization of the electromigration performance of advanced interconnects by means of low frequency noise measurements	107
L. B. Kish – Mathematical model for the impact of political correctness on science	109
A. Dubkov – The problems of finding the steady-state probabilistic characteristics for nonlinear dynamical systems driven by white Poisson noise	110
Z. Kolodiy – Flicker noise problem	112
J. Spiechowicz, J. Łuczka – Subdiffusion via dynamical localization induced by thermal equilibrium fluctuations	114
M. Majka – How to embed the self-assembly dynamics in the Langevin equations with spatio-(temporally) correlated noise?	115
V. Holubec, T. Novotný – Effects of noise-induced coherence on the performance of quantum absorption refrigerators	116
POSTERS	
H. Asada, K. Akehi, M. A. Farahani, N. Itakura, T. Mizuno – A study on simple measurement of mental and physical burden of patients during dental treatment	117
S. Babicz, B. Stawarz-Graczyk – Fluctuations of the red blood cells	119
A. Bednorz, M. Frączak, S. Sołtan, W. Belzig – Is energy conserved when nobody looks?	121
A. Crépieux, S. Sahoo, T. Q. Duong, R. Zamoum, M. Lavagna – Finite-frequency noise in a Kondo quantum dot with asymmetric coupling to the reservoirs	122
Z. Czaja, M. Kowalewski – A noise signal generation method for microcontrollers with DACs	124
A. Geremew, S. Romyantsev, M. A. Bloodgood, T. T. Salguero, A. A. Balandin – Low-frequency noise in quasi-1D van der Waals nanowires implemented with transition metal trichalcogenides	126

J. Glemža, V. Palenskis, S. Pralgauskaitė, J. Matukas – The relation between electrical fluctuations and current-voltage characteristics of the mid-IR laser diodes in the subthreshold region	128
R. Kumagai, M. Uchida – Fluctuation analysis of synchronous repetitive handwriting	130
Ł. Lentka, J. Smulko – Simplified method of trend removal to determine noise observed during supercapacitor's discharging	132
F. Mívalt, J. Majzner, V. Sedláková, P. Kuberský, J. Smulko, P. Sedlák – Effect of analyte flow on the voltage fluctuations of gas chemiresistors	134
T. Murata, M. A. Farahani, K. Akehi, K. Mito, N. Italura, T. Mizuno – Investigate of feeling estimation for content viewer focusing on skin surface temperature distribution using facial thermal images	136
M. Panek – Application of the correlation methods to measurement of the IR detectors noise spectral density	138
S. Sakamoto, K. Akehi, M. A. Farahani, N. Itakura, T. Mizuno – Study on mental load measurement of center of gravity fluctuation in sitting position	140
J. Siódmiak, P. Beldowski – Hyaluronic acid dynamics and its interaction with synovial fluid components as a source of the color noise	142
A. Szewczyk, Ł. Lentka, J. Smulko – Noise measurements in supercapacitors at selected floating voltages	143
M. Tretjak, S. Pralgauskaitė, J. Matukas, J. Macutkevič, J. Banys – Low frequency noise and resistivity characteristics of epoxy composites with onion-like carbon and multi-walled carbon nanotubes	145
I. S. Virt, M. Bester, O. Didovska – Determination of low frequency noise in polycrystalline ZnO	147
Alphabetical list of authors	149

Program of UPoN 2018 conference

Conference venue: the Main Building of Gdańsk University of Technology

Breakfasts for participants staying in Student Dorms will be served in the IMP PAN building (3 Smaki, see map) on the way between the Student Dorm and the Main Building

July 9, Monday

- 16:30 – 18:00 Registration (Hall in a front of the main library)
18:00 – 20:00 Welcome reception (J. Hevelius' Courtyard: beer & wine & cakes)

July 10, Tuesday

- 08:00 – 08:50 Breakfast (3 Smaki, see map)
09:00 – 09:15 Welcome of delegates to UPoN 2018 (Main Hall – Aula)
09:15 – 11:05 **Plenary session**, (Main Hall – Aula, Session Chair: J. Smulko)
09:15 – 09:45 L. B. Kish – Is there thermal noise in thermal equilibrium at zero temperature? (*opening talk*)
09:45 – 10:25 S. M. Bezrukov – Unsolved problems in ion channel dynamics (*keynote talk*)
10:25 – 11:05 P. Hakonen – Quantum vacuum, noise, and entanglement (*keynote talk*)
- 11:05 – 11:30 Coffee break
11:30 – 13:00 Parallel Sessions
Session I *Fluctuations in biological systems*, (Main Hall – Aula, Session Chair: S. Bezrukov)
11:30 – 12:00 I. Goychuk – Molecular motors operating in a highly dissipative, noisy and subdiffusive interior of living cells: How a highly efficient operation is possible, lessons from the fluctuation-dissipation theorem (*invited talk*)
12:00 – 12:20 G. Gonnella, F. Cagnetta, F. Corberi, A. Suma – Large fluctuations and dynamic phase transition in active Brownian particle systems
12:20 – 12:40 M. Lechelon, M. Gori, M. Pettini, Y. Meriguet, J. Torres, L. Varani – Can noise and diffusion help to solve the puzzle of biomolecules interactions?
12:40 – 13:00 D. Makowiec, D. Wejer, B. Graff, Z. R. Struzik – Multiscale approach in discovering cardiovascular couplings from cardiovascular time series
- Session II** *Fluctuations in materials and devices*, (Room 264, Session Chair: P. Hakonen)
11:30 – 12:00 G. Jung – Macroscopic random telegraph noise (*invited talk*)
12:00 – 12:20 J. Müller – Origin of $1/f$ - noise of strongly-correlated electrons in low-dimensional molecular metals
12:20 – 12:40 R. Pedurand, G. Hansali, V. Dolique, G. Cagnoli, L. Bellon – The CryoQPDI: a new research instrument for mechanical thermal noise investigation
12:40 – 13:00 S. Pralgauskaitė, M. Tretjak, J. Matukas, J. Macutkevič, J. Banys – Low-frequency fluctuations in composite materials with carbon nanoparticles
- 13:00 – 14:30 Lunch (J. Hevelius' Courtyard)
14:30 – 16:00 Parallel Sessions
Session III *Fluctuations in biological systems*, (Main Hall – Aula, Session Chair: I. Goychuk)
14:30 – 15:00 D. R. Chialvo – Life at the edge, complexity and criticality in biological function (*invited talk*)
15:00 – 15:20 L. B. Kish – Information storage and channel capacity of brain; an unsolved problem of noise
15:20 – 15:40 M. Barabash, W. A. T. Gibby, D. G. Luchinsky, C. Guardiani, I. A. Khovanov, P. V. E. McClintock – Combining molecular dynamics and the Chapman-Kolmogorov theory of ion transport in biological channels
15:40 – 16:00 Y. Kutovy, I. Zadorozhnyi, V. Handziuk, H. Hlukhova, M. Petrychuk, S. Vitusevich – The impact of biomolecules binding on low-frequency noise in Si NW FET biosensors
- Session IV** *Fluctuations in materials and devices*, (Room 264, Session Chair: P. Sedlák)
14:30 – 15:00 Y. F. Suprunenko, A. Stefanovska – Noise generated from a small network of time-varying phase oscillators (*invited talk*)

- 15:00 – 15:20 E. A. Miranda, A. Mehonic, W. H. Ng, J. Suñé, A. J. Kenyon – Correlated fluctuation and variability in SiO_x-based memristors: a simplified approach for circuit simulation environments
- 15:20 – 15:40 G. Cywiński, J. Przybytek, D. But, I. Yahniuk, P. Kruszewski, M. Grabowski, K. Nowakowski-Szkudlarek, P. Prystawko, P. Sai, W. Knap, G. S. Simin, S. L. Rumyantsev – Low frequency noise in wire-channel GaN/AlGaIn transistors
- 15:40 – 16:00 J. Przybytek, G. Jung – Noise features of metastable resistivity states in La_{0.86}Ca_{0.14}MnO₃ manganite
- 16:00 – 16:30 Coffee break
- 16:30 – 19:00 **Poster session**, (Main Hall – Aula)
- 17:30 – 20:00 **Committee meeting**, (Senate's Hall)

July 11, Wednesday

- 08:00 – 08:50 Breakfast (3 Smaki, see map)
- 09:00 – 10:40 **Plenary session**, (Main Hall – Aula, Session Chair: B. Andò)
- 09:00 – 09:40 F. Danneville, I. Sourikopoulos, S. Hedayat, C. Loyez, V. Hoel, A. Cappy – Open problems in brain emulating-hardware (*keynote talk*)
- 09:40 – 10:10 E. Barkai – 1/f noise on the nanoscale (*invited talk*)
- 10:10 – 10:40 M. V. Feigel'man – Non-equilibrium noise in a simple model of ageing in glassy dynamics (*invited talk*)
- 10:40 – 11:10 Coffee break
- 11:10 – 12:40 Parallel Sessions
Session V *Fluctuations in materials and devices*, (Main Hall – Aula, Session Chair: L. Varani)
- 11:10 – 11:30 E. Colomés, X. Oriols, J. Mateos, T. González – Is the nanoscale scaling of electron devices ultimately limited by noise?
- 11:30 – 11:50 E. Colomés, Z. Zhan, D. Pandey, X. Oriols – Can linear or parabolic band dispersions in 2D materials be tested by noise?
- 11:50 – 12:10 M. Petrychuk, I. Zadorozhnyi, Y. Kutovyi, S. Karg, H. Riel, S. Vitusevich – 1D electron transport in InAs nanowires
- 12:10 – 12:30 M. Seif, F. Pascal, B. Sagnes, J. El-Beyrouthy, A. Hoffmann, S. Haendler, P. Chevalier, G. Gloria – Localization of 1/f noise sources in Si/SiGe:C HBTs
- Session VI** *Theory of noise and fluctuations*, (Room 264, Session Chair: P. McClintock)
- 11:10 – 11:40 W. Belzig, J. Bülte, A. Bednorz, B. Reulet, C. Bruder – Noisy quantum measurements: just a nuisance or fundamental physics? (*invited talk*)
- 11:40 – 12:00 A. Fontana, R. Pedurand, L. Bellon – Fluctuations in a NESS: is there any universal behavior?
- 12:00 – 12:20 B. Dybiec, E. Gudowska-Nowak, I. M. Sokolov – Damped underdamped non-equilibrium stochastic harmonic oscillator
- 12:20 – 12:40 I. A. Khovanov – What is a form of the escape rate for white non-Gaussian noise?
- 12:40 – 14:00 Lunch (J. Hevelius' Courtyard)
- 14:00 – 15:50 Parallel Sessions
Session VII *Fluctuations in biological systems*, (Main Hall – Aula, Session Chair: Ł. Machura)
- 14:00 – 14:20 W. A. T. Gibby, D. G. Luchinsky, M. L. Barabash, C. Guardiani, O. F. Fedorenko, S. K. Roberts, P. V. E. McClintock – Towards a resolution of the conductivity-selectivity paradox in the NaChBac ion channel
- 14:20 – 14:40 G. Muñoz-Gil, M. A. Garcia-March, C. Manzo, A. Celi, M. Lewenstein – Anomalous diffusion in structured environments
- 14:40 – 15:00 R. Shinagawa, K. Sasaki – Enhanced diffusion in a model of molecular motors with potential switching
- 15:00 – 15:20 M. A. Farahani, M. Takagi, K. Akehi, K. Mito, T. Mizuno, N. Itakura – The analyze of conducting waves of lower leg muscle using Multichannel Surface EMG

Session VIII *Theory of noise and fluctuations*, (Room 264, Session Chair: X. Oriols)

- 14:00 – 14:30 J. Łuczka, P. Bialas – On the principle of equipartition of kinetic energy: classical versus quantum (*invited talk*)
- 14:30 – 14:50 M. Kapfer, P. Roulleau, I. Farrer, D. A. Ritchie, D. C. Glattli – Measuring the Josephson frequency of fractional charges with shot noise
- 14:50 – 15:10 K. Ptaszyński – First-passage times in single-reset and multiple-reset discrete Markovian systems
- 15:10 – 15:30 H. Zhan, G. Rastelli, W. Belzig – Light emission from noise in ac-driven contact
- 15:30 – 15:50 S. Yuvan, M. Bier – Characterizing deviations from Poissonian and IID statistics with compressed exponentials
- 15:50 – 16:10 Coffee break
- 16:10 – 17:50 Parallel Sessions
- Session IX** *Applications of noise*, (Main Hall – Aula, Session Chair: S. Pralgauskaitė)
- 16:10 – 16:30 G. Vadai, A. Antal, Z. Gingl – Spectral analysis of fluctuations in humans' daily motion using location data
- 16:30 – 16:50 J. Song, L. B. Kish – Standalone cold virtual resistor? Can we cool by a linear amplifier without non-linearity, switches, or phase transition?
- 16:50 – 17:10 V. Handziuk, F. Gasparyan, L. Vandamme, M. Coppola, V. Sydoruk, M. Petrychuk, D. Mayer, S. Vitusevich – Transport regimes in tunable gold nanoconstrictions: proposed solution by low-frequency noise spectroscopy
- 17:10 – 17:30 S. Galla, Ł. Lentka, A. Szewczyk – Supercapacitor's temperature fluctuations during charging/discharging processes
- Session X** *Noise in complex and non-linear systems*, (Room 264, Session Chair: J. Łuczka)
- 16:10 – 16:30 I. V. Tyulkina, L. S. Klimenko, D. S. Goldobin, A. Pikovsky – Effect of intrinsic noise on Chimera states in coupled Kuramoto ensembles: Towards constructing the perturbation theory for the Ott-Antonsen theory
- 16:30 – 16:50 A. Dubkov, O. Chichigina, A. Krasnova – White noise as a model of harmonic input for billiard-like systems
- 16:50 – 17:10 G. Nadzinski, M. Dobrevski, C. Anderson, P. V. E. McClintock, A. Stefanovska, M. Stankovski, T. Stankovski – Noise robustness analysis and experimental implementation of the coupling function secure communications protocol
- 17:10 – 17:30 M. Melhem, L. B. Kish – How to defend against loop current attacks in the KLJN secure key exchange scheme?
- 17:30 – 17:50 Y. Tadokoro, H. Tanaka, M. I. Dykman – Signal detection with a noisy nanomechanical bifurcation amplifier
- 19:00 – 23:00 Banquet (J. Hevelius' Courtyard)
Banquet talk by Michael Shlesinger – Pitfalls and paradoxes in the history of probability theory

July 12, Thursday

- 08:00 – 08:50 Breakfast (3 Smaki, see map)
- 09:00 – 10:40 **Plenary session**, (Main Hall – Aula, Session Chair: S. Romyantsev)
- 09:00 – 09:40 M. Levinshtein, V. Dergachev, A. Dmitriev, P. Shmakov – Lorentzians vs global warming hysteresis (*keynote talk*)
- 09:40 – 10:10 B. Andò, S. Baglio, A. R. Bulsara, V. Marletta – Open problems of utilizing noise in energy harvesting systems (*invited talk*)
- 10:10 – 10:40 N. Lörch, Y. Zhang, C. Bruder, M. I. Dykman – Fluctuations and time-translation symmetry breaking in vibrational Floquet systems (*invited talk*)
- 10:40 – 11:10 Coffee break

- 11:10 – 12:50 Parallel Sessions
Session XI *Noise in complex and non-linear systems*
Other topics of noise and fluctuations including weather and society, (Main Hall – Aula, Session Chair: N. Lörch)
- 11:10 – 11:40 C. Ciofi, G. Scandurra, G. Giusi – Unsolved problems in instrumentation for noise measurements (*invited talk*)
- 11:40 – 12:00 T. Kosztołowicz – How fluctuations of membrane permeability parameter influence on subdiffusion in a membrane system
- 12:00 – 12:20 G. Scandurra, S. Beyne, G. Cannatà, G. Giusi, C. Ciofi – On the design of an automated system for the characterization of the electromigration performance of advanced interconnects by means of low frequency noise measurements
- 12:20 – 12:40 L. B. Kish – Mathematical model for the impact of political correctness on science
- Session XII** *Theory of noise and fluctuations*, (Room 264, Session Chair: W. Belzig)
- 11:10 – 11:30 A. Dubkov – The problems of finding the steady-state probabilistic characteristics for nonlinear dynamical systems driven by white Poisson noise
- 11:30 – 11:50 Z. Kolodiy – Flicker noise problem
- 11:50 – 12:10 J. Spiechowicz, J. Łuczka – Subdiffusion via dynamical localization induced by thermal equilibrium fluctuations
- 12:10 – 12:30 M. Majka – How to embed the self-assembly dynamics in the Langevin equations with spatio-(temporally) correlated noise?
- 12:30 – 12:50 V. Holubec, T. Novotný – Effects of noise-induced coherence on the performance of quantum absorption refrigerators
- 12:50 – 13:10 Closing Ceremony, (Main Hall – Aula)
- 13:10 – 14:30 Lunch (J. Hevelius' Courtyard)
- 16:00 – 20:00 Excursion to Old Town (meeting at the front of the Main Building)

July 13, Friday

- 08:00 – 09:00 Courtesy Breakfast and Goodbye – Social (3 Smaki, see map)

POSTERS

(in an alphabetical order)

- H. Asada, K. Akehi, M. A. Farahani, N. Itakura, T. Mizuno – A study on simple measurement of mental and physical burden of patients during dental treatment
- S. Babicz, B. Stawarz-Graczyk – Fluctuations of the red blood cells
- A. Bednorz, M. Frączak, S. Sołtan, W. Belzig – Is energy conserved when nobody looks?
- A. Crépieux, S. Sahoo, T. Q. Duong, R. Zamoum, M. Lavagna – Finite-frequency noise in a Kondo quantum dot with asymmetric coupling to the reservoirs
- Z. Czaja, M. Kowalewski – A noise signal generation method for microcontrollers with DACs
- A. Geremew, S. Rumyantsev, M. A. Bloodgood, T. T. Salguero, A. A. Balandin – Low-frequency noise in quasi-1D van der Waals nanowires implemented with transition metal trichalcogenides
- J. Glemža, V. Palenskis, S. Pralgauskaitė, J. Matukas – The relation between electrical fluctuations and current-voltage characteristics of the mid-IR laser diodes in the subthreshold region
- R. Kumagai, M. Uchida – Fluctuation analysis of synchronous repetitive handwriting
- Ł. Lentka, J. Smulko – Simplified method of trend removal to determine noise observed during supercapacitor's discharging
- F. Mívalt, J. Majzner, V. Sedláková, P. Kuberský, J. Smulko, P. Sedlák – Effect of analyte flow on the voltage fluctuations of gas chemiresistors

- T. Murata, M. A. Farahani, K. Akehi, K. Mito, N. Italura, T. Mizuno – Investigate of feeling estimation for content viewer focusing on skin surface temperature distribution using facial thermal images
- M. Panek – Application of the correlation methods to measurement of the IR detectors noise spectral density
- S. Sakamoto, K. Akehi, M. A. Farahani, N. Itakura, T. Mizuno – Study on mental load measurement of center of gravity fluctuation in sitting position
- J. Siódmiak, P. Bełdowski – Hyaluronic acid dynamics and its interaction with synovial fluid components as a source of the color noise
- A. Szewczyk, Ł. Lentka, J. Smulko – Noise measurements in supercapacitors at selected floating voltages
- M. Tretjak, S. Pralgauskaitė, J. Matukas, J. Macutkevič, J. Banys – Low frequency noise and resistivity characteristics of epoxy composites with onion-like carbon and multi-walled carbon nanotubes
- I. S. Virt, M. Bester, O. Didovska – Determination of low frequency noise in polycrystalline ZnO

Is there thermal noise in thermal equilibrium at zero temperature?

Laszlo B. Kish

Department of Electrical and Computer Engineering, Texas A&M University, TAMUS 3128, College Station, TX 77843-3128, USA
e-mail address: Laszlokish@tamu.edu

I. INTRODUCTION

This talk is addressing a 60 years old, famous unsolved problem of noise (UPoN). With the organizers we have made an effort to attract a "critical mass" of related theorists and experimentalists at this meeting with the hope that, at the end of the conference, the major UPoN questions about the zero-point thermal noise will be answered. (Yet the problem may be harder than that due to the lack of deep-enough understanding of quantum measurements.)

The question is clear:

II. IS THERE THERMAL NOISE AT ZERO TEMPERATURE?

Advanced quantum theories (Fluctuation-Dissipation Theory, FDT) treating the problem are incomplete because they do not involve the measurement process. This may seem unimportant because Johnson noise in a classical physical system is independent from the way of measurement however quantum physics is a different issue.

Even though, zero-point energy does exist, noise is much more than that: a stochastic energy exchange with the coupled environment. A zero-point noise in thermal equilibrium can directly lead to a perpetual motion machine [1].

There is a long list of papers objecting zero-point thermal noise (see references in [1]) and among the many arguments the Second Law [1] and standard solid state physics [2] also forbid its existence in *thermal equilibrium*. Many theorists believe that zero-point thermal noise exists but there are others who allow systems without this noise component, too [3].

Theoreticians Kyle Sundqvist and later Mark Dykman have recently pointed out in private communications that, in the more advanced second quantization theories of the FDT, the claimed zero-point noise comes from "negative" frequencies. This is interpreted as an absorption process indicating the need of an external energy drive. If it is so, the puzzle is partially solved and the answer is:

There is no thermal noise at zero temperature, because the fundamental notion of thermal noise inherently means a *noise in thermal equilibrium* and no energy drive can be supposed to generate this noise then.

Indeed, in all the experiments showing quantum corrections in thermal noise, the resistor was fed power, including during the most recent ones [4].

Yet, such a simple interpretation is only a step toward the correct direction and it does not provide the final solution because it triggers a number of new unsolved problems to be shown.

-
1. L.B. Kish, G.A. Niklasson, C.G. Granqvist, "Zero-point term and quantum effects in the Johnson noise of resistors: A critical appraisal", *J. Stat. Mech.* (2016) 054006.
<http://arxiv.org/abs/1504.08229>
 2. L.B. Kish, G.A. Niklasson, C.G. Granqvist, "Zero thermal noise in resistors at zero temperature", *Fluct. Noise. Lett.* **15** (2016) 1640001. Online:
http://www.researchgate.net/publication/303959024_Zero_Thermal_Noise_in_Resistors_at_Zero_Temperature
 3. A. Crepieux, P. Eymeoud, F. Michélini, "Getting information from the mixed electrical-heat noise", Proc. 24th ICNF, Lithuania, 2017.
 4. P. Lahteenmaki, Gh. Sorin Paraoanu, P.J. Hakonen, "Vacuum-noise-induced multimode correlations in a superconducting cavity", Proc. 24th ICNF, Lithuania, 2017.

Unsolved problems in ion channel dynamics

Sergey M. Bezrukov

National Institutes of Health, NICHD, Section on Molecular Transport

9000 Rockville Pike, Bethesda, MD 20892, USA

e-mail address: bezrukos@mail.nih.gov

Analytical understanding of particle escape from deep wells over energy and/or entropy barriers belongs to the unsolved problems of ion channel dynamics. Recent experimental examples are multiple; among others they include trapping and escape of charged polymer molecules from voltage-biased beta-barrel channels of biological membranes^{1,2}. Unsurprisingly, barrier crossing dynamics have attracted attention of many researchers, who frequently model these processes as one-dimensional diffusion of a particle in a potential of mean force. To gain deeper insights into such dynamics, we analyze the “fine structure” of particle trajectories in such systems. We divide the escape trajectories into two segments: a looping segment, when the particle unsuccessfully tries to escape but returns to the trap bottom, and a direct-transit segment, when it finally escapes moving without returning to the bottom. By using both the analytical approaches and Brownian dynamics simulations, we show that the force/potential dependences of the two corresponding mean times are qualitatively different. The mean looping time monotonically increases with the external force

pushing the particle to the trap bottom or with the increasing entropic barrier at the exit. In contrast to this intuitively appealing result, the mean direct-transit time shows rather counterintuitive behavior: it is reduced by force application independently of whether the force pushes the particles to the trap bottom or to the trap exit³. Also, one of the intriguing findings is that the direct-transit time of a particle escaping from the entropy potential well of a three-dimensional regular cone turns out to be independent of the depth of this well, i.e., the escape occurs as in free diffusion⁴. Are entropic traps special?

ACKNOWLEDGEMENTS

This study was supported by the Intramural Research Program of the Eunice Kennedy Shriver National Institute of Child Health and Human Development.

¹ D.P. Hoogerheide, P.A. Gurnev, T.K. Rostovtseva, and S.M. Bezrukov. Real-time nanopore-based recognition of protein translocation success. *Biophys. J.* 114, 772–776 (2018).

² J. Comer. Chasing a protein’s tail: Detection of polypeptide translocation through nanopores. *Biophys. J.* 114, 759–760 (2018).

³ A.M. Berezhkovskii, L. Dagdug, and S.M. Bezrukov. A new insight into diffusional escape from a biased cylindrical trap. *J. Chem. Phys.* 147, 104103 (2017).

⁴ A.M. Berezhkovskii, L. Dagdug, and S.M. Bezrukov. First passage, looping, and direct transition in expanding and narrowing tubes: Effects of the entropy potential. *J. Chem. Phys.* 147, 134104 (2017).

Quantum vacuum, noise, and entanglement

Perti Hakonen¹

¹ *Low Temperature Laboratory, Department of Applied Physics, Aalto University, Espoo, Box 15100, FI-00076 AALTO, e-mail address: pertti.hakonen@aalto.fi*

I. INTRODUCTION

The role of quantum noise in mesoscopic physics has been investigated intensively since the end of 80ies. Studies of quantum noise can be crudely divided into three categories: shot noise, full counting statistics, and quantum measurement and entanglement. At present, the main stream research of quantum noise deals with fundamental questions in quantum measurement and entanglement. This field is closely connected to quantum information science and technology, and various basic problems remain to be solved, in particular concerning how to use the quantum vacuum as a resource for producing entanglement, multifrequency correlations, or even teleportation.

II. NOISE AND ITS MEASUREMENT

Shot noise on nanoscale, including its frequency and temperature dependence, is excellently described by the scattering approach pioneered by Landauer and Buttiker¹. It was quickly realized that typical experiments do not measure the symmetrized correlator as expected in classic textbooks such as Landau and Lifshitz², but instead an unsymmetrized correlator is the proper one. The success of the scattering theory and the necessity of an unsymmetrized correlator has been verified in several experiments³. Full counting statistics on its part has increased our understanding of current-current correlations by providing a complete picture of current fluctuations and their distributions⁴.

In recent years, cavity quantum electrodynamics at microwave frequencies has become one of the major thrusting platforms for studies of noise, correlations, and entanglement in nanocircuits. Qubits have been shown to act as excellent noise detectors, in which the dephasing and relaxation times are sensitive to different combinations of noise correlators⁵.

When employing qubits as detectors, the actual quantum measurement process becomes important. Many of the theoretical concepts of weak quantum measurements⁶ have been verified recently in qubit experiments owing to the availability of quantum limited Josephson junction parametric and traveling wave amplifiers. It has also been recognized that a cross correlation measurement may provide indispensable information concerning entanglement, for example, in a Cooper pair splitter⁷.

Essentially, the questions to be addressed in this field are related to specific settings in which a particular experiment is carried out: the experimental setup specifies what kind of noise correlator enters the interpretation of the measured correlations and noise distributions.

III. ENTANGLEMENT

Dynamical Casimir effect. It has been known already for some time that quantum vacuum itself can induce correlations and entanglement.⁸ In the nanoscale, a large amount of effort has been

put on studies of the Dynamical Casimir effect (DCE), in which virtual quanta in the quantum vacuum are converted into real photons, as has well been demonstrated in experiments on superconducting quantum circuits^{9,10}.

In DCE systems, the quantum noise is squeezed by parametric driving of the boundary condition (mirror) or the dielectric constant (speed of light). In the case of a single frequency, the amount of fluctuations is redistributed between two quadratures. In the case of two mode squeezing, the correlations exist between the quadratures of two separate frequencies. Consequently, a 4x4 covariance matrix is needed to characterize fully the correlations in the system. The degree of entanglement can be described by the relative magnitude of the diagonal and off-diagonal matrix elements of the covariance matrix⁹.

There are still basic open problems in the generation of quanta by DCE. These are related to the frequency dependence of the generated power. Instead of white or linearly growing spectrum, the power has a distinct parabolic spectrum¹¹. The observation of this spectrum has turned out to be challenging, both due to measurement sensitivity issues as well as calibration problems in cryogenic mK measurement setups. Furthermore, the behavior under multiple pump signals presents questions how the created entanglement behaves under conflicting tendencies from different pumps. Well-controlled multifrequency correlation at microwave frequencies may present an useful resource for “one way quantum computation”, if clever computational schemes can be conceived for it^{12,13}. Finally, how do these correlations become generated as a function of time when the pumping is turned on? This issue is closely related to the so called past future entanglement (see below).

Unruh effect and Hawking radiation. A quite related effect to DCE is the Unruh effect^{14,15}, which is a basic characteristics of general relativity. An accelerating observer sees the vacuum as a thermal bath with a noise temperature $T = \hbar a / k_B$. The Unruh effect is kin to generation of Hawking radiation¹⁶. Hawking radiation is brought about by a “black hole boundary” in the propagation of radiation: virtual photon-pair fluctuations are split apart on the two sides of such a boundary, which can be created e.g. by spatial control of the speed of light vs the propagation of the boundary¹⁷. Hawking radiation has recently been observed in acoustic analog experiments based on scrutiny of density-density correlation functions in modulated Bose Einstein condensates¹⁸. There are several ideas for further analog experiments for testing our understanding of Hawking radiation. One recent, promising setting deals with two dimensional electron gas with modulated particle and hole distributions¹⁹. Its prediction for the emitted noise power is on the order of 1 K, which would be easy to measure. The general problem with all these analog Hawking radiation and Unruh effect experiments is the question how well they correspond to the actual cosmological problem and what one can really conclude from them.

Past future entanglement. Recently, a cavity QED setting was proposed as an analog of the Unruh effect^{20,21}. This is based on the fact that quantum vacuum can produce entanglement between the past and the future. Thus, if one starts a measurement at time $t = 0$,

the detector records a signal because of the past-future entanglement. In certain sense, the switching on of the detector acts like the modulation of the mirror in the DCE effect, and the virtual fluctuation is pulled into existence by the switching. According to the estimates of Ref. 20, these experiments are marginally possible with present-day techniques as they require extremely fast and precise microwave pulses on time scales of a few tens of picoseconds.

¹ Yu. Nazarov and Ya. Blanter, *Quantum transport: Introduction to Nanoscience* (Cambridge University Press, 2009).

² L. D. Landau and E. M. Lifshitz, *Statistical Physics*, Vol 5 (Elsevier, Amsterdam, 1980).

³ Ya. M. Blanter, M. Büttiker, *Phys. Rep.* **336**, 1 (2000).

⁴ G. B. Lesovik and I. A. Sadovskyy, *Physics-Uspekhi* **54**, 1007 (2011).

⁵ R. J. Schoelkopf, A. A. Clerk, S. M. Girvin, K. W. Lehnert, M. H. Devoret, in *Quantum Noise in Mesoscopic Physics*, (Yu. V. Nazarov, ed., Kluwer Academic, 2003).

⁶ A. Korotkov in *Quantum Machines: Measurement and Control of Engineered Quantum Systems* (M. Devoret, B. Huard, R. Schoelkopf, and L. Cugliandolo, eds, Oxford University Press, 2014).

⁷ Z. B. Tan, D. Cox, T. Nieminen, P. Lähteenmäki, D. Golubev, G. B. Lesovik, and P. J. Hakonen, *Phys. Rev. Lett.* **114**, 96602 (2015).

⁸ See, e.g., B. Reznik, *Found. Phys.* **33**, 167 (2003).

⁹ P. Lähteenmäki, G.S. Paraoanu, J. Hassel, and P.J. Hakonen. *Proc. Natl. Acad. Sci. U. S. A.* **110**, 4234 (2013).

ACKNOWLEDGEMENTS

I wish to thank Sorin Paraoanu and Alexander Korotkov for useful discussions. This work has been supported by the Academy of Finland grant no. 314448, the Center of Excellence in Quantum Technology (grant no. 312295), and the ERC Adv grant no. 670743. The DCE work benefited from the facilities of the Low Temperature Laboratory infrastructure at Aalto University which is part of the European Microkelvin Platform.

¹⁰ P. Lähteenmäki, G. S. Paraoanu, J. Hassel, and P. J. Hakonen, *Nat. Commun.* **7**, 12548 (2016).

¹¹ J.R. Johansson, G. Johansson, C.M. Wilson, and F. Nori, *Phys. Rev. Lett.* **103**, 147003 (2009).

¹² N. C. Menicucci, S. T. Flammia, and O. Pfister, *Phys. Rev. Lett.* **101**, 130501 (2008).

¹³ D. E. Bruschi, C. Sabín, P. Kok, G. Johansson, P. Delsing, and I. Fuentes. *Sci. Rep.* **6**, 18349 (2016).

¹⁴ W. G. Unruh, *Phys. Rev. D.* **14**, 870 (1976).

¹⁵ L. C. B. Crispino, A. Higuchi, and G. E. A. Matsas, *Rev. Mod. Phys.* **80**, 787 (2008).

¹⁶ P. D. Nation, J. R. Johansson, M. P. Blencowe, and F. Nori, *Rev. Mod. Phys.* **84**, 1 (2012).

¹⁷ P. D. Nation, M. P. Blencowe, A. J. Rimberg, and E. Buks, *Phys. Rev. Lett.* **103**, 87004 (2009).

¹⁸ J. Steinhauer, *Nat. Phys.* **12**, 959 (2016).

¹⁹ M. Stone, *Class. Quantum Grav.* **30**, 085003 (2013).

²⁰ C. Sabín, B. Peropadre, M. Del Rey, and E. Martín-Martínez, *Phys. Rev. Lett.* **109**, 033602 (2012).

²¹ S. J. Olson and T. C. Ralph, *Phys. Rev. Lett.* **106**, 110404 (2011).

Molecular motors operating in a highly dissipative, noisy and subdiffusive interior of living cells: How a highly efficient operation is possible, lessons from the fluctuation-dissipation theorem.

Igor Goychuk

Institute of Physics and Astronomy, University of Potsdam, Karl-Liebknecht-Str. 24/25, 14476 Potsdam-Golm, Germany
e-mail address: igoychuk@uni-potsdam.de

I. INTRODUCTION

Thermodynamic efficiency of molecular motors can be very high. For example, ATPase has efficiency reportedly near to 100% at its operating frequency¹. This is taken by many physicists with a misbelief. Indeed, how can it be in a highly dissipative interior of living cells? Many physicists believe that one should minimize friction to arrive at the highest efficiency of nanomotors and/or go to very low temperatures. Others believe that thermodynamic efficiency at maximum power cannot exceed 50%. These two misbeliefs are deeply based on misunderstanding the role played by the fluctuation-dissipation theorem (FDT), thermal noises and nonlinearity in micro- and nanoworld², especially for isothermal Brownian and molecular motors. They gave rise to such misleading concepts as Hamiltonian dissipation-less ratchets, which in fact operate at zero thermodynamic efficiency². In this talk, I will show within some basic models of molecular motors that such a very high efficiency can be achieved even in crowded viscoelastic environments like cytosol, even with formally infinite, in the Markovian approximation, effective viscous friction²⁻⁵. Though Markovian approximation cannot be applied in such media with long-ranging viscoelastic correlations⁶.

II. MAIN CONCEPTS

Every enzyme, including molecular motors such as kinesins, performs cyclic operation in its conformation space⁷, which can be modeled by sliding down in a periodic potential under the driving force provided e.g. by ATP hydrolysis, see in Fig. 1,

$$\eta\dot{\phi} = -\frac{\partial V(\phi)}{\partial \phi} + F - f_L + \xi(t), \quad (1)$$

where $V(\phi + 2\pi) = V(\phi)$ is periodic energy profile of enzyme cycling among its conformational states (e.g. free, substrate bound, product bound). Furthermore, $F = \Delta\mu/2\pi$ is the driving force provided by the free energy $\Delta\mu$ released at the substrate (e.g. ATP molecule) transformation into the products, f_L is load, $\xi(t)$ is thermal force, and η is frictional constant. The heat is dissipated by the frictional force $\eta\dot{\phi}$. However, thermal random force supplies energy to a molecular machine. This is a crucial point which some

still fail to recognize, and the reason why Brownian motion never stops. At thermal equilibrium at temperature T , the both processes are balanced on average which yields the (second) FDT by Kubo, $\langle \xi(t')\xi(t) \rangle = 2\eta k_B T \delta(t' - t)$.

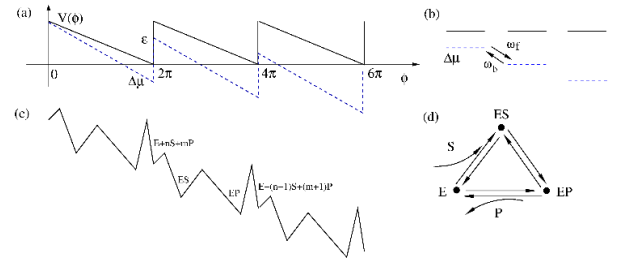


FIG1. Cyclic enzyme operation (in part **d**) as sliding in a tilted periodic “chemical phase space” potential (in **c**) for the system of Enzyme +Substrate+Product^{2,7}. Each period corresponds to transforming one molecule of substrate (e.g. ATP) to product (ADP + P_i). Free energy of ATP hydrolysis $\Delta\mu$ is used to drive one cycle. Ratchet potential in part **a** provides a simplest abstraction in the continuous diffusion space. Likewise, “chemical bi-cycle”^{2,7} in part **b** is the minimal discrete state model. Sliding down in chemical space can be used to do e.g. a mechanical work against a load until some equivalent stalling force $F = \Delta\mu/2\pi$ will be reached.

Notice that periodic potential does not contribute to the energy balance in a very long run. Hence, the mean energy supplied by the driving force, $P_{in}(t) = F\langle\dot{\phi}(t)\rangle \sim t$ scales linearly in time. Likewise scales also the useful work done against the load, $W(t) = f_L\langle\phi(t)\rangle \sim t$. Thermodynamic efficiency in this model is $R = f_L\langle\dot{\phi}(t)\rangle / F$, independently of $V(\phi)$. Clearly, it is close to 100% when $f_L \rightarrow F$. However, then the motor operates infinitesimally slow, at zero power. The turnover frequency of the “catalytic wheel”, $\omega = \langle\dot{\phi}\rangle \rightarrow 0$, vanishes. One is more interested, of course, in the operation at maximal power, $P_W = \dot{W}$. Consider first, the simplest toy model with $V(\phi)=0$. Then, $\omega = (F - f_L)/\eta$ and $P_W = \frac{f_L(F - f_L)}{\eta}$, optimizes at $f_L = F/2$, with $R = 0.5$. This gave rise to misbelief that 50% is the principal bound for operation at the maximum power. However, already the simplest nonlinear model with ratchet potential in Fig. 1, a, which can be solved exactly, see Eq. (19) and Fig. 2 in Ref.², dismantles this belief completely. For a sufficiently large driving force $\Delta\mu \gg k_B T$ in can also approach 100%.

However, what happens if the enzyme dynamics is subdiffusive and it is governed by a generalized (fractional) Langevin equation? It reads⁶,

$$\eta_\alpha \frac{d^\alpha \phi}{dt^\alpha} = -\frac{\partial V(\phi)}{\partial \phi} + F - f_L + \xi_\alpha(t), \quad (2)$$

where $\frac{d^\alpha \phi}{dt^\alpha} := \frac{1}{\Gamma(1-\alpha)} \int_0^t \frac{\dot{\phi}(t') dt'}{(t-t')^\alpha}$, $0 < \alpha < 1$, is fractional Caputo derivative, η_α is fractional friction coefficient, and $\xi_\alpha(t)$ is fractional Gaussian noise obeying FDT, $\langle \xi_\alpha(t) \xi_\alpha(t') \rangle = k_B T \eta_\alpha / |t - t'|^\alpha$. Then, in the potential-free case, $\langle \phi(t) \rangle = \frac{(F-f_L)t^\alpha}{\eta_\alpha \Gamma(1+\alpha)}$ is sublinear in time. Enzyme cannot be characterized by a turnover frequency anymore, but rather by a fractional turnover velocity $\omega_\alpha = \frac{F-f_L}{\eta_\alpha}$. Both the driving energy and the useful work scale sub-linearly in time with the same exponent α . The notion of power must be replaced with sub-power, and, nevertheless, in this simplest illustrative case, thermodynamic efficiency is the same $R = f_L/F$. It can reach 100%. Moreover, the optimal operation at maximum sub-power is also arrived at $f_L = F/2$, with thermodynamic efficiency of 50%.

However, the real life is more complex and more realistic models of molecular motors must be considered⁸, like one in Fig.2.

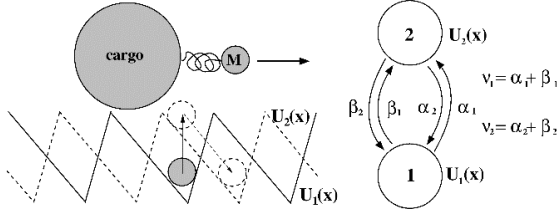


FIG. 2 Flashing ratchet motor driven by a chemical “bi-cycle”⁶ with spatially-dependent (allosteric) normal rates, like in Fig. 1, b. The motor pulls cargo on an elastic linker³ in subdiffusive environment. Useful work is done against an extra load f_L applied to the motor (not shown).

Here, kinesin motor moves in a periodic electrostatic binding potential along microtubule, which fluctuates upon the motor conformational changes caused by ATP binding and hydrolysis (driving “catalytic wheel”) that in turn are influenced by the motor position along microtubule (allostery)⁸. In addition³, the motor pulls on an elastic linker some cargo subjected to viscoelastic memory friction like in Eq. (2). It has been shown³⁻⁵ that a sufficiently strong motor (large amplitude of the binding potential U_0) can easily beat subdiffusional slowness and realize a perfect normal ratchet transport of sufficiently small cargos. For larger cargos, transport is anomalous, $\langle x(t) \rangle \propto t^{\alpha_{eff}}$, with $\alpha \leq \alpha_{eff} \leq 1$. Thus scales also the useful work done against the load, $W(t) \propto t^{\alpha_{eff}}$. The input energy is proportional to the number of ATP molecules hydrolyzed (or the number of chemical cycles accomplished in the forward, “sliding” direction, cf. Fig. 1, b). Generally, $P_{in}(t) \propto t^\gamma$, and

thermodynamic efficiency slowly decays, $R(t) \propto 1/t^\lambda$ with $0 < \lambda = \gamma - \alpha_{eff} \leq 1 - \alpha_{eff}$. For small cargos and/or $U_0 \leq \Delta\mu$, $\gamma \approx 1$, and the ratchet model with constant switching rates^{4,5} applies. However, for a strong motor carrying a large cargo the mechanical motion can result into subdiffusive enzyme turnovers: see the blue curve in Fig. 3, where $\gamma \approx 0.62$ at the maximum efficiency with $\alpha_{eff} \approx 0.56$. In this case, anomalously slow enzyme turnovers are nearly synchronized with subdiffusive transport of cargo. Thermodynamic efficiency exceeds 70% on a biologically relevant time scale and it decays very slow with $\lambda \approx 0.06$.

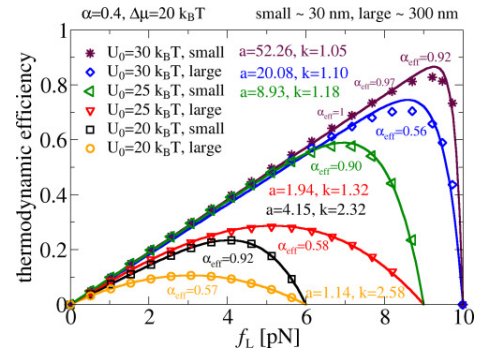


FIG. 3. Thermodynamic efficiency (snapshot at largest time in simulations, corresponding to 3 sec) vs. load³. It can be over 50% at maximal sub-power.

Fit (full lines) is done with $R = \frac{(f_L/F)}{k} [1 - (f_L/F)^a]$, where F is the corresponding stalling force, which depends on U_0 . $R_{max} = \frac{1}{k} a / (1+a)^{1+1/a}$, at $f_L = F / (1+a)^{1/a}$, with fitting parameters a and $k \geq 1$ shown in the plot.

ACKNOWLEDGEMENTS

Funding of this research by the Deutsche Forschungsgemeinschaft (German Research Foundation), Grant GO 2052/3-1 is gratefully acknowledged.

- 1 S. Toyabe and E. Mineyuki, New J. Phys. **17**, 015008 (2015).
- 2 I. Goychuk, Beilstein J. Nanotechnol. **7**, 328 (2016).
- 3 I. Goychuk, Phys. Biol. **12**, 016013 (2015).
- 4 I. Goychuk, V.O. Kharchenko, R. Metzler, Phys. Chem. Chem. Phys. **16**, 16524 (2014).
- 5 I. Goychuk, V.O. Kharchenko, R. Metzler, PLoS ONE **9**, e91700 (2014).
- 6 I. Goychuk, Adv. Chem. Phys. **150**, 187 (2012); Phys. Rev. E **80**, 046125 (2009).
- 7 T. L. Hill, Free Energy Transduction and Biochemical Cycle Kinetics (Berlin, Germany, 1980).
- 8 R. D. Astumian and M. Bier, Biophys. J. **70**, 637 (1996); F. Jülicher, A. Ajdari, and J. Prost, Rev. Mod. Phys. **69**, 1269 (1997).

Large fluctuations and dynamic phase-transition in active brownian particle systems

Giuseppe Gonnella¹, Francesco Cagnetta², Federico Corberi³, and Antonio Suma⁴

¹ Dipartimento di Fisica, Università di Bari, via Amendola 173, 70126 Bari, Italy
e-mail: gonnella@ba.infn.it

² SUPA, School of Physics, University of Edinburgh - Edinburgh EH9 3JZ, UK
e-mail: francesco.cagnetta.91@gmail.com

³ Dipartimento di Fisica E.R. Caianiello, Università di Salerno, via Giovanni Paolo II 132, 8408 Fisciano (SA), Italy
e-mail: corberi@sa.infn.it

⁴ Institute for Computational Molecular Science, College of Science and Technology, Temple University, Philadelphia, PA 19122
e-mail: antonio.suma@gmail.com

I. INTRODUCTION

We study the statistics, in stationary conditions, of the work W_τ done by the active force in different systems of self-propelled particles in a time τ . We show the existence of a critical value W_τ^\dagger such that fluctuations with $W_\tau > W_\tau^\dagger$ correspond to configurations where interaction between particles plays a minor role whereas those with $W_\tau < W_\tau^\dagger$ represent states with single particles dragged by clusters. The twofold behavior of fluctuations is fully mirrored by the probability distribution $P(W_\tau)$ of the work, which does not obey the large deviation principle for $W_\tau < W_\tau^\dagger$, and presents a singularity at W_τ^\dagger . The behavior of $P(W_\tau)$ can be interpreted as due to a phase transition occurring at the level of fluctuating quantities, and can be contextualized in the general mathematical framework of large deviation theory (LDP)¹.

II. ACTIVE BROWNIAN PARTICLES

We considered several two-dimensional systems of N active particles² with different shapes, such as spherical colloids, dumbbells, tetra-bells, or convex rod-like molecules. For concreteness, we will refer to the simplest case of colloids, with other cases governed by analogous equations of motion. The position \mathbf{x}_i of particle i follows the Langevin equation of motion:

$$m \frac{d^2 \mathbf{x}_i}{dt^2} = -\gamma \frac{d\mathbf{x}_i}{dt} - \nabla_i U + \mathbf{F}_a + \sqrt{2k_B T \gamma} \boldsymbol{\xi}_i(t), \quad (1)$$

with m being the mass, γ the friction coefficient and T the temperature. U is a Weeks-Chandler-Anderson repulsive potential between particles, while \mathbf{F}_a is a self-propulsion force term, which has constant modulus and direction θ ruled by another stochastic equation of motion:

$$\frac{d\theta_i}{dt} = \sqrt{2D_R} \xi_i^R(t). \quad (2)$$

Both ξ_i and ξ_i^R are uncorrelated Gaussian white noises, with zero mean and variance 1. D_R is the rotational diffusion coefficient, set to $D_R = \frac{3k_B T}{\sigma^2 \gamma}$, with σ being the diameter of the disks. The most relevant dimensionless numbers are the area fraction covered by the particles $\phi = \frac{N\pi\sigma^2}{4A}$, with A the area of the simulation domain, and the Péclet number $Pe = \frac{2F_a \sigma}{k_B T}$.

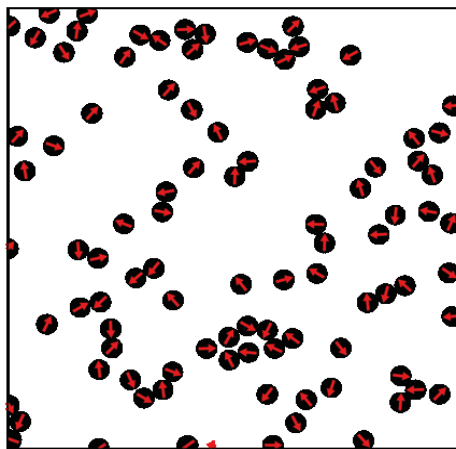


FIG. 1. A snapshot of active colloids. The arrow shows the direction of the active force.

At sufficiently high Péclet number and covered area fraction, both disks and dumbbells have been demonstrated to undergo a motility induced phase separation (MIPS)^{3,4}, with two phases of different densities coexisting together. The first phase is gaseous, with the particles being distributed randomly, while in the second phase particles cluster in a highly-packed state. This behavior is somehow reminiscent of a liquid-gas phase transition, even if in absence of any sort of attractive interactions. It is the active force, alone, that favors aggregation.

In this work⁵ we consider a different region of the parameter space, at low densities, where macroscopic aggregation is not observed. A typical configuration of active disks in this region is shown in Fig.1.

III. WORK FLUCTUATIONS

In the low density regime previously described we have evaluated the probability distribution $P(W_\tau)$ of the quantity

$$W_\tau = \frac{1}{\tau} \int_t^{t+\tau} \mathbf{F}_a(t') \cdot \mathbf{v}_i(t') dt' \quad (3)$$

that we called active work and that, at least for disks, can be directly related to the active component of the pressure exerted by each particle. The large deviation function would correspond to the large τ limit of

$$I(W_\tau) = -\frac{1}{\tau} \ln P(W_\tau). \quad (4)$$

Our main results concern the behavior of the distribution $P(W_\tau)$, shown in Fig. 2 for the disks at $\phi = 0.1$ and different Pe . In the case without active force and at $Pe=1$ the distributions are not significantly different from a gaussian (continuous line in Fig. 2), corresponding to the single-particle case which can be computed analytically. On the other hand, the character of the distributions changes dramatically by increasing Pe . The curves remain peaked around a value close to the maximum analytically found for the case of a single active particle $\langle W_\tau \rangle_0$, and are still Gaussian on the whole region to the right of the peak and immediately on its left. However, for W_τ smaller than a critical threshold W_τ^\dagger (represented as a vertical arrow in Fig. 2) we have an abrupt change, with $\ln P(W_\tau)$ having an approximately linear behavior. These result suggest the occurrence of a singular behavior in the large deviation function $I(W_\tau)$.

In order to understand which events do contribute to the linear tails of $\ln P(W_\tau)$, we isolated particles trajectories with a fixed value of W_τ . We found that events with a value of W_τ smaller than W_τ^\dagger correspond to particles having their polar axis pointing against a cluster moving in the opposite direction and therefore are related to the presence of anomalous and significant fluctuations in the system. We observed this behavior for all the active particle models considered.

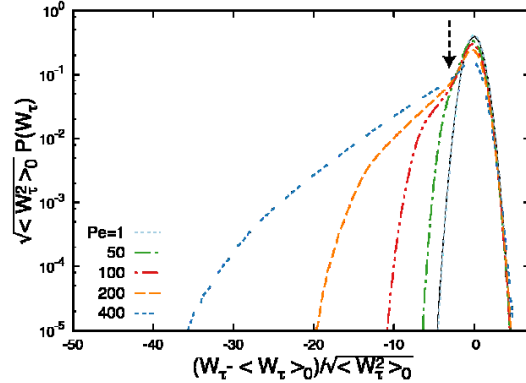


FIG. 2. Probability distributions (on log-scale) of W_τ for disks at $\phi = 0.1$ and $\tau = 10$, at $Pe = 1, 50, 100, 200, 400$. The distributions are rescaled using $\langle W_\tau \rangle_0$ and $\langle W_\tau^2 \rangle_0$ of the single particle distribution, plotted here as a continuous line. The threshold is signaled by a vertical black arrow.

IV. CONCLUSIONS

We have shown that, beyond the macroscopic MIPS transition previously discussed, active particles also exhibit a transition at fluctuating level. This is between a gaseous phase, where the particle internal energy is spent into self-propulsion, and one where this energy supports cluster formation, even on short time scales. The associated breakdown of the LDP reflects the importance, in terms of probabilistic weight, of clustering-related fluctuations with respect to thermal ones.

¹ H. Touchette, Phys. Rep. **478**, 1 (2009).

² J. Elgeti, R. Winkler, and G. Gompper, Rep. Prog. Phys. **78**, 056601 (2015).

³ Y. Fily, M. C. Marchetti, Phys. Rev. Lett. **108**, 235702 (2012)

⁴ L. F. Cugliandolo, P. Digregorio, G. Gonnella, A. Suma, Phys. Rev. Lett. **119**, 268002 (2017).

⁵ F. Cagnetta, F. Corberi, G. Gonnella, and A. Suma, Phys. Rev. Lett. **119**, 158002 (2017).

Can Noise and Diffusion Help to Solve the Puzzle of Biomolecules Interactions?

M. Lechelon¹, M. Gori¹, M. Pettini¹, Y. Meriguet², J. Torres², L. Varani²

¹Center of Theoretical Physics, Aix-Marseille University, CNRS UMR 7332, Marseille, France,

²Institute of Electronics and Systems, Montpellier university, CNRS UMR 5214, Montpellier, France

e-mail address: luca.varani@umontpellier.fr

I. THE UNSOLVED PROBLEM

Living beings are able to interact with or react to their environment and regulate the processes occurring at many levels down to the molecular one in remarkable ways. This property is called homeostasis and is driven by many complex interactions in cells through biomolecules mainly proteins and nucleic acids¹. Two major questions arise in this context:

- **What makes the biomolecules to interact and stick together at short distances?**
- **How can these biomolecules find each others in cells at a large distance, that is, up to several hundreds of nanometers?**

While interactions among biomolecules such as DNA, RNA or proteins do not exhibit strict spatial organization, the maintenance of the homeostasis and of the cell functions are based on a precise timing, with temporally, or dynamically, driven patterns. It implies that the right biomolecules have to be at the right place, at the right time and following the right sequence/organization. Biomolecules are generically experiencing Brownian diffusion, due to random collisions with water molecules, however such efficient encounters between cognate partners of biochemical reactions can hardly be explained only by such random forces, especially when the concentration of one interactor is low, because random encounters alone would lead to average meeting times much larger than the observed ones.

II. STATE OF THE ART

During the last decades, an attempt to account for accelerating mechanisms resorted to the idea of facilitated diffusion, that has been proposed by Richter and Eigen² to describe the unspecifically binding of the repressor to the DNA and its diffusion along the chain to the operator region that serves as a target for this process. But while this model explains how molecules can quickly find their targets by sliding on the DNA strands, it fails to explain how free simple components in bulk cytoplasm can be recruited with such a precision.

Consequently, the present understanding and description of the biomolecular dynamics can be considered incomplete, and, in fact, a progress was sought by putting forward the hypothesis of the existence of mutual interactions between the biomolecular components within the cellular length scale (distances between 0.1 and 1 μm), making the cognate partners able to interact dynamically and with precision. The selectivity of the interactions is another major characteristic to establish the encounter between the right molecules, and an activation mechanism is required in order to make these interactions act only at the right moment.

Nowadays biomolecular interactions are mainly described as physical contacts considering hydrophobic or electrostatic interactions, protrusion, planarity, accessible surface area and

many other parameters, some being obligatory, some permanent and some others transient³. Most of these protein-protein interactions are due to hydrophobic effects, though hydrogen bonds, electrostatic interactions, and covalent bonds are also found. But could long-range electrodynamic interactions enter the protein-protein interactions schemes? These electrodynamic interactions could bring new information about protein association prediction and the way they interact.

III. THEORETICAL APPROACH

Modeling a system of interacting molecules can be treated by molecular dynamics simulations considering a system composed of N identical molecules, modeled as spherical Brownian particles of radius R , mass M and a net number of electric charges Z , moving in a fluid with viscosity η at a fixed temperature T , interacting through a pairwise potential $U(r)$ which depends only on the distance r between their centers. Under the assumption that the friction exerted by the fluid environment on the particles is described by Stokes' law, the dynamics of the system is given by N coupled Langevin equations⁴ that, in the overdamped limit, can be written as:

$$\gamma \frac{d\vec{r}_i}{dt} = - \sum_{j=1, j \neq i}^N \nabla U(|\vec{r}_i - \vec{r}_j|) + \sqrt{2\gamma k_B T} \vec{\xi}_i(t) \quad (1)$$

where \vec{r}_i is the coordinate of the center of i -th particle, $\gamma = 6\pi\eta R$ is the friction coefficient and k_B is the Boltzmann constant. The stochastic displacements are uncorrelated so that $\vec{\xi}_i$ is 3N-dimensional random process modeling the fluctuating force due to the collisions with water molecules, usually represented as a Gaussian white noise process. The explicit forms of the pairwise potential used in our simulations are the electrostatic interaction among identical molecules in electrolytic solution described by the Debye-Hückel potential and the long-range attractive dipolar potential^{5,6}. For an experimental detectability of long-range interactions we chose the long-time diffusion coefficient D as main observable of the system described by Eq. (1):

$$D = \lim_{t \rightarrow \infty} \frac{\langle |\Delta \vec{r}_i(t)|^2 \rangle}{6t} \quad (2)$$

In the following we will use the diffusion coefficient defined in Eq. (2) as relevant quantity to investigate biomolecular interactions.

IV. EXPERIMENTAL APPROACH

An interesting complement to the theoretical approach is represented by the experimental techniques called FCS (Fluorescence Correlation Spectroscopy) and FCCS (Fluorescence

Cross-Correlation Spectroscopy) since they can provide direct measurements of the diffusion process of biomolecules. Indeed the principle of the technique sketched in Fig. 1 is to record the fluctuations of fluorescence emitted in a confocal volume, then correlate the recorded trace which gives information about the diffusion time through the confocal volume⁷. It is frequently used to investigate translational and rotational diffusion, active transport and flow, photophysical and photochemical transformations, chemical reactions or molecular aggregation.

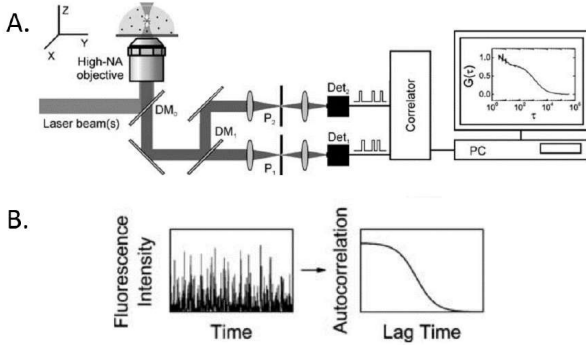


Fig. 1. Panel A shows a typical FCS setup. DM is used for dichroic mirror, P for pinhole and Det for detector. The excitation beam comes from the left of the figure, it is reflected by DM0, then is focused on the sample with the objective. The fluorescence light is emitted in response to the excitation beam, it passes through DM0, through the pinholes to improved the focus, and hits the detectors. The correlation is then performed. Panel B is a cartoon illustrating the concept of FCS. Adapted from Ref.⁷

The signals of fluorescence recorded are analyzed after correlation, which is an efficient method to study the fluctuations, as the following second-order intensity correlation function

$$G_{ij}(\tau) = \frac{\langle \delta F_i(t) \delta F_j(t + \tau) \rangle}{\langle F_i \rangle \langle F_j \rangle} \quad (3)$$

with δF_{ij} the fluorescence signals fluctuations. If $F_i = F_j$ (signals recorded by the same detector) then Eq. (1) is referred to as auto-correlation function while if $F_i \neq F_j$ then it is a cross-correlation function. One can show that the analytical model for G_{ij} essentially depends on the diffusion time of the tracer through the confocal volume τ_D , the number of molecules in the confocal volume N , the shape of the confocal volume and particularly the

structure parameter s describing the spatial properties of the detection volume $s = \omega_{xy}/\omega_z$ (where ω are $1/e^2$ radii of the sample volume directed perpendicularly to the optical axis and directed along the optical path). For a one-component system in a 3D environment the function $G(\tau)$ can be expressed as:

$$G(\tau) = \frac{1}{N} \left[\frac{1}{(1 + \tau/\tau_D) \sqrt{1 + s^2 \tau/\tau_D}} \right] \quad (4)$$

The analysis of the correlation functions obtained by the FCS setup can provide the diffusion coefficient linked to the correlation time by the relation $\tau_D = \omega_{xy}^2 / 4D$ and the average number of particles $\langle N \rangle$ in the detection volume through the relation $G(0) = 1 / \langle N \rangle$, that can be useful to obtain the particles concentration.

V. DISCUSSION

At the conference we will present and discuss recent theoretical and experimental results⁸ comparing the correlation functions and diffusion coefficients of samples constituted by proteins in watery solutions with different concentrations.

We have found that Fluorescence Correlation Spectroscopy is certainly appropriate to detect intermolecular interactions in dilute systems, that is, when the solvated molecules interact at large distances. Significant variations of the diffusion coefficient are exhibited by theoretical as well as experimental results when the intermolecular distance becomes smaller than some characteristic value. Furthermore, this excellent quantitative agreement between the experimental outcomes and the corresponding numerical simulations has a twofold relevance. From the one side it confirms that the observed phenomenology, namely, the sudden bending of the diffusion coefficient when the average intermolecular distance is lowered below a critical value, as well as its pattern as a function of the intermolecular distance, are actually due to the electrostatic interaction among the solvated molecules. From the other side this validates the numerical algorithm and approximations adopted, suggesting that this numerical scheme can be safely applied to interpret the readouts of experiments.

¹ B. Albert, *Molecular Biology of the Cell*, Garland Science (6th edition, December 2014)
² M. Bauer and R. Metzler. *Generalized facilitated diffusion model for DNA-binding proteins with search and recognition states*. Biophysical Journal, 102(10):2321–2330, may 2012
³ S. Jones and J. M. Thornton. *Principles of protein-protein interactions*. Proc Natl Acad Sci USA, 93(1):13–20, 1996.
⁴ C. Gardiner, *Stochastic Methods: A Handbook for the Natural and Social Sciences*, Springer (2009)
⁵ J. Preto, E. Floriani, I. Nardecchia, P. Ferrier, and M. Pettini, *Experimental assessment of the contribution of electrodynamic interactions to long-distance recruitment of*

biomolecular partners: Theoretical basis. Phys. Rev. E, vol. 85, p. 041904, (2012).
⁶ J. Preto and M. Pettini, *Resonant long-range interactions between polar macromolecules*, Phys. Lett. A, vol. 377, no. 8, pp. 587 – 591, (2013).
⁷ E. P. Petrov and P. Schuille. *State of the art and novel trends in fluorescence correlation spectroscopy*. In Springer Series on Fluorescence, pages 145–197. Springer Berlin Heidelberg.
⁸ M. Lechelon, *Long-range electrodynamic interactions among biomolecules*, PhD dissertation (University of Aix-Marseille, 2017)

Multiscale approach in discovering cardiovascular couplings from cardiovascular time series

Danuta Makowiec¹, Dorota Wejer², Beata Graff³ and Zbigniew R. Struzik^{4,5}

¹ Department of Mathematics, Physics and Informatics, Institute of Theoretical Physics and Astrophysics, University of Gdańsk, Gdańsk, ul. Wita Stwosza 57, e-mail address: fizdm@univ.gda.pl

² Department of Mathematics, Physics and Informatics, Institute of Experimental Physics, University of Gdańsk, Gdańsk, ul. Wita Stwosza 57, e-mail address: dorota.wejer@ug.edu.pl

³ Department of Hypertension and Diabetology, Medical University of Gdańsk, Gdańsk, ul. Marii Skłodowskiej-Curie 3a, e-mail address: bgraff@gumed.edu.pl

⁴ RIKEN Brain Science Institute, 2-1 Hirosawa, Wako-shi 351-0198, Japan,

⁵ The University of Tokyo, Graduate School of Education, 7-3-1 Hongo, Bunkyo-ku, Tokyo 113-0033, Japan
e-mail address: z.r.struzik@p.u-tokyo.ac.jp

INTRODUCTION

Cardiovascular couplings are aimed on maintaining the blood pressure homeostasis. Baroreceptor activation or deactivation – basic receptor of autonomic nervous system (ANS), occurs during transient changes in blood pressure. In response, a cardiac period is modified. It is believed that in fluctuations of the heart period or/and blood pressure, complex interactions between the cardiovascular system and ANS are hidden. However, though many efforts have been undertaken, our knowledge about these couplings is far from being satisfactory.

Signals with recordings of heart accelerations and decelerations accompanied with drops and rises in blood pressure invoked by the controlled body change during the head-up tilt (HUT) test could be an important source of information about the organization of the cardiovascular regulatory system. The asymmetry between accelerations and decelerations has been proposed as a measure of sympathetic activity of ANS, which is considered as crucial for efficiency in maintenance of the blood pressure balance. In accordance, the Generalized Porta Index (GPI) has been proposed¹ to quantify asymmetry between positive and negative changes in a heart rate period by comparing the role of decelerations and accelerations by their probabilities. However, this comparative approach is not the only possible one, and the structure of the asymmetry between decelerations and accelerations can be investigated from an alternative perspective, namely by using the Multistrukture Index² (MI), which addresses the sizes of events. Here, we will discuss whether these two indices GPI and MI provide similar or complimentary information about the organization of regulatory mechanisms in cardiovascular system.

MEASURES OF SIGNAL CHANGES

If by $\Delta(i)$ one marks a change between subsequent i and $i-1$ values of either time intervals (RR-intervals) between subsequent heart beats or values of systolic blood pressure (SBP) then, for any real q , one can consider the functions:

$$GPI(q) = \frac{\sum_{\Delta \neq 0} p^q(\Delta^-)}{\sum_{\Delta \neq 0} p^q(\Delta^+)}, \quad MI(q) = \frac{\sum_{\Delta^+(i)^+} [\Delta^+(i)]^q}{\sum_{\Delta^{\neq 0}(i)} |\Delta^{\neq 0}(i)|^q} \quad (1)$$

with $\Delta^+(i) / \Delta^-(i) / \Delta^{\neq 0}(i)$ denoting a positive/negative/non-zero change, respectively. When Δ refers to RR-intervals, functions defined in Eq.(1) provide estimates for the participation of the

probability that heart accelerates (case GPI) or for the participation of decelerations (case MI). When Δ represents changes in SBP, then GPI(q) quantifies the probability of falls, while MI(q) measures the role of the increases in SBP. So, both indices are estimators of the asymmetry of signals. But each index proposes a different frame for the asymmetry. GPI evaluates the proportions between accelerations and decelerations when events are quantified by their probability of occurrence. MI evaluates dynamical balance between decelerations and accelerations of the same size, and the deviation from such balance in the case of dominance of events of particular size. Both GPI and MI provide multiscale estimates of time series. The events with the highest probability dictate properties of GPI for large q . Rare events, from the tails of probability distributions, fix properties of GPI for negative q . Therefore, one can say that GPI(q) identifies asymmetry between the most typical dynamics ($q \gg 0$) and then moves with q crossing 0 to characterize the asymmetry of the dynamics among rare events ($q \ll 0$). The values of MI are driven by the size of an event. Positive and far from 0 values of q measure the proportion of occurrences of large size positive increments to all increments of the similar size. For $q < 0$, MI describes this proportion among the smallest size events. Consequently, one can say that MI separates asymmetric features of fast dynamics ($q \gg 0$) from slow dynamics ($q \ll 0$).

The signals of RR-intervals and levels of SBP recorded during the HUT test have been used by us for GPI and MI estimates. The HUT tests were performed under paced breathing protocol what means that all the subjects synchronized their breathing rhythm with a recorded voice instruction to breathe in and out at a frequency of 0.25 Hz. Surface ECG (lead II) and beat-to-beat blood pressure were simultaneously measured using the Task Force Monitor system. Each subject remained in the supine position for 20 minutes for adaptation. Then the table was tilted to 60 degrees and each subject stayed in the upright position for the next 20 minutes (passive part of the HUT test). Each subject who did not faint before this time was administrated 400 micrograms of nitroglycerine (aerosol, sublingually) to stimulate active fainting, and the test was continued for the additional 10 minutes or until syncope occurred (active part of the HUT test). Only signals with completed passive and active parts of the HUT test were included into the further study. In the following we discuss properties of signals recorded during the adaptation part, but in relation to the overall effect of the HUT test: the subject fainted or not during the test.

From a numerical point of view, the functions defined in Eq.1 are sensitive to unbalanced extremes - minimal and maximal changes

in the signal. But minimal changes are related with properties of the equipment used, rather than with physiology arising from signals recorded. On the other side, maximal changes might refer to more individual features of a subject than be representative of the features of the group. Therefore, our calculations were performed under the restrictions: $3 \text{ ms} \leq \Delta RR(i) \leq 200 \text{ ms}$ and $0.2 \text{ mmHg} \leq \Delta SBP(i) \leq 10 \text{ mmHg}$.

RESULTS

Both indices capture properties of the distributions of increments. A typical distribution of ΔRR or ΔSBP is sharply peaked around the zero. Hence, the smallest increments are usually the most probable events, and the largest changes coincide with the least probable events. In consequence, for any signal, when q is far from 0, the profiles of functions $GPI(q)$ and $MI(q)$ are related with each other by a point symmetry with respect to the point $(0, 0.5)$. In Fig.1, plots of $MI(q)$ and $GPI(q)$ are shown in a way which emphasizes this symmetry. Properties of the most probable events (GPI) and of the smallest size (MI) are in the right parts of figures while the most rare events (of the largest size) are in the left parts of the figures.

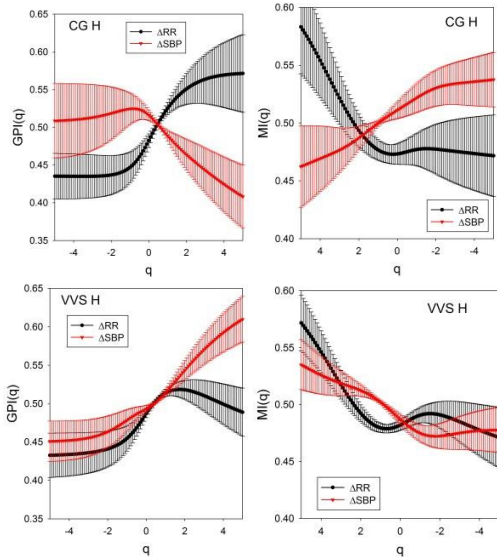


FIG.1 Plots of the mean $GPI(q)$ and $MI(q)$ with std errs obtained for the group of healthy people (**CG**: 29 people) and vasovagal sensitive patients with a history of syncope and who fainted in the HUT test (**VVS**: 54 patients). H stands for recordings in horizontal position when the subjects were at rest, awaiting for tilting.

From Fig.1 we see that properties of $MI(q)$ and $GPI(q)$ should be considered in the following three regimes:

- $q \geq +2$, namely to MI describing the fastest dynamics, and GPI describing the most typical dynamics;
- $q \leq -2$, describing the slowest dynamics in the case of MI , and the extraordinary events in the case of GPI ;
- $-2 \leq q \leq 2$, mid-size events, corresponding to the transient scales.

The mean values of the indices are not much distant from the value 0.5 which describes the balanced participation of the negative and positive increments. However, in the case of **CG**

group, there is a clear asymmetry with domination of accelerations displayed by MI when $q < 2$ (statistically significant for $-1 < q < 2$) and by GPI when $q > 1$. There are also noticeable turns in predominance in SBP signals detected by both indices when q is changing from negative to positive values. This predominance means smooth transition to the opposite asymmetry when q changes from $q < -2$ to $q > 2$. From that, we see that both indices consistently describe a homeostatic state of SBP in **CG** group as maintained by more frequent rises of smaller size which are balanced by rare larger falls. Accordingly, the heart rhythm presents a slight domination of small and mid-size accelerations, balanced by occasional large decelerations. These changes can be summarized as follows. Steady sympathetic activity is rarely switched off by activation of the parasympathetic system. All together indicates at the stable regulation served by the ANS.

The profiles of $MI(q)$ and $GPI(q)$ obtained from signals of the patient group **VVS** are quite different from the profiles found for the **CG** group. In particular, the indices do not provide plots symmetrical with respect the line $f(q) = 0.5$ or the point $(0, 0.5)$ as it is evident in case of healthy people. The GPI plots indicate that the most probable events exhibit domination of falls in SBP, while in the case of the healthy subjects rises dominate over falls. Also over presence of large rises is evident. The overall profiles of indices of ΔRR are more-less in agreement with the profiles obtained for healthy people. Consequently, it seems that changes in SBP are driven more strongly by some other term than the autonomic regulation. Probably, the circulation of nitric oxygen in vascular tissue serves this regulation. Hence, in **VVS** patients, a homeostatic state of BP after large rises is restored by local processes in which the vascular tissue is involved.

DISCUSSION AND CONSLUSIONS

It occurs that from changes in time series describing the cardiovascular system, we can learn how the regulation is driven. The considered indices enhance different aspects of couplings in the cardiovascular system. GPI scales with the event probability, hence evaluates statistics of typical vs rare events. MI scaling with the event size gives insight into fast vs slow processes. As different proportions and time scales could be related to various physiological phenomena, the indices provide consistent but supplementary of insights into properties of the underlying dynamics. Concluding, both indices support each other and provide supplementary information.

Multiscale approach, applied to RR-intervals and SBP signals recorded on people during the HUT test, have provided different quantifications for the activity of the sympathetic part of ANS in healthy people and vasovagal sensitive patients. In particular, we have found that in case of **VVS** patients stability of blood pressure could be strongly influenced by processes undergoing in the vascular tissue than by the ANS which is the main driver in case of healthy people.

¹ D. Makowiec, B. Graff, W. Miklaszewski, D. Wejer, A. Kaczkowska, Sz. Budrejko and Z.R. Struzik, Europhysics Letters **110**(2), 28002 (2016).

² D. Makowiec, B. Graff, Z.R. Struzik, Scientific Reports **7**:419 (2017).

Macroscopic random telegraph noise

Grzegorz Jung^{1,2}

¹ Department of Physics, Ben Gurion University of the Negev, 84105 Beer Sheva, Israel
e-mail address: jung@bgu.ac.il

² Institute of Physics Polish Academy of Sciences, Al. Lotników 32/46, 02-668 Warsaw, Poland
e-mail address: jung@ifpan.edu.pl

I. INTRODUCTION

Random Telegraph Noise (RTN) typically appears in fluctuations of the conductivity of mesoscopic systems, when the size of the system is reduced to such extent that it contains only few, or just a single active two-level fluctuator (TLF). An elementary two-level fluctuator, such as a defect capable of trapping/detrapping charge carriers, randomly switches the conductivity of the entire system between two fixed values, referred to as *up* and *down* RTN states, and corresponding to a loaded/empty charge trap. With increasing system size, the number of TLFs in the system volume increases and their incoherent superposition leads to appearance of $1/f$ -like conductivity noise. Therefore, in macroscopic systems the individual elementary TLF switchers should not be visible. Nevertheless, in strongly correlated electron systems, such as superconductors, in particular high- T_c cuprates, or magnetic systems such as colossal magnetoresistive (CMR) manganites, RTN shows out also in macroscopically large samples.^{1,2}

Macroscopic RTN cannot be due to an elementary TLF, associated with a single defect, but to a macroscopic size TLF capable of changing the state of the system on the length scale comparable with the size of the investigated system. Only in the most trivial case of strongly inhomogeneous and bulk materials with percolation-like conductivity, even above the percolation threshold there will be always local "bottlenecks" in the conducting paths, which funnels the current and leads to large local voltage drops. Active microscopic two-level fluctuators located near such a bottlenecks can give rise to RTN fluctuations in the conductivity of the entire large system.

II. MACROSCOPIC RTN IN TYPE-II SUPERCONDUCTING SYSTEMS

The macroscopic RTN appearing in superconducting systems is characterized by strong dependence of its parameters on applied magnetic field and bias conditions.^{1,3-5} The dependence of RTN amplitude on bias current are markedly different in the low and high bias regime. In a low bias regime, the RTN amplitude depend on bias current in a nonlinear and a non-monotonic way. It initially increases rapidly with increasing current, and then reaches the maximum and slowly decreases with further current increase.⁴ The average lifetimes of the opposite RTN states, τ_{uo} and τ_{dn} , depend differently on applied bias. When the lifetime of the *up* RTN state increases exponentially with bias current, suggesting a linear increase of the activation energy barrier with bias current, the lifetime of the *down* state varies in a non-exponential and a non-monotonic way with increasing bias current. Moreover, the behavior of the lifetimes at low bias current mirrors that at high currents, meaning that the type of bias

dependencies of τ_{uo} and τ_{dn} are exchanged. In addition, macroscopic RTN in superconducting systems shows some exotic features such as an additional RTN amplitude or frequency modulation of the basic RTN waveform.

Several features of the macroscopic RTN in superconductors indicate magnetic flux origin of the noise.³⁻⁵ Indeed, the system of magnetic flux vortices in type-II superconductors occupies the entire volume of a superconducting specimen and its motion leads to dissipation and appearance of voltages across a superconductor biased with current exceeding the pinning current of the vortex system. However, the understanding of the physical mechanism generating the macroscopic RTN by the vortex system and proper explanation of the noise characteristics are still missing and remain one of the unsolved problems of noise.

The presentation will propose a possible solution of the problem by proposing that macroscopic RTN is due to the dynamic coexistence of disordered and ordered vortex matter in a superconducting specimen.^{6,7} The disordered phase is dominated by the vortex-pin interactions and has higher critical current than the ordered phase in which vortex-vortex interactions dominate, resulting pinning is a weaker pinning. The vortex density in the disordered phase is also higher than the density of the ordered phase. These factors lead to the crossing of the I - V characteristics of both phases,⁸ what allows for two metastable voltage states at a single constant current bias. The two phases dynamically coexist in a superconducting specimen sample due to the edge vortex contamination mechanism.^{6,7} In the superconducting dissipative state, the disordered vortex phase is continuously randomly injected into the sample through the surface energy barrier against vortex penetration. The disordered phase randomly anneals then into the ordered phase while flowing deeper into the sample, away from the edge.

This scenario allows one to understand many of the exotic features of the macroscopic RTN in superconductors but requires significant modifications to the two-level fluctuator concept. The standard TLF, composed of two energy wells separated by a barrier, has to be replaced by a fluctuator with one energy well only. A plane with randomly distributed holes models the second RTN state. The lifetime in this state corresponds to the time elapsing before the system, thermally ejected from the energy well of the first RTN state to the plane of the second state, falls into one of the holes of the random billiard. The system falling into any hole is immediately reinjected directly back to the energy well of the first RTN state.

III. MACROSCOPIC RTN IN CMR MANGANITES

Random telegraph noise in colossal magnetoresistive (CMR) manganites is ascribed to two possible mechanisms. It may be

UPON 2018, GDANSK, JULY 9-13, 2018

regarded as a spectacular manifestation of phase separation and coexistence of percolating paths with significantly different conductivity.^{2,9-14} Alternatively, it can be ascribed to strong fluctuations of magnetic moments, most prone to occur in the vicinity of the paramagnetic (PM) to ferromagnetic (FM) phase transition. Magnetic moment fluctuations couple to the resistivity through pronounced CMR effect.⁹⁻¹⁰

Two-level resistance switching with amplitudes ranging from 0.01% to 0.2% of the total sample resistance were observed in single crystals and thin films of $\text{La}_{1-x}\text{Ca}_x\text{MnO}_3$ (LCMO).⁹⁻¹² Multi-level RTN with amplitudes in the range of 10% of the total sample resistance was found in highly resistive $\text{Pr}_{1-x}\text{Ca}_x\text{MnO}_3$ system, characterized by current induced switching into metastable high resistivity states.^{2,13} We have reported bias sensitive giant RTN with amplitude exceeding 10% of the total sample resistance in LCMO Ca-doped at $x=0.18$.¹⁵ RTN fluctuations were also associated with electronic phase transitions in manganites at low temperatures.^{16,17}

All above manifestations of macroscopic RTN in CMR manganites are typically limited to relatively narrow temperature ranges and show strongly applied magnetic field and bias dependent switching rates.

We have recently reported on appearance of unusual macroscopic RTN conductivity fluctuations in ferromagnetic insulating $\text{La}_{0.86}\text{Ca}_{0.14}\text{MnO}_3$ manganite single crystals.¹⁸ The observed RTN was very robust and persisted in extremely large, more than 50 K, temperature range, while the standard macroscopic RTN in manganites can be followed only in temperature intervals of few

degrees Kelvin only. Moreover, the robust RTN demonstrates switching rates, which are, surprisingly, completely bias and magnetic field independent while its amplitude is a non-monotonic function of temperature and decreases with increasing bias.

The mechanism of the robust macroscopic RTN is one more unsolved problem of noise. Although in our recent paper it was tentatively associated with dynamic current redistribution and feedback mechanism provided by the current dependent resistivity, the physical mechanism governing both phenomena is still not fully known. In particular, we have gathered convincing evidence that the feedback mechanism is due to Meyer-Neldel compensation rule (NMR),²⁰ but the nature of the multi-excitation entropy behind the NMR in mixed valence low-doped manganites remains obscure.

Finally, one notes that macroscopic random telegraph fluctuations in various strongly correlated systems have profoundly different physical origin. However, the common denominator to all of them is the phase separation and dynamic coexistence of phases with markedly different properties. Among different types of phase separation, only the electronic phase separation is restricted to strongly correlated systems. Thus, the following last open problem of the discussed subject emerges: are the nontrivial, not the bottleneck type, macroscopic random telegraph noise manifestations limited only to strongly correlated materials.

- ¹ G. Jung, M. Bonaldi, J. Konopka, and S. Vitale, *J. Appl. Phys.* **70**, 5440 (1991).
- ² A. Anane, B. Raquet, S. von Molnar, L. Pinsard-Godart and A. Revcolevschi, *J. Appl. Phys.* **87**, 5025 (2000).
- ³ G. Jung, B. Savo and A. Vecchione *Europhys. Lett* **21**, 947 (1993).
- ⁴ M. Bonaldi, G. Jung, B. Savo, A. Vecchione, and S. Vitale, *Physica B* **194**, 2037 (1994).
- ⁵ G. Jung and B. Savo, *J. Appl. Phys.* **80**, 2939 (1996).
- ⁶ Y. Paltiel, E. Zeldov, Y. Myasoedov, M. L. Rappaport, G. Jung, S. Bhattacharya, M. J. Higgins, Z. L. Xiao, E. Y. Andrei, P. L. Gammel, and D. J. Bishop, *Phys. Rev. Lett.* **85**, 3712 (2000).
- ⁷ Y. Paltiel, G. Jung, Y. Myasoedov, M. L. Rappaport, E. Zeldov, S. Bhattacharya, M. J. Higgins, *Europhys. Lett.* **58**, 112 (2002).
- ⁸ Y. Paltiel, E. Zeldov, G. Jung, Y. Myasoedov, M. L. Rappaport, D. Feldman, M. J. Higgins, and S. Bhattacharya, *Phys. Rev. B* **66**, 060503 (2002).
- ⁹ H. T. Hardner, M. B. Weissman, M. Jaime, R. E. Treece, P. C. Dorsey, J. S. Horwitz, D. B. Chrisey, *J. Appl. Phys.* **81**, 272 (1997).
- ¹⁰ R. D. Merithew, M. B. Weissman, F. M. Hess, P. Spradling, E. R. Nowak, J. O'Donnell, J. N. Eckstein, Y. Tokura, and Y. Tomioka, *Phys. Rev. Lett.* **84**, 3442 (2000).
- ¹¹ B. Raquet, A. Anane, S. Wirth, P. Xiong, and S. von Molnar, *Phys. Rev. Lett.* **84**, 4485 (2000).
- ¹² A. Palanisami, R. D. Merithew, M. B. Weissman, and J. N. Eckstein, *Phys. Rev. B* **64**, 132406 (2001).
- ¹³ A. Asamitsu, Y. Tomioka, H. Kuwahara and Y. Tokura, *Nature*, **388**, 50 (1997).
- ¹⁴ S. Wirth, A. Anane, B. Raquet, S. von Molnar, *Journal of Magnetism and Magnetic Materials* **290**, 1168 (2005).
- ¹⁵ V Markovich, G. Gorodetsky, G. Jung, D. A. Shulyatev and Ya. M. Mukovskii, *Fluct. Noise Lett.* **1**, L105 (2001).
- ¹⁶ A. Bid, A. Guha, and A. K. Raychaudhuri, *Phys. Rev. B* **67**, 174415 (2003).
- ¹⁷ T. Z. Ward, X. G. Zhang, L. F. Yin, X. Q. Zhang, Ming Liu, P. C. Snijders, S. Jesse, E. W. Plummer, Z. H. Cheng, E. Dagotto, and J. Shen, *Phys. Rev. Lett.* **102**, 087201 (2009).
- ¹⁸ J. Przybytek, J. Fink-Finowicki, R. Puźniak, A. Shames, V. Markovich, D. Mogilyansky, and G. Jung, *Phys. Rev. B* **95**, 125101 (2017).
- ¹⁹ J. Przybytek, J. Fink Finowicki, R. Puźniak, V. Markovich, and G. Jung, *J. Appl. Phys.* **118**, 043903 (2015).
- ²⁰ A. Yelon, B. Movaghar and R. S. Crandall, *Rep. Prog. Phys.* **69**, 1145 (2006).

Origin of $1/f$ -Noise of Strongly-Correlated Electrons in Low-Dimensional Molecular Metals

Jens Müller

Institute of Physics, Goethe-University Frankfurt, Max-von-Laue-Str. 1, 60438 Frankfurt(M), Germany
e-mail address: j.mueller@physik.uni-frankfurt.de

I. INTRODUCTION

Quasi-two-dimensional organic charge-transfer salts (BEDT-TTF)₂X based on the donor molecule bisethylenedithio-tetrathiafulvalene (BEDT-TTF) and a monovalent anion X have been recognized as model systems to study the Mott metal-insulator transition (MIT) – a key phenomenon in modern condensed-matter physics – in reduced dimensions¹. At the Mott transition, a charge gap opens due to the strong electron-electron interactions characterized by the ratio of bandwidth W to on-site Coulomb interaction U . The model character of these materials becomes manifest in (i) their rich phase diagrams, and (ii) the possibility of fine-tuning the materials via the ratio W/U and therefore the strength of electronic correlations by using subtle physical or chemical means.

In the phase diagram of κ -(BEDT-TTF)₂Cu[N(CN)₂]Z, the phase boundary of the first-order Mott MIT, which terminates in a second-order critical point², separates an antiferromagnetic insulating/ferroelectric state (for low pressure, small W/U , $Z = \text{Cl}$) from a metallic/superconducting one (for high pressure, large W/U , $Z = \text{Br}$). By fine-tuning across the transition, the various phases and the properties of the finite-temperature critical endpoint of the Mott transition can be accessed. Fundamental aspects that recently have attracted considerable interest are the question of the universal critical properties (unconventional criticality vs. 2D Ising), the description of the anomalous metallic state (pseudogap behavior), the symmetry of the superconducting ground state (s -wave vs. d -wave pairing), the role of phase separation and percolation, and the interrelation of disorder and strong electronic correlations.

About ten years ago, we have employed fluctuation spectroscopy for the first time to these materials in order to study the low-frequency dynamics of charge carriers, see Ref.³ for an overview of earlier studies. Since then, a number of interesting physical problems related to the above-mentioned aspects have been addressed and better understood, namely (1) spatial electronic inhomogeneities, i.e. electronic phase separation and percolation in the coexisting region of competing ground states⁴, (2) glass-like structural excitations, involving the coupling of molecular degrees of freedom to the electronic transport⁵, (3) charge crystallization and vitrification leading to heterogeneous slow dynamics⁶, and (4) critical charge carrier dynamics at the Mott transition leading to critical slowing down of the charge fluctuations and ergodicity breaking⁷. Current efforts involve the investigation of (5) the low-frequency charge carrier dynamics deep in the insulating phase of dimer Mott systems showing intriguing dielectric relaxation or ferroelectricity.

II. ANALYSIS OF $1/f$ -NOISE

Due to relatively large Hooge parameters, generic $1/f$ -type fluctuations are widely observed in the molecular conductors (BEDT-TTF)₂X. A microscopic theory to explain the $1/f$ -noise, however, is lacking. Therefore, the phenomenological DDH model⁸ of non-exponential kinetics is employed, and very often works successfully.

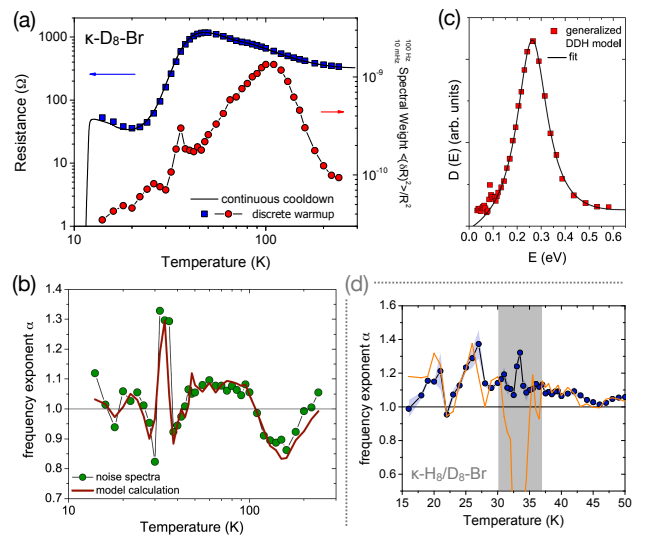


FIG. 1 (a) Resistance (blue) and resistance noise (red) of deuterated κ -(BEDT-TTF)₂Cu[N(CN)₂]Br^{9,5} (in short: κ -D₈-Br). (b) Frequency exponent $\alpha(T)$ measured and calculated after Eq. (2). (c) Distribution of activation energies $D(E)$ extracted from the DDH model, Eq. (3). (d) Frequency exponent of a different, partially deuterated sample κ -H₈/D₈-Br located at a different position in the phase diagram.

FIG. 1(a) shows a typical noise measurement on a deuterated system κ -(BEDT-TTF)₂Cu[N(CN)₂]Br (in short: κ -D₈-Br), which in the phase diagram is located on the insulating side, only slightly away from the critical point^{9,5}. Black line is the continuous resistance measurement during cooldown. During warmup in discrete steps, the resistance (blue squares) and $1/f$ -noise spectra (red circles) have been obtained. The latter are shown as the spectral weight integrated over the measured frequency range $f = 10 \text{ mHz} - 100 \text{ Hz}$. Clearly, the fluctuation properties reveal additional information, not present in the mean value of the resistance.

Strikingly, the temperature dependence of the observed $1/f^{\alpha}$ -noise is described very well by the extended¹⁰ DDH model⁸

$$S_R(f, T) \propto \int g(T) \frac{\tau(E)}{1 + [\tau(E)2\pi f]^2} D(E) dE, \quad (1)$$

for which the distribution of activation energies $D(E)$ determines both the temperature dependence of the noise magnitude and the deviations of the frequency exponent $\alpha(T)$ from being equal to 1. This allows for a consistency check of the assumptions of the model, namely independent (Gaussian) fluctuators $\tau = \tau_0 \exp(E/k_B T)$ that are thermally activated and couple linearly to the measured resistance, by comparing

$$\alpha(T) = 1 - \frac{1}{\ln(2\pi f \tau_0)} \left[\frac{\partial \ln S_R(f, T)}{\partial \ln T} - \frac{\partial \ln g(T)}{\partial \ln T} - 1 \right] \quad (2)$$

with the measured data, which is shown in FIG. 1(b) for the noise data of FIG. 1(a). The function $g(T)$ often is invoked to explain a temperature dependent change of the number of fluctuators or their coupling to the resistance fluctuations resulting in a constant offset if $g(T) = aT^b$. A good correspondence of measured $\alpha(T)$ and model calculation then justifies to determine $D(E)$ by

$$D(E) \propto \frac{2\pi f S_R(f, T)}{k_B T} \frac{1}{g(T)} \quad (3)$$

where the large logarithmic factor in $E = -k_B T \ln(2\pi f \tau_0)$ allows to access ordinary activation energies in solids. The distribution $D(E)$ determined from the data in FIG. 1(a) is shown in FIG. 1(c). Note that the fluctuators in the DDH model are not specified *a priori*. However, the energy $E = 260 \text{ meV}$ of the pronounced maximum of $D(E)$ is well known in κ -(BEDT-TTF)_x and can be assigned to the rotational degrees of freedom of the ethylene endgroups of the BEDT-TTF molecules⁵. These structural degrees of freedom undergo a glassy freezing transition at $T_g \sim 76 \text{ K}$ and their thermal motion result in the large noise peak at about 100 K in our frequency window. In contrast, the fine-structure at lower temperatures, which is also described well by the DDH model, is attributed to electronic correlations, namely a sudden slowing down of the charge fluctuations due to the vicinity to the critical endpoint of the Mott metal-insulator transition⁹. Indeed, in a different, partially deuterated sample, which has been tuned through the critical region of the phase diagram, we observe a diverging increase of the resistance fluctuations (amplitude of the $1/f$ -noise) and the critical slowing down of the order-parameter fluctuations (dramatic shift of spectral weight to low frequencies)⁷.

III. UNSOLVED PROBLEMS

Besides the ubiquitous $1/f$ -noise in low-dimensional molecular metals that can often be well described with the generalized DDH model, a number of technical and also fundamental questions remain to be understood.

FIG. 1(d) shows the measured $\alpha(T)$ and the DDH model calculation for a different, partially deuterated sample κ -H₈/D₈-Br

being located closer to the critical endpoint of the Mott metal-insulator transition. Strikingly, there is a distinct temperature region, where the model description fails, whereas at higher and lower temperatures the agreement is very good. Obviously, in a distinct temperature region, the basic assumptions of the model (independent fluctuators, linear coupling to the resistivity) are not fulfilled.

In the context of $1/f$ -noise measurements on multiferroic organic Mott insulators / paramagnetic superconductors (BEDT-TTF)_x and related compounds, we will present a systematic study of the applicability of the DDH model and discuss scenarios, where a satisfying understanding of the experimental observations has not yet been achieved. Selected open issues are:

- The assignment of calculated activation energies resulting in the observed enhanced $1/f$ -noise.
- The meaning of the relatively large width of the distribution function $D(E)$.
- The relevance of the vertical offset function $g(T)$ in certain sections of the temperature axis and the physical meaning of $g(T)$, e.g. for electronic scattering processes (i.e. the sample resistance).
- A frequently observed horizontal offset of the measured and calculated $\alpha(T)$ on the temperature axis.
- The physical origin of (occasionally observed) good qualitative but not satisfying quantitative agreement.
- Distinct temperature regions, where obvious deviations from the DDH model have a physical meaning, see e.g. FIG. 1(d). Signature of ergodicity breaking?
- Understanding diverging, extremely slow fluctuations in correlated electron systems in general. Signature of a glassy electronic state? Does the coupling to the elastic properties of the underlying crystal lattice¹¹ have to be taken into account? What about the low-frequency cutoff?
- Models beyond DDH.

ACKNOWLEDGEMENTS

Work is funded by the Deutsche Forschungsgemeinschaft (DFG) within the Collaborative Research Center SFB/TR49 ‘‘Condensed-matter systems with Variable Many-Body Interactions’’.

Work has been done in collaboration with students from Goethe-University Frankfurt: Jens Brandenburg, Robert Rommel, Benedikt Hartmann, David Zielke, Jana Polzin, and Tatjana Thomas. Samples have been grown by Dr. John A. Schlueter, Argonne National Laboratory, USA, and Prof. Takahiko Sasaki, Tohoku University, Sendai, Japan.

- ¹ N. Toyota, M. Lang, J. Müller, *Low-Dimensional Molecular Metals* (Springer Series in Solid-State Sciences, Berlin Heidelberg, 2007).
- ² Furukawa et al., *Nature Phys.* **11**, 221 (2015).
- ³ J. Müller, *Fluctuation Spectroscopy: A New Approach for Studying Low-Dimensional Molecular Metals* (Review), *ChemPhysChem* **12**, 1222 (2011).
- ⁴ J. Müller et al., *Phys. Rev. Lett.*, **102**, 047004 (2009).
- ⁵ J. Müller et al., *New J. Phys.* **17**, 083057 (2015).
- ⁶ S. Sasaki et al., *Science* **357**, 1381 (2017).

- ⁷ Hartmann et al., *Phys. Rev. Lett.* **114**, 216403 (2015).
- ⁸ P. Dutta, P. Dimon, P. Horn, *Phys. Rev. Lett.* **43**, 646 (1979)
- ⁹ J. Brandenburg et al., *New J. Phys.* **14**, 023033 (2012).
- ¹⁰ B. Raquet et al., *Phys. Rev. B* **59**, 12435 (1999).
- ¹¹ E. Gati et al., *Sci. Adv.* **2**, e1601646 (2016).

The CryoQPDI: a new research instrument for mechanical thermal noise investigation

Richard Pedurand^{1,2}, Ghaouti Hansali³, Vincent Dolique^{1,2}, Gianpietro Cagnoli¹ and Ludovic Bellon²

¹Laboratoire des Matériaux Avancés, CNRS/IN2P3, F-69622 Villeurbanne, France

²Univ Lyon, ENS de Lyon, Univ Claude Bernard Lyon 1, CNRS, Laboratoire de Physique, F-69342 Lyon, France
r.pedurand@lma.in2p3.fr / ludovic.bellon@ens-lyon.fr

I. INTRODUCTION

Ground based, kilometer scale Gravitational Waves Detectors (GWD) like Advanced Virgo¹, Advanced LIGO² and KAGRA³, use laser interferometry to monitor the length variations between two mirrors with extremely high resolution. The mechanical thermal noise coming from the fundamental Brownian motion of the surface of these mirror is expected to set the ultimate limit to their resolution. According to the fluctuation-dissipation theorem, this thermal noise originates in the mechanical dissipation of the optical coating materials used to give these mirrors their reflectivity⁴. KAGRA will be the first GWD to operate with mirrors cooled down to 10 K, as a mean to reduce this thermal noise, and future GWD project like the Einstein Telescope⁵ will also use cryocooled mirrors. Several fundamental and metrological issues arise. As temperature is lowered, changes in the coating properties may lead to additional dissipation, defeating the purpose of cryogenic operation⁶. Also, mirrors both cooled via thermal conduction and heated via the unwanted absorption of laser power will be subjected to a thermal gradient, a non-equilibrium state where both the temperature of the system and the fluctuation-dissipation relation need to be redefined.

To help in solving these noise problems, we propose a new instrument, the CryoQPDI, able to measure directly the thermal noise induced motion of micromachined cantilever in high vacuum and down to 7 K, using a special homodyne laser interferometer. Measurements made before and after a coating deposition allow us to extract meaningful information about the coating intrinsic dissipation⁷. Absorption of laser light power can be used to submit a cantilever to a controlled temperature gradient, also making our system an appealing platform for out-of-equilibrium thermodynamic experiments⁸.

II. THE CRYOQPDI PROJECT: AN OVERVIEW

The acronym CryoQPDI stand for “Quadrature Phase Differential Interferometry on cryocooled microresonator”. Our system consists in the combination of a pulse-tube based cryostat and an improved quadrature phase differential interferometer (QPDI), based on optical scheme developed by Bellon & al⁹ (Fig. (1)). The fundamental thermal noise induced motion of rectangular micromachined cantilever – see the sketch in the inset of Fig. (2) – can be measured at a pressure between 10^{-6} and 10^{-8} mbar, anywhere between 7 K and room temperature.

As shown in Fig. (2), the power spectral density (PSD) of the displacement is characterized by a set of independent quasi-harmonic oscillators corresponding to the out-of-plane normal mode of the cantilever. Such a thermal noise spectrum contains information about the elastic properties of the materials the cantilever is made from, and about the internal dissipation

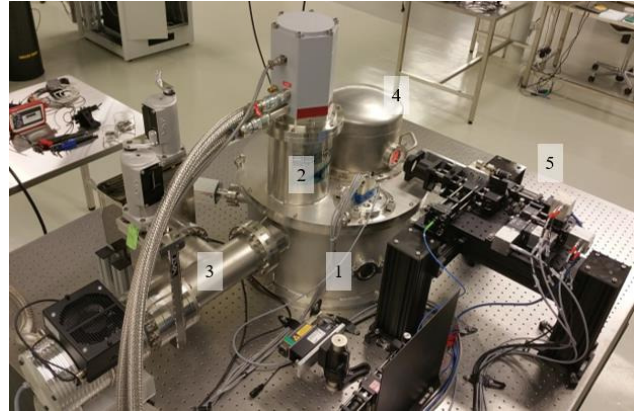


FIG. 1: An overview of the CryoQPDI. 1-cryostat; 2-Pulse tube cryocooler; 3-hybrid high vacuum pumping stage; 4-sample cold plate, accessible through optical windows; 5-QPDI

processes at work^{10,11}. We interpret these spectra with a combination of continuum mechanic and thermodynamic models. An example of this procedure, based on a curve fit of the thermal noise spectrum, has been published⁷. This reference also gives the model used to extract coatings mechanical properties from the measurements made on coated cantilevers.

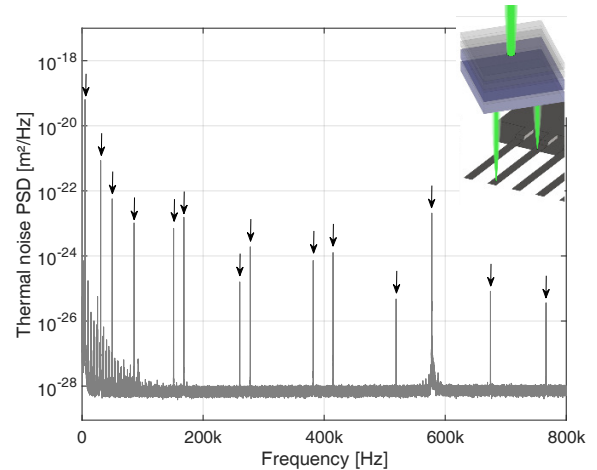


FIG. 2: Thermal Noise spectrum measured on a $500 \times 90 \times 1 \mu\text{m}$ silicon cantilever. Fourteen vibration mode are measured. We can achieve a typical noise floor of $10 \text{ pm}/\sqrt{\text{Hz}}$ on an 800 kHz bandwidth.

III. THE PRESENTATION

For each mode n of stiffness k_n , the mean square deflection $\langle d_n^2 \rangle$ from thermal noise is given by the equipartition theorem:

$$\frac{1}{2}k_n \langle d_n^2 \rangle = \frac{1}{2}k_B T \quad (1)$$

For the cantilevers used here, we expect a typical $\sqrt{\langle d_n^2 \rangle}$ of 0.1 nm. Even if the very low stiffness of our cantilevers makes direct detection of thermal noise possible, it remains a challenging measurement. Additionally, in our quest for accurate result, we identified many published sources of error, related to e.g. optical spot size and position correction¹², the curve fitting procedure¹³, or the interferometer calibration¹⁴.

In this presentation, we plan to review the thermal noise problem in gravitational wave detectors, together with the theories used to model thermal noise for coated and uncoated resonators. We will then give a presentation of our system, disclosing how the many challenges associated with direct thermal noise measurement have been addressed, and explaining how our experimental strategy improve upon currently available methods and results. Eventually, we will set forth our first measurement at both room and cryogenic temperature. But beyond the measurement of coating materials parameters, we want to provide experimental results to help a better understanding of a set of open problems related to coating thermal noise interpretation:

- A typical high reflectivity coating is made from a multilayer stack forming a Bragg reflector. A model summing the contribution of each layer fails to predict the dissipation of the stack. Additional interfacial losses between layers have been proposed as a possible explanation, but currently available results give incompatible conclusion⁴.
- Some currently available results from dissipation measurement at low temperature show additional coating dissipation around 10 to 30 K, lacking an explanation⁶.
- Unwanted absorption of laser power may apply a temperature gradient both on our cantilevers and GWD mirrors. The resulting out-of-equilibrium state demand a new theoretical framework. Cryogenic operation is expected to emphasize this issue¹⁵.

IV. ACKNOWLEDGMENTS

The authors are grateful to the LABEX Lyon Institute of Origins (Grant No. ANR- 10-LABX-0066) of the Université de Lyon for its financial support within the program “Investissements d’Avenir” (Grant No. ANR-11-IDEX-0007) of the French government operated by the National Research Agency (ANR). This work has been also partially supported by the Fédération de Physique A.M. Ampère in Lyon.

5. <http://www.et-gw.eu/>
6. Class. Quantum Grav. 28 (2011) 195017 (12pp)
7. Physical Review D 89, 092004 (2014)
8. Journal of Applied Physics 117, 234503 (2015)
9. Review of Scientific Instruments 84, 095001 (2013)
10. Nanotechnology 6 (1995) 1-7
11. Phys. Rev. D 42, 2437 (1990)
12. Nanotechnology 15 (2004) 1344–1350
13. Review of Scientific Instruments 81, 075103 (2010)
14. Meas. Sci. Technol. 22 (2011) 085301 (8pp)
15. The ET Science Team, technical note ET-0106C-10, <http://www.et-gw.eu/etdsdocument>

1. <http://public.virgo-gw.eu>
2. <https://www.advancedligo.mit.edu/>
3. <http://gwcenter.icrr.u-tokyo.ac.jp/en/>
4. Physical Review D 91, 022005 (2015)

Low-frequency fluctuations in composite materials with carbon nanoparticles

Sandra Pralgauskaitė, Marina Tretjak, Jonas Matukas, Jan Macutkevič, and Jūras Banys
Institute of Applied Electrodynamics and Telecommunications, Vilnius University, Sauletekio 3, 10257 Vilnius, Lithuania
e-mail address: sandra.pralgauskaitė@ff.vu.lt

I. INTRODUCTION

Carbon nanoparticles' (nanotubes, onion-like carbon, exfoliated graphite, etc.) based composite materials are potential candidates for numerous applications in nanostructure electronics and bioelectronics^{1,2}. Carbon nanoparticles enable fabrication of materials with desired electrical, chemical, thermal characteristics. These composites distinguish by high mechanical stability and flame resistance. Also devices with carbon nanoparticles are presumed to have immunity to excess electrical noise that in general tends to increase as the dimensions of the structure decrease^{3,4}.

The composite material is the disordered structure. Carbon inclusions can be treated as conductive particles (that make up a percolation network) in dielectric matrix. Electromagnetic properties of such composites varies from metallic to non-metallic behavior and are greatly dependent on the carbon particle's features: geometry, functionalization type, density, orientation and distribution in the matrix⁵. Studies of electrical conductivity in disordered solids are a topic of considerable interest⁶ and clearance of charge carrier transport mechanisms in new materials is important for many of their applications.

The low frequency noise measurement is well known sensitive experimental tool that gives information on physical processes in various materials, structures and devices⁷⁻¹⁰. Analyses of noise characteristics enables clearing-up the charge carrier transport and conduction mechanisms in composite materials^{7,10}. On the other hand, the low frequency noise is a limiting factor for signal detection in sensor applications.

The noise in epoxy-carbon composites is caused by the impurities in carbon particles or defects in their structure, and, as well as conductivity, depends on the particles' dimensions, density, and distribution^{1,2,11,12}. $1/f$ -type fluctuations are mainly observed in such materials^{7,13}. Also the contribution of the fluctuations in the polymer matrix should be taken into account^{7,8,12}.

TABLE 1. Parameters of the investigated materials (the presented resistivity value is at room temperature at the voltage region, where constant resistivity was observed).

No.	Type of carbon particles	Density of fillers, wt.%	Percolation threshold, wt.%	Resistivity, k Ω -m	Special features
1.	OLC + MWCNT	7 + 0.5		0.030	
2.	EG	2	1.5	0.045	
3.	OLC + MWCNT	7 + 1		1.3	
4.	MWCNT	0.3	0.05-0.08	1.6	amino-grafted CNTs
5.	MWCNT	0.3	0.03-0.05	1.9	epoxy-grafted CNTs
6.	CHB	2	0.5	2.3	
7.	SWCNT	2	0.25	26	plus curing agent A1
8.	OLC	7		56	
9.	SWCNT	2	0.25	182	
10.	MWCNT	0.08	0,05-0,08	2073	amino-grafted CNTs
11.	OLC + MWCNT	5 + 0.5		17175	

In this paper we present comprehensive investigation of low frequency noise characteristics in wide temperature range of epoxy-based composite materials with carbon nanoparticles: single-walled carbon nanotubes, multi-walled carbon nanotubes, exfoliated graphite, carbon black, and onion-like carbon. The aim of the work was to clear up the charge carrier transport mechanisms in the epoxy-carbon composites, to determine, how low frequency noise characteristics of the investigated materials depend on the carbon nanoparticles type, their surface treatment, density.

II. MATERIALS AND EXPERIMENTAL DETAILS

Composites with different carbon particles dispersed in epoxy resin were investigated: single-walled carbon nanotubes (SWCNTs), multi-walled carbon nanotubes (MWCNTs), exfoliated graphite (EG), high surface-area carbon black (CBH), and onion-like carbon (OLC) (Table 1). The features of fabrication process, geometry, electromagnetic and mechanical properties of the corresponding composites were reported in^{11, 12, 14-16}. All investigated materials were above the percolation threshold. The resistivity of the materials was constant in particular voltage range and at higher electrical field the resistance of such composites starts to decrease^{7,17}. Therefore, the resistivity value presented in Table 1 corresponds the lower voltage region where it is constant.

Features of CNT's surface has noticeable influence to the dielectric behavior and the electrical conductivity of composite materials^{5,19}. For the investigation of this influence the materials with the same MWCNTs, but with different their surface treatment have been investigated: samples No. 4 (amino-grafted) and 5 (epoxy-grafted) (Table 1). Epoxy-grafted material was fabricated by mechanically dispersing MWCNTs in bisphenol-A based liquid epoxy resin on the first stage of the fabrication, while amino-grafted CNTs were dispersed in polyethylene polyamine hardener¹⁴.

It is relevant to find composites that distinguish by low percolation threshold with a minimal concentration of expensive fillers and at the same time have optimal mechanical properties. Therefore, we have investigated materials with MWCNT and onion-like carbon particles: with single type of inclusions and with both of them with different density of fillers (samples No. 1, 3, 8, and 11 (Table 1)).

The low-frequency fluctuations were measured in frequency range from 10 Hz to 20 kHz at temperatures ranging from 73 K to 380 K. The voltage noise was measured under constant current operation and noise spectral density was evaluated by comparing to the thermal noise of the standard resistor.

III. RESULTS

Low frequency noise spectra of investigated materials are $1/f^\alpha$ -type. For some samples at particular temperature Lorentzian-type components with characteristic times in the range of hundreds of microseconds were observed. The noise spectral density is mainly proportional to the squared voltage (Fig. 1), what shows on the resistance fluctuations. The dominant conduction mechanism in the investigated composites is tunneling inside and between carbon nanoparticles controlled by the charge carrier capture and release processes in localized states.

Some investigated materials (samples No. 8, 9 and 10) demonstrate slower increase of noise spectral density with voltage (Fig. 1). This behavior is characteristic for materials with large resistivity (low density of conductive fillers) and can be attributed to the tunneling through defects in the polymer matrix. These materials also demonstrate higher noise level if compare noise spectral density normalized to the voltage.

Low frequency noise characteristics dependency on temperature is weak. More rapid noise intensity variation with temperature is observed in the range (250-340) K. At this temperature region expansion of polymer matrix starts, what increases distances between carbon nanoparticles, and resistivity of the material increases¹⁸. Above 340 K the conductivity in the matrix becomes significant. Therefore more rapid noise intensity changes with temperature were observed in the temperature range where changes of the conduction mechanism occur.

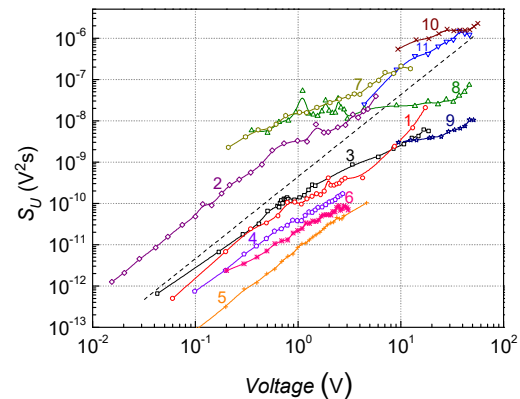


FIG. 1. Voltage noise spectral density dependency on voltage at room temperature and fixed 86 Hz frequency.

Composites with amino-grafted MWCNT's have shown lower resistivity and more intensive low frequency fluctuations comparing to the epoxy-grafted MWCNTs material, what shows that MWCNTs' surface treatment by polyethylene polyamine leads to the larger density of the surface states.

IV. CONCLUSIONS

Low-frequency noise spectra of investigated epoxy-based composites with carbon nanoparticles comprises of $1/f^\alpha$ -type and Lorentzian-type components. The noise spectral density is proportional to the voltage square – resistance fluctuations are prevailing.

The dominant conduction mechanisms in the investigated composites are tunneling inside the carbon nanoparticles and between them controlled by the random charge carrier capture and release processes in localized states in the polymer matrix.

Differences of the investigated materials lead to the different conductivity value and the different noise level, but have no influence to the prevailing conduction mechanisms.

- 1 T. Kawahara, S. Yamaguchia, Y. Ohnob, et al., Appl. Surface Science **267** (2013).
- 2 A. Maffucci, 2015 IEEE Comp. Soc. Annual Symposium on VLSI, **450** (2015).
- 3 S. Agarwal, S K Manhas, S. Dasgupta and N. Jain, 2016 29th Int. Conf. VLSI Design and 2016 15th Int. Conf. Embedded Syst. **361** (2016).
- 4 Q. Cao, J. Tersoff, D. B. Farmer, et al., Science **356** (2017).
- 5 T. W. Ebbesen, H. J. Lezec, H. Hiura, et al., Nature **382** (1996).
- 6 C. Qiu, Z. Zhang, M. Xiao, et al., Science **355** (2017).
- 7 S. Pralgauskaitė, J. Matukas, M. Tretjak, et al., J. App. Phys. **121**, 114303 (2017).
- 8 S. Pralgauskaitė, V. Palenskis, J. Matukas, et al., Solide-State Electronis **79** (2013).
- 9 B.K. Jones, IEEE Trans. Electron Dev. **41**, 2188 (1994).
- 10 C. Barone, S. Pagano, and H. C. Neitzert, Appl. Phys. Lett. **97**, 152107 (2010).
- 11 J. Macutkevic, P. P. Kuzhir, A. G. Paddubskaya, et al., J. Nanophotonics **7**, 073593 (2013).

- 12 P. Kuzhir, A. Paddubskaya, A. Plyushch, et al., J. Appl. Phys. **114** 164304 (2013).
- 13 F. N. Hooge, Physica B **83**, 14 (1976).
- 14 R. Kotsilkova, E. Ivanov, D. Bychanok, et al., Composites Science and Technol. **106**, 85 (2015).
- 15 A. Celzard, S. F. Mareche, G. Furdin, Prog. Mater. Sci. **50**, 93 (2005).
- 16 I. Kranauskaite, J. Macutkevic, J. Banys, et al., Phys. Status Solidi B **252**, 1799–1803 (2015).
- 17 P. Sheng, Phys. Rev. B **21**, 2180 (1980).
- 18 P. G. Collins, M. S. Fuhrer, A. Zettl, Appl. Phys. Lett. **76**, 894 (2000).

Life at the edge, complexity and criticality in biological function

Dante R. Chialvo

*Center for Complex Systems & Brain Sciences (CEMSC³)
CONICET /Universidad Nacional de San Martin
San Martin, (1650), Buenos Aires, Argentina
e-mail address: dchialvo@gmail.com*

The organisation of biological form and function is a classic problem, cut-crossing disciplines, which include a variety of complex spatiotemporal patterns. Historically, work first focused into understanding oscillations and, more recently, attention included scale-free collective fluctuations, some of them shown to correspond to critical phenomena [1, 2]. In this lecture we will review our most recent work across several scales characterizing such phenomena in brain function [3, 4], proteins [5] and mitochondria networks [6].

REFERENCES

1. Emergent complex neural dynamics. Chialvo DR, *Nature Physics* 6 (10), 744-750 (2010)
2. La mente es crítica. J. Marro & D. Chialvo. Univ. of Granada Editora, Spain (2017).
3. Brain organization into resting state networks emerges from the connectome at criticality. Haimovici et al., *Physical Review Letters*, 110 (17), 178101 (2013).
4. Large-scale signatures of unconsciousness are consistent with a departure from critical dynamics". *Journal of The Royal Society Interface*, 13 (114), 20151027 (2016).
5. Critical Fluctuations in the Native State of Proteins" Tang QY et al., *Physical Review Letters* 118 (8), 088102 (2017).
6. Mitochondrial network complexity emerges from fission/fusion dynamics" Zamponi N, et al. *Nature Scientific Reports* 8 (1), 363 (2018).

Information storage and channel capacity of brain; an unsolved problem of noise

Laszlo B. Kish

*Department of Electrical and Computer Engineering, Texas A&M University, TAMUS 3128, College Station, TX 77843-3128, USA
e-mail address: Laszlokish@tamu.edu*

Much guess work has been published about the information storage capacity of the brain, including a petabyte assumption [1]. However the fact that the brain is a noise-based processor and its exact function and "coding" is unknown, make these guesses questionable.

Suppose a neural logic system where all the neurons and synapses are involved with storage. How large is the information storage capacity M expressed in bits? The synapse numbers S is much higher than neuron number N , $S \gg N$, but the synapse connections are probabilistic. Some preliminary considerations and questions:

- The simplest situation: assume deterministic synapses: $P = 0$ or 1 probability of transfer. What is then the storage capacity?
- How does this change if the connections are probabilistic?
- Is the $P = 0.5$ situation special somehow?
- Lower limit, upper limit? Is it $M = N$ and $M = S$, or more involved?
- How much is the information channel capacity? Its maximum must be in the order of the total firing frequency.
- But how to define it? What is the input, what is the output?
- Associate memory: Does the smaller logic unit contain the larger one and, if so what is the implication?

1. Salk Institute, "Memory capacity of brain is 10 times more than previously thought", Science Daily, January 20, 2016.

Combining molecular dynamics and the Chapman-Kolmogorov theory of ion transport in biological channels

Miraslau L. Barabash^{1a}, William A.T. Gibby^{1b}, Dmitry G. Luchinsky^{1,2}, Carlo Guardiani^{1,3},

Igor A. Khovanov³, and Peter V.E. McClintock¹

¹*Department of Physics, University of Lancaster, Lancaster, UK*

^a*m.barabash@lancaster.ac.uk*; ^b*w.gibby@lancaster.ac.uk*

²*SGT Inc., Greenbelt MD, 20770, USA*

³*School of Engineering, University of Warwick, Coventry, CV4 7AL, UK*

I. INTRODUCTION

Ion channels are pores within proteins that are embedded in biological cellular membranes and which control the passive transfer of ionic species into and out of a cell [1]. They present important, open problems that are at the focus of intensive research in biophysics, physiology, and pharmacology. The central challenge is to relate a channel's crystal structure to its function. One promising method of doing so is molecular dynamics (MD) simulations, modelling explicitly the motion of ions, proteins and water molecules. However, current computer facilities do not allow MD to trace stochastic ionic trajectories through an open channel over a sufficiently long time, so that the structure-function problem remains. Here, we combine the powers of MD with differential Chapman-Kolmogorov (DCK) theory to describe the conductance and selectivity of ion channels with narrow selectivity filters (SF).

II. METHOD

Motion of a “superion”. Ion channels quite commonly possess selectivity filters (SFs) that are about 1Å wide and 1nm in length. Due to the narrowness of the filter, permeating ions cannot pass each other and therefore move one-dimensionally. This allows one to describe their collective motion as the motion of a “superion” [2], i.e. a quasi-particle representing the center of mass of the ions in the SF. As long as the SF accommodates only a discrete number of ions, the energy levels for a “superion” are also discrete.

Using MD, we may obtain potentials of the mean force (PMF) [3, 4], and calculate the effective potentials $U_{eff}^N(x)$ for the motion [5] of an N -particle “superion” [2]. We introduce the probability density $\rho^N(x, t)$ to find a “superion”, consisting of N ions, at position x at time t in the selectivity filter. The discreteness of system's energy levels requires the spatiotemporal evolution of the probability density to be described by the differential Chapman-Kolmogorov (DCK) equation

$$\begin{aligned} \frac{\partial \rho^N}{\partial x} &= -D_N \frac{\partial}{\partial x} \left[\frac{\partial U_{eff}^N(x)}{\partial x} \rho^N + \frac{\partial \rho^N}{\partial x} \right] - W_{n \rightarrow n-1} \rho^N + W_{n+1 \rightarrow n} \rho^{N+1} \\ \frac{\partial \rho^{N+1}}{\partial x} &= -D_{N+1} \frac{\partial}{\partial x} \left[\frac{\partial U_{eff}^{N+1}(x)}{\partial x} \rho^{N+1} + \frac{\partial \rho^{N+1}}{\partial x} \right] - W_{n+1 \rightarrow n} \rho^{N+1} + W_{n \rightarrow n+1} \rho^N \end{aligned} \quad (1)$$

with zero-current boundary conditions. We compare the ionic current, obtained by that approach, with Brownian dynamics (BD) simulations.

Brownian dynamics simulations. We consider the channel's SF coupled to two ionic reservoirs (Fig.1). In the SF

(ellipse), ions undergo one-dimensional motion. We employ the Grand Canonical Monte-Carlo (GCMC) routine [6] in adjacent buffers to maintain ionic concentrations. This allows simulation of the required concentrations using relatively small reservoir volumes, thus speeding up the BD simulations at low solution concentrations.

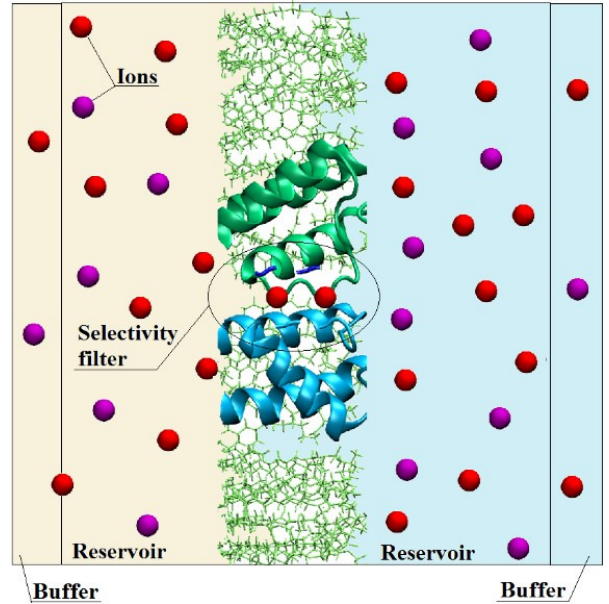


FIG 1. Scheme of the simulation domain. The selectivity filter, reservoirs, buffers and ions are shown.

BD simulations rely on solution of the Langevin equation

$$m_i \frac{d\mathbf{v}_i}{dt} = -m_i \gamma_i \mathbf{v}_i - \frac{dU(\mathbf{r}_i)}{d\mathbf{r}_i} + \mathbf{F}_i^R \quad (2)$$

for each i -th ion in the bulks and SF. Here, standard notation is used, with \mathbf{F}_i^e representing the external electric field due to voltage drop, and \mathbf{F}_i^R standing for white Gaussian noise. The single-ion potential $U(\mathbf{r}_i)$, seen by individual ions only in the selectivity filter, is a weighted average over the multi-ion PMF (see e.g. Fig. 3 in [7]) and thus is a function of the number and type of ions inside the SF. These single- and multi-ion PMFs are obtained from the MD simulations, and thus reflect the structure of the channel protein.

The proposed method can be applied to any PMF for individual and collective ionic motion. At present, we are conducting calculations for the KcsA PMF shown in the inset of Fig. 2 [8].

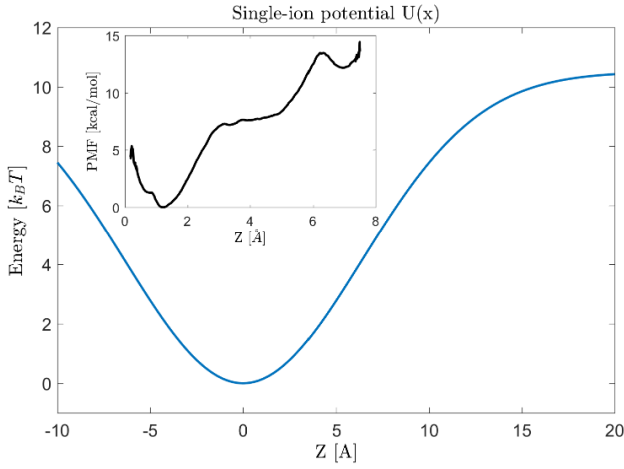


FIG 2. Gaussian approximation for the single-ion PMF [2]. Inset: PMF derived from unbiased all-atom MD simulations (adapted from [8]).

The preliminary results discussed below were obtained for a simple Gaussian approximation of the PMF (Fig. 2) in the KcsA potassium channel [2]. The motion of ions in the bulks is governed by pairwise ion-ion interactions, modelled by the screened Coulomb law

$$\phi(r) = \frac{q_1 q_2}{4\pi\epsilon_w\epsilon_0} \frac{e^{-r/\lambda}}{r} + F_0 \left(\frac{r_0}{r}\right)^9, \quad (3)$$

with the Lennard-Jones term standing for ion-ion repulsion at small distances.

III. RESULTS

We will demonstrate that the model produces conductance and current saturation, as well as K^+/Na^+ and K^+/Ba^{++} selectivity, in KcsA. Preliminary results of Brownian dynamics simulations (Fig. 3) demonstrate agreement with experimental data [7].

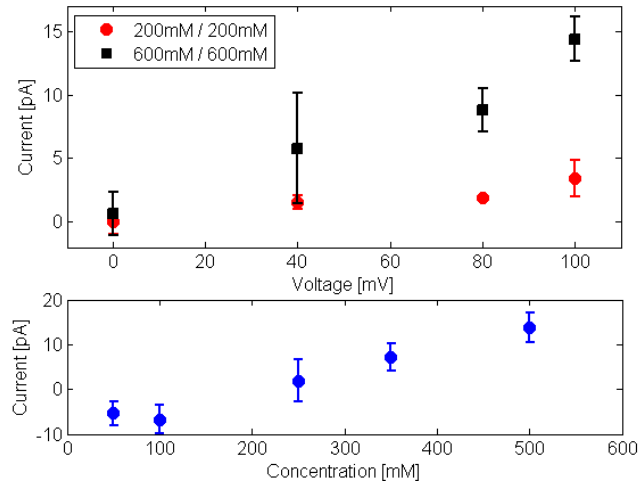


FIG 3. BD simulations. Top: Current-voltage curve. The inset annotation shows the concentrations of left and right bulks. Data are shown as mean \pm STD. Bottom: Current vs. left bulk concentration. The right bulk is kept at 150mM concentration, and the voltage is zero.

UPON 2018, GDANSK, JULY 9-13, 2018

IV. CONCLUSIONS AND OPEN QUESTIONS

We have proposed a method coupling a channel's crystal structure with its properties via MD, thus paving the way to a solution of the structure-function problem. Filling the present gap between MD simulations and single-channel currents, our method allows for fast computation of the conductivity and selectivity properties of narrow channels. The results offer potential applications in physiology, as well as in nanoscale fluid filters, graphene nanopores, and biomimetic artificial channels.

Our new method bridges molecular dynamics simulations (e.g. [8]), stochastic Chapman-Kolmogorov theory, and the statistical theory of selectivity in biological ion channels [9,10] including ionic Coulomb blockade [11]. This bridge holds out the promise of answers to future questions, including: (a) the inverse approach, namely what PMF should govern ions in order for the channel to exhibit required properties; and (b) the relationship between the multi-particle probability density of the differential Chapman-Kolmogorov Eq. (1) and that of the Bogoliubov–Born–Green–Kirkwood–Yvon hierarchy of kinetic equations [12].

ACKNOWLEDGEMENTS

The work was funded by a PhD Scholarship from the Faculty of Science and Technology of Lancaster University, the Engineering and Physical Sciences Research Council (grants EP/M016889/1 and EP/M015831/1), and by a Leverhulme Trust Research Project Grant RPG-2017-134.

1. B. Hille, *Ion Channels of Excitable Membranes*, Sinauer Associates, Sunderland, MA, 3 ed. (2001)
2. S. O. Yesilevskyy, V. N. Kharkyanen, *Phys. Chem. Chem. Phys.* **6** 3111-3122 (2004)
3. J. G. Kirkwood, *J. Chem. Phys.* **3** 300 (1935)
4. B. Roux *et al.*, *Q. Rev. Biophys.* **37**(1) 15–103 (2004)
5. M.A. Wilson *et al.*, *J. Chem. Phys.* **141**, 22D519 (2014)
6. W. Im *et al.*, *Biophys. J.* **79**(2): 788–801 (2000)
7. M. LeMasurier *et al.*, *J. Gen. Physiol.* **118**(3) 303-314 (2001)
8. S. M. Cosseddu *et al.*, *EPJ ST* **222**(10), 2595–2605 (2013)
9. D. G. Luchinsky *et al.*, arXiv:1604.05758 (2016)
10. D. G. Luchinsky *et al.*, *International Conference on Noise and Fluctuations (ICNF) 2017*, Vilnius, 188
11. I. Kh. Kaufman *et al.*, *New J. Phys.* **17** 083021 (2015)
12. N. N. Bogoliubov, *J. Phys. USSR* **10**(3): 265–274 (1946)

The impact of biomolecules binding on low-frequency noise in Si NW FET biosensors

Y.Kutovyi¹, I.Zadorozhnyi¹, V.Handziuk¹, H.Hlukhova¹, M.Petrychuk² and S.Vitusevich¹

¹Institute of Complex Systems (ICS-8), Forschungszentrum Jülich
52428 Jülich, Germany
s.vitusevich@fz-juelich.de

²Faculty of Radiophysics, Electronics and Computer Systems
Taras Shevchenko National University of Kyiv
Kyiv, Ukraine

I. INTRODUCTION

A great deal of attention has been recently paid to silicon nanowire field-effect-transistors (Si NW FETs) as a powerful diagnostic platform due to their high biocompatibility and tunable electrical properties^{1,2}. Sensing principle of such charge-sensitive bio-devices is based on label-free approach which allows the direct monitoring of biorecognition processes between receptor and target biomolecules. Being dissolved in a liquid biomolecules like proteins possess a positive or negative charge, which depends on pH and ionic strength of the solution. Therefore, when charged biomolecules selectively bind to the receptor molecules, which are covalently linked to the nanowire surface, the biomolecular recognition events induce changes in surface potential, which modulates the charge carrier flow in the nanowire channel, generating an electrically detectable signal^{3,4}. According to current trends in FET-based biosensing the pronounced changes in channel conductance induced by the biorecognition event, e.g. the antigen-antibody binding, can be measured and correlated to the analyte concentration^{5,6}. However, the development of a robust diagnostic platform based on FET biosensors requires a careful consideration of noise. Usually, fluctuations in the measured electrical signal have several noise sources, including thermal fluctuations and intrinsic device noise due to mobility and/or carrier number fluctuations in the channel⁷⁻⁹. At the same time, fluctuations in the NW FETs while operating in liquid containing biomolecules have not been explained in detail yet.

Here we report the results demonstrating that selective binding of target biomolecules to the silicon nanowire surface produced increased excess noise, which has characteristics and behavior that considerably differ for those recorded for the same transistor operated in solution without target molecules. As the analyte, we chose cardiac troponin I (cTnI) molecules which are very sensitive biomarker for acute myocardial infarction diagnosis^{10,11}.

II. EXPERIMENTAL DETAILS

The fabrication of liquid-gated Si NW array FETs was performed by applying “top-down” method to p-type <100>-oriented silicon-on-insulator (SOI) wafers with 75nm thick active silicon layer and 145nm thick buried oxide layer (BOX). All fabrication processes were carried out at the Helmholtz Nanoelectronic Facility (HNF) of Forschungszentrum Jülich. The steps involved in the fabrication of silicon nanowire devices are presented in our previous work¹². After fabrication the wafers were cut into single chips, wire-bonded and encapsulated for liquid measurements. In order to provide sensing capability of Si NW FETs the surface of nanowires were functionalized with highly specific monoclonal cTnI antibodies.

For the noise measurements we used the homemade ultra-low noise measurement setup. More detailed description of the noise

measurement setup is previously presented elsewhere¹³. Briefly, the gate-source and drain-source biases were applied to the sample using a battery and a variable resistor. A capacitance of 9400 μ F was used in parallel to the variable resistor in order to additionally stabilize the voltages. The drain-source voltage fluctuations were amplified to the measurable range using a home-made ultra-low noise preamplifier and then amplified by Stanford low noise voltage preamplifier SR560. The output of the amplifier was fed to HP (Hewlett Packard) 35670 dynamic parameter analyzer that performs the fast Fourier transform on the time domain signal to frequency domain yielding the voltage noise power spectral density (S_V) in the range from 1Hz to 100kHz. In order to get reliable noise spectra, the number of averages was set at 100. The processed noise data was then transferred via GPIB interface to a PC.

III. RESULTS AND DISCUSSIONS

Si NW array FET consisted of 50 nanowires nominally 100 nm wide and 5 μ m long was used in a sensing experiment. During the noise measurements the device was operated in a linear regime by applying a constant drain-source bias of 100mV. Silicon nanowires were exposed to 1mM phosphate-buffered saline (PBS) solution with pH=7.4 and gated via Ag/AgCl reference electrode. The normalized noise spectra of the transistor modified with monoclonal cTnI antibodies are presented in Fig. (1).

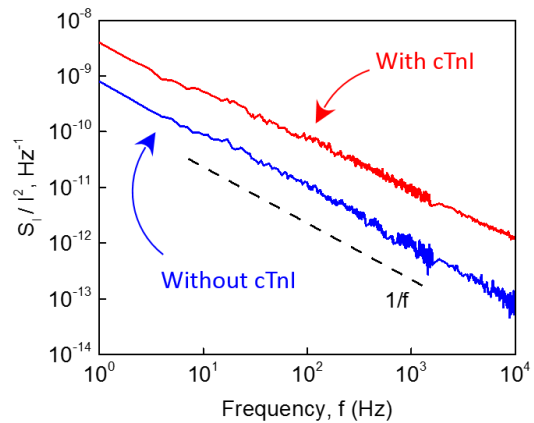


FIG. 1. Measured noise spectra for the liquid-gated Si NW array FET at a drain bias of 0.1V and overdrive liquid gate voltage of 0.47V before and after cTnI binding from 10ng/mL solution.

Flicker 1/f noise originating from the interaction between slow traps in the gate oxide and charge carriers in the channel was observed as a dominant component in the noise spectra at low frequencies (see Fig. (1), blue curve). However, after introducing

the PBS solution containing 10ng/mL of cTnI antigens to the NW sensor, the noise of the transistor increased by almost one order of magnitude (see Fig. (1), red curve). In addition, distinct conductance decrease was also observed indicating on the negative electrical gating effect when negatively charged troponin molecules selectively bind to the n-type Si NW FET. In order to understand and analyze the spectra acquired after the biomolecule binding on a Si NW FET sensor surface, we calculated equivalent input voltage spectral density S_U of the transistor and plotted the values in Fig. (2) as a function of overdrive gate voltage ($V_{LG}-V_{Th}$) at frequency of 30Hz.

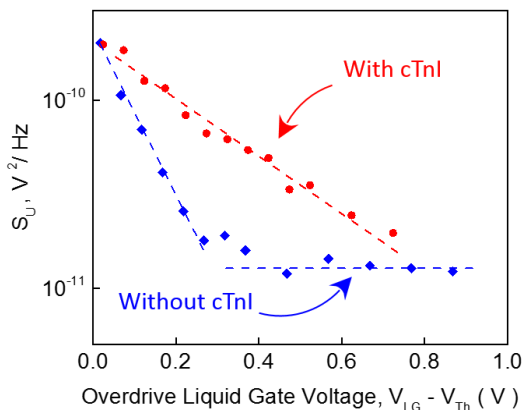


FIG. 2. The equivalent input noise S_U of the Si NW FET plotted versus overdrive liquid gate voltages before and after binding of troponin molecules in 1mM PBS solution. The lines are guides for the eye.

For the case of pure PBS solution (without troponin antigens), at $V_{LG}-V_{Th} > 0.3V$ the S_U value didn't change (in the range from 0.3 to 0.9V) with overdrive gate voltage indicating on the carrier number fluctuation model (McWhorter's model^{14, 15}). However, binding of troponin molecules resulted in a substantial increase of the input referred noise in all ranges of applied gate voltages, i.e.

contribution of an additional noise component. We registered that the noise behavior after binding of cTnI antigens differs considerably from that measured in pure buffer solution. This fact indicates that excess noise is not caused by changes in the dielectric layer of Si NW FET, but it is determined by fluctuations of the effective charges introduced by troponin molecules selectively attached to antibodies on the sensor's surface. Moreover, the amplitude of the excess noise decreases with increasing of effective gate voltage (see Fig. (2)) pointing out on the fact that the additional noise is also related with movement of ions through the membrane¹⁶ formed by troponin molecules attached to antibodies on the nanowire surface. Our results demonstrate that charged antigen molecules influence on the penetration of small ions resulting in excess drain current fluctuations of the transistor.

IV. CONCLUSIONS

We fabricated liquid-gated Si NW array FETs and applied them for the selective detection of cTnI biomarker molecules. The low-frequency noise of Si NW FETs operated in a solution without target molecules was determined by tunneling of the charge carriers to/from the interface traps in the oxide layer, i.e. pure transistor-determined noise. However, with the addition of troponin molecules to the buffer solution, the charge fluctuations resulted in additional excess noise deriving from the negatively charged troponin molecules. Our results show that the additional noise is related to the troponin molecules and has characteristics which considerably differ for those usually recorded for conventional FETs. We demonstrated that noise spectroscopy can be successfully applied for investigation of dynamic processes associated with the biomolecular recognition events.

ACKNOWLEDGEMENTS

The authors would like to acknowledge Prof. Dr. A. Offenhäusser and Dr. S. Pud for valuable and useful discussions. Y. Kutovy greatly appreciates a research grant from the German Academic Exchange Service (DAAD).

- ¹ Z. Wang, S. Lee, K. Koo and K. Kim, IEEE Transactions and Nanobioscience, vol. **15**, pp. 186-199, 2016.
- ² Y. Cui, Q. Wei, H. Park and C. M. Lieber, Science, vol. **293**, pp. 1289-1292, 2001.
- ³ F. Patolsky, G. Zheng and C. M. Lieber, Nanomedicine, vol. **1**, pp. 51-65, 2006.
- ⁴ A. C. Mazarin de Moraes and L. T. Kubota, Chemosensors, vol. **4**, pp. 1-26, 2016.
- ⁵ X. P. Gao, G. Zheng and C. M. Lieber, Nano Lett., vol. **10**, pp. 547-552, 2010.
- ⁶ K.-I. Chen, B.-R. Li, Y.-T. Chen, Nano Today, vol. **6**, pp. 131-154, 2011.
- ⁷ L. K. J. Vandamme and D. Rigaud IEEE Trans. Electron Devices, vol. **41**, pp. 1936-1945, 1994.
- ⁸ I. Zadorozhnyi, J. Li, S. Pud, H. Hlukhova, V. Handziuk, Y. Kutovy, M. Petrychuk and S. Vitusevich, Small, vol. **14**, pp. 1-8, 2017.
- ⁹ S. Vitusevich, I. Zadorozhnyi, Semiconductor Science and Technology - Topical Review, vol. **32**, pp. 1-21, 2017.
- ¹⁰ S. Korff, H.A. Katus and E. Giannitsis, Heart, vol. **92(7)**, pp. 987-993, 2006.

- ¹¹ G. Boriani, M. Biffi, V. Cervi, G. Bronzetti, G. Magagnoli, R. Zannoli, A. Branzi, Chest, vol. **118(2)**, pp. 342-347, 2000.
- ¹² S. Pud, F. Gasparyan, M. Petrychuk, J. Li, A. Offenhausser and S. Vitusevich, J. Appl. Phys., vol. **115**, pp. 1-12, 2014.
- ¹³ S. Pud, J. Li, M. Petrychuk, S. Feste, S. Vitusevich, B. Danilchenko, A. Offenhäusser, and S. Mantl, J. Appl. Phys., vol. **113**, pp. 3-10, 2013.
- ¹⁴ M. J. Kirton and M. J. Uren, Advances in Physics, vol. **38**, pp. 367-468, 1989.
- ¹⁵ I. Zadorozhnyi, J. Li, S. Pud, M. Petrychuk and S. Vitusevich, MRS Advances, vol. **6**, pp. 1-6, 2016.
- ¹⁶ R.B.M. Schasfoort, P. Bergveld, R.P.H. Kooyman and J. Greve, Analytica Chimica Acta, vol. **238**, pp. 323-329, 1990.

Noise generated from a small network of time-varying phase oscillators

Yevhen F. Suprunenko¹ and Aneta Stefanovska¹

¹*Physics Department, Lancaster University, Lancaster, UK, LA1 4YB*
e-mail address: aneta@lancaster.ac.uk

I. INTRODUCTION

We have investigated the dynamics of a finite number of interacting phase oscillators with time-varying parameters. The work is motivated by the inherent finiteness of systems in the real world, both in terms of the time on which the dynamics evolves, as well as in terms of the finite number of elements that contribute to the collective dynamics that we observe and measure at microscopic level.

II. MODEL

The model is defined as:

$$\frac{d\phi_n}{dt} = \omega_n(t) + \frac{K(t)}{N} \sum_{m=1}^N \sin(\phi_m - \phi_n), \quad (1)$$

where ϕ_n is the phase of n^{th} oscillator, $n = 1, \dots, N$, $\omega_n(t)$ and $K(t)$ are time-varying natural frequencies and a coupling strength respectively. For the sake of simplicity, we consider periodic sinusoidal variations. The size N of the ensemble can be up to several hundred oscillators.

The model describes how changes in the microscopic dynamics of each oscillator and interaction among the oscillators influence the macroscopic dynamics, observed as their mean field defined as:

$$r e^{i\psi} = \frac{1}{N} \sum_{n=1}^N e^{i\phi_n} \quad (2)$$

III. RESULTS

We will show that this model, although fully deterministic at the microscopic level, can result in three general scenarios:

- a) Macroscopic dynamics is fully deterministic and oscillatory. This corresponds to a strong synchronization in the system¹.
- b) Macroscopic dynamics is in a mixed state, where both the deterministic and stochastic components are strongly represented.
- c) Macroscopic dynamics is nearly indistinguishable from stochastic. In this case, the system is not synchronized.

The dynamic properties were tested by several standard methods, such as power spectral density², self-similarity and detrended fluctuation analysis^{3,4}, and represented in the time-frequency domain using the wavelet transform⁵. It will be shown that time-variability enables stochastic dynamics to emerge, even in smaller systems. We will argue that this is a very frequent scenario in nature, including metabolic oscillations in the cells⁶ or the firing of neurones in the brain, as well as condensed matter systems.^{7,8}

IV. SUMMARY

We provide a model that can account for creation of noise quite generally.

ACKNOWLEDGEMENTS

This work has been funded by the EU's Horizon 2020 research and innovation program under the Marie Skłodowska-Curie Grant Agreement No. 642563, and the EPSRC grant EP/M006298/1.

¹ M. Lucas, J. Newman and A. Stefanovska. Stabilization of dynamics of oscillatory systems by nonautonomous perturbation. *Phys Rev E* **97**, 042209 (2018).
² P. T. Clemson and Aneta Stefanovska. Discerning non-autonomous dynamics. *Phys Rep* **542**, 297 (2014).
³ J. M. Hausdorff and C.-K. Peng. Multiscaled randomness: A possible source of 1/f noise in biology. *Phys Rev E* **54**, 2154 (1996).

⁴ P. Clemson, G. Lancaster and A. Stefanovska. Reconstructing time-dependent dynamics. *Proc IEEE* **104**, 223 (2016).
⁵ D. Iatsenko, P. V. E. McClintock and A. Stefanovska. Linear and synchrosqueezed time-frequency representations revisited: overview, standards of use, resolution, reconstruction, concentration, and algorithms. *Dig Sig Proc* **42**, 1 (2015).

- ⁶ A. Gustavsson, D. D. Van Niekerk, C. B. Adiels, F. B. Preez. Sustained glycolytic oscillations in individual isolated yeast cells. *FEBS* **279**, 2837 (2012).
- ⁷ M. B. Weissman. $1/f$ noise and other slow, nonexponential kinetics in condensed matter. *Rev Mod Phys* **60**, 537 (1988).
- ⁸ E. Paladino, Y. M. Galperin, G. Falci, B. L. Altshuler. $1/f$ noise: Implications for solid-state quantum information. *Rev Mod Phys* **86**, 361 (2014).

Correlated Fluctuation and Variability in SiO_x-Based Memristors: A Simplified Approach for Circuit Simulation Environments

E. Miranda¹, A. Mehonic², W.H. Ng², J. Suñé¹ and A.J. Kenyon²

¹Departament d'Enginyeria Electrònica, Universitat Autònoma de Barcelona, Cerdanyola del Valles, Spain
e-mail address: enrique.miranda@uab.cat

² Department of Electronic & Electrical Engineering, University College London, London, UK
e-mail address: adnan.mehonic.09@ucl.ac.uk

I. INTRODUCTION

Current-voltage fluctuation (IVF), cycle-to-cycle (C2C) and device-to-device (D2D) variability are hot topics in the field of memristive devices because they are crucial factors for the performance, endurance and integration capability of such structures in complex systems [1,2]. Briefly, a memristor is a resistor with nonvolatile memory that can be not only used for information storage but also as an electrical synapse in neuromorphic networks. The physics behind this device is the formation and destruction of a vacancy or metal atoms bridge spanning an oxide layer in a MIM stack (Fig.1). The switching is caused by the application of an electric field with alternate sign (bipolar switching) (Fig.2). The filament formed this way can suffer modifications from C2C because of the different arrangement of atoms. To a lesser extent, IVF is also expected to occur during a voltage sweep as a consequence of atomic displacement induced by the electron wind force and electron trapping/detrapping effects. In general, IVF is investigated using random telegraph noise (RTN) analysis techniques but these experiments require constant voltage signals [3,4]. In addition, C2C variability is often treated as an uncorrelated process without trend [5,6]. Here, a simplified approach that tries to tackle both effects is attempted. D2D variability is out of the scope of this work but can be included as well. A first issue is that IVF and C2C are self-correlated random processes which are somehow linked: the current fluctuates around a certain current determined by the morphology of the filament core. A second issue is that the considered conduction model must represent the I - V curve in the whole voltage span and must always satisfy the "pinched" condition $I(V=0)=0$. Finally, a third issue is that programming languages used by the most popular circuit simulator environments (SPICE-like) are severely limited (if not interfaced with other softwares like MATLAB), which makes the solution to this problem challenging. In this regard, since the proposed approach is intended for easy implementation and use, Monte Carlo/Worst Case analysis tools provided by the simulator (LTspice in our case) will be exclusively referenced here.

II. MODEL EQUATIONS AND RESULTS

Figure 2 shows a typical resistive switching experiment with multiple I - V loops. The devices are Au/Ti/SiO_x(35nm)/Mo stacks. The current changes from a high (HRS) to a low (LRS) resistance state alternately as a consequence of the formation and dissolution of a filamentary pathway. The morphology of the HRS filament is ultimately determined by the reset process. In this work, we will focus the attention on the HRS regime (Fig.3) but the analysis can be extended to LRS as well. Electron transport in HRS is assumed

to follow the quantum-point contact (QPC) model in agreement with previous observations for SiO_x [7,8]:

$$I = \frac{2e}{h\alpha} \exp(-\alpha\Phi_0) \{ \exp[e\alpha(\gamma + 1)V] - \exp[e\alpha\gamma V] \} \quad (1)$$

where Φ_0 is an effective confinement barrier height, α a parameter related to the longitudinal barrier profile and $0 \leq \gamma \leq 1$ a coupling factor. For $\alpha \rightarrow 0$ (collapse of the tunneling barrier) the standard Landauer formula $I = G_0 V$ is recovered. $G_0 = 2e^2/h = 77.5 \mu\text{S}$ is the quantum-conductance unit. A fitting result to the median experimental curve using Eq.(1) is shown in Fig.3. For the sake of simplicity, the barrier height for cycle i , φ_{0i} will be expressed as an autoregressive process of order one AR(1) with trend Φ_{0i} :

$$\varphi_{0i} = (1 - \rho_C)\Phi_{0i} + \rho_C\varphi_{0i-1} + \sigma_C^2\epsilon_i \quad (2)$$

ρ_C is the C2C self-correlation coefficient, σ_C the standard deviation, and $\epsilon_i \sim N(0,1)$ a Wiener process. This is the simplest process in which the past values of the barrier height have an effect on the current value. For AR(1), $\varphi_{0i} \sim N(\Phi_{0i}, \sigma_C^2)$, where $\sigma_C^2 = \sigma_C^2 / (1 - \rho_C^2)$ is the effective variance. The effects of ρ_C and σ_C on the HRS current are illustrated in Fig.4. As can be seen, consecutive I - V curves follow a trend but they are not completely ordered. It is also assumed that during voltage sweep i , the confinement barrier $\varphi_{ij} = \varphi_i(V_j)$ fluctuates around the value φ_{0i} dictated by (2) with $\epsilon_j \sim N(0,1)$ (see Fig.5):

$$\varphi_{ij} = (1 - \rho_F)\varphi_{0i} + \rho_F\varphi_{ij-1} + \sigma_F^2\epsilon_j \quad (3)$$

Here ρ_F is the IVF self-correlation coefficient and σ_F the standard deviation. Again, $\varphi_{ij} \sim N(\varphi_{0i}, \sigma_F^2)$ where $\sigma_F^2 = \sigma_F^2 / (1 - \rho_F^2)$ is the effective variance of the process. Since we are dealing with two nested AR(1) processes, variability and fluctuations, the combined variance reads $\sigma_{eff}^2 = \sigma_C^2 + \sigma_F^2$. In our case, $\sigma_C^2 \gg \sigma_F^2$. The final result is a log-normal current distribution compatible with tunneling processes in disordered systems [9]. From the practical viewpoint, random barrier heights are obtained using the Monte Carlo Gaussian function (Box-Muller transform [10]):

$$.func MCG(x, y, z) = x + y\sqrt{-2\ln[rand(z)]}\cos[2\pi \text{rand}(z + 1)] \quad (4)$$

where x is the mean value, y the standard deviation and z the seed. Since LTspice treats each cycle independently (C2C correlation is introduced through the effective variance), the variable *run* in the directive `.step param run 1 Max 1` plays the role of index i in (2). *Max* is the number of cycles. This is used to calculate the trend function Φ_{0i} (Fig.4.c) and z . Typical simulation results from LTspice (including variability in the transition profiles and in LRS - not shown here) are illustrated in Fig.6. The complete model and its unsolved questions will be presented at the conference site.

III. REFERENCES

- [1] R. Naous, M. Al-Sheivat, K. Salama, IEEE Trans Nano 15, 15 (2016)
- [2] F. García-Redondo, R. Gowers, A. Crespo-Yepes, M. López-Vallejo, L. Jiang, IEEE Trans Circ Syst 63, 1255 (2016)
- [3] S. Choi, Y. Yang, W. Lu, Nanoscale 6, 400 (2014)
- [4] S. Balatti, S. Ambrogio, A. Cubeta, A. Calderoni, N. Ramaswamy, D. Ielmini, IEEE IRPS (2014)
- [5] T. Schultz, T. Bailey, R. Jha, IEEE, p. 372 (2016)
- [6] A. Crespo-Yepes, J. Martin-Martinez, I. Rama, M. Maestro, R. Rodriguez, M. Nafria, X. Aymerich, M.B. Gonzalez, F. Campabadal. Eurosoi-Uluis, p. 84 (2016)
- [7] A. Mehonic, A. Vrajitoarea, S. Cuff, S. Hudziak, H. Howe, C. Labbé, R. Rizk, M. Pepper, A.J. Kenyon. Sci Rep 3, 2708 (2013)
- [8] E. Miranda, A. Mehonic, J. Suñe, A.J. Kenyon. Appl Phys Lett 103, 222904 (2013)
- [9] V. Karpov, D. Niraula. IEEE TED 38, pp. 1240-1243 (2017)
- [10] D. Thomas, P. Leon, J. Villasenor, ACM Comp Surveys 39, 11 (2007)

ACKNOWLEDGEMENTS

EM and AJK acknowledge financial support from the Leverhulme Trust, UK and Project TEC2017-84321-C4-4-R, MEIyC, Spain.

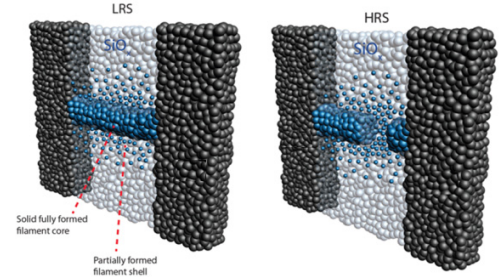


Fig.1- Formed (LRS) and partially formed (HRS) filament.

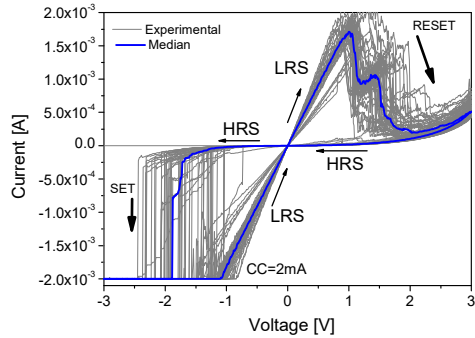


Fig.2- Typical $I-V$ loops. Current compliance is $CC=2mA$.

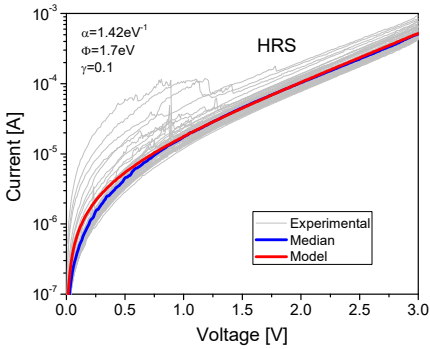


Fig.3- Fitting of the median experimental HRS curve (blue line) using Eq.(1) (red line).

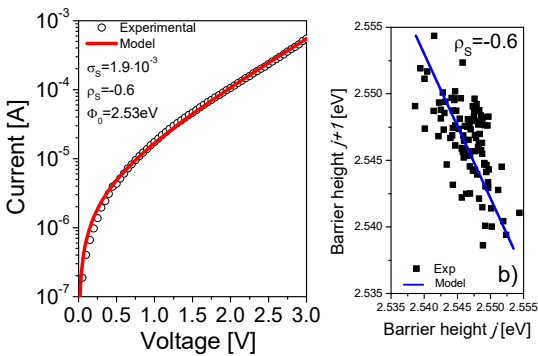


Fig.4- Variability with trend at a fixed voltage ($V=1.5V$). Model results are shown in log and linear scales

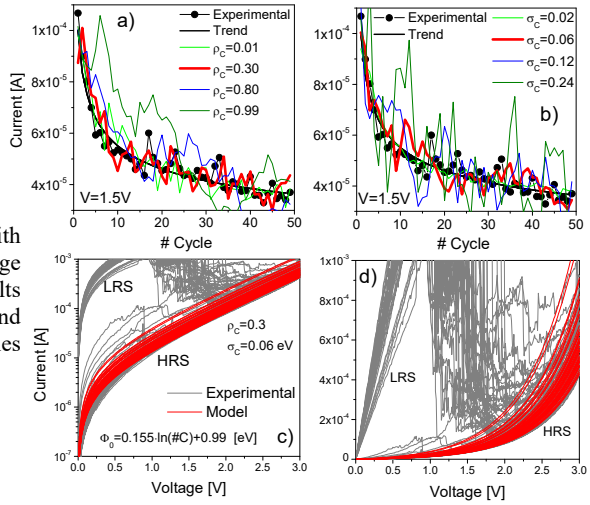


Fig.5- Fluctuations in the barrier height and its self-correlation. The effect is hardly visible in the $I-V$ curve.

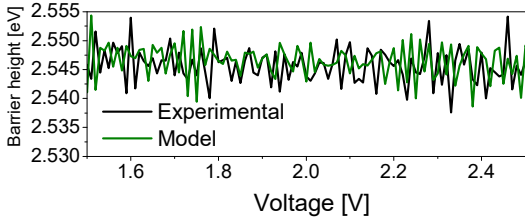
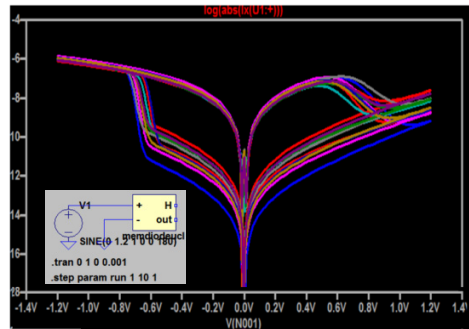


Fig.6- Typical simulations obtained with LTspice.



Low frequency noise in wire-channel GaN/AlGaIn transistors

G. Cywiński¹, J. Przybytek¹, D. But¹, I. Yahniuk¹, P. Kruszewski^{1,2}, M. Grabowski¹, K. Nowakowski-Szkudlarek¹, P. Prystawko¹, P. Sai¹, W. Knap^{1,3}, G. S. Simin⁴, and S. L. Rumyantsev⁵

¹Institute of High Pressure Physics, Polish Academy of Sciences, ul. Sokolowska 29/37, 01-142 Warsaw, Poland
e-mail address: gc@unipress.waw.pl

²TopGaN Ltd., ul. Sokolowska 29/37, 01-142 Warsaw, Poland

³Laboratoire Charles Coulomb (L2C), UMR 5221 CNRS, Montpellier University, Pl. E. Bataillon, 34095 Montpellier, France

⁴Department of Electrical Engineering, University of South Carolina, Columbia, SC 29208, USA

⁵National Research University of Information Technologies, Mechanics, and Optics, St. Petersburg, 197101, Russia

I. INTRODUCTION

The classical configuration of field effect transistor assumes the gate width, W , somewhat higher than the gate length, L , with the actual ratio $W/L > 1$ dependent on the specific application. Some applications require the ratio $W/L < 1$. Among them are transistors for terahertz applications whose principle of operation is based on the plasma waves¹. The transistors with $W/L < 1$ should allow to reduce the effect of the oblique plasma waves leading to an increase of the responsivity of the plasma waves detectors as well as to an increase of the emitter efficiency.

Recently, a new type of fin-shaped channel GaN/AlGaIn field-effect transistors with $W/L < 1$ was proposed in ref. [2].

The schematic view of the design is shown in Fig.1. The design resembles the FinFET structure. However, unlike common FinFET transistors the gates only to the sides of the two dimensional electron gas channel are designed. As a result, gate voltage reduces the width of channel while keeping the concentration and mobility virtually unchanged. At sufficiently high gate voltage, the 2DEG can be squeezed to a wire.

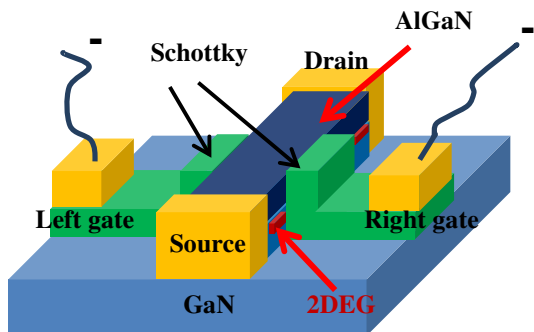


FIG. 1. Schematic view of GaN/AlGaIn FET under study

We report on the experimental and computer simulation studies of electrical and noise properties of these transistors. Open questions related to the devices characteristics are discussed.

II. RESULTS AND DISCUSSIONS

The AlGaIn/GaN structures were grown by Metalorganic Vapour Phase Epitaxy in the Aixtron reactor on c -plane sapphire. The epitaxial structure consisted of 2 nm GaN-cap, 26.3 nm $\text{Al}_{0.15}\text{Ga}_{0.85}\text{N}$ barrier layer, 0.7 μm intentionally undoped GaN layers and 1 μm high resistive GaN:C buffer. The ohmic and Schottky contacts

consisted of Ti/Al (200/1000 Å) and Ni/Au (250/750 Å) metal stacks, respectively.

Symbols in Fig. 2 show experimental transfer characteristics of two FETs with gate length and width $L=3 \mu\text{m}$ and $W=2 \mu\text{m}$ respectively. Solid line in Fig. 2 is a result of Synopsys Sentaurus simulations.

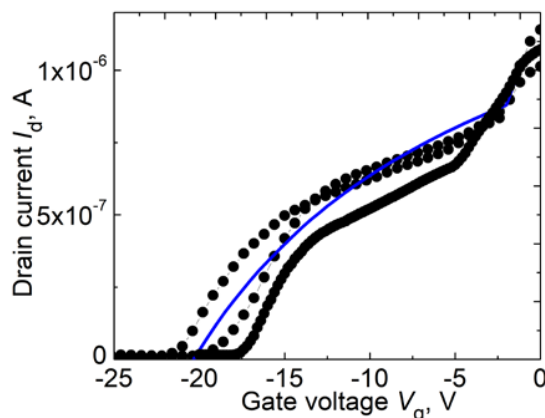


FIG. 2. Transfer characteristics of the FETs under study. $V_d=0.1 \text{ V}$. Symbols show experimental results for two FETs. $L=3 \mu\text{m}$ and $W=2 \mu\text{m}$. The solid line is the results of the simulations.

Differences in the experimental characteristics of nominally identical devices are due to photolithography misalignment and accuracy of the mesa etching. Particularly, as a result of misalignment the edge gate metallization overlaps the top of the AlGaIn layer. This metallization creates a narrow top-gate FET connected in parallel with a wire FET. The kink seen on the characteristics in Fig. 2 at gate voltages $V_g \sim -2 \text{ V}$ is due to pinch off of this top gate transistor.

A reasonable agreement between experimental and theoretical characteristics confirms applicability of our model in which mobility does not depend significantly on the gate voltage.

It is important to point out that this kind of transistor can be pinched-off by a reasonable voltage $V_g \sim -25 \text{ V}$. Approximately two orders of magnitude higher voltage is required to pinch off 3D channel with the same doping level of $2 \times 10^{18} \text{ cm}^{-3}$.

Figure 3 shows the noise spectra at different gate voltages and small drain voltage $V_d=0.1 \text{ V}$ (linear regime). One can see significant contribution of the generation recombination (GR) noise at frequency ca 10-100 Hz. Interestingly, the GR bulge is seen at

zero gate voltage, where the access resistance dominates and noise also originates from the access resistance. With the increase of the absolute value of the gate voltage the GR bulge disappears ($V_g = -4.5$ V). It appears again at $V_g < -12$ V. This kind of behavior indicates, probably, different origin of GR noise at different gate voltages.

Figure 4 shows the dependence of noise on the drain current at constant drain voltage $V_d = 0.1$ V at two frequencies, $f = 10$ Hz and $f = 100$ Hz.

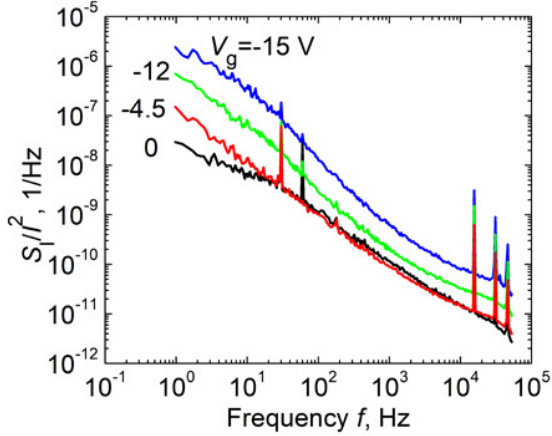


FIG. 3. Noise spectra of drain current fluctuations at different gate voltages. $V_d = 0.1$ V.

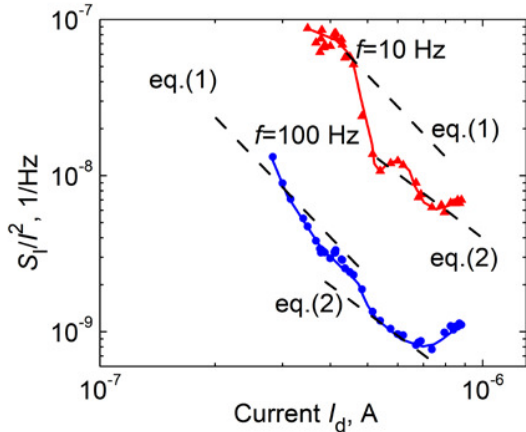


FIG. 4. Drain current dependences of relative spectral noise density of the drain current fluctuations at constant drain voltage $V_d = 0.1$ V.

As seen, noise decreases with the current decrease, which is typical behavior for regular FETs. Bulges seen on these dependences can be attributed to the gate voltage dependent GR noise.

However, the open question is, what is the correct way to analyze these dependences? In a regular FET, in accordance with McWhorter model noise is proportional to $1/n^2$, where n is the channel concentration. At gate voltage independent mobility, it results in the $S_I/I^2 \sim 1/I^2$ dependence. If the access resistance is not negligible

$$\frac{S_I}{I^2} \propto \frac{1}{I^2} \left(\frac{R_{Ch}}{R_{Ch} + R_{acc}} \right)^2, \quad (1)$$

where R_{Ch} is the gate voltage dependent channel resistance and R_{acc} is the access resistance.

In the device under study gate voltage changes predominately the channel width keeping concentration virtually constant. In this case:

$$\frac{S_I}{I^2} \propto \frac{1}{I} \left(\frac{R_{Ch}}{R_{Ch} + R_{acc}} \right)^2 \quad (2)$$

In Fig. 4 dashed line show the slope calculated in accordance with eq. 1 and eq. 2. As seen none of them describes well the full experimental dependences – suggesting that McWhorter model can not be applied for these devices.

In summary, GaN/AlGaIn transistors with the gates on the sides of 2D electron gas with relatively wide gate of $2 \mu\text{m}$ can be pinched off by the gate voltage $V_g \sim -20$ V. Computer simulations describe well the shape of the experimental characteristics. Control of the side gates allows changing the width of 2D electron gas and forming a wire, which should be beneficial for THz detection and emission applications. The noise spectra are the superposition of the $1/f$ and gate voltage dependent GR noise. The gate voltage dependence of noise cannot be described by the McWhorter model. The nature of noise in this new kind of GaN/AlGaIn transistor is an open question that clear needs future complementary studies.

ACKNOWLEDGEMENTS

This project was partially supported by the National Science Centre, Poland allocated on the basis of Grant No. 2016/22/E/ST7/00526, by the ERANET RUS PLUS – TERASENS project, and by the Foundation for Polish Science through Grants No. TEAM/2016-3/25 and No. TEAM/2016-3/26.

¹ M. I. Dyakonov and M. S. Shur, IEEE Trans. Electron. Dev. **43**, 1640 (1996).

² G. Cywiński, et al., Appl. Phys. Lett., submitted (2018)

Noise features of metastable resistivity states in $\text{La}_{0.86}\text{Ca}_{0.14}\text{MnO}_3$ manganite

Jacek Przybytek^{1,2} and Grzegorz Jung^{3,4}

¹ Institute of High Pressure Physics, ul. Sokolowska 29/37, 01-142 Warsaw, Poland

² Faculty of Physics, University of Warsaw, Pasteura 5, 02-093 Warsaw, Poland

e-mail address: jacek.przybytek@fuw.edu.pl

³ Institute of Physics Polish Academy of Sciences, Al. Lotników 32/46, 02-668 Warsaw, Poland

⁴ Department of Physics, Ben Gurion University of the Negev, 84105 Beer Sheva, Israel

I. INTRODUCTION

Despite decades of intensive investigations, electronic transport in mixed-valance manganites still lacks comprehensive theoretical explanations. In particular, the physical mechanism behind spontaneous and current driven transitions to metastable resistivity states in low hole-doped manganite single crystals and thin films reminds obscure. Low doped $\text{La}_{1-x}\text{Ca}_x\text{MnO}_3$ (LCMO) manganite possesses a peculiar ferromagnetic insulating (FMI) ground state. At higher temperatures, it is characterized by a pronounced magnetic and electronic phase separation. Along with FMI phase, it also contains ferromagnetic metallic (FMM), and paramagnetic (PM) phases.¹ Pristine LCMO single crystals, grown by FZ method (for closer description see¹) exhibit strong aging effect with resistivity that generally increases with time.² In this communique, we report on noise features observed in different metastable resistivity states of $\text{La}_{0.86}\text{Ca}_{0.14}\text{MnO}_3$ manganite.

We have studied the electronic-noise of dc current biased freshly synthesized $\text{La}_{0.86}\text{Ca}_{0.14}\text{MnO}_3$ single crystal in its pristine high-resistivity state (HRS) and in spontaneously created low-resistivity state (LRS). For more details on crystal evolution between metastable resistivity states see.² The power spectral density (PSD) of the conductivity noise in a pristine HRS-state has almost exclusively $1/f$ -like character. However, upon a transition to the LRS-metastable state, the noise exhibits additional excess lorentzian components that in many cases could have been associated with clear random telegraph fluctuations of the conductivity.¹ The level of the normalized $1/f$ voltage noise in the LRS is markedly higher than the corresponding noise of the HRS-state. This feature allows one to suggest that the polaron melting scenario^{3,4} may be responsible for the transitions from HRS to LRS state in low-doped manganite crystals. However, the detailed understanding of specific noise fingerprints,² and the life spans of metastable resistivity states remain to be unsolved problems of noise in the discussed systems.

II. RESULTS AND DISCUSSION

Details of the measuring techniques, sample fabrication and characterization have been published elsewhere, see e.g.¹ In brief, dc, ac, and magnetic resonance studies revealed the existence of the ferromagnetic phase not only below the Curie temperature $T_c = 167$ K, but also above T_c , up to some 240 K. The coexistence of insulating and metallic-like phases (FM and PM above T_c and FMI and FM below T_c) and electronic phase separation at the nanoscale are the reasons for highly nonhomogenous carrier

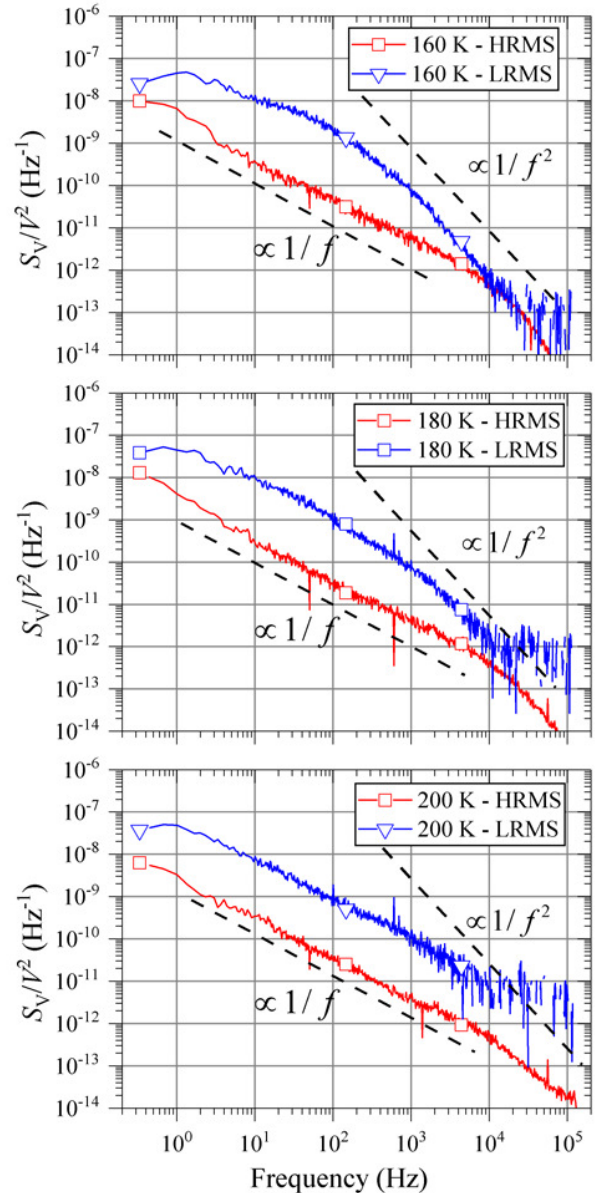


Fig. 1. Normalized PSD spectra for temperatures $T=140$ K, 160 K, 180 K and 200 K. The HRS and LRS spectra differ by shape and magnitude. The HRS-spectra (in red) are mainly of $1/f$ -character, whereas the LRS-spectra (in blue) reveals an additional lorentzian components.

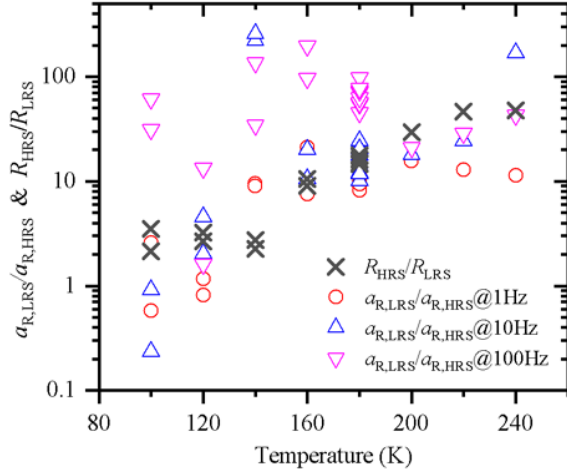


Fig. 2. The black crosses show the resistance ratio in HRS and LRS. The highest difference is at high temperatures and decreases with temperature down to ca 140 K and then remains constant. Other, open symbols show the ratio of the normalized noise power density in HRS and LRS at frequencies 1, 10, and 100 Hz.

transport, local high density current in the sample and percolation-like hopping transport via chains of metallic-like clusters.

In both HRS and LRS states, the dominant noise component is $1/f$ noise, see Fig. (1).

To compare this noise in different states of the sample we use the quantity $a_R = \Omega \int f^\alpha S_V(f) / V^2$, where Ω is the sample volume and α is the noise exponent in $1/f^\alpha$. The density n of charge carriers relates a_R to the Hooge parameter $\gamma = a_R n$.^{5,6}

In Fig. (2) (open symbols) we show the ratio $a_{R,LRS} / a_{R,HRS}$ of these quantities in HRS and in LRS state as a function of temperature.

The resistivities of the HRS and LRS differ by more than one order of magnitude (Fig. (2), black crosses) at high temperatures,

whereas at low temperatures below 140 K their ratio remain nearly constant at the level of 2–3. Changes in the normalized noise levels $a_{R,LRS} / a_{R,HRS}$ are similar to the change in resistivity. HRS noise level differs from the LRS one by more than an order of magnitude at higher temperatures and become closer to each other below 140 K. This suggests that physical mechanism behind the temperature change of resistivity and of its fluctuations is probably the same.

The question arises what is responsible for this change? Is it the carrier density (higher in HRS and lower in LRS state) or the change in mobility and its fluctuations? Or both?⁷

Hole transport mechanism in the presence of strong hole-lattice interactions leads to self-trapping of holes and results in formation of quasi-localized states of very small mobility, small-polarons. Phonon-assisted hopping and instantaneous conversion of holes to small polarons (and vice-versa) will be considered as a dominant mechanism of transport and noise observed in our sample. Emin suggested that current flowing across phase boundary between metallic and polaronic phases leads to the accumulation of small polarons at the boundary.^{3,4} At sufficiently high density, small polarons become unstable with respect to conversion into nonpolaronic high mobility carriers. As a result of such polaron “melting” event, the HRS current carried by a large number of low mobility small polarons, will turn into LRS current of small number of high mobility nonpolaronic carriers, what seems to be consistent with our noise data.

In the presentation we will use the polaronic transport concept to explain other UPoN-like experimental features. Among them, the unusual noise dependence on the bias current which is not proportional to I^2 , and sometimes even not monotonic, and the appearance of Meyer–Neldel rule⁸ in the bias dependence of the resistivity.

- ¹ J. Przybytek, J. Fink-Finowicki, R. Puźniak, A. Shames, V. Markovich, D. Mogilyansky, and G. Jung, Phys. Rev. **B 95**, 125101 (2017).
- ² J. Przybytek, J. Fink Finowicki, R. Puźniak, V. Markovich, and G. Jung, J. Appl. Phys. **118**, 043903 (2015).
- ³ D. Emin, Phys. Rev. **B 74**, 035206 (2006).
- ⁴ D. Emin, Polarons (Cambridge University Press, 2013).
- ⁵ F. N. Hooge, Phys. Lett. **29A**, 139 (1969).
- ⁶ F.N. Hooge, *Discussion of recent experiments on $1/f$ noise*, Physica (Amsterdam) **60**, 130 (1972).
- ⁷ L.K.J. Vandamme, Proceedings of the 22nd International Conference on Noise and Fluctuations (ICNF 2013), June 24–28 2013, Montpellier, France. - Piscataway : Institute of Electrical and Electronics Engineers (IEEE), p. 1–6, (2013).
- ⁸ A. Yelon, B. Movaghar and R. S. Crandall, Rep. Prog. Phys. **69**, 1145 (2006).

Open problems in Brain Emulating-Hardware

François Danneville^{1,2}, I. Sourikopoulos¹, S. Hedayat¹, C. Loyez^{1,2}, V. Hoel^{1,2}, and Alain Cappy^{1,2}

¹Univ. Lille, CNRS, USR 3380 – IRCICA

²Univ. Lille, CNRS, ISEN, Univ. Valenciennes, UMR 8520 – IEMN
francois.danneville@iemn.univ-lille1.fr

I. INTRODUCTION

In a context of the end of MOORE's law, new paradigms for data processing are required [1] to respond to a broad range of applications (IA, IoT,...). In particular, there is an urgent need for advanced information processing featuring high energy efficiency. In this context, brain emulating hardware (BEH) is very attractive; note however that BEH is not to rigorously copy biology but rather to outperform biology performance. Thus, BEH needs to extract a coherent set of features from the biology while to identifying the best hardware technology that will allow developing ultra-low power applications. In this paper, essential features about the brain will be first recalled, prior highlighting key open questions raising during the path from a biological to an artificial brain. The paper will end up with the presentation of a highly energy efficient neuromorphic technology recently developed.

II. BIOLOGICAL BRAIN FEATURES

(i) Generalities

The brain structure is known for a long time. Its volume is ranged between 1100 and 1300 cm³, having about 10¹¹ neurons connected up to 10¹⁵ synapses, for a global power consumption of 10 W. Brain energetics is worth mentioning: in the grey matter [2], 25 % of the energy consumption is devoted to “housekeeping” (cell maintenance) while 75 % is consumed under electrical form. The latter is decomposed as follows: 15% for the resting potential, 17% for the action potentials and 43% for synaptic transmission. Neurons average firing frequency is rather low, about 10 Hz.

Schematically, the neocortex is made of regular structures, the cortical columns. Numerous recurrent connections exist within a cortical column, but also between cortical columns.

Highly parallel sensory information (visual, auditory,...) are coded asynchronously and continuously as (electrical) actions potentials (AP) in elementary semantic representations that are identically processed throughout the cortex.

(ii) Homeostasis

From a system point of view, it is essential that brain neurons maintain a minimal firing rate, and, despite the variability (size, area, volume) of dendrites, axons and cells, the brain maintains a stable regime thanks to homeostatis. Homeostatis allows a excitatory neural network having recurrent connections with (plastic) inhibitory neural network to stand in a “balance fluctuation-driven regime”, in which neurons fire irregularly and sparsely [3]. Note that a neuron, connected at its input to a feedforward neural network (having both excitatory and inhibitory neurons), is capable in this regime of fast learning [3].

(iii) Information Coding

Basically, neuron firing frequency and exact timing between action potentials (AP) encode the entire information. A neuron is

constituted of a dendritic tree connected to the soma, itself connected to an axon that propagates an action potential (AP) (if the membrane potential reaches a voltage threshold) to other neurons through the axonal tree connected to synapses. It is important to mention that the computing at the soma input level is analog while at its output, the computing result is an “all or nothing” signal. Thus, the computing is analog while the communication is digital

(iv) Neurons/Synapses

Neurons present a high variability: their area is comprised between 5.10³ to 10⁵ μm² and their volume varies from 10³ to 10⁴ μm³. An important parameter is the membrane capacitance (C_m) of neurons, whose average value is in the order of 100s of pF. Synapses exist in two forms, that are, chemical and electrical. Synapses are “plastic” and embed (under a weight form) “memory”.

(v) Action Potential (Soma), Charge Transfer, Energy Efficiency

Action potential (AP), generated at the soma level, which is propagated along the axon membrane, has been initially studied in [4]. The AP generation process is well known. Without synaptic current excitation, the neuron is its resting state, with a membrane potential around -70 mV. In presence of excitation synaptic current (ESC), the membrane potential (MP) depolarizes; when the MP is reaching a particular threshold, an AP is generated. If the ESC is upheld, the neuron will fire at a particular frequency. The typical voltage sweep is about 100 mV. In order to change the voltage across the membrane capacitance “C_m” by ΔV, an amount of charge ΔQ = C_m ΔV (the number of ions ΔN_{ion} are ΔQ/q_e, with q_e the electron charge) is required to move from one side of the membrane to the other. The concomitant energy that is dissipated is ΔQ = ½ C_m ΔV². Considering the generation and propagation of a spike (charge and discharge), the total energy dissipated by the cell will be ΔE = C_m ΔV². As previously mentioned, neurons are highly variable leading to variable C_m. If one considers that C_m varies between 10 pF to 1 nF and taking ΔV = 100mV, energy efficiency is ranged between 0.1 to 10 pJ; this clearly highlights that a significant improvement is likely possible for artificial neurons.

(vi) Neuron Membrane Voltage Fluctuations

Many authors have studied the membrane voltage fluctuations of a neuron, while it is in his quiescent state (no AP). If one considers the neuron as a basic RC circuit and assuming pure thermal noise, the RMS voltage δV_m (= √(k.T/C_m)) using the variation range previously given for C_m should vary between 1 to 10 μV. Such values are considerably lower than actual ones, which have been theoretically or experimentally reported between 0.1 mV (when ionic channel noise is -only- taken into account [5,6]) to few mV (also accounting for synaptic bombardment [7]). When rigorously calculating in frequency domain the overall spectral density of “intrinsic” membrane noise voltage (related to

opening/closing fluctuations of ionic channels), it converges towards $1/f$ noise variation, as the result of superposed “Lorentzian like” shapes related to the different intrinsic membrane ionic channels (potassium, sodium).

The spontaneous firing rate (SFR) due to thermal agitation of these ionic channels, varying the cell diameter of a neuron, was studied in [6, 8]. In this study, it was clearly shown that the SFR is maintained to a low rate, provided the cell diameter stands higher than $10\ \mu\text{m}$. Thus, as stated in [9], “thermodynamic noise in individual ion-channel proteins sets an upper limit to the wiring densities of the whole brain”.

III. FROM BIOLOGICAL BRAIN TO ARTIFICIAL BRAIN: OPEN QUESTIONS

After having recalled key features of a biological brain, let us raise open questions related to the path towards an artificial brain achievement (or at least brain inspired data processing), highlighting some key differences.

Basics

In biology, AP generation requires for the transport two different ions (for example, Na and K). Can we generate a biomimetic AP with only one type of carrier, i.e., electrons ?

In biology, an AP propagates with a $1\ \text{m/s}$ speed while in artificial it propagates at the speed of light. At first sight, such a propagation speed is an advantage in artificial, nevertheless, for applications requiring human being time constants (robotics), it leads to more difficulty for designing delay circuits.

Connectivity, Down-Scaling

The biological brain is ultra-connected, in 3D. Are 3D interconnects required in artificial or 2D are sufficient ?

Biology is ultra-connected and communicates via low frequency rates. Is that possible to process data in artificial at much higher frequency while decreasing at the same time the number of synapses ? Note that in artificial, a neuron can be connected to an excitatory either inhibitory synapse.

Most AI applications rely on artificial neural networks (ANN) featuring deep learning architecture, while biology neural networks feature highly recurrent ANN. Should we look towards such recurrent ANN in artificial ?

Does the down-scaling (of CMOS technology) constitute a real advantage ?

Synapses

In order to deploy ANN at ultra-large scale, different technologies are available for synapses. They are mostly inspired by non-volatile based memories [10] : ferroelectrics, phase change (PCM), ferromagnetics, resistive.

These synapses are attractive, but feature major drawbacks to be coupled to ultra-low power artificial neurons: (i) when they are transistors based, their supply voltage stands around 1V (or higher), (ii) when other technologies operate below 1V , the synapse is a dipole, meaning that there is no natural isolation between a pre-neuron and a post-neuron. Moreover, most of them are using complex material that does not ensure the required reliability so far. Should we use these synapses or “classical” synapse architectures using transistors (CMOS) ? [11].

IV. TOWARDS ULTRA LOW POWER NEUROINSPIRED HARDWARE TECHNOLOGY

Our research work is in progress to answer the open questions raised in Section III. In particular, we have recently developed an artificial neuron in CMOS technology [12], by scaling down the membrane capacitance as low as to few fF as well as the supply voltage to $200\ \text{mV}$. A tremendous artificial neuron energy efficiency improvement was achieved compared to those of a cortical neuron (two orders of magnitude, energy efficiency of few fJ/spike, neuron frequency in the tens of kHz). This neuromorphic technology was already used in two applications context. First, to emulate the bursting (mode using a basic neural circuit; this mode is important for deep brain stimulation but also to generate locomotion rhythms. Second, to highlight the stochastic resonance phenomena, useful to detect an electrical signal buried in noise. These applications already allow envisioning the use of this ultra-low power neuromorphic technology to develop highly integrated neuro-processor for vision applications. The AN characteristics may also be tuned to address applications in robotics, neuroscience or medical applications.

V. REFERENCES

- [1] A. Boahen “A Neuromorph’s prospectus”, IEEE Journals & Magazines, Computing in Scie. & Engineering, 2017, 19, 2
- [2] J. J. Harris and D. Attwell, “The Energetics of CNS White Matter”, 356 • The Journal of Neuroscience, January 4, 2012 , 32 (1):356–371
- [3] P. Yger, M. Stimberd, R. Brette, “Fast Learning with Weak Synaptic Plasticity”, The Journal of Neuroscience, September 30, 2015 • 35(39):13351–13362
- [4] A. L. Hodgkin, A. F. Huxley, "A quantitative description of membrane current and its application to conduction and excitation in nerve", The Journal of Physiology., 117 (4): 500–544, 1952
- [5] K. Diba, H. A. Lester, C. Koch, “Intrinsic Noise in Cultured Hippocampal Neurons: Experiment and Modeling”, The Journal of Neuroscience, October 27, 2004, 24, (43):9723–9733
- [6] C. O’Donnell, M. C. W. Van Rossum, “Systematic analysis of the contributions of stochastic voltage gated channels to neuronal noise”, Frontiers in Computational Neuroscience, Volume 8, Article 105, 1, September 2014
- [7] M. Rudolph, A. Destexhe, “Inferring network activity from synaptic noise”, Journal of Physiology - Paris 98 (2004) 452–466
- [8] B. Sengupta, A. A. Faisal, S. B. Laughlin and J. E. Niven. “The effect of cell size and channel density on neuronal information encoding and energy efficiency”, Journal of Cerebral Blood Flow & Metabolism (2013) 33, 1465–1473
- [9] A. A. Faisal, L. P. Selen and D. M. Wolpert, “Noise in the nervous system”, Nature (2008), 3, 292-302.
- [10] D. S. J. Inho Kim, M. Zieglerb, H. Kohlstedtb, “Towards artificial neurons and synapses: a material point of view”, RSC Advances, 2013, 3, 3169
- [11] C. Bartolozzi, G. Indiveri, "Synaptic Dynamics in Analog VLSI", Neural Computation 19, 2581–2603 (2007) C _ 2007 Massachusetts Institute of Technology].
- [12] I. Sourikopoulos, S. Hedayat, C. Loyez, F. Danneville, V. Hoel, E. Mercier and A. Cappy A., “A 4-fJ/spike artificial neuron in 65 nm CMOS technology”, Frontiers in Neuroscience, Volume 11, Article 123, March 2017.

1/f Noise on the nanoscale

Eli Barkai

Physics Dept., Bar-Ilan University, Ramat Gan, Israel
e-mail address: barkai@biu.ac.il

The widespread measurement of $1/f^\alpha$ noise, is still a paradox, as it is non-integrable at low frequencies implying that the total energy in the system is finite when $\alpha \geq 1$. As pointed out by Mandelbrot this infrared catastrophe suggests that one should abandon the stationary mind set and hence go beyond the widely applicable Wiener-Khinchin formula for the power spectrum.

In this talk ageing, intermittency, ergodicity breaking, and critical exponents of the sample power spectrum are discussed. A

generalisation of Wiener-Khinchin theorem, to ageing processes with an autocorrelation function which is scale invariant, provides a new spectral theory for $1/f$ noise. This framework describes power spectrum of blinking quantum dots and noise of interface fluctuations with KPZ dynamics.

- ¹ M. Niemann, H. Kantz, E. Barkai *Fluctuations of $1/f$ noise and the low frequency cutoff paradox* **Phys. Rev. Lett.** **110**, 140603 (2013).
- ² N. Leibovich and E. Barkai, *Aging Wiener-Khinchin Theorem* **Phys. Rev. Lett.** **115**, 080602 (2015).
- ³ S. Sadegh, E. Barkai, and D. Krapf *$1/f$ noise for intermittent quantum dots exhibits non-stationarity and critical exponents* **New. J. of Physics** **16** 113054 (2014).
- ⁴ K. A. Takeuchi *$1/f^\alpha$ power spectrum in the Kardar-Parisi-Zhang universality class* **J. Phys. A** **50**, 264006 (2017)

Non-equilibrium noise in a simple model of ageing in glassy dynamics

Mikhail V. Feigel'man^{1,2}

¹*L.D.Landau Institute for Theoretical Physics, Chernogolovka, Moscow Region, Russia*
e-mail address: feigel@landau.ac.ru

²*Skolkovo Institute of Science and Technology, Moscow, Russia*

I am going to present and discuss properties of fluctuations and noise in a relatively general model for non-equilibrium dynamics of glassy systems. This is a model of particle moving according to simplest dissipative equation of motion in a generalized random potential $U(x)$ which is defined by the simplest correlation function of its derivative (i.e. random force) $F(x) = -dU/dx$. Namely, we assume take the irreducible correlation function in the form $\langle\langle F(x) F(y) \rangle\rangle = G f(x-y)$ where $f(x)$ decays fast beyond some microscopic length-scale l at $x > l$. Average value of the force $\langle F(x) \rangle = F$ and bath temperature T are the key parameters of the problem. It is known for some decades that at low enough

temperatures and/or average force F , dynamics of such a model is non-stationary and sub-ohmic: average displacement of a particle after a time t increases slower than linear in time: $\langle x(t) - x(0) \rangle \sim t^a$ where $a < 1$. Such an unusual behavior is the result of a very broad distribution of effective barriers which the particle must overcome to move further on along the coordinate x . I am going to present results of the study of noise spectrum for such a model, i.e. statistics of fluctuations on a top of the above-described non-equilibrium dynamics.

Is the nanoscale scaling of electron devices ultimately limited by noise?

E. Colomés¹, X. Oriols¹, J. Mateos² and T. González²

¹ *Departament d'Enginyeria Electrònica Universitat Autònoma de Barcelona, Spain*
xavier.oriols@uab.cat, enrique.colomes@uab.cat

² *Departamento de Física Aplicada Universidad de Salamanca, Spain*
javierm@usal.es, tomasg@usal.es

I. THE TRANSIT TIME LIMIT

Nowadays, the electronic industry has moved completely into the nanoscale regime, with typical channel lengths of tens of nanometers, implying hundreds of electrons inside the device active region.

During decades, the relation between the clock frequency f and the channel length L has been determined by the transit time limit¹. The clock frequency of a CPU is usually set to 1/3 of the cut-off frequency. Thus, neglecting parasitic effects, f is inversely proportional to the electron transit time τ :

$$f \leq \frac{1}{3\tau} = v/(3L) \quad (1)$$

For ballistic velocities v and nanoscale dimensions, frequencies well beyond the THz range are envisioned. However, the commercial transistors used in the CMOS technology are still far from such frequencies. In Fig. (1), we plot the clock frequency f as a function of the typical size of the Si MOSFETs obtained from the data of CPUs in Table (1). The clock frequencies of all transistors follow the trend associated with the transit time limit, plotted with a solid blue curve (with v obtained from Ref. [2]).

II. OPEN QUESTION

Since 2005, as seen in Table (1), the clock frequency has stagnated around $f = 5$ GHz independently of the channel length to keep acceptable values of the heat dissipated by the 10^9 - 10^{10} transistors present in a CPU (see orange line in Fig. 1). This heat is a global CPU limit, not a limit on each individual transistor as in Eq. (1). At this point, *we wonder if after improving the cooling strategies, there is any fundamental requirement that will still limit the clock frequency, or we will really reach the THz clock frequencies announced for individual nanoscale transistors through Eq. (1)*. This is the open question that we address in this conference. Answering it has fundamental importance for the electronic industry. The existence of such limit would imply that the traditional scaling strategy for CMOS transistors, based on decreasing the channel length to get faster devices, needs to be revisited for nanoscale devices.

The current at high frequency³ is not only due to the particle current (motion of electrons), but also to the displacement current (variations of electric field). In fact, the total current is carried by very few discrete electrons present at the nanoscale active region. Thus, stochastic variations in the number of electrons directly lead to fluctuations of the current. The lower the number of electrons, the higher their influence on the current noise. In this conference, we propose that the ultimate limit that determines the maximum value of the clock frequency of nanoscale transistors is not related to the transit time, but to the noise.

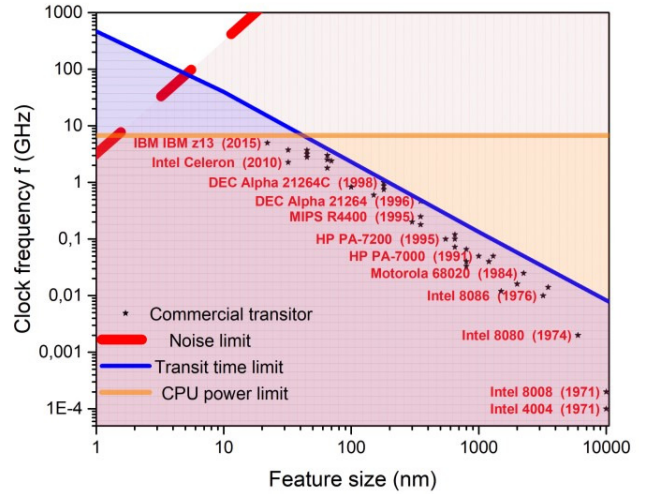


FIG. 1. Clock frequency f from a set of commercial transistors available in last decades as a function of the typical size. Future nanoscale transistors have to work in the triangle given by the transit time (solid blue line) and the noise (dashed red line) limits, above the power (orange line) limit for improved cooling strategies.

III. THE NOISE LIMIT

According to the Ramo-Schokley-Pellegrini theorem, the total classical or quantum (particle plus displacement) current generated by N electrons inside the active region is given by:

$$I(t) = \sum_{i=1}^N I_i = \sum_{i=1}^N q \frac{v_i(t)}{L} \quad (2)$$

with q the electron charge. The important point is that the fluctuations in the current given by Eq. (2), when there is stochastic variation on N , are inversally proportional to the channel length L . Thus, the limit $L \rightarrow 0$ for nanoscale transistors with low N implies an increment of the noise in the current, i.e. an increment of the bit error for logic applications. The errors can be decreased by time-averaging the total current in Eq. (2) during a time interval $T \gg \tau$, but this implies reducing the clock frequency to a value well below the transit time limit in Eq. (1), i.e. $f = 1/T \ll 1/(3\tau)$.

Thus, we argue that the clock frequency f for nanoscale devices has to be fixed well-below the transit time limit to avoid unacceptable bit error rates. This novel noise limitation is usually ignored in the scientific community (with relevant exceptions⁴) because the quantum understanding of nanoscale devices is based

on the wave (probability) nature of electrons, ignoring its particle (discrete) nature⁵. The bit error can be quantified through the square root of the variance of the T-averaged current $\sigma_T \equiv \sigma(T, L)$. The signal-to-noise ratio is given by⁶:

$$SNR = \frac{\langle I \rangle_{DC}}{\sigma_T} \approx \frac{q \frac{\langle N_\tau(t) \rangle}{\tau}}{\frac{q}{\sqrt{\tau}} \sqrt{\frac{var(N_\tau(t))}{\tau}}} \approx \frac{\sqrt{\tau} \langle N_\tau \rangle}{\sqrt{\tau} \sqrt{var(N_\tau)}} \quad (3)$$

where $\langle I \rangle_{DC}$ is the (average) current and N_τ is the amount of electrons entering in the device during a time τ . It is relevant to notice that Eq. (3) has no dependence on the channel length L (contrarily to the transit time limit) because the L -dependence of τ and $\langle N_\tau \rangle$ balances. We have tested this result through Monte Carlo simulations in Fig. (2). We clearly see that (for times greater than the transit time) the three curves of the noise $\sigma_T \equiv \sigma(T, L)$ converge and are independent of L at the indicated operating time T .

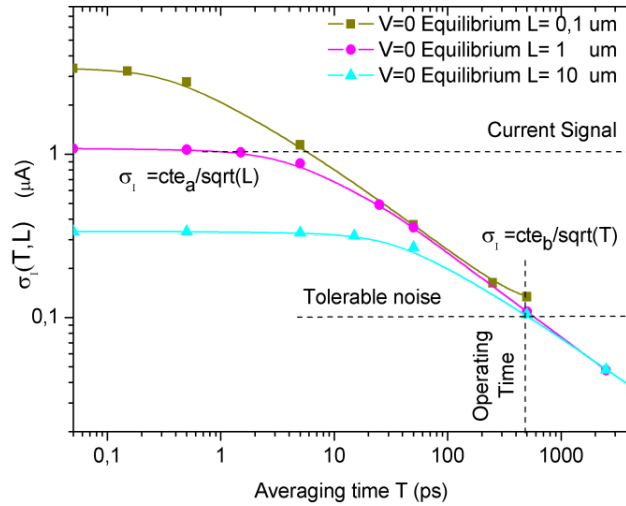


FIG. 2. Noise vs averaging time for three transistors with different channel lengths. The current signal and tolerable noise are also plotted with grey dotted lines.

We can obtain a new analytic expression for the maximum value of clock frequency f based on this novel noise limit⁶. We consider that N_τ electrons attempt to be injected during the time τ following a binomial probability distribution with probability of success p with $var(N_\tau) = \langle N_\tau \rangle (1-p)$. If we compute the number of electrons inside a 3D active region from the phase-space density, $N_\tau = g \cdot L \cdot W \cdot H \cdot k_f^3 / \pi^3$, we get from Eq. (3):

$$f \leq \frac{g \cdot v \cdot W \cdot H \cdot k_f^3}{\pi^3 \cdot SNR^2} \frac{p}{(1-p)} \quad (4)$$

where g is the (spin or valley) degeneration, $W \cdot H$ the lateral area of the transistor and k_f the wave vector associated to the Fermi energy E_f . In Fig. (1), the red dashed line corresponds to the noise limit given by Eq. (4) and obtained with $E_f = 0.026$ eV, $W = H$ and given by the feature size as seen in Table (1), $p = 0.5$, $g = 2$.

The Silicon velocity is obtained from Ref. [2] and a typical value of $SNR \approx 11$ from Ref. [4].

Year	Designer	Model	f (MHz)	L (nm)	F. size (nm)
1971	Intel	4004	0,1	10000	10000
1971	Intel	8008	0,2	10000	10000
1974	Intel	8080	2	6000	6000
1976	Intel	8086	10	3200	3200
1979	Motorola	68010	14	3500	3500
1982	Intel	80286	12	1500	1500
1984	Motorola	68020	25	2250	2250
1986	MIPS	R2000	16	2000	2000
1987	Motorola	68030	50	1300	1300
1988	MIPS	R3000	40	1200	1200
1991	AMD	80386	40	800	800
1991	Motorola	68040	33	800	800
1991	HP	PA-7000	50	1000	1000
1992	Intel	80486	66	800	800
1992	Intel	Pentium	66	800	800
1992	Ross	hyperSPARC	72	650	650
1993	Cyrix	486DX	100	650	650
1993	Cyrix	5x86	120	650	650
1994	MIPS	R4400	200	300	300
1995	MIPS	R10000	180	350	350
1995	MIPS	R4400	250	350	350
1995	HP	PA-7200	100	550	550
1996	DEC	Alpha 21264	466	350	350
1998	IBM	RS64 IV	750	100	180
1998	HP	PA-8700+	875	100	180
1998	DEC	Alpha 21264C	1000	100	180
2002	Fujitsu	SPARC64 GP	600	150	150
2005	Intel	Core 2 Duo	1800	35	65
2005	Intel	Core 2 Quad Extreme	3000	35	65
2007	AMD	Phenom II	3200	25	45
2007	AMD	Opteron	2800	25	45
2008	Fujitsu	SPARC64 VII	2520	30	65
2010	IBM	Power7	3700	25	45
2010	Intel	Celeron	2267	18	32
2010	Intel	Core i5	3730	18	32
2015	IBM	IBM z13	5000	25	22

TABLE. 1. Characteristics of some commercial transistors in last four decades. Data obtained from <http://cpudb.stanford.edu>

As a conclusion, in this conference we present a noise limit for the clock frequency of transistors due to the electron discreteness. For individual nanoscale transistors, this limit in Eq. (4) competes with the well-known transit time limit in Eq. (1). As seen in Fig. (1), at low clock frequencies, this noise limit does not play any role at all. However, due to the device miniaturization, the noise limit cannot longer be neglected and it will represent the true fundamental limitation to reach THz transistors

ACKNOWLEDGEMENTS

This work is supported by the FEDER and the “Ministerio de Ciencia e Innovación” through the Spanish Project TEC2015-67462-C2-1-R and from the EUs Horizon 2020 research program under Grant Agreement No. 696656.

- ¹ J. Singh, *Semiconductor Devices: Basic Principles* (Wiley, NY, USA, 2001).
- ² K. Rais, G. Ghibaudo, F. Balestra and M. Dutoit, *J. Phys. IV C6*, 19 (1994).
- ³ Z. Zhan, E. Colomés and X. Oriols, *IEEE Trans. Electron Devices* **64**, 2617 (2017).
- ⁴ L. B. Kish, *Phys. Rev. A* **305**, 144 (2002).
- ⁵ X. Oriols, *Phys. Rev. Lett.* **98**, 066803 (2007).
- ⁶ E. Colomés, X. Oriols, J. Mateos and T. González, in preparation.

Can linear or parabolic band dispersions in 2D materials be tested by noise?

E. Colomés¹, Z. Zhan², D. Pandey¹ and X. Oriols¹

¹ *Departament d'Enginyeria Electrònica Universitat Autònoma de Barcelona, Spain*

² *School of Physics and Technology, Wuhan University, China*
xavier.oriols@uab.cat, enrique.colomes@uab.cat

I. INTRODUCTION

New 2D materials, such as graphene with a 2D linear dispersion or black-phosphorus with 2D parabolic dispersion, have many revolutionary properties for fundamental physics and practical applications^{1,2,3}. In this conference, we discuss the electron injection model for the simulation of nano devices based on 2D materials. In time dependent (classical or quantum) particle-based simulators⁴, an algorithm, to determine when (and with what properties) electrons are injected from the reservoir into the simulation box, is needed. Our injection model shows important differences between linear and parabolic materials in the frequency spectrum of the noise of the current. Such differences open many unexplored possibilities to use noise as band structure tester.

II. 2D INJECTION MODEL

When developing an injection model, we are interested in the number of electrons crossing a particular surface per unit time. It is well known that the maximum number of electrons, whose positions $\{x, z\}$ and wave vectors $\{k_x, k_z\}$ fit inside the (2D) phase-space region $\Delta x \cdot \Delta k_x \cdot \Delta z \cdot \Delta k_z$ is $N = g_s \cdot g_v \cdot \Delta x \cdot \Delta k_x \cdot \Delta z \cdot \Delta k_z / (4\pi^2)$, with g_s spin and g_v valley degeneracies. In a 2D material, all electrons in the (small) phase-space region $\Delta x \cdot \Delta k_x \cdot \Delta z \cdot \Delta k_z$ move to another spatial region during the time interval $T = \Delta x / v_x$, being v_x the x-component electron velocity. Therefore, the time between injection of two consecutive electron is⁶:

$$t_0 = \frac{T}{N} = \frac{4\pi^2}{g_s \cdot g_v \cdot \Delta k_x \cdot \Delta z \cdot \Delta k_z \cdot v_x} \quad (1)$$

where the velocity for a parabolic band (like black-phosphorus) is:

$$v_x^p = \frac{\hbar \cdot k_x}{m^*} \quad (2)$$

where m^* is the parabolic effective mass. For a linear band (like graphene) the velocity is given by:

$$v_x^l = \frac{s v_f \cdot k_x}{\sqrt{(k_x)^2 + (k_z)^2}} \quad (3)$$

being v_f the Fermi velocity and s the band index, with $s = 1$ for the conduction band (CB) and $s = -1$ for the valence band (VB). The phase space density of the attempts of injecting electrons is plotted in Fig. 1 for materials with parabolic and linear band structures. Almost all graphene electrons move at the maximum velocity v_f , while a much larger velocity dispersion appears in 2D parabolic materials.

Technically, since v_x in a linear dispersion depends on both wave vector components, the graphene electron injection model requires a 2D mesh of the wave vector space. On the contrary, a

1D mesh is required for a parabolic band. The injection is successful if the Fermi-Dirac function $f(E_f, E)$ is greater than a random number $r \in [0,1]$, with E_f the Fermi energy and E the electron energy. This model introduces a binomial probability distribution which is later translated into fluctuations in the device current.

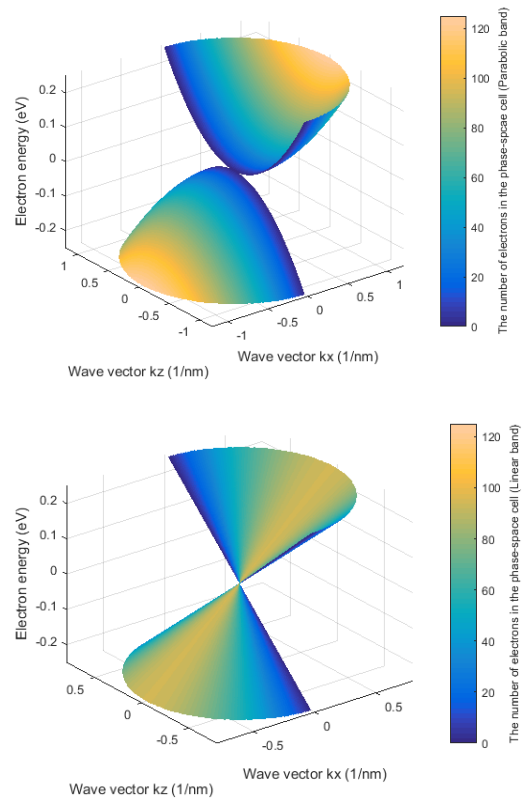


FIG. 1. Number of attempts of injecting electrons computed from Eq. (1), plotted for a 2D material with parabolic velocity given by Eq. (2) in the top figure and with a linear velocity given by Eq. (3) for the figure in the bottom for a phase space cell $\Delta x \cdot \Delta k_x \cdot \Delta z \cdot \Delta k_z$ during a simulation time of 10 ns at 300 K. The parameter $m^* = 0.2 \cdot m_0$, m_0 being the free electron mass, $g_s = 2$, $g_v = 2$, fermi velocity $v_f = 5 \cdot 10^5$ m/s, the dimensions of the phase-space cell are $\Delta x = \Delta z = 20$ nm, $\Delta k_x = \Delta k_z = 3 \cdot 10^6$ 1/m.

III. LINEAR AND PARABOLIC NOISE

For a very simple ballistic model, the (instantaneous) current computed from⁷ $I = q \cdot v_x / L_x$ provides dramatic differences between parabolic (Fig. 2 top) and linear (Fig. 2 bottom) band

structures. The current dispersion (noise) of both types of dispersion are radically different.

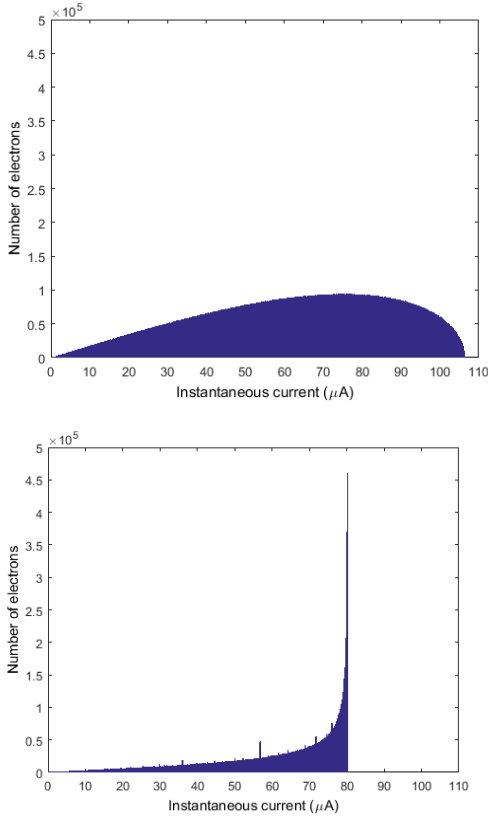


FIG. 2. Number of electrons as a function of current I during a simulation time of 10 ns at temperature $T = 300$ K, with Fermi level $E_f = 0.1$ eV for materials with a parabolic band structure (top) and linear band structure (bottom).

The power spectral density of the source, drain and gate currents for two field effect transistors, with a 2D parabolic dispersion (black-phosphorus) and linear dispersion (graphene) materials are plotted in Fig. 3. The noise in the drain and source contacts of the transistor with a linear dispersion has a maximum around 1 THz. The physical origin of this peak is that almost all electrons in graphene have roughly the same velocity (see Fig. 2 down) when entering into the device active region. In a transistor with a parabolic band, however, the uncertainty in the velocities (see Fig 2 top) washes out such mentioned peak in the power spectral density.

IV. CONCLUSIONS

We present a (time dependent) electron injection model for 2D linear dispersion (graphene) and parabolic dispersion (black-phosphorus) materials. The model includes the thermal noise and discrete nature of charges. We see in Fig. 3 that the noise generated by a parabolic or linear band structure is very different. A peculiar peak appears in the power spectral density of the current noise in the linear-band materials, while such peak is missing for parabolic-band ones. This feature opens many unexplored possibilities to test (linear or parabolic) band structures in 2D materials from the noise performance.

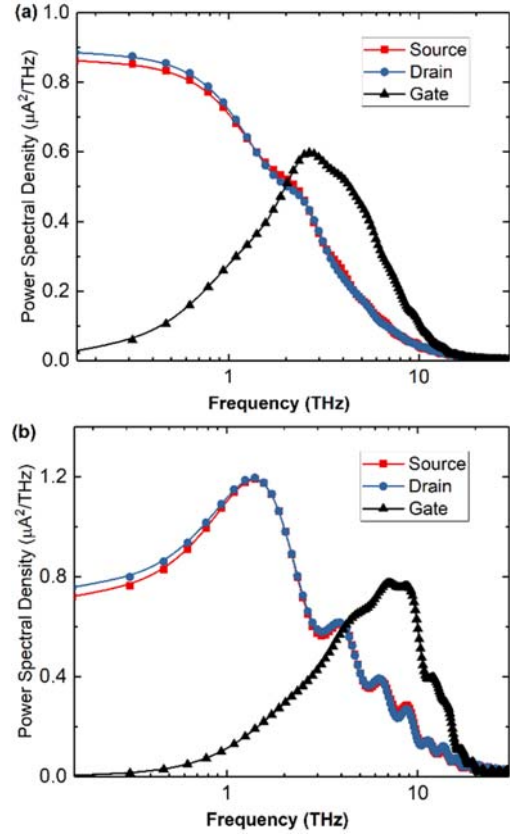


FIG. 3. Power spectral density of the current fluctuations as a function of frequency for a Monte Carlo simulation of transistors based on a black-phosphorus with parabolic band (top) and on graphene with linear band (bottom). Both devices have the same device geometry and under a DC conditions: the gate polarization $V = 0$ V and applied drain bias is 0 V. Electrons are only injected from the source contact.

ACKNOWLEDGEMENTS

This work is supported by the FEDER and the “Ministerio de Ciencia e Innovación” through the Spanish Project TEC2015-67462-C2-1-R and from the EUs Horizon 2020 research program under Grant Agreement No. 696656.

- 1 R. Roldán, L. Chirolli, E. Prada, J. A. Silva-Guillén, P. San-Jose and F. Guinea, *Chem. Soc. Rev.* **46**, 4387 (2017).
- 2 N. Kumada, et al. *Nat. Commun.* **4**,1363 (2013).
- 3 L. Li et al, *Nature Nanotechnology* **9**, 372 (2014).
- 4 X. Oriols and D. K. Ferry, *Journal of Computational Electronics*, **12**(3), 317-330 (2013).
- 5 X. Oriols, *Phys. Rev. Lett.* **98**, 066803 (2007).
- 6 Z. Zhan, E. Colomé, D. Pandey and X. Oriols, in preparation.
- 7 Z. Zhan, E. Colomé and X. Oriols, *IEEE Trans. Electron Devices* **64**, 2617 (2017).

1D electron transport in InAs nanowires

M.Petrychuk^{1,*}, I.Zadorozhnyi¹, Y.Kutovyi¹, S.Karg², H.Riel², S.Vitusevich¹

¹Bioelectronics(ICS-8),Forschungszentrum Jülich, 52425 Jülich, Germany
e-mail address: s.vitusevich@fz-juelich.de

²IBM Research Zurich, Säumerstrasse 4, 8803 Rüschlikon, Switzerland
e-mail address: hei@zurich.ibm.com

I. INTRODUCTION

InAs nanowires (NW) are very promising materials for nanoscaled electronic transistors due to high-mobility channel transport, one dimensional conductivity and low power consumption^{1,2}. The low effective mass of electrons in these materials may allow utilization of novel quantum effects and single-electron phenomena³⁻⁵. In this respect fluctuation phenomena in such unique nanowire structures have to be studied to understand working principles of nanowire structures at nanoscale.

Here we report on the results of transport and noise properties investigation of InAs nanowires with 30nm diameter and different lengths. We registered that the quantization effect determines noise properties in nanostructures. The effect is more pronounced with decreasing temperature and nanowire length.

II. EXPERIMENTAL DETAILS

InAs nanowire samples with diameter of 30nm and different lengths were studied. The optical image of InAs nanowire chip under study is shown in Fig. (1). The InAs NW is contacted with electrodes for studies according to the transmission line model⁶. The chip was encapsulated and investigated at different temperatures. The noise spectra of the samples were measured in the frequency range 1 Hz - 3 kHz at different temperatures and substrate voltages in the linear mode: source-drain voltage $V_{DS} = 20$ mV.

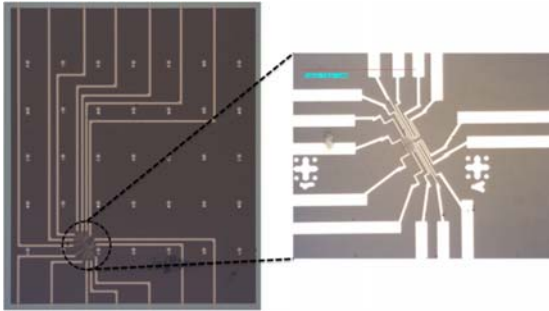


FIG. 1. The optical image of InAs NW chips under study.

We have studied several NW segments with lengths of 600 nm, 900 nm, 1200 nm and 3000 nm. The Si substrate was used as a gate electrode for the current flow control.

III. RESULTS AND DISCUSSION

In general, InAs nanowires demonstrated n-type FET behavior. Fig.(2) shows a typical dependence of drain current on back gate voltage applied to the InAs nanowire biased at $V_{DS} = 10$ mV. The characteristic was measured at room temperature. It should be noted, that the leakage current was negligibly small for all cases.

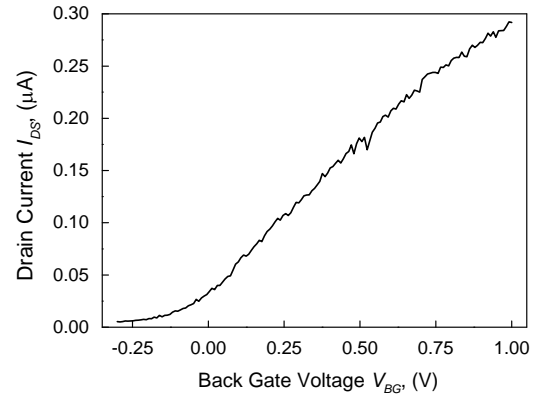


FIG. 2. Typical transfer characteristic of InAs NW segment with length of 600 nm measured at room temperature. $V_{DS} = 10$ mV.

The noise measurement results are shown in the Fig.(3). Measured noise spectra of InAs nanowires demonstrated mainly $1/f^\gamma$ (flicker) noise behavior with exponent depending on back gate voltage. Value γ changes from 1.5 to 1 with decreasing of temperature from $T=300$ K to 100K. Several Lorentzian components related to random telegraph signal (RTS) noise can be resolved on the noise spectra of InAs NW at relatively high temperatures. Such noise components are associated with slow generation-recombination (GR) fluctuations that results in deviation from $1/f$ behavior at low frequencies. With temperature decrease, the contribution of these components decreased and completely disappeared at temperatures lower than $T=175$ K. The value of normalized flicker noise S_I/I_{DS}^2 was weakly temperature dependent at temperatures below 175K.

The Lorentzian component of noise reflects generation-recombination processes, S_I^{GR} , and can be described using following relation:

$$S_I^{GR} = I^2 \frac{\overline{\Delta N^2}}{N} \frac{1}{N} \frac{1}{1 + (2\pi f\tau)^2} \quad (1)$$

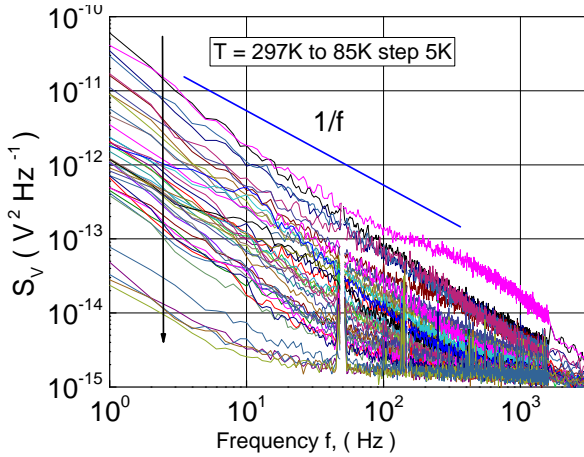


FIG. 3. Noise spectra measured for sample with $L = 3000\text{nm}$ at $V_{BG} = 0$ and $V_{DS} = 20\text{mV}$ at different temperatures from $T = 300\text{K}$ down to $T = 85\text{K}$ with a step equal to 5K .

As it can be derived from equation (1), S_I^{GR} changes are related to the changes of τ . This reflects that the amplitude of the relative dispersion $\frac{\Delta N^2}{N}$ for each Lorentzian component in the noise spectrum decreases with increasing of charge carriers number N . In addition, extracted characteristic times as a function of gate voltage $\tau(V_{BG})$ are reflecting capture and emission processes related to several active centers (1 to 5 centers) which are present in InAs nanowire structure. At low gate voltages $\tau(V_{BG})$ can be linear fitted in semi-logarithmic scale followed by saturation region at voltages greater than $V_{BG} = 0.3\text{V}$. The value of low frequency Lorentzian-shape noise plateau, $S_I(0)$, extracted from measured noise spectra, demonstrate similar behavior as a function of back-gate voltage. The results reflect excellent controllability of trapped centers using back gate voltage and, in turn, communication with 1D channel transport, as it will be shown below.

Amplitude of flicker noise, obtained at certain frequency in subthreshold regime, strongly decreases with voltage decrease. Surprisingly, the value of dimensionless Hooge parameter, α_H , decreases considerably in about two orders of magnitude. The fact reflects that interaction of electrons with traps of dielectric layer became negligibly small. This can be explained by decreasing of free carrier concentration near the interface between InAs and dielectric layer caused by

increasing of conductive channel confinement $\alpha_H(V_{BG} - V_{th})$ dependence considerably differs for samples with different lengths at large voltages. It should be noted that α_H decreases with $(V_{BG} - V_{th})$ decrease as well as α_H decreases with temperature decrease. The results cannot be explained by the increased contribution of contact resistance, since in the latter case the dependence has to be opposite. In addition, threshold voltage dependencies on temperature, obtained for samples with different lengths, reflect non trivial behavior as a function of sample length. The shorter length the stronger correlation effect is registered resulting in single electron phenomena and dynamic barrier processes. This is in good agreement with reported in literature formation of 1D conductivity at temperatures below 295K . Noise spectra allow us detailed study of dynamic barrier processes which are observed with temperature decrease. Moreover noise spectroscopy allows us to identify the stronger 1D conductivity and formation of ballistic transport in the channel. This is confirmed by the linear dependence of the $1/f$ noise component on the current in power equal unity obtained in the experiment. Such noise behavior in structures with 1D conductivity can be described by similar model⁷ as in the case of carbon nanotube sample in frame of Hooge-Kleinpenning phenomenological model.

IV. CONCLUSIONS

Transport and noise properties of InAs NW samples with different lengths are studied in a wide temperature range down to 85K . We registered space quantization of electron gas and formation of 1D conductivity with stronger quantization effect in low temperature range. Transport and noise characteristic behavior as a function of length support the reliability of this explanation and strong influence of dynamic barrier effect on transport and current fluctuations.

*On leave from Radiophysics Faculty, Taras Shevchenko National University Kyiv, 03022 Kyiv, Ukraine

ACKNOWLEDGEMENTS

Y. Kutovyi greatly appreciates a research grant from the German Academic Exchange Service (DAAD).

- ¹ S.Chuang, Q.Gao, R.Kapadia, A.C.Ford, J.Guo and A.Javey, Nano Letters. Vol. **13**, pp. 555-558, 2013.
- ² J.A.del Alamo, Nature, Vol. **479**, pp.317-323, 2011.
- ³ J.Li, S.Pud, M.Petrychuk, A.Offenhäusser, S.Vitusevich, Nano Letters, Vol. **14**, pp.3504-3509, 2014.
- ⁴ I. Zadorozhnyi, J. Li, S. Pud, H. Hlukhova, V. Handziuk, Y. Kutovyi, M. Petrychuk and S. Vitusevich, Small, vol. **14**, pp. 1-8, 2017.
- ⁵ S. Vitusevich, I. Zadorozhnyi. Semicond. Sci. Technol. Topical Review, vol. **32**, pp. 1-21, 2017.

- ⁶ S. Karg, V. Schaller, A. Gaul, K. Moselund, H. Schmid, B. Gotsmann, J. Gooth, H. Riel, Solid-State Device Research Conference (ESSDERC), DOI: [10.1109/ESSDERC.2016.7599656](https://doi.org/10.1109/ESSDERC.2016.7599656), 2016.
- ⁷ B. A. Danilchenko, N.A. Tripachko, S. Lev, M.V. Petrychuk, V.A. Sydoruk, B. Sundquist, S.A. Vitusevich., Carbon, Vol. **49**, pp. 5201 -5206, 2011.

Localization of 1/f noise sources in Si/SiGe:C HBTs

M. Seif¹, F. Pascal¹, B. Sagnes¹, J. El-Beyrouthy¹, A. Hoffmann¹, S. Haendler², P. Chevalier² and G. Gloria²

¹ IES, Univ Montpellier, CNRS, Montpellier, France

e-mail address: Fabien.pascal@ies.univ-montp2.fr

² STMicroelectronics, 850 rue Jean Monnet
38926 Crolles Cedex, France

I. INTRODUCTION

Most of the models that can be found in the literature, concerning bipolar transistors, attempt to describe experimental results and behaviors. Mainly, the evolution of the 1/f noise level versus the polarization is used for the establishment of this models¹⁻⁵. In Si/SiGe:C Heterojunction Bipolar Transistors (HBTs) the base current spectral density, S_{IB} , is the most frequently measured quantity. Its evolution in power of the base current I_B^{α} is then the starting point for a physical approach of the involved mechanisms in the origin and localization of 1/f noise sources in HBTs.

Over the last twenty years, with the evolution of integrated electronics and very high frequency electronics, specific studies based on various geometrical and technological parameters have been conducted. These studies were mainly conducted to establish electrical models, but have also been used to try to refine the localization and origin of the 1/f noise sources. The main study of the 1/f noise level is the study of its evolution versus the emitter area and the bias. The most recent studies on Si/SiGe HBTs, including our work³, indicates a quadratic evolution of the 1/f noise level ($S_{IB}^{1/f}$) versus the base current I_B and an inversely proportional evolution versus the emitter area A_e . Based on the literature and theoretical models, these results show that the main sources of the 1/f noise could be homogenously distributed in the emitter-base area and more specifically at the polysilicon/silicon interface in the emitter structure.

Even if the assumptions indicate that the 1/f noise sources are located at the input of the Si/SiGe HBTs and are homogenously distributed at the emitter base area, there is no clear evidence of their exact localization (spacer, emitter perimeter, series resistances, poly-silicon/silicon interface ...). This is thus always a topic to visit and one of the unsolved problems in the Si/SiGe HBTs low frequency noise domain.

II. RESULTS AND DISCUSSION

In order to try to find more evidence on the origin of the 1/f noise at the input of Si/SiGe HBTs, we have studied recently the impact of the collector doping on its evolution². We have studied three types of HBTs named HS, MV and HV for which the collector doping was adapted to the applications High Speed, Medium Voltage and High Voltage.

For the three types of transistors we have found that $S_{IB}^{1/f}$ is proportional to I_B^2 and $1/A_e$, and the 1/f noise amplitude is of same order of magnitude as can be seen in FIG. (1). This indicates that

the collector doping has no impact on the 1/f noise origin and is coherent with the general hypothesis concerning the localization of the 1/f noise sources in modern bipolar transistors which is to incriminate the intrinsic Emitter- Base junction.

Moreover, in recent work, we have studied the low frequency noise at the output of Si/SiGe HBTs with the base AC short circuited to eliminate the noise sources coming from the input of the transistor⁴. This allows us to measure the output collector current fluctuations. We have studied the evolution of the collector current spectral density S_{IC} versus the collector current I_C and emitter area A_e . In FIG. (2) we present various spectra of S_{IC} with the base AC short circuited. We have found that the 1/f noise level at the output of the transistor is proportional to $I_C^{1.7}$ and $\frac{1}{\sqrt{A_e}}$, which is different of what was observed for S_{IB} at the input of the transistors. The 1/f output noise origins are thus different than the ones at the input of the transistor. The localization of the 1/f noise sources at the output of Si/SiGe HBTs remains also a problem to be solved especially when there are too few studies in the literature.

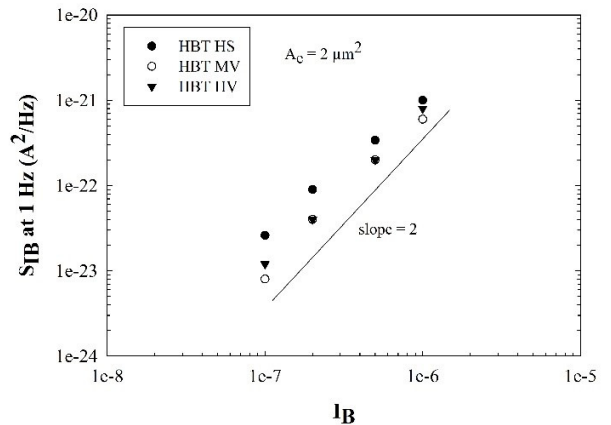


FIG. 1. Evolution of the 1/f noise level versus I_B for HS, MV and HV transistors.

ACKNOWLEDGEMENTS

This work was done in the frame of the “RF2TH SiSoC” project of the EUREKA program CATRENE and funding of the French Ministry of Economy, Finance and Industry and of the new “TARANTO” H2020 ECSEL project.

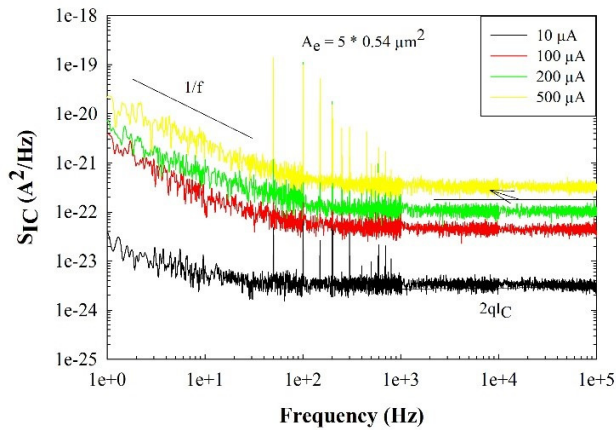


FIG. 1. Collector current spectral density S_{IC} for different collector currents with the base AC short circuited.

REFERENCES

¹ MJ Deen, and F Pascal, 'Review of Low-Frequency Noise Behaviour of Polysilicon Emitter Bipolar Junction

Transistors', *IEE Proceedings-Circuits, Devices and Systems*, 151 (2004), 125-37.

² B. Sagnes, F. Pascal, M. Seif, A. Hoffmann, S. Haendler, P. Chevalier, and D. Gloria, 'Low Frequency Noise in Advanced 55nm Bicomos Sigec Heterojunction Bipolar Transistors: Impact of Collector Doping', in *2017 International Conference on Noise and Fluctuations (ICNF)* (2017), pp. 1-4.

³ M Seif, F Pascal, B Sagnes, A Hoffmann, S Haendler, P Chevalier, and D Gloria, 'Study of Low Frequency Noise in Advanced Sigec Heterojunction Bipolar Transistors', in *Solid State Device Research Conference (ESSDERC), 2014 44th European* (IEEE, 2014), pp. 373-76.

⁴ M. Seif, F. Pascal, B. Sagnes, A. Hoffmann, S. Haendler, P. Chevalier, and D. Gloria, 'Measurement and Characterization of Low Frequency Noise Collector Current in 0.13 μM Sigec Hbts', in *2015 International Conference on Noise and Fluctuations (ICNF)* (2015), pp. 1-4.

⁵ Albert van der Ziel, Xiaonan Zhang, and Adam H Pawlikiewicz, 'Localization of 1/F Noise Sources in Bjt's and Hbjt's—I. Theory', *IEEE Transactions on Electron Devices*, 33 (1986), 1371-76.

Noisy quantum measurements: just a nuisance or fundamental physics?

Wolfgang Belzig¹, Johannes Bülte¹, Adam Bednorz², Bertrand Reulet³, and Christoph Bruder⁴

¹Department of Physics, University of Konstanz, D-78457 Konstanz, Germany

e-mail address: Wolfgang.Belzig@uni-konstanz.de

²Faculty of Physics, University of Warsaw, ul. Hoza 69, PL00-681 Warsaw, Poland

³Département de Physique, Université de Sherbrooke, Sherbrooke, Québec J1K2R1, Canada

⁴Department of Physics, University of Basel, Klingelbergstrasse 82, CH-4056 Basel, Switzerland

I. INTRODUCTION

The interpretation of quantum measurements is a question which has already led to discussions in the early days of quantum mechanics with the famous debate between Einstein and Bohr. The emerging Copenhagen interpretation was an elegant solution, since it effectively states that the outcome of a measurement will result in an eigenvalue of the measured operator and the wave function collapses to the corresponding eigenstate. While this works in many cases, where simply the arrival of a particle (e.g. electron or photon) is detected by a “click”, in that way one circumvents the question of what happens afterwards and since the system has either vanished (photon) or is thrown away (electron). In a statistical sense, the average of an observable is then given by the expectation value $\langle A \rangle$.

On the other hand, the question becomes more interesting, if two observables A and B are measured in the same system, especially if they correspond to non-commuting operators¹. The outcome of such measurements performed by two different detectors and averaged over many realizations is given by $\langle ab \rangle$, where a and b denote the measured c-numbers. The problem is then which quantum mechanical expectation value this corresponds to. Some options are

- $\langle \{A, B\} \rangle$ (symmetrized, Wigner order)
- $i\langle [A, B] \rangle$ (“responsive”, Kubo order)
- $\xi_s \langle \{A, B\} \rangle + i\xi_a \langle [A, B] \rangle$ (generalized order)
for arbitrary (real) parameters $\xi_{s,a}$.

Obviously, the choice will strongly affect the interpretation of an experiment measuring such a correlation. One may argue that a given experiment will be designed to give one of the solutions, but in many cases this assignment is not clear since a measurement will contain several amplification stages and circuitry with possibly unknown states.

The above problem becomes even more striking if one considers time-resolved measurements. This can be done by adding time arguments to the measurement results $a \rightarrow a(t_a)$, ... and to the operators $A \rightarrow A(s_a)$, Now an additional question is how the time of the results, t_a , is related to the time associated with the corresponding operators, s_a . In general, the relation might even be non-local in time in the sense of a convolution $a(t_a) \rightarrow \int \chi(t_a, s_a) A(s_a) ds_a$. At this point, we should note that such measurements will be at odds with the projection principle, since a projection will strongly alter the system dynamics and a later measurement rather measures the result of the projection than

the dynamics of the system. Hence, in the following we will mainly concentrate on *weak measurements*, in which the backaction of the measurement is negligibly small. Such a limit can always be achieved in theory, but in practice there might be limitations. A consequence of the generalized uncertainty relation is that such a weak measurement is accompanied by detector noise¹. This added noise makes it possible to measure non-commuting observables, since the overall results are again described by a positively defined probability distribution.

In the following we first discuss a phenomenological approach to time-resolved correlation measurements before presenting a microscopic picture giving additional insight on the detector properties necessary to perform a measurement of a given order.

II. PHENOMENOLOGICAL APPROACH

We start by formulating a possible theory of non-Markovian weak measurements using purely phenomenological arguments. On quite general grounds, one might argue that for weak measurements a linear relation between the measurement outcome and the corresponding operators exists. E.g. assuming the measurement addresses the symmetrized correlator, such a relation might look like

$$\langle a(t)b(s) \rangle = \int dt' ds' \chi_A(t, t') \chi_B(s, s') \langle \{A(t'), B(s')\} \rangle / 2 \quad (1)$$

Here, we assume that causality will be obeyed by the response-type functions, i.e. $\chi_{A/B}(t, t') = 0$ for $t < t'$. For the often assumed instantaneous response $\chi_{A/B}(t, t') \sim \delta(t - t')$, we obtain the Markovian order $\langle a(t)b(s) \rangle = \langle \{A(t), B(s)\} \rangle / 2$, which also follows from a more general argument using Kraus operators¹.

Now, we might ask if other orders might occur as well. Without further specifying the detectors, we make the Ansatz

$$\begin{aligned} \langle a(t)b(s) \rangle &= \frac{1}{2} \int dt' ds' \chi_A(t, t') \chi_B(s, s') \langle \{A(t'), B(s')\} \rangle \\ &+ \frac{i}{2} \int dt' ds' \tilde{\chi}_{AB}(t, t', s, s') \langle [A(t'), B(s')] \rangle \end{aligned} \quad (2)$$

On general grounds, the function $\tilde{\chi}_{AB}(t, t', s, s')$ can be decomposed as $\sim \chi_A(t, t') S_B(s, s') + S_A(t, t') \chi_B(s, s')$.² Both functions χ and S are a priori unknown and one can try to determine them for a given situation using physical arguments. One example discussed in Ref. 2 was to assume that the detectors are in thermal equilibrium, resulting in a temperature-dependent

universal function $S_{eq}(\omega) = i\hbar\omega\coth(\frac{\hbar\omega}{kT})$, here represented as Fourier transform of $S(t-t')$ for an equilibrium situation.

By applying this scheme to measurements of a harmonic oscillator, an interesting connection to the quantum optical detection theory could be established. We distinguish three cases for the detectors: zero temperature, equilibrium with the system and “negative temperature”, where the latter corresponds e.g. to a two-level detector in the excited state. Grouping the operators of the harmonic oscillator in terms of ladder operators $a(a^+) = (x \pm ip)/\sqrt{2}$, we find for the second-order correlators:

$kT = 0$	$\langle a^+ a \rangle$	Normal order
$kT \rightarrow \infty$	$\langle aa^+ + a^+ a \rangle / 2$	Symmetrized order
$kT = 0^-$	$\langle aa^+ \rangle$	Antinormal order

This intuitive result tells us that a zero-temperature detector can only absorb energy quanta and, hence, leads to the normal ordering known from photon detectors. In contrast an inverted detector cannot absorb anything and will rather perform a measurement by emitting an energy quantum. The infinite temperature case is as close as possible to a classical detector.

III. MICROSCOPIC PICTURE

It is clearly desirable to establish a more microscopic understanding of the different measurement schemes. In Ref. 3, such a picture has been developed by treating the full quantum dynamics of the system and the detectors. For that purpose, one assumes a coupling between the system and the detector of the form $H_A \sim D_A A$, where A is the system variable to be measured and D_A is a detector variable. The coupling parameter can in general be a time-dependent function but is in the following assumed to be constant. Finally, the variable M_A of detector A is read off at a later time. In principle, the result depends itself on how strongly the detector is measured, but we can assume that the detector measurement is done weakly as well.

The result of the full quantum treatment is indeed of the form anticipated in Sec. II, viz. we obtain the microscopic expressions

$$\chi_A(t, t') = -\frac{i}{\hbar} \theta(t - t') \langle \{M_A(t), D_A(t')\} \rangle \quad (3)$$

$$S_A(t, t') = \langle \{M_A(t), D_A(t')\} \rangle / 2 \quad (4)$$

Hence, we find an intuitive interpretation of the general weak-measurement result:

1. The linear kernel χ of the Markovian part is related to the Kubo formula known from general linear response theory according to (3).
2. The non-symmetrized term in (2) can be seen as *system-mediated detector-detector interaction*, i.e. the

¹ A. Bednorz and W. Belzig, *Formulation of Time-Resolved Counting Statistics Based on a Positive-Operator-Valued Measure*, Phys. Rev. Lett. **101**, 206803 (2008).

² A. Bednorz, C. Bruder, B. Reulet, and W. Belzig, *Nonsymmetrized Correlations in Quantum Noninvasive Measurements*, Phys. Rev. Lett. **110**, 250404 (2013).

³ J. Bülte, A. Bednorz, C. Bruder, and W. Belzig, *Noninvasive Quantum Measurement of Arbitrary Operator Order by*

noise correlation function of one detector (e.g. S_B) excites the system and its linear response is measured by the other detector. Naturally the Kubo formula of the system variables comes into play.

In thermal equilibrium, due to the fluctuation-dissipation relation, commutators and anti-commutators are related, which leads to the interesting consequence that no additional information is gained in the weak measurement setup. A second consequence is that in order to measure the non-symmetrized correlators of the system in the quantum regime at $k_B T \rightarrow 0$, the detectors have to be dominated by quantum fluctuations themselves, because otherwise the intrinsic thermal fluctuations will dominate the system response and the detectors act again as classical objects.

IV. OPEN PROBLEMS

A large number of open questions emerge from the problem of weak, non-Markovian measurement:

- Generalization to higher-order correlations functions. So far, we have considered mainly second-order correlators. A phenomenological approach to general correlators was proposed in Ref. 2, but the microscopic extension is missing. In particular, many more combinations of measurement outcomes are possible by mixing commutators and anticommutators, like $\langle \{A, [B, \{C, D\}] \rangle$.
- Experimental design for different correlators. To test the various predictions experimentally, one would like to establish circuits which can be tuned to detect different quantum correlators. For second-order correlators, a quantum dot-based scheme has been proposed in Ref. 3, but more general schemes and different materials are desirable.
- The microscopic model can be considered in classical physics too and one expects a similar picture. It is an open problem to determine if there is a clear quantum-classical border in weak measurements.
- Fundamental question and open problem: Can weak measurements be used to replace the projection postulate of quantum mechanics.

ACKNOWLEDGEMENTS

The research was financially supported by the DFG through SFB 767.

Engineered Non-Markovian Detectors, Phys. Rev. Lett. **120**, 140407 (2018).

Fluctuations in a NESS: is there any universal behavior ?

Alex Fontana¹, Richard Pedurand^{1,2}, Ludovic Bellon^{1,*}

¹Univ Lyon, ENS de Lyon, Univ Claude Bernard Lyon 1, CNRS, Laboratoire de Physique, F-69342 Lyon, France

²Laboratoire des Matériaux Avancés, CNRS/IN2P3, F-69622 Villeurbanne, France

*ludovic.bellon@ens-lyon.fr

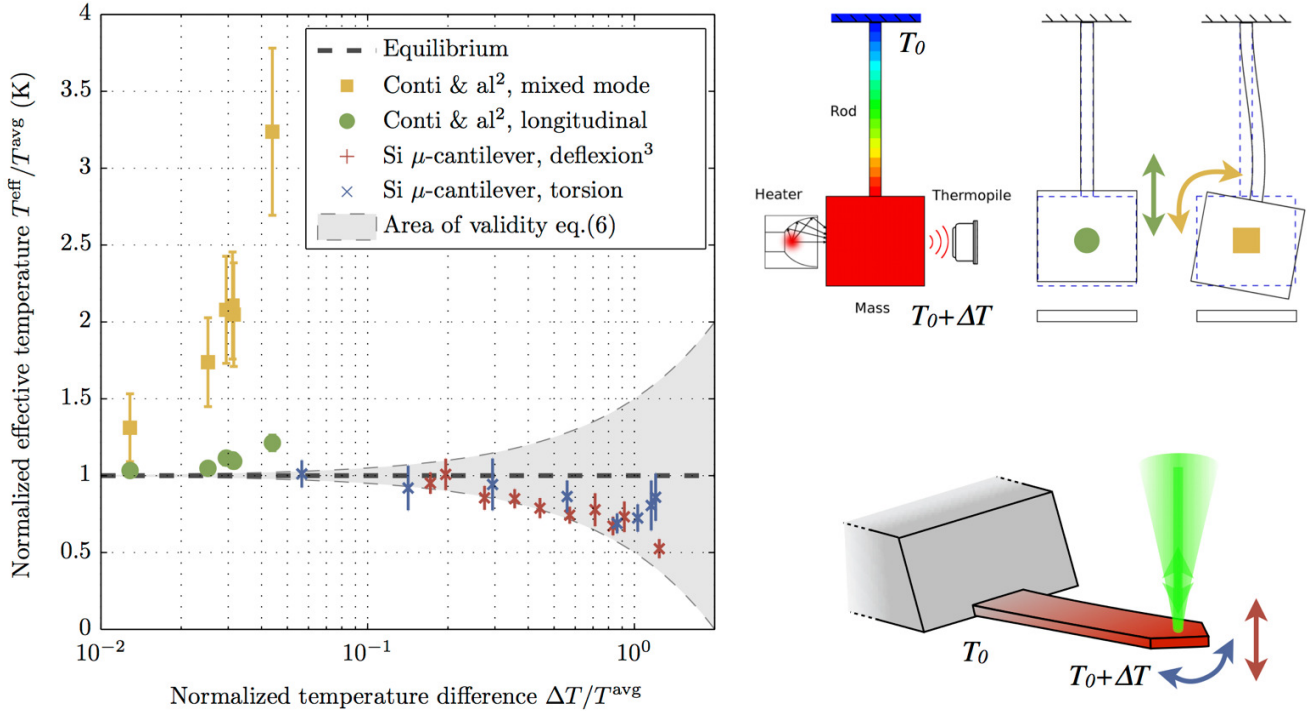


Fig. (1) - Effective temperature T^{eff} of a system under a heat flow depending on the difference of temperature at its extremities. T^{eff} quantifies the amplitude of the thermal noise driven fluctuations. All temperatures are normalized to the average temperature of the system. The experiment of Conti et al.² is shown in the upper right corner: they study a longitudinal mode and a mixed one of an aluminum rod. They observed a strong excess of fluctuations in respect to an equilibrium situation. Our system is shown in the lower right corner: we study the flexion and the torsion of a silicon micro-cantilever. We observe a deficit of fluctuations. Even if we propose a reasonable model that explains our data (a spatial average of the real temperature weighted by the dissipation), it cannot account for the Italian group results.

I. INTRODUCTION

Though most of the time unnoticeable, thermal fluctuations are present in any system having a non-zero temperature. When an extreme precision is required, such as in Gravitational Waves Detectors, or when the system size decreases, at nanoscale for example, thermal noise is the factor that prescribes the ultimate resolution of a device. Its understanding is thus fundamental.

The cardinal tool in this sense is the Fluctuation-Dissipation Theorem (FDT) from Callen and Welton¹. Let's consider a system that presents some form of energy dissipation that we can study through an observable θ . The FDT links the fluctuations of θ with the dissipation of the response function related to this observable and the temperature, and writes in the Fourier space:

$$S_{\theta}(\omega) = \frac{2k_B T}{\pi\omega} \text{Im} \left(\frac{1}{G(\omega)} \right) \quad (1)$$

with $S_{\theta}(\omega)$ the power spectrum density, T the equilibrium temperature, $G(\omega)$ the mechanical response function associated to θ and ω the angular frequency. This relation then yields the Equipartition Principle:

$$\frac{1}{2} G(\omega = 0) \langle \theta^2 \rangle = \frac{1}{2} k_B T \quad (2)$$

All of this is granted at *equilibrium*. When we try to adventure ourselves out of this region the two equations are not necessarily true. In order to find some extension of the FDT, experiments are then necessary. Out of equilibrium, an *excess* of fluctuations is usually expected, as found for example by Conti et al.² and reported in Fig. (1): the fluctuations of a solid body subject to a constant heat flow are larger than that expected from its mean temperature. On the contrary in the work of Geitner et al.³ a *lack* of fluctuations is observed: the *deflection* of a micro-cantilever is almost insensitive to the heat flowing through it, however strong the temperature gradient induced by a laser focused on its tip. There is then a clear disagreement between these two experiments corresponding to a Non-Equilibrium Steady State (NESS).

In this presentation we show how we can further explore this difference, studying the *torsion* of a heated micro-cantilever. We first present the experimental setup, an Atomic Force Microscope (AFM) micro-cantilever in vacuum. This system is ideal to study this NESS: it's both large enough to present a strongly non-uniform temperature profile and small enough to have uncoupled degrees of freedom and measurable thermal fluctuations. We then briefly show how we can measure the real temperature of the system thanks to the frequency shift of the resonant peaks in its thermal noise spectrum. We proceed to calculate the effective temperature from the FDT and we show how also for the torsional motion it is much inferior to the average temperature. We then see that the missing noise in the deflection modes is not to be expected in the torsional ones. We propose an extension of the FDT similar to the one of Geitner et al.³ We conclude with open questions on the possible ways we can extend the FDT for the torsional modes and the origin of the missing noise.

II. EXPERIMENT

The sample is a single crystal silicon cantilever with nominal length 500 μm , width 90 μm and height 1 μm . In order to measure its thermal fluctuations, we use an optical beam deflection setup. We consider a Saint-Venant model to describe the motion of our observable $\theta(x,t)$, the torsional angle along the length of the cantilever. This is described by Eq. (3) in the Fourier space:

$$\left[-mI\omega^2 + \frac{\partial}{\partial x} \left(C(x, \omega) \frac{\partial}{\partial x} \right) \right] \theta(x, \omega) = \Gamma^{\text{ext}}(x, \omega) \quad (3)$$

with m the mass of the cantilever, I its second moment of area, C its torsional stiffness and Γ^{ext} the external torque per unit length. We consider a normalized position x that spans from 0 to 1.

Increasing the laser power, we can notice that the resonant frequencies are redshifted, caused by a softening of the cantilever when it gets hotter. We used this effect to calculate the real temperature profile of our system following Paolino et al.⁴

From the spectra we then measure the mean quadratic torsion $\langle \theta^2 \rangle$, that we use to calculate the effective temperature of the cantilever.

III. EFFECTIVE TEMPERATURE

In Eq. (3) our observable θ is linearly coupled with the external torque Γ^{ext} in the Hamiltonian. We can hereby apply the FDT at equilibrium to the amplitude θ_n of torsional mode n :

$$S_{\theta_n} = \frac{2k_B T}{\pi \omega} \frac{\int dx \psi_n(x) \partial_x (C^I(x, \omega) \partial_x \psi_n(x))}{(C_n^R(\omega) - mI\omega^2)^2 + (C_n^I(\omega))^2} \quad (4)$$

with $C_n^{R,I}(\omega) = \int dx C^{R,I}(x, \omega) (\partial_x \psi_n(x))^2$ the real and imaginary parts of the torsional stiffness, the latter responsible for dissipation, and $\psi_n(x)$ is the mode n shape, the spatial solution of equation (3). Our aim is to extend this relation to a NESS.

Due to the heat flow, the cantilever temperature is a function of the position along its length, $T(x)$. To insert it inside (4), we are facing three different scenarios:

- 1) we can place it inside the integral.
- 2) inside the first derivative.

3) inside the second derivative.

The right choice is an open question. The lead we can follow comes from the work of Y. Levin⁵ where it is shown how the thermal noise is proportional to a time-averaged dissipated power. As in Geitner et al.³ we seek a formulation that leads us to this result. We have hereby inserted $T(x)$ inside the first derivative. Taking the integral over the frequency we can express a possible extension of the Equipartition Principle:

$$\frac{1}{2} C_n^R(\omega_n) \langle \theta^2 \rangle = \frac{1}{2} k_B T_n^{\text{eff}} \quad (5)$$

with

$$T_n^{\text{eff}} = \frac{\int dx T(x) C^I(x, \omega) (\partial_x \psi_n(x))^2}{\int dx C^I(x, \omega) (\partial_x \psi_n(x))^2} = \int dx T(x) W_n^{\text{diss}}(x) \quad (6)$$

with $W_n^{\text{diss}}(x)$ the mode-dependent normalized dissipation power that weights the temperature $T(x)$.

We show in Fig. (1) this measured effective temperature for both deflection and torsional modes along with the results of Conti et al.² Even if T_n^{eff} rises with the laser power, it is well below the actual system temperature. This means that the Equipartition Theorem is not valid in the case of our NESS, again in an opposite direction with respect to the Italian experiment which effective temperatures stand well above the average one. This result is analogous to the one of Geitner et al.³ where the system's mechanical noise remains almost constant even if the tip is heated up to the melting point.

IV. OPEN PROBLEMS

In our experiment we study a system in a NESS that presents surprising fluctuation properties. Our setup allows us to carefully control our out of equilibrium state and to measure fluctuations and response for various degrees of freedom. We extend the study of the deflection modes and demonstrate that also for the torsional modes there is a strong lack of fluctuations. We could expect a higher effective temperature than an equilibrium state, instead we are facing a much lower one.

In our quest for the missing noise we have pointed out some leads that will be discussed in the presentation:

- Which is a formally correct extension of the FDT in the presence of a non-uniform temperature?
- Is expressing the effective temperature as a weight on dissipation the only way possible?
- Let's suppose that the temperature dependence on the dissipation is correct. We can then argue that we have a strong non-uniform dissipation that occurs just at the base of the cantilever, where the temperature is the environment one T_0 . In this way it's natural that T_n^{eff} is really close to this value. But is this the only possible explanation?
- Why does a similar physical system like Conti's experiment show an increase of the fluctuations instead?
- Any suggestion will be welcomed during the discussion!

¹ H. B. Callen and T. A. Welton, Physical Review **83**, 34, (1951).

² L. Conti, P. De Gregorio, G. Karapetyan, C. Lazzaro, M. Pegoraro, M. Bonaldi and L. Rondoni, J. Stat. Mech., **P12003** (2013).

³ M. Geitner, F. A. Aguilar Sandoval, E. Bertin, L. Bellon. Physical Review E, APS, **95**, pp.032138 (2017).

⁴ P. Paolino, F. Aguilar Sandoval and L. Bellon, Rev. Sci. Instrum. **84**, 095001 (2013).

⁵ Y. Levin, Phys. Rev. D **57**, 659 (1998).

Damped underdamped non-equilibrium stochastic harmonic oscillator

Bartłomiej Dybiec*, and Ewa Gudowska-Nowak^{†1} and Igor M. Sokolov²

¹*Institute of Physics, Jagiellonian University, Lojasiewicza 11, 30-348 Krakow, Poland*
*e-mail addresses: *bartek@th.if.uj.edu.pl, †gudowska@th.if.uj.edu.pl*

²*Institut für Physik, Humboldt-Universität zu Berlin, Newtonstrasse 15, D-12489 Berlin, Germany*
e-mail address: igor.sokolov@physik.hu-berlin.de

I. INTRODUCTION

Many situations in natural sciences can be successfully investigated adopting the stochastic level of description, considering the system of interest as a dynamical system responding to external perturbations represented by a noise. In the simplest situations this noise is assumed to be white and Gaussian. The white type of the noise is the consequence of the large number of independent interactions bounded in time. Its Gaussian character arises due to the assumption that the interactions are bounded in their strength. In many far from equilibrium cases the second assumption fails; the interactions still can be of the white type (i.e. independent) but described by heavy-tailed distributions frequently of the α -stable Lévy type¹. Such heavy-tailed fluctuations², among others, are abundant in heartbeat dynamics, neural networks, search on a folding polymers, animal movement, financial time series, and even in spreading of diseases and dispersal of banknotes.

II. MODEL

Here we study influence of the α -stable Lévy type fluctuations on the damped underdamped harmonic oscillator. We examine the distributions of the kinetic and potential energy and of their ratio as well as the position and velocity distributions. In the dimensionless variables the system is described by the following Langevin equation:

$$\ddot{x}(t) = -\gamma\dot{x}(t) - x(t) + \sigma\zeta_\alpha(t), \quad (1)$$

The white α -stable noise $\zeta_\alpha(t)$ is a formal time derivative of the α -stable motion³ $L_\alpha(t)$. It results in stochastic increments which are distributed according to the symmetric α -stable density whose characteristic function is given by^{1,3} $\phi(k) = \exp[-\sigma^\alpha|k|^\alpha]$. The parameter α ($0 < \alpha \leq 2$) is the so called stability index describing asymptotics of α -stable densities which for $\alpha < 2$ is of the power-law type $p(x) \propto |x|^{-(\alpha+1)}$. In the $\alpha = 2$ limit the α -stable noise is equivalent to the Gaussian white noise. The strength of fluctuations in Eq. (1) is controlled by the scale parameter σ and its similarity properties are governed by the parameter α . Contrary to the $\alpha = 2$ case, due to the divergence of the second moment $\langle v^2 \rangle$, for $0 < \alpha < 2$, there is no fluctuation-dissipation relation of the Smoluchowski-Sutherland-Einstein type^{4,5}. Consequently, damping coefficient γ and fluctuation intensity σ are independent parameters. Moreover, in Eq. (1), the white Lévy noise $\zeta_\alpha(t)$ with the scale parameter set to unity is used. The instantaneous kinetic and potential energies of the system are denoted by $\mathcal{E}_k = v^2/2$ and $\mathcal{E}_p = x^2/2$, respectively.

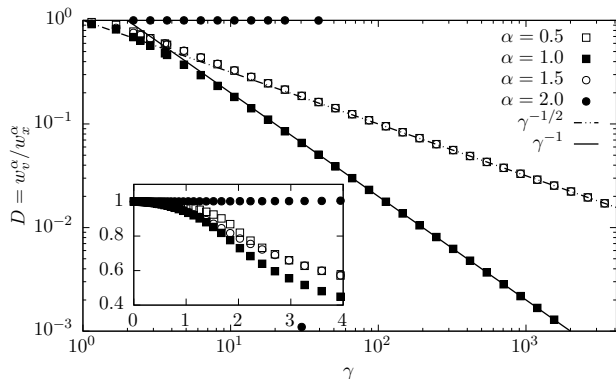


FIG. 1. The quotient of the corresponding prefactors $D = w_v^\alpha/w_x^\alpha$ for various values of the stability index α . Please note the double logarithmic scale in the main plot and the linear scale in the inset.

The characteristic function of the joint probability distribution of (x, v) can be obtained explicitly^{6,7}. The formal solution of the problem is astonishingly different from the solution under Gaussian noise. The $p(x, v)$ distribution is the 2D α -stable density from which marginal densities $p_x(x)$ and $p_v(v)$ can be calculated. The large $|x|$ and $|v|$ asymptotics of the corresponding PDFs are

$$p_x(x) \propto \frac{w_x^\alpha}{|x|^{1+\alpha}} \quad \text{and} \quad p_v(v) \propto \frac{w_v^\alpha}{|v|^{1+\alpha}}, \quad (2)$$

i.e. they are of the of the α -stable type with the same stability index like the driving noise. However, contrary to the stochastic oscillator driven by Gaussian white noise variables (v, x) are no longer independent, i.e. the stationary distribution does not factorize⁶.

The numerically calculated quotient of the corresponding prefactors $D = w_v^\alpha/w_x^\alpha$ is depicted in the Fig. 1 as a function of the damping coefficient γ . Various curves correspond to different values of the stability index α . The inset shows small γ dependence. The quotient D follows the pattern derived in⁷

$$D = \frac{w_v^\alpha}{w_x^\alpha} = \begin{cases} \gamma^{-\alpha} & \text{for } 0 < \alpha < 1 \\ \gamma^{\alpha-2} & \text{for } 1 \leq \alpha \leq 2 \end{cases}. \quad (3)$$

Numerical simulations presented in Fig. 1 perfectly confirm the scaling predicted by Eq. (3). Please note, that results for $\alpha = 0.5$ (empty squares) and $\alpha = 1.5$ (empty circles) coincide.

Through the change of variables $x = \pm\sqrt{2\mathcal{E}_p}$, $v = \pm\sqrt{2\mathcal{E}_k}$ one can show that energy distributions have following asymp-

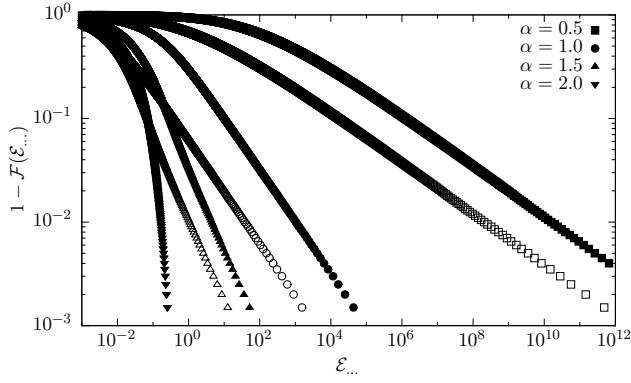


FIG. 2. Distributions of the potential \mathcal{E}_p (full symbols) and kinetic \mathcal{E}_k (empty symbols) energies for $\gamma = 10$. Various curves correspond to various values of the stability index α .

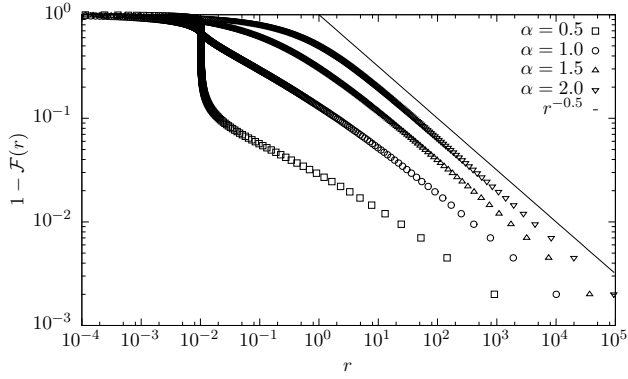


FIG. 3. Distribution of the energy ratio $r = \mathcal{E}_k/\mathcal{E}_p$ for $\gamma = 10$.

otics

$$p(\mathcal{E}_p) \propto \frac{w_x^\alpha}{\mathcal{E}_p^{1+\frac{\alpha}{2}}} \quad \text{and} \quad p(\mathcal{E}_k) \propto \frac{w_v^\alpha}{\mathcal{E}_k^{1+\frac{\alpha}{2}}}. \quad (4)$$

Figure 2 presents sample potential \mathcal{E}_p (full symbols) and kinetic \mathcal{E}_k energy (empty symbols) distributions.

The instantaneous quotient of the kinetic and potential energy $r = \mathcal{E}_k(t)/\mathcal{E}_p(t) = v^2(t)/x^2(t)$ has the universal asymptotics

$$p(r) \propto r^{-3/2} \quad (5)$$

which is independent of α . The universal $r^{-3/2}$ asymptotics of $p(r)$, see Eq. (5), originates due to lack of independence be-

tween position and velocity. If x and v were independent the behavior would be very different of the non-universal type⁷. Figure 3 presents the ratio r of instantaneous kinetic \mathcal{E}_k and potential \mathcal{E}_p energy. Solid line presents theoretical asymptotic given by Eq. (5).

III. SUMMARY AND CONCLUSIONS

For the stochastic harmonic oscillator driven by the Gaussian white noise, in the stationary state, the distribution of variables (x, v) is a bivariate Gaussian. Since this distribution factorizes into a product of x - and v -distributions, the phase variables are independent. The independence of x and v carries over to the equipartition theorem of equilibrium statistical physics. In the case of Lévy noises other than the Gaussian one none of these properties holds. The distribution of (x, v) is a non-elliptic 2D α -stable density. Thus, the variables x and v are dependent, and the dependence is stronger⁶ in the overdamped (large γ) case than in the underdamped one (small γ). This dependence is responsible for violation of basic concepts of equilibrium statistical mechanics.

Kinetic and potential energies of a harmonic oscillator driven by a symmetric α -stable noise have the same power-law asymptotics of $\mathcal{E}^{-(1+\alpha/2)}$ type determined by the noise type. Contrary to the classical Gaussian case, showing the equipartition between the kinetic and the potential energy, $\langle \mathcal{E}_k \rangle = \langle \mathcal{E}_p \rangle$, we demonstrate that no such equipartition is observed for the Lévy noise, except for the case of vanishing damping. In the limit of $\gamma \rightarrow 0$ both densities have the same widths. With the increasing damping larger fraction of energy is stored in the form of the potential energy. In the limit of $\gamma \rightarrow \infty$ the system is fully overdamped. It is fully characterized by its position only and the kinetic energy vanishes.

The distribution of the ratio $r = \mathcal{E}_k(t)/\mathcal{E}_p(t)$ of instantaneous kinetic and potential energies in the stationary state has the universal $r^{-3/2}$ asymptotics independent on the stability index α , which differs strikingly from the situation when the position and the velocity of the oscillator were independent.

ACKNOWLEDGMENTS

This project has been supported in part by the grant from National Science Center (2014/13/B/ST2/020140). Computer simulations have been performed at the Academic Computer Center Cyfronet, Akademia Górniczo-Hutnicza (Kraków, Poland)

¹ G. Samorodnitsky and M. S. Taqqu, *Stable non-Gaussian random processes: Stochastic models with infinite variance* (Chapman and Hall, New York, 1994).

² A. A. Dubkov, B. Spagnolo, and V. V. Uchaikin, *Int. J. Bifurcation Chaos. Appl. Sci. Eng.* **18**, 2649 (2008).

³ A. Janicki and A. Weron, *Simulation and chaotic behavior of α -stable stochastic processes* (Marcel Dekker, New York, 1994).

⁴ M. Von Smoluchowski, *Ann. Phys.* **21**, 756 (1906).

⁵ A. Einstein, *Ann. Phys.* **17**, 549 (1905).

⁶ I. M. Sokolov, B. Dybiec, and W. Ebeling, *Phys. Rev. E* **83**, 041118 (2011).

⁷ B. Dybiec, E. Gudowska-Nowak, and I. M. Sokolov, *Phys. Rev. E* **96**, 042118 (2017).

What is a form of the escape rate for white non-Gaussian noise?

Igor A Khovanov¹

¹School of Engineering, University of Warwick, Coventry, CV4 7AL, United Kingdom
e-mail address: i.khovanov@warwick.ac.uk

For Gaussian noise the form of the escape rate, r , describing a transition from a metastable state, is well known as Arrhenius equation or as Kramer's rate¹:

$$r = Z \exp\left(\frac{\Delta U}{D}\right) \quad (1)$$

where Z is a prefactor, ΔU is a height of barrier to overcome for escape to occur, and D is an intensity of Gaussian noise. This form (1) is in the heart of a vast number of theoretical approaches and practical applications, where form (1) is used explicitly or implicitly. The prefactor Z is often a research question for a particular system, but scaling in the following form

$$r \propto \exp\left(\frac{\Delta U}{D}\right) \quad (2)$$

is considered as universal, at least for the case of an additive noise. In fact, the scaling law (2) has been confirmed for potential, non-potential and non-equilibrium multidimensional systems². Such scaling separates system's properties describing via the barrier ΔU , from properties of fluctuations representing via the intensity D . Therefore if a system is changed, it would affect the barrier ΔU only, and the scaling law allows us to predict changes in the escape rate for varying D .

Gaussian noise is widely used and it is proven to be a very useful approximation of real fluctuations, in particular thermal fluctuations. However, there are many situations when fluctuations are not Gaussian. In photonics and electronics shot noise is abundant, whereas Gaussian noise is a limiting case of shot noise with small amplitude and high frequency. Fluctuations in coupled nonlinear systems and networks of systems can be quite complicated. Fluctuations in many biological systems can be distinct from Gaussian on different scales from cell level to population's dynamics. In many branches of engineering fluctuations have very complicated statistics, for example in fluid dynamics, vibrating structures. Non-Gaussian fluctuations are important in signal detection. In all mentioned examples the task of a transition from a metastable state is often considered and the rate for non-Gaussian noise is a quantity to estimate. For example, recently an approach for characterizing properties of shot noise in a mesoscopic system via measuring the escape rate has been extensively discussed theoretically and experimentally^{3,4}. In neuroscience fluctuations have very complicated nature and non-Gaussian noise is considered as an important contribution to firing rate of neurons⁵.

Thus, non-Gaussian noise is a part of many theoretical and practical problems, including the problem of transition from a metastable state when an escape rate as a function of noise's and system's properties needs to be defined. A possible attractive approach for tackling this problem consists of considering the rate in a form similar to (2) which lead to straightforward practical measuring of the barrier as a slope of $\log(r) \propto 1/D$. Such

approach is adopted in many publications, for example, for characterizing statistics of shot noise in mesoscopic systems^{2,3}. Shot noise is an example of non-Gaussian noise and the task consists of the estimation of so called full counting statistics⁶ which includes the third- and higher-order cumulants of noise. In experiments, non-Gaussian noise corresponds to a mixture of Gaussian and Poisson noises, both noises are assumed to be white. An amplitude of Poisson noise can be positive or negative, therefore the resulting probability density of non-Gaussian noise is characterized by an asymmetry depending on sign of the amplitude. A comparison of the escape rate for noises with different asymmetry in noise's distribution leads to an estimation of cumulants^{2,3}. An experimentally measured escape rate is suggested^{2,3} to be described as

$$r \propto \exp\left(\frac{S_a}{D}\right) \quad (3)$$

where D corresponds to the second cumulant (intensity) of non-Gaussian noise, and the effect of higher cumulants contributes to the change of the barrier S_a . Note that third and higher cumulants are equal to zero for Gaussian noise. Therefore, if the effect of non-Gaussian contribution is weak, the barrier S_a tends to ΔU . The rate (3) was applied for theoretical considerations of overdamped and underdamped potential systems and the rate was compared with numerical and experimental results^{7,8}; some disagreements between the theory, numerical simulations and experiment were reported.

Billings et al⁹ consider similar type of non-Gaussian noise for an overdamped system and suggested a different form of the rate:

$$r \propto \exp\left(\frac{\Delta U}{D}\right) A_{ng} \quad (4)$$

where A_{ng} is a factor describing the effect of non-Gaussian noise and it depends on a ratio between D and an amplitude of Poisson noise. A comparison between theoretical and numerically calculated escape rates demonstrated an agreement, but a discrepancy is also present.

The case of pure Poisson noise acting on an overdamped potential system was considered by Dykman¹⁰ and the following form for the escape rate was suggested:

$$r \propto \exp(Q) \quad (5)$$

where Q is an action of an auxiliary Hamiltonian system which includes parameters of Poisson noise explicitly. This form (5) was used for describing Poisson noise induced switching in a driven underdamped micromechanical resonator¹¹. In brief, it was implicitly shown^{10,11} that the use of forms (2) and (3) are questionable. Note that a frequency of Poisson noise was used for analyzing scaling properties of the escape rate, but the frequency does not definite uniquely the noise intensity and/or high-order cumulants of non-Gaussian noise.

The form (5) is rigorously derived, and the suggested derivation¹⁰ should be also valid for a large family of non-Gaussian noises with corresponding assumptions. The key assumption of this derivation is that the escape is a rare event with respect to characteristic times of system and noise, and this assumption is valid in a majority of cases of interest. However form (5) does not include noise's parameters, and an additional consideration is required for analyzing the dependence of escape rate on noise's properties. Thus, a separate consideration should be done for a particular type of non-Gaussian noise, that it is not a universal description.

In turn, non-Gaussian noise can be comprehensively described by cumulants. One of unsolved problem in the current theoretical development can be formulated as the following: what is a parametrization of the escape rate via the cumulants of non-Gaussian noise and what are leading factor(s) which define the dependence of the escape rate on the cumulants? In fact, the forms (3) and (4) can be considered as representing a case when second cumulant is a leading factor. Performed experimental and numerical analysis⁸ of non-Gaussian noise as a mixture of Gaussian and Poisson noises, demonstrates that a contribution of high-order cumulants is relatively weak and the use of scaling (2) is reasonable, especially in the presence of uncertainties in measurements of system's parameters.

Another open question, could high-order cumulants' contribution leads to a qualitative (rather than quantitative) change in scaling of the escape rate? So far, overdamped and underdamped potential system driven by non-Gaussian noise was considered. Could the effect of non-Gaussian noise be increased or suppressed in a particular form of non-potential and/or non-equilibrium system?

In considered above papers, shot noise in a form of Poisson noise plays the role of non-Gaussian contribution. What are other important models non-Gaussian noise? For example, the noise with a log-normal distribution is often mention in neuroscience. Is this type of noise applicable in other scientific fields?

Note, that there is a well-established class of non-Gaussian noises with α -stable or Levy distribution. The escape rate was comprehensively considered for such type of noises and the main conclusion^{13,14} is that escape induced by jumps, corresponding to heavy tails of the distribution, are always faster than those induced by diffusive behavior, which is the main topic of the consideration above.

REFERENCES

- ¹ P. Hänggi, P. Talkner, and M. Borkovec, *Rev. Mod. Phys.*, **62**, 251 (1990).
- ² D.G. Luchinsky, P.V.E. McClintock and M. Dykman, *Rep. Prog. Phys.*, **61**, 889 (1998).
- ³ J. Tobiska and Y. V. Nazarov, *Phys. Rev. Lett.*, **93**, 106801 (2004).
- ⁴ J.P. Pekola, *Phys. Rev. Lett.* **93**, 206601 (2004).
- ⁵ F. Freyer, K.Aquino, P.A. Robinson, P. Ritter, and M. Breakspear, *The Journal of Neuroscience*, **29**,8512 (2009).
- ⁶ L.S. Levitov, H. Lee, and G. B. Lesovik, *J. Math. Phys.*, **37**, 4845 (1996).
- ⁷ T. Novotny, *J. Stat. Mech.: Theory Exp.*, P01050 (2009)
- ⁸ B. Huard, H. Pothier, N. O. Birge, D. Esteve, X. Waintal, and J. Ankerhold, *Ann. Phys. (Berlin, Ger.)*, **16**, 736 (2007).
- ⁹ L. Billings, M. Dykman, and I.B. Schwartz, *Phys. Rev E*, **78**, 051122 (2008).
- ¹⁰ M.I. Dykman, *Phys. Rev. E*, **81**, 051124 (2010).
- ¹¹ J. Zou, S. Buvaev, M. Dykman, and H.B. Chan, *Phys. Rev. E*, **86**, 155420 (2012)
- ¹² G. Buzsáki, and K. Mizuseki, *Nat. Rev. Neurosci.*, **15**, 264 (2014).
- ¹³ P. Imkeller, I. Pavlyukevich, and T. Wetzel, *Eur. Phys. J. Special Topics*, **191**, 211 (2010).
- ¹⁴ A.V. Chechkin, O.Yu. Sliusarenko, R. Metzler, and J. Klafter, *Phys. Rev. E*, **75**, 041101 (2007).

Towards a resolution of the conductivity-selectivity paradox in the NaChBac ion channel

W.A.T Gibby¹, D. G. Luchinsky^{1,2}, M. L. Barabash¹, C. Guardiani^{1,3}, O. F. Fedorenko⁴, S. K. Roberts⁴, P.V.E McClintock¹

¹Lancaster University, department of Physics, UK, LA1 4YB

e-mail address: w.gibby@lancaster.ac.uk

²SGT Inc., Greenbelt MD, 20770, USA

³School of Engineering, University of Warwick, Coventry, CV4 7AL, UK

⁴Division of Biomedical and Life Sciences, Lancaster University, Lancaster, UK

I. INTRODUCTION

The passage of physiologically relevant ions across cellular membranes presents an unsolved problem of noise that is of crucial importance in biology. It involves a passive, stochastic, transport process that occurs via biological ion channels¹. Such channels are essential in physiology for maintaining and regulating cells. For example, voltage-gated sodium channels are well known to play an important role in the transmission of action potentials.

Ion channels possess a number of confounding properties and, in particular, they can be highly selective and yet conduct ions at close to the rate of free diffusion, $\sim 10^8 \text{s}^{-1}$. Na^+ channels can select Na^+ in preference to other monovalent ions e.g. K^+ , and also in preference to divalent ions such as Ca^{++} ; and yet allow permeation at $\sim 10^7 \text{s}^{-1}$. This paradoxical combination of properties is known within the community as the ‘‘conductivity-selectivity paradox’’, and has been a multi-decade-long standing problem². We will focus in particular on this paradox with the ultimate goal of describing the function of a channel from knowledge of its structure.

To tackle the paradox we will consider the statistics of a narrow model selectivity filter, develop a kinetic model, and compare the theoretical current with that for NaChBac from *Bacillus halodurans* (see Fig. (1)). This is a prokaryotic voltage-gated Na^+ channel for which a homology model structure exists; and its wild-type (WT) selectivity filter contains the amino acid sequence of residues LESWAS, where the glutamate E provides a negative fixed charge^{3,4} of $-4e$. Recent analysis suggests, however, that this charge might not be exact due to protonation; and thus that the channel actually has an effective fixed charge that is much smaller^{5,6}.

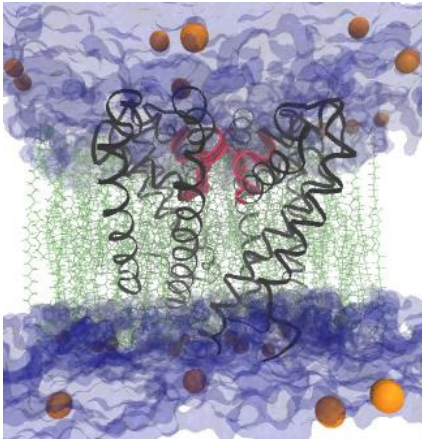


FIG 1. Representation of NaChBac^{3,4} embedded in a cell membrane made using VMD⁷. The channel (in black) crosses the membrane with its selectivity filter highlighted in red.

II. STATISTICAL THEORY

We start by defining our system as a pore of length L_c and radius R_c , thermally and diffusively coupled to intra- (L) and extra-cellular (R) bulk reservoirs. These contain arbitrary concentrations of mixed species. The pore contains 4 binding sites; however we shall reduce the system by considering isoenergetic sites meaning that each site possesses the same interaction strength. Molecular dynamics (MD) simulations have demonstrated Na^+ permeation to be a transition between 2 ions and 3 ions in the pore^{3,4}, and so we shall reduce the system by treating dual occupation as the ground state. The interactions in the system are defined by electrochemical potentials in the bulk, interaction with the charge n_f of the filter, nonideal chemical interactions via the excess chemical potential $\overline{\Delta\mu}_i$ and influence from the driving force $\phi^L - \phi^R$. Hence the Gibbs free energy describing each state can be written as^{8,9,10},

$$G = \epsilon + \sum_i kT \ln(n_i!) - kT \ln(x_i^s) - n_i \Delta\tilde{\mu}_i \quad (1)$$

where: ϵ represent the interaction with the charge in the filter $\epsilon = U_c(n_f + \sum_i n_i)$, where U_c depends on the pore geometry via $q^2 L_c / 8\pi\epsilon_w \epsilon_0 R_c^2$; the mole fraction in each s bulk is introduced via x_i^s ; and $\Delta\tilde{\mu}_i$ contains the excess and voltage terms $\overline{\Delta\mu}_i + qz_i(\phi^s - \eta\phi^L)$. This latter contribution is zero in symmetrical solutions, or equal to the Nernst potential for asymmetrical solutions. The equilibrium distribution therefore takes the following form

$$P(\{n_j\}) = Z^{-1} \prod_i \frac{(x_i^s)^{n_i}}{n_i!} e^{\sum_i n_i \Delta\tilde{\mu}_i - \epsilon / kT}. \quad (2)$$

We have demonstrated through rigorous analysis that the fluctuations and statistical properties are calculable from the partition function Z, and lead to conductivity and Fick’s law in the linear response regime. However our ultimate goal is to go beyond this to calculate and predict current when far-from-equilibrium.

III. KINETIC THEORY

The system in non-equilibrium can be described through a set of master equations¹¹ describing the probabilities of each state and the transitions between them,

$$0 = P(\{n_j\})\Gamma_{n,n+1}^i - P(\{n_j + n_i\})\Gamma_{n+1,n}^i. \quad (3)$$

These can easily be solved under steady state conditions with each non-equilibrium probability reducing to a function of transition rates. The electrical current can be calculated from the balance of fluxes,

$$I_i^L = q \left(\Gamma_{n,n+1}^{L,i} P(\{n_j\}) - \Gamma_{n+1,n}^{L,i} P(\{n_j + n_i\}) \right). \quad (4)$$

The transition rates are derived following the grand canonical Monte-Carlo method^{9,11,12}, with a normalisation that at equilibrium the rates must be diffusion limited. This normalisation is still being analysed in conjunction with results from the mean-first-passage-time and Brownian Dynamics in a tilted potential, and will be

discussed in further detail in the presentation. The rates therefore take the following form,

$$\Gamma_{n,n+1}^{s,i} = \frac{\alpha D^s / L_c^2}{1 + e^{\Delta G_i / kT}}, \Gamma_{n+1,n}^{s,i} = \frac{\alpha D^s / L_c^2}{1 + e^{-\Delta G_i / kT}} e^{-\frac{qz_i(\phi^s - \chi\phi^s)}{kT}}. \quad (5)$$

Thus in the equilibrium limit it is clear that we can recover a Kramers like exponent with a large energy barrier, rates proportional to D^s / L_c^2 in barrier-less transition and diffusion limited rates for downhill barriers. The terms: α and χ represent fitting parameters defining the diffusion coefficient in the filter which is known to be less than the bulk value and the electrostatic symmetry. If we first consider only the transition of 2 to 3 ions in their most optimal energy states, then we can derive the following linear response relations for the conductance,

$$G_{Na} = \frac{q^2 \alpha D_{Na}^s}{2L_c^2} \times \frac{e^{-\frac{\Delta G_{Na}}{kT}}}{\left(1 + e^{-\frac{\Delta G_{Na}}{kT}} + e^{\frac{\Delta G_{Ca}}{kT}}\right)^2 \times \left(1 + e^{-\frac{\Delta G_{Ca}}{kT}}\right)} \Delta \mu_{Na} \quad (6)$$

$$G_{Ca} = \frac{q^2 \alpha D_{Ca}^s}{2L_c^2} \times \frac{e^{\frac{\Delta G_{Ca}}{kT}}}{\left(1 + e^{-\frac{\Delta G_{Na}}{kT}} + e^{\frac{\Delta G_{Ca}}{kT}}\right)^2 \times \left(1 + e^{-\frac{\Delta G_{Na}}{kT}}\right)} \Delta \mu_{Ca}$$

whence it is clear that conduction maximises when we have large selectivity and barrier-less transitions. Hence we recover Coulomb blockade phenomena^{5,6} and this results in resonant peaks vs. n_f because conduction maximises when n_f is tuned to allow a barrier-less transition and hence a maximal fluctuation rate between states (see Fig. (2)).

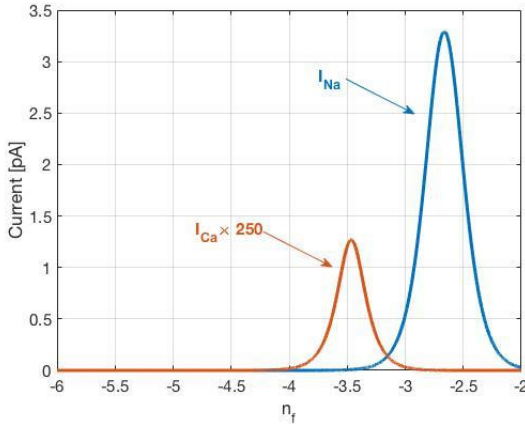


FIG 2. Current vs. n_f for Ca^{++} and Na^+ . Ca^{++} conductance has a smaller amplitude and is shifted in due to the influence from Na^+ .

Single channel current-voltage (I-V) data has been collected using the patch-clamp technique for NaChBac (LESWAS) and its mutant

(LEDWAS) under symmetrical 0.14M Na^+ solutions (and LESWAS under 0.5M conditions in the inset). The theoretical current has been successfully fitted to these data (see Fig. (3)) for the following fitting parameters: $\alpha = 0.11, \chi = 0.4, \Delta \bar{\mu}_{Na}^{LES} = 3.3kT, \Delta \bar{\mu}_{Na}^{LED} = -1.5kT$; assuming that the fixed charges of the channel were slightly reduced to $-2.5e$ and $-3.5e$ respectively. The effect of the mutation is clearly that of lowering the value of the excess chemical potential difference, and hence reversing the chemical binding interaction.

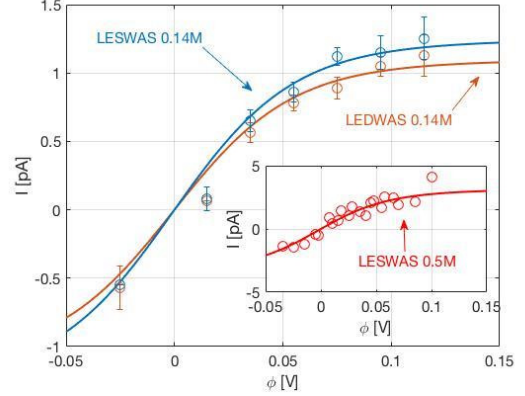


FIG 3. Theoretical current (solid lines) plotted against experimental data (coloured circles) for NaChBac and a mutant.

IV. CONCLUSION

In conclusion, we have made significant progress towards the resolution of the paradox introduced in the introduction. We have motivated a multi-species kinetic model that is capable of describing the permeation of mixed-valence ions through the selectivity filter of NaChBac. It has been used successfully to fit experimental data from NaChBac, in a reduced state-space example. In the linear response regime we observe maximal conduction occurring when it is possible for a barrier-less transition i.e. Coulomb blockade. To extend the work we will continue our analysis of the NaChBac channel by consideration of the full state space, and relaxation of the isoenergetic sites approximation.

ACKNOWLEDGEMENTS

The work was funded by a Leverhulme Trust Research Project Grant RPG-2017-134 and by the Engineering and Physical Sciences Research Council under Grant No. EP/M015831/1.

- ¹ B. Hille, 3rd ed., Ion Channels of Excitable Membranes, (Sinauer Associates, Sunderland, 2001).
- ² G. Eisenman, Biophys. J., 2, 259-323, (1962).
- ³ C. Guardiani, et. al., J. Chem. The. & Comp., 12, 1389-1400, (2016).
- ⁴ C. Guardiani, et. al., Phys. Chem. Chem. Phys., 19, 29840-29854, (2017).
- ⁵ I. Kaufman et. al. EPJ Nonlinear Biomed. Phys. 5, (2017).
- ⁶ I. Kaufman et. al. N.J.P., (2015).
- ⁷ W. Humphrey et. al., J. Molec. Graphics, 14.1, 33-38, (1996).

- ⁸ B. Roux, Biophys. J., 77, 139-153, (1999).
- ⁹ D.G. Luchinsky et. al. aXiv (2016).
- ¹⁰ D.G. Luchinsky et. al. ICNF (2017).
- ¹¹ W.A.T. Gibby et. al., ICNF (2017).
- ¹² W. Im and B. Roux, Biophys. J., 79, 788-801, (2000).

Anomalous diffusion in structured environments

G. Muñoz-Gil¹, M.A. Garcia-March¹, C. Manzo², A. Celi¹ and M. Lewenstein^{1,3}

¹ICFO-Institut de Ciències Fotoniques, The Barcelona Institute of Science and Technology, 08860 Castelldefels (Barcelona), Spain
e-mail address: gorka.munoz@icfo.eu

² Universitat de Vic - Universitat Central de Catalunya (UVic-UCC), C. de la Laura,13, 08500 Vic, Spain

³ ICREA - Pg. Lluís Companys 23, 08010 Barcelona, Spain

I. INTRODUCTION

Recent advances in single particle tracking techniques have led to a growing interest in the theoretical study of the motion of microscopic particles in biological environments¹. It is of key importance for the field of biology to characterize the diffusion of such particles. This diffusion, which often is anomalous and non-ergodic, is related to the interaction of the particles with the surrounding environment. However, due to the complexity of the system, there is still the need of theoretical descriptions of the experimentally observed diffusion phenomena. In this context, we have proposed different models to explain such phenomena: the patch model², the hunters model³, the Ising environment approach⁴ and the confinement approach⁵. Here, we discuss the last two models, which take advantage of the geometry/interactions of the environment.

II. ISING ENVIRONMENT

We model the environment with a 2D Ising lattice, i.e., a set of particles with two possible spin states, up or down⁴. The spins interact with their nearest neighbors and the system is considered at certain temperature T . At the critical temperature, T_c , the particles with spins pointing in the same direction tend to form clusters (see Fig. 1 (a)). The size of those clusters is given by the distribution $P(S) \propto S^{-\xi-1}$, where $\xi + 1 \approx 2,05$ ⁹.

We consider that, in such environment, a particle performs a continuous time random walk (CTRW), i.e. a random walk in which the waiting time between each step is stochastic. In our model, the diffusivity of the particle is a function of the area of the cluster that the particle visits at each step, $D = S^{-\eta}$ (see Fig. (1)(b)). Here η could be considered as the strength of the interaction between the particle and its environment. To find how many steps the particle moves within certain domain it is important to consider the temperature of the Ising environment and how fast the environment evolves with respect to the impurity dynamics. We propose that this effect can be addressed in a simplified way by considering that the mean number of steps in each cluster is $\bar{n} = S^\mu$ and we check it numerically. It is crucial to consider in this system the possible finite size and departure from the critical temperature in the environment, as both effects introduce a largest value of a domain in the distribution of domains, i.e., a cut-off in the power law distribution of sizes, termed as κ . Considering the previous two effects, we can calculate the waiting time PDF of the CTRW performed by the particle to give

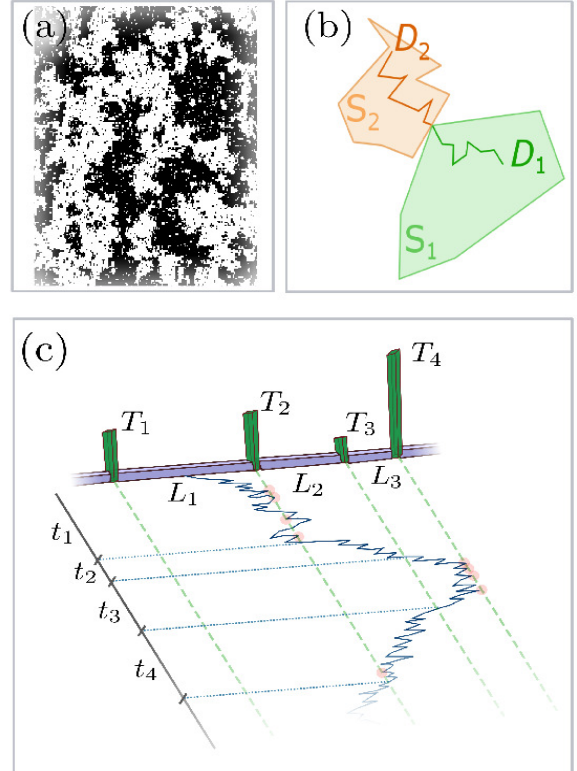


Fig. 1 (a) Example of a Ising spin configuration at T_c . (b) Scheme of the motion of a particle through an Ising environment. (c) motion of a random particle in segments of random length L and barrier height q .

$$\psi(t) \propto t^{-\sigma} \left[\Gamma\left(\sigma, \frac{t}{\kappa}\right) - \Gamma(\sigma, t) \right], \quad (1)$$

which implies that the mean squared displacement (MSD) shows subdiffusion for a transient time, with slope given by $M_2(t) \propto t^{\alpha(\mu, \eta)}$ with $\alpha = \frac{\xi-1-\mu}{\eta}$, and normally diffuses afterwards [see Fig. 2(a), and Ref.⁴].

III. COMPARTMENTS & BARRIERS

We consider now the case where the environment is composed of compartments of size L , which boundaries are partially reflective, i.e. porous. This means that when a particle reaches the boundary of a compartment, it has a certain probability T of being transmitted [see Fig. 1 (c)]. A particle performs a random walk in

this compartmentalized environment, where the size and transmittance are stochastically distributed, $g(L) = \beta L^{-\beta-1}$ and $P(T) = \alpha \left(\frac{1}{T}\right)^{-\alpha-1}$. One can then differentiate two different scales to the study of the particle. The first one considers that we can track the full trajectory of the particle. This means that we have access to the motion of the particle in the interior of the compartments. We consider this to be the *microscopic scale*. In this, we show how the particle anomaly diffuses, and more particularly, the motion of the particle is subdiffusive and nonergodic.

The other scale considers that we can only access the particle when it exits a compartment. We call it the *macroscopic scale*. From the first observation of the particle to the next one, we can extract two useful parameters: the distance it has travelled, corresponding to the size of the compartment, and the time it has taken to travel such distance. The behavior of the particle can then be described as a Lévy Walk⁶, where the particle performs jumps with distribution $g(L)$. The behavior of the particle can then be studied by means of the joint distribution of being at point x at time t

$$\psi(x, t) = \int_0^1 \phi(t|x, T)P(T)g(x)dq. \quad (2)$$

The conditional probability $\phi(t|L, T)$ is in fact the time a particle takes to exit a compartment of size L and transmittance T . We show that this conditional probability is an exponential of the form

$$\phi(t|L, T) = \frac{T}{L} \exp\left(-\frac{tT}{L}\right) \quad (3)$$

From Eq. (3) one can calculate the waiting time PDF $\psi(t)$. In Fig. 2 (b) we compare this distribution with the ones calculated numerically from simulations of the model described. In order to characterize the motion of the particle we proceed to calculate the mean squared displacement (MSD) as⁷

$$M_2(t) \propto t^{2-\alpha-\beta}, \quad (4)$$

(see details for the case $\alpha = \beta$ in Ref.⁵). It is interesting to see here that by changing the slope of the distributions of jumps and transmittances, we can access a very wide range of behaviors for the motion of the particle, covering superdiffusion for $\alpha + \beta < 1$ to subdiffusion for the opposite regime.

IV. CONCLUSIONS

We have discussed models of CTRW in structured environments. When the environment is described with a critical Ising model, the system can show subdiffusion but only during a transient time, under realistic finite system or departure of T_c conditions. For

¹ C. Manzo *et al.*, Phys. Rev. X **5**, 011021 (2015)
² P. Massignan *et al.*, Phys. Rev. Lett. **112**, 150603 (2014)
³ C. Charalambous *et al.*, Phys. Rev. E **95**, 032403 (2017)
⁴ G. Muñoz-Gil *et al.*, Phys. Rev. E **96**, 052140 (2017)
⁵ G. Muñoz-Gil *et al.*, *In prep.* (2018)

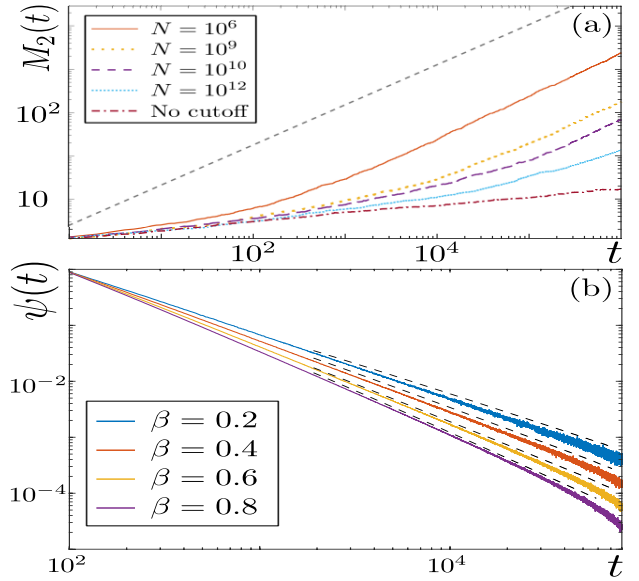


Fig. 2 (a) MSD of a particle moving in an Ising environment of finite size. (b) Waiting time distribution of the macroscopic behavior of a particle moving in a compartmentalized environment. Dashed lines are theoretical predictions.

random confinement, we find different anomalous diffusion processes at different space scales. For the macroscopic scales (times and lengths measured when the particles exit a compartment) we find a Lévy flight process whose microscopic origin is simply Brownian motion with partial transmittance. Remarkably, depending on the coefficients describing the distribution of sizes and transmittances we find either a superdiffusive and a subdiffusive regime.

ACKNOWLEDGEMENTS

The authors acknowledge financial support from the ERC Advanced Grant OSYRIS, EU IP SIQS, EU PRO QUIC, EU STREP EQuaM (FP7/2007-2013, No. 323714), Fundació Cellex, the Spanish MINECO (SEVERO OCHOA GRANT SEV-2015-0522, FISICATEAMO FIS2016-79508-P), and the Generalitat de Catalunya (SGR 874 and CERCA/Program). MGP acknowledges European Commission (FP7-ICT-2011-7, Grant No. 288263) and the Spanish Ministry of Economy and Competitiveness ('Severo Ochoa' Programme for Centres of Excellence in R&D SEV-2015-0522, and FIS2014-5617-R). CM acknowledges funding from the Spanish Ministry of Economy and Competitiveness (MINECO) and the European Social Fund (ESF) through the Ramon y Cajal program 2015 (RYC-2015-17896). GMG acknowledges funding from the Fundació Social LaCaixa.

⁶ V. Zaburdaev *et al.*, Rev. Mod. Phys. **87**, 483 (2015)
⁷ J. Klafter and I. M. Sokolov, First Steps in Random Walks, (Oxford University Press, Oxford, 2011)
⁸ G. J. Lapeyre Jr., arXiv:1504.07158 (2015)
⁹ M.E. Fisher. Physics **3**, 255 (1967)

Enhanced diffusion in a model of molecular motors with potential switching

Ryota Shinagawa and Kazuo Sasaki

Department of Applied Physics, Graduate School of Engineering, Tohoku University, Sendai 980-8579, Japan
e-mail address: shinagawa@camp.apph.tohoku.ac.jp, sasaki@camp.apph.tohoku.ac.jp

I. INTRODUCTION

Diffusion is a fundamental phenomenon, which occurs in systems with noise. It is easy to imagine a Brownian particle in a one-dimensional system as an example of such systems. The diffusion of such a particle is characterized by the diffusion coefficient D , which is defined as

$$D = \lim_{t \rightarrow \infty} \langle x(t) - x(0) - vt \rangle^2 / 2t, \quad (1)$$

where $x(t)$ is the particle position at time t and v is the average velocity of the particle. In free diffusion (without external forces) D is given by the Einstein relation

$$D_0 = k_B T / \gamma, \quad (2)$$

where k_B is the Boltzmann constant, T is the absolute temperature of the environment, and γ is the drag coefficient.

At the end of the 20th century, it was found^{1,2} that D can be enhanced significantly as compared to D_0 when a constant external force F is applied to a particle in a one-dimensional periodic potential $V(x)$. This phenomenon is called diffusion enhancement (or giant enhancement of diffusion). The enhancement occurs for F values close to the maximum slope of $V(x)$. This means that the information about the potential of a system can be extracted by measuring the peak position of D as a function of F .

In 2015, the diffusion enhancement was observed in a molecular motor for the first time in the absence of the energy source, i.e., the adenosine triphosphate (ATP)³. The rotary motor F_1 -ATPase (F_1) was used in the experiment with a constant external torque applied to its rotor. The height of the periodic potential of the rotor due to its interaction with the stator was estimated from the peak position of the rotational diffusion coefficient of the rotor as a function of the external torque.

The rotary motor F_1 rotates spontaneously in the presence of ATP. In this case, the binding of ATP to F_1 and its hydrolysis cause the structural changes in F_1 , which result in switching of the rotor-stator interaction that driving the rotation of the rotor. This paper shows that the diffusion enhancement occurs even in the model for molecular motors (with potential switching) in the presence of the energy source and that information about the molecular motors can be obtained from enhanced diffusion.

II. MODEL

Our model for a rotary molecular motor is analogous to the one⁴ studied previously in the literature. The motor changes its state by switching of the potential of the rotor due to the hydrolysis of ATP. The angle of the rotor is expressed as x and the motor's state is represented by an integer n . We assume that the potential in state n , $V_n(x)$, is a parabolic function as shown below.

$$V_n = \frac{1}{2} K (x - nl)^2, \quad (3)$$

whose minimum position is shifted by $\pm l$ upon a switching $n \rightarrow n \pm 1$. The curvature K of the parabola is determined by the stiffness of the interaction between the rotor and the stator.

The transition from state n stochastically occurs at a rate $w_n^+(x)$ for the forward process ($n \rightarrow n + 1$, see Fig. (1)) or $w_n^-(x)$ for the backward process ($n \rightarrow n - 1$). The transition rates depend on x and meet the following detailed balance condition for any x .

$$\frac{w_n^+(x)}{w_{n+1}^-(x)} = \exp \left\{ -\frac{1}{k_B T} [V_{n+1}(x) - V_n(x) - \Delta\mu] \right\}, \quad (4)$$

where $\Delta\mu$ is the free energy released by the ATP hydrolysis. It was experimentally found⁵ that the transition rate for F_1 depends exponentially on x . For this reason, we assume the following expression for $w_n^+(x)$.

$$w_n^+(x) = k^+ [\text{ATP}] \exp(ax), \quad (5)$$

where k^+ is the rate constant, $[\text{ATP}]$ is the concentration of ATP, and a is a constant characterizing the angular dependence of the transition rate.

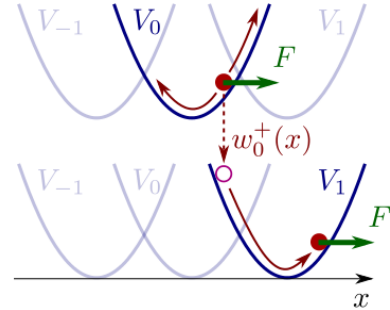


FIG. 1. Our model for molecular motors. Stochastic switching of the potential (the transition) drives a motor.

The probability density function $P_n(x, t)$ of the rotor angle in state n at time t can be calculated by the Fokker-Planck equation

$$\frac{\partial P_n}{\partial t} = D_0 \frac{\partial^2 P_n}{\partial x^2} + \frac{\partial}{\partial x} \left[\frac{1}{\gamma} \left(\frac{dV_n}{dx} - F \right) P_n \right] - (w_n^+ + w_n^-) P_n + w_{n-1}^+ P_{n-1} + w_{n+1}^- P_{n+1}, \quad (6)$$

where F is the external torque applied to the rotor. Let $P_n^{\text{st}}(x)$ be the steady-state solution of Eq. (6). The rotational velocity of the motor can then be expressed as

$$v = \frac{1}{\gamma} \int_{-\infty}^{\infty} dx \left(F - \frac{dV_n}{dx} \right) P_n^{\text{st}}. \quad (7)$$

It has also been proved⁶ that D can then be obtained from

$$D = D_0 + \int_{-\infty}^{\infty} dx \left[\frac{1}{\gamma} \left(F - \frac{dV_n}{dx} \right) - v \right] Q_n, \quad (8)$$

where $Q_n(x)$ is the solution of the equation

$$\left[v - \frac{1}{\gamma} \left(F - \frac{dV_n}{dx} \right) + 2D_0 \frac{d}{dx} \right] P_n^{\text{st}} = D_0 \frac{d^2 Q_n}{dx^2} + \frac{d}{dx} \left[\frac{1}{\gamma} \left(\frac{dV_n}{dx} - F \right) Q_n \right] - (w_n^+ + w_n^-) Q_n + w_{n-1}^+ Q_{n-1} + w_{n+1}^- Q_{n+1} \quad (9)$$

with $Q_{n\pm 1}(x) = Q_n(x \mp l)$.

III. RESULTS

Fig. (2) shows the F dependence of D , obtained⁷ by numerically solving Eqs. (6) and (9) and carrying out the integrations in Eqs. (7) and (8). $D(F)$ has two or three peaks depending on the value of $[ATP]$, which is proportional to the transition rate (see Eq. (5)). It means that the diffusion enhancement occurs even in the model for molecular motors.

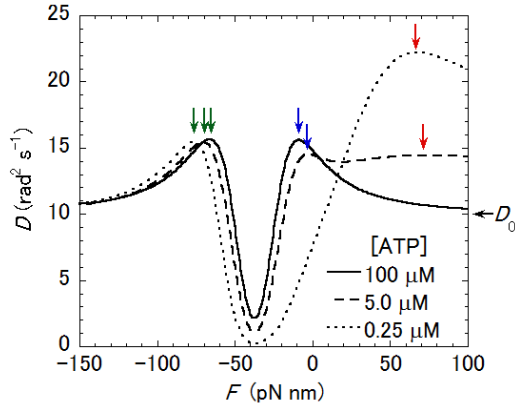


FIG. 2. Diffusion coefficient D as a function of the external torque F for our model. Arrows indicate the peaks.

As seen in Fig. (2), the positions and heights of the peaks shift with the change of $[ATP]$. Fig. (3) shows their dependence on $[ATP]$. Three peaks are observed for $[ATP]$ larger than a critical value $[ATP]_c$ (about 4 μM in this example) and two peaks for $[ATP] < [ATP]_c$; of the three peaks present for $[ATP] > [ATP]_c$, the right most peak is referred to as branch 1, the left most as branch 3, and the middle one as branch 2.

The peak positions for $[ATP] \ll [ATP]_c$ and those of branches 2 and 3 for $[ATP] \gg [ATP]_c$ can be understood as follows⁷. At low ATP concentrations, the time needed for achieving the equilibrium distribution of x in potential $V_n(x) - Fx$, $\tau_{\text{eq}} = \gamma/K$, competes with the waiting time, τ_w , for the transition to occur from the equilibrium distribution. The waiting time τ_w^+ (τ_w^-) for the forward (backward) transition increases (decreases) with F because it depends exponentially on x as shown by Eq. (5) and the

average of x in the equilibrium state varies linearly with F . It has turned out⁷ that when these time scales are comparable ($\tau_{\text{eq}} \sim \tau_w^\pm$), the diffusion is enhanced and the dependence of the peak positions on $[ATP]$ are predicted to be given by

$$F^\pm = \frac{K}{a^\pm} \ln[ATP] + \text{const.}, \quad a^\pm = \frac{Kl}{2k_B T} \mp \frac{Kl}{2k_B T} - a, \quad (10)$$

where F^+ and F^- correspond to branch 1 and branch 3, respectively. The dashed lines in Fig. (3) are straight lines whose slopes are given by the coefficients of the logarithmic term in Eq. (10). At high ATP concentrations, the transitions occur faster than appreciable changes in x . As a result, it can be regarded that the rotor moves in a single effective potential⁴

$$V_{\text{eff}}(x) = -k_B T \ln \left\{ \sum_{n=-\infty}^{\infty} \exp \left[-\frac{V_n(x) - n\Delta\mu}{k_B T} \right] \right\}, \quad (11)$$

which is a tilted periodic potential. Therefore, as the previous theory² predicts, the peaks of $D(F)$ are located at the values of F close to the maximum positive slope (branch 2) and the maximum negative slope (branch 3) of $V_{\text{eff}}(x)$.

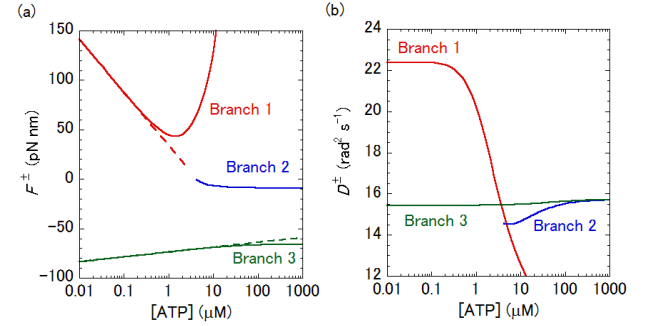


FIG. 3. The $[ATP]$ dependence of the (a) positions and (b) heights of the peak for the torque dependence of the diffusion coefficient, $D(F)$, shown in Fig. (2).

The above arguments imply that if the $[ATP]$ dependence of the peak position of $D(F)$, such as the one shown in Fig. (3a), is obtained experimentally, parameters K and a can be inferred from the result for large and small $[ATP]$, respectively.

IV. UNSOLVED PROBLEMS

We have not understood why the peak of Branch 1 in Fig. (3) appears for $[ATP] > [ATP]_c$, where Branch 2 exists. It is also desirable to obtain a closed form expression for $D(F)$, which will make the analysis much easier.

ACKNOWLEDGEMENT

We thank Kumiko Hayashi and Takashi Yoshidome for their useful discussion and constructive comments.

⁴ K. Kawaguchi, S.-I. Sasa, and T. Sagawa, *Biophys. J.* **106**, 2450 (2014).

⁵ R. Watanabe, D. Okuno, S. Sakakihara, K. Shimabukuro, R. Iino, M. Yoshida, and H. Noji, *Nat. Chem. Biol.* **8**, 86 (2012).

⁶ T. Harms and R. Lipowsky, *Phys. Rev. Lett.* **79**, 2895 (1997).

⁷ R. Shinagawa and K. Sasaki, *J. Phys. Soc. Jpn.* **85**, 064004 (2016).

¹ G. Constantini and F. Marchesoni, *Europhys. Lett.* **48**, 491 (1999).

² P. Reimann, C. Van den Broeck, H. Linke, P. Hänggi, J. M. Rubi, and A. Pérez-Madrid, *Phys. Rev. Lett.* **87**, 010602 (2001).

³ R. Hayashi, K. Sasaki, S. Nakamura, S. Kudo, Y. Inoue, H. Noji, and K. Hayashi, *Phys. Rev. Lett.* **114**, 248101 (2015).

The analyze of conducting waves of lower leg muscle using Multichannel Surface EMG

Marzieh Aliabadi Farahani¹, Misa Takagi, Kota Akehi, Kazuyuki Mito, Tota Mizuno and Naoaki Itakura
*The University of Electro-Communications, Graduate School of Informatics and Engineering,
1-5-1 Chofugaoka, Chofu, Tokyo 182-8585, Japan
e-mail address¹: a1740002@edu.cc.uec.ac.jp*

I. INTRODUCTION

A skeletal muscle is a striated type of muscle attached to the skeleton. It is being used to facilitate movements by applying a force to the bones and joints via contraction. Skeletal muscles are composed of thousands of parallel muscle fibers running through the length of the muscle. Each muscle fiber contains several parallel contractile units called myofibrils running through the length of each muscle fiber. An action potential originates from a brain signal and occurs when the membrane potential of a specific axon location rapidly rises and falls¹. It is communicated to the “end plate” of a muscle fiber; the neuromuscular junction between a motor neuron and the muscle fiber. The action potential propagates from the end plate to both sides of the tendons. The electrical signal of the action potential can be measured by a surface electromyogram (EMG).

The Muscle Fiber Conduction Velocity (MFCV) is the propagation speed of an action potential along a muscle fiber². Generally, a surface EMG is used to measure simultaneously the action potential of a large number of motor units in muscle and it is not possible to measure them individually. In addition to that, muscle fibers, depending on their type and activity, may have an effect on the conducting waves. Hence, it is hard to measure or give an estimation of the action potential of an individual motor units.

The multichannel surface EMG developed in this research project has the ability to examine the characteristics of conducting waves individually and quantify them. Doing so, it is possible simultaneously analyze and individually identify a large number of motor units.

In the previous research conducted³⁻⁵, a multi-channel method (m-ch method) was used to identify the conducting waves under fixed conditions. A calculation method was designed to measure the conducting waves' propagation speed. Results about the detailed mechanism of the muscle contraction could be achieved. The focus for the test muscle was on the human biceps only.

The main purpose of this research is 1) To use m-ch method and examine the effect of it on another muscle; the lower leg muscle 2) By changing the configuration of the electrodes adapted to lower leg measurements, are there any differences on the conducting waves patterns 3) Checking the effect of deep muscle on conducting waves.

Such information would support the study of the effect of muscle contraction on the different types of muscle fiber in triceps surae muscle. It would also complete the data and our understanding of the muscle contraction mechanism.

II. EXPERIMENT

The tests were conducted on five healthy adult people (3 male and 2 female) with an average age of 22 years old. The test muscle was Tricep Surae muscle, commonly known as the muscles of the calf, comprises of a pair of muscles known as the Gastrocnemius

and Soleus muscles. The participants were asked to stand on their tiptoes and keep the heel 5 cm above floor for 10 seconds. The measurement were done 3 times, at 3 different locations of their legs for all the participants, with the probes located alternatively on the external, internal and central side of the lower leg.

The electrodes are made of pure silver wires, 1 mm diameter and 10 mm length. The distance between the central side of each electrode is 5 mm. The electrodes array were placed vertically on the lower legs of the participants in the same direction as of muscle fibers.

In this research, a 17 electrodes was used with 16 channel being measured. The experimental system is shown in Fig. (1) and the results and analysis presented in this paper were achieved using the results of this system.

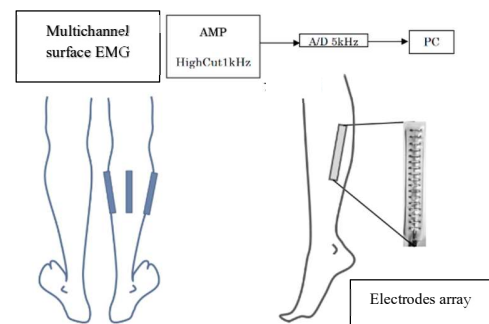


FIG.1 Experimental System

III. METHOD

The method used for this research is the m-ch method. After data collection the samples have to be processed and analyzed. In this method, the time interval between two zero crossing of the wave pattern is set as the analysis unit. The wave pattern from the analysis unit is referred to as the conduction source, and the adjacent channels around conduction sources as the conduction destination.

To be accepted as a conducting wave according to m-ch method, a correlation coefficient of 0.9 or more, amplitude ratio of 0.7 m or more, wavelength ratio of 0.8 m or more, and Muscle Fiber Conduction Velocity within 30% are needed. Using the m-ch method on the 16 channels, the conducting wave pattern respecting all the conditions mentioned above were only found on 3 channels.

IV. RESULTS AND DISCUSSION

The m-ch method was used for the analysis in this project and the relative frequency distribution chart was designed using the amplitude and conduction velocity of all participants in Fig. (2). The figure highlights the relevance of the m-ch method for conducting waves measurements in the lower leg.

In J.Polgar et al's research⁶, the composition ratio (fast/slow muscle) of different type of muscle fiber is shown according to

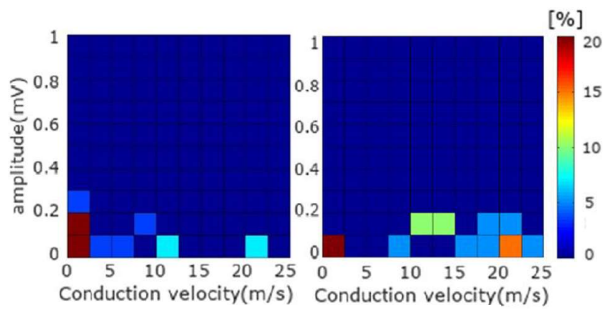


FIG.2 Relative Frequency Distribution

physiological data. It had been mentioned that soleus muscle has 86.4% of slow contracting muscle fiber and 13.6% of fast contracting muscle fiber but in Gastrocnemius muscle it is divided almost to half.

In this research, the slow contracting speed muscle fiber are considered within 0~12 m/s and the fast contracting speed muscle fiber within 12~25 m/s. The percentage of slow contracting muscle fiber and fast contracting muscle fiber of all participants is shown in Table. (1).

Confronting the results of this research with the physiological data of J.Polgar et al⁶, as for central side of lower leg, different results were found. It could be due to the fact that participants were asked to stand on their tiptoes or a lack of representative data for the experiment. From these results, we observed that Multichannel surface EMG does not show the same results about the percentage of muscle fiber as the physiological data from reference⁶.

It is generally accepted that if the electrodes are placed on central side of lower leg, it is possible to measure the conducting waves of Soleus muscle which is a deep muscle and has low contracting muscle fiber.

Our results shows that the rate of slow contracting muscle fiber of most of participants in the area of 0~12 m/s was above 20%. But at the same time, the rate of fast contracting muscle fiber was high in most of them. So there is a paradox between general information and the data of this research. The results are displayed in Chart. (1). The explanation could be that the Gastrocnemius muscle, which is located on the outer layer of the Soleus muscle and contains fast contracting muscle fibers, had some effect on Soleus muscle.

Also it is generally accepted that if the electrodes are placed on external or internal side of the lower leg, it is possible to measure the conducting waves of the external or internal side of Gastrocnemius muscle.

In this research, for the external and internal side of lower leg or at least one of them, fast contracting muscle fiber of most of participants in the area of 12 m/s or more was found. So it explains that the Gastrocnemius muscle mainly contains fast contracting muscle fibers. But at the same time, the rate of slow contracting muscle fiber of most of participants in the area of 0~12 m/s was above 20%. It shows that the rate of low contracting muscle fiber in the Gastrocnemius muscle is not low.

¹ A. Hodgkin et al, A quantitative description of membrane current and its application to conduction and excitation in nerve, *The Journal of Physiology*, 117 (4), pp.500–544 (1952)
² R. Beck, *Muscle Fiber Conduction Velocity*, Wiley Encyclopedia of Biomedical Engineering (2006)
³ S. Odan, N. Itakura, Analysis of Propagating Wave in Multi-Channel Surface Electromyogram (in Japanese). HIP2008-136, pp.75-78 (2008)

Table (1) shows that the propagation speed of conducting waves in internal side of lower leg is higher than the external side. So it is possible to say that, internal side of the Gastrocnemius muscle has more fast contracting muscle fiber than external side. But in this research, due to standing on tiptoes, the weight is put mainly on internal side of muscle. It means that low contracting muscle fibers were working first and whenever more energy was needed, fast contracting muscle fibers were working. It explains the high rate of high contracting muscle fibers of internal side of leg in Table (1). In Table. (2), shows some difference between results of different participants which means, different participants use different muscles of same area in lower leg during the test. Further, it shows that the propagation speed of conducting waves for central side of female participants (A, B) were higher than male participants (C, D, E). So it shows that also depends on the gender there are different way of using Tricep Surae muscle.

Table.1 Speed of conducting waves in different muscle

(%)	Gastrocnemius (external)		Gastrocnemius (internal)		Soleus (central)	
	Slow	Fast	Slow	Fast	Slow	Fast
A	92.9	7.1	60	40	50	50
B	85.7	14.3	50	50	63.2	36.8
C	77.8	22.2	100	0	0	100
D	100	0	73.5	26.5	75	25
E	67.4	32.6	62.9	37.1	100	0
Average	84.8	15.2	69.3	30.7	57.6	42.4

Table.2 Conducting waves of different part of lower leg / sec

Participants	external	internal	central
A	4.3	2.2	3.9
B	0.9	0.6	2.2
C	0.9	0.4	0.5
D	3.9	4.1	0.4
E	4.5	4.9	0.8

V. Conclusion

The m-ch method is relevance for conducting waves measurements in the lower leg. We observed that Multichannel surface EMG does not show the same results about the percentage of muscle fiber as the physiological data from reference.

The Gastrocnemius muscle, which is located on the outer layer of the Soleus muscle and contains fast contracting muscle fibers, had some effect on Soleus muscle.

The rate of low contracting muscle fiber in the Gastrocnemius muscle is not low.

Internal side of the Gastrocnemius muscle has more fast contracting muscle fiber than external side. But in this research, due to standing on tiptoes, the weight is put mainly on internal side of muscle.

⁴ T. Kosuge et al, A Study for Conducting Waves by Using the Multi-channel Surface EMG, 4th International conference, DHM 2013, HCI International 2013, pp.223-231 (2013)
⁵ T. Kosuge et al, Conducting wave using multi-channel surface EMG (in Japanese). IEEJ, C 134(3), pp. 390-397 (2014)
⁶ J.Polgar et al, Data on fibre Size in thirty-six human muscles. An autopsy study, *Journal of the Neurological Sciences*, 19:307-318(1973)

On the principle of equipartition of kinetic energy: classical versus quantum

Jerzy Łuczka¹ and Paweł Białas²

¹ *Department of Theoretical Physics, University of Silesia, ul. 75 Pułku Piechoty 1A, 41-500 Chorzów
e-mail address: jerzy.luczka@us.edu.pl*

² *Department of Theoretical Physics, University of Silesia, ul. 75 Pułku Piechoty 1A, 41-500 Chorzów*

One of the enduring milestones of classical statistical physics is the theorem on the equipartition of energy, which states that energy is shared equally amongst all energetically accessible degrees of freedom of a system and relates average energy to the temperature T of the system. In particular, for each degree of freedom, the average kinetic energy is equal to $E = k T/2$, where k is the Boltzmann constant. This relation is exploited in various aspects of many areas of physics, chemistry and biology. However, in many cases, it is applied in an unjustified way forgetting about assumptions used in proving this theorem. One can notice confusion and mess, in particular in the case of quantum systems.

We discuss a quantum counterpart of the equipartition energy theorem. In the framework of the Generalized Langevin Equation (GLE), we derive the exact expression for averaged kinetic energy of a quantum free Brownian particle in an equilibrium state. We assume a relatively general form of the integral kernel of GLE and analyse kinetic energy in selected regimes like high or low temperature limits.

Measuring the Josephson frequency of fractional charges with shot noise

M. Kapfer¹, P. Roulleau¹, I. Farrer², D.A. Ritchie², & D. C. Glatli

¹ Service de Physique de l'Etat Condensé, IRAMIS/DRF (CNRS UMR 3680), CEA Saclay, F-91191 Gif-sur-Yvette, France.

e-mail address: christian.glatli@cea.fr

² Cavendish Laboratory, University of Cambridge, J.J. Thomson Avenue, Cambridge CB3 0HE, UK.

I. INTRODUCTION

In some quantum matter states, the electrical current may surprisingly be transported by carriers bearing a fraction e^* of the elementary charge e . This occurs for the topological ordered states of the fractional Quantum Hall Effect (FQHE)^{1,2}, in two-dimensional electron systems in high magnetic field. When the magnetic flux, in quantum units h/e , is a rational fraction $\nu=p/q$ of the electron number, a dissipationless current flows around the sample edges carried by anyons with fractional charge $e^*=e/q$. Among the early attempts to observe these fractional charges³⁻⁸, the most reliable ones⁵⁻⁸ were based on measuring the tiny current noise⁹⁻¹¹ that produces their granularity. However, for complex FQHE states¹² like filling factors $\nu=2/5$ or $2/3$, noise measurements gave unexpected charges^{13,14} depending on experimental conditions while neutral modes^{14,15} contribute to the charged mode current noise, calling for new approaches. Here we present novel fractional charge measurements based on their Josephson frequency $f_J=e^*V/h$ ¹⁶ which manifests when irradiating contacts at microwaves frequency f by marked signatures in the photo-assisted shot noise (PASN) versus voltage V when $f_J=nf$. Our results, validating FQHE PASN¹⁶⁻¹⁸ models, enable the future realization of on-demand anyon sources¹⁹ based on levitons²⁰⁻²²

I. JOSEPHSON FREQUENCY SIGNATURES IN SHOT NOISE.

Here we show that by combining microwave frequencies and low frequency shot noise measurements we can provide a novel quasiparticle charge determination from their Josephson frequency $f_J=e^*V/h$. The Josephson frequency has a long history starting from the discovery of Josephson Effects²⁶. When two tunnel coupled superconductors are biased by a voltage V , a steady current oscillation occurs at frequency f_J with $e^*=2e$, the Cooper pair charge. Reciprocally, irradiating the superconducting junction at frequency f gives photon-assisted singularities in the I-V characteristics when the bias voltage Josephson frequency matches multiple of f . The Josephson effects arise from the quantum beating between two Cooper pairs condensate at energies separated by eV . For normal metals, described by a Fermi sea, no steady Josephson oscillations are expected but transient current oscillations at frequency $f_J=eV/h$ were recently demonstrated in numerical quantum simulations for two voltage shifted Fermi seas put in quantum superposition in an electronic interferometer²⁷. Still in normal metals, the Josephson frequency manifests in the high frequency shot noise when the bias voltage equals the emission noise frequency. Reciprocally, the low frequency photo-assisted shot noise (PASN) shows singularities when microwaves irradiate

a contact at frequency $f=f_J$. In the following, we will focus on PASN. Predicted²⁸ for mesoscopic normal conductors, PASN has been theoretically found to occur in all electronic systems, even interacting like the FQHE, providing here a mean to determine e^* from the Josephson frequency¹⁶⁻¹⁸.

Shot noise results from carrier scattering in a quantum conductor when a current flows under dc voltage bias V_{dc} . It results from the beating of two voltage shifted Fermi seas when mixing occurs due to scattering. When adding an ac voltage: $V(t)=V_{dc}+V_{ac}\cos(2\pi ft)$, photon-created electron-hole pairs scattering increase the noise. Using voltage in Josephson frequency units $f_J=e^*V_{dc}/h$, the PASN spectral density is given by:

$$S_I^{PASN}(f_J)=\sum_{l=-\infty}^{l=\infty} |p_l|^2 S_I^{dc}(f_J-lf) \quad (1)$$

S_I^{dc} is the dc-Shot Noise measured when $V_{ac}=0$, $p_l=J_l(e^*V_{ac}/h)$ is the 1-photon absorption probability amplitude, J_l an integer Bessel function. Indeed under ac driving, the Fermi sea of the driven contact is put in a quantum superposition of identical Fermi Seas but energy shifted by lhv . Thus (1) expresses that observables become the sum of observables calculated for $V_{dc}\rightarrow V_{dc}+lhv/e$ and weighted by the probability $|p_l|^2$. In (1), the zero bias voltage dc-shot noise singularity, $\sim|V_{dc}l-lf|$, is replicated whenever $f_J=e^*V_{dc}/h=lf$, signalling the Josephson frequency.

PASN observations are well documented in normal conductors^{29,31-32} ($e^*=e$). They were observed for microwave frequencies in diffusive metallic wires²⁹, in Quantum Point Contacts³¹, and in tunnel junctions³². Regarding interactions, (1) has been tested in superconducting/normal junctions ($e^*=2e$)³⁰. In FQHE, expression (1) is implicit in PASN theoretical expressions of refs^{17,22} and the concept of fractional Josephson frequency first appeared in the work of X. G. Wen¹⁶. No experiment is yet available as combining high magnetic fields, sub-fA/Hz^{1/2} current noise and >10 GHz microwaves at ultra-low temperature (~ 20 mK) is highly demanding.

II. EXPERIMENTAL RESULTS

The present work fills this gap. A schematic view of the set-up is sketched in Fig.1(a,b). In topologically insulating QHE conductors the current flows along chiral edge modes. To inject current or apply microwave excitation, metallic contacts connect the edges to an external circuit. A narrow tuneable constriction called Quantum Point Contact (QPC) is formed using negative voltage V_G on split gates to locally couple counter-propagating edge modes. In the example of Fig.1, starting from two edge channels for bulk filling factor $\nu_B=2$ or $2/5$ in respectively the IQHE or FQHE regimes, the outer edge channel is fully reflected at the QPC by locally creating a filling factor $\nu_C=1$ (or respectively $1/3$) using electron depletion with negative V_g . A current $I_0=(\nu_B e^2/h)V_{dc}$ injected by biasing

contact 1 at voltage V_{dc} , is thus partitioned at the QPC into a transmitted $I_{T0}=(v_{ce}^2/h)V_{dc}$ and a backscattered $I_{B0}=(v_B-v_c)(e^2/h)V_{dc}$ currents. To probe the inner edge channel carriers, quasiparticle backscattering through the v_c region is further induced for more negative V_G resulting in total backscattered current $I_{B0}+I_B$, with $I_B=R(v_{ce}^2/h)V_{dc}$ and R the reflection probability, while the total transmitted current is $I_{T0}+I$, with $I=(1-R)(v_{ce}^2/h)V_{dc}$. In FQHE, the edge channels form chiral Luttinger liquids. Transport becomes energy dependent giving non-linear variations to $I_B(V_{dc})^{9-11}$. Complete modelling is difficult and comparison to experiments is only reliable in the two following weak coupling regimes. For weak backscattering (WB) ($R \ll 1$), the quasiparticle transfer follows Poissonian statistics. The dc shot noise is⁹⁻¹¹

$$S_I^{dc}(V_{dc}) = 2e * I_B(V_{dc}) \quad (2)$$

With $e^*=e$ or $e^*=e/3$ for the IQHE and $1/3$ -FQHE regimes respectively considered here. For strong backscattering (SB) ($1-R \ll 1$), only electrons tunnel through an opaque barrier between left and right side of the sample⁹⁻¹¹:

$$S_I^{dc}(V_{dc}) = 2eI(V_{dc}) \quad (3)$$

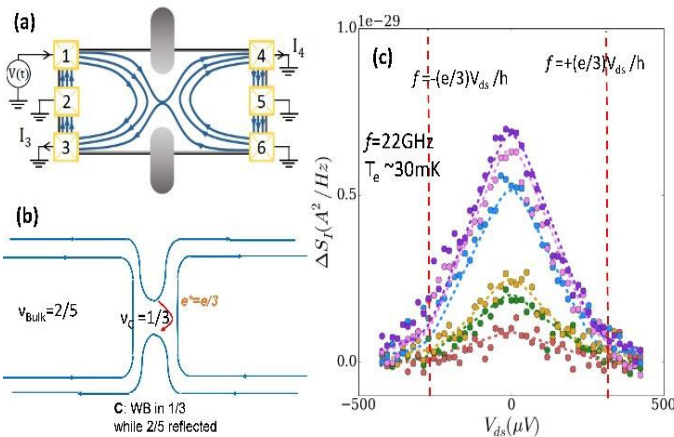
To better see the change in the noise, the excess noise, i.e. the shot noise with microwave ON minus the shot noise with microwave OFF, versus dc bias :

$$\Delta S_I = S_I^{PASN}(V_{dc}) - S_I^{dc}(V_{dc}) \quad (4)$$

is considered. We will present measurements in the IQHE regime for $v_{Bulk}=2$ and 3 while $v_c=1$ showing clear signatures of Josephson frequency when $f_j=eV_{dc}/h=\pm f$. We will then show results in the FQHE regime at $v_{Bulk}=2/5$ while $v_c=1/3$ both in the weak and strong backscattering regime.

Fig.1(c) shows the excess shot noise in these FQHE conditions for different microwave power. From the data one sees clear signatures of the fractional Josephson frequency when $f_j=eV_{dc}/h=\pm f$ giving $e^*=e/3$. Equation (1) has been quantitatively confirmed by comparing the FQHE PASN data to the shifted experimental dc shot noise curve weighted by the appropriate $|p|^2$. Dashed lines show the good comparison between (1) and the data.

We have repeated the experiment in the strong backscattering regime and found $e^*=e$ according to the weak/strong backscattering duality. In the weak backscattering of $v_{Bulk}=2/5=v_c$ we found Josephson frequency signatures corresponding to $e^*=e/5$ and similarly at $v_{Bulk}=2/3=v_c$ we found $e^*=e/3$. We hope these new reliable determination of the fractional charges will contribute to a better understanding of the FQHE.



III. REFERENCES

- 1 D.C. Tsui, H.L. Stormer, A.C. Gossard, , Physical Review Letters, 48, 1559 (1982)
- 2 Laughlin R. B., Phys. Rev. Lett.,50, 1395 (1983)
- 3 Clark R.G. Mallett J.R., Haynes S.R., Harris J.J. and Foxon C.T., Phys. Rev. Lett. 60, 1747 (1988)
- 4 Goldman, V. J. & Su, B.. Science 267, 1010–1012 (1995)
- 5 Saminadayar L., Glattli D. C., Jin Y., and Etienne B., Phys. Rev. Lett. 79, 2526 (1997)
- 6 de-Picciotto R, et al.. Nature 389,162-164 (1997)
- 7 Reznikov M, De Picciotto R, Griffiths TG, Heiblum M, Umansky V Nature 399,238–241 (1999)
- 8 M. Dolev, M. Heiblum, V. Umansky, Ady Stern, and D. Mahalu Nature 452 829 (2008)
- 9 Wen, X. G. Phys. Rev. B 50, 5420 (1994).
- 10 Kane, C. L. & Fisher, M. P. A. Phys. Rev. Lett. 72, 724–727 (1994).
- 11 Fendley, A., Ludwig, W. W. & Saleur, H. Phys. Rev. Lett. 75, 2196-2199 (1995)
- 12 Jain J. K., Phys. Rev. Lett.,63, 199 (1989)
- 13 Chung Y C, Heiblum M and Umansky V Phys. Rev. Lett. 91 216804 (2003)
- 14 Bid A, Ofek N, Heiblum M, Umansky V and Mahalu D , Phys. Rev. Lett. 103 236802 (2009)
- 15 Bid A., Nissim O., Inoue H. , Heiblum M., Kane C. L., Umansky V., and Mahalu D., Nature 466, 585 (2010)
- 16 Wen, X. G. Edge Phys. Rev. B 44, 5708 (1991)
- 17 MauraSasseti UlrichWeiss Bernhard Kramer, Solid State Communications 97, (1996), 605-609
- 18 Crépieux A., Devillard P., Martin T., Phys. Rev. B 69, 205302 (2004)
- 19 Ferraro D., Rech J., Jonckheere T, and Martin T., Phys. Rev. B 91 205409 (2015)
- 20 Levitov, L. S., Lee, H. & Lesovik, G. J. Math. Phys. 37, 4845–4886 (1996)
- 21 Dubois, J. et al.. Nature 502, 659–663 (2013)
- 22 Rech J., Ferraro D., Jonckheere T., Vannucci L., Sasseti M., and Martin T. Phys. Rev. Lett. 118 076801 (2017)
- 23 Arovas D., Schrieffer J. R., and Wilczek F., Phys. Rev. Lett. 53, 722 (1984)
- 24 Klitzing K. v., Dorda G., and Pepper M., Phys. Rev. Lett. 45, 494 (1980).
- 25 Moore, G. & Read, N.. Nucl. Phys. B 360, 362–396 (1991)
- 26 Josephson B. D., Phys. Lett., 1, 251 (1962).
- 27 Gaury B., Weston J., and Waintal X Nature Comm. 6524 (2015)
- 28 Lesovik G. B. and Levitov L. S., Phys. Rev. Lett. 72, 538 (1994)
- 29 Schoelkopf R., Kozhevnikov A., Prober D., and Rooks M. Phys. Rev. Lett. 80 2437 (1998)
- 30 Kozhevnikov A. A. , Schoelkopf R. J. , and Prober D. E. Phys. Rev. Lett. 84 3398 (2000)
- 31 Reydellet L.-H. , Roche P., Glattli D. C., Etienne B., and Jin Y, Phys. Rev. Lett. 90 176803 (2003)
- 32 Gabelli J. and Reulet B., Phys. Rev. Lett. 100 026601 (2008)

First-passage times in single-reset and multiple-reset discrete Markovian systems

Krzysztof Ptaszyński

Institute of Molecular Physics, Polish Academy of Sciences, M. Smoluchowskiego 17, 60-179 Poznań, Poland
e-mail address: krzysztof.ptaszynski@ifmpan.poznan.pl

I. INTRODUCTION

Fluctuations in stochastic systems can be characterized using the fixed-time or the fluctuating-time approaches¹. An example of the former is the full counting statistics², which analyzes the statistical distribution of the number of events occurring in a given time interval. In particular, the long-time full counting statistics, which assumes the time interval tending to infinity, is usually studied. To the latter group belongs the analysis of first-passage times³, i.e. time delays after which the number of events reach a defined threshold value.

It is natural to ask whether the fixed-time and fluctuating-time approaches are equivalent, or if they may provide distinct information. The previous studies of this issue were concerned with the study of the relation between the long-time full counting statistics (FCS) and the waiting time distribution (WTD), which is a special case of the first-passage time distribution for the case of unidirectional processes (such as unidirectional electron tunneling or irreversible chemical reactions). It has been shown^{4,5}, that when the renewal theory applies, i.e. the subsequent waiting times are uncorrelated, there exist exact relations between the cumulants (or, equivalently, statistical moments) of the full counting statistics and the waiting time distribution. In such a case these approaches are equivalent. The situation is different when the subsequent waiting times are correlated, and thus the renewal theory does not apply. In such a case cumulants of the full counting statistics and the waiting time distribution are independent of each other, and may provide distinct information^{6,7}. In some situations, waiting time distribution may even provide information about details of the short-time dynamics of the system which have no influence on the long-time fluctuations characterized by the full counting statistics⁷.

Here I generalize these previous studies to the case when the observed process is bidirectional. Examples of such processes are electronic transport in a small voltage regime⁸ (when the thermally-excited tunneling against the bias is possible) or bidirectional stepping of a molecular motor⁹. First-passage time is here a distribution of times after which the jump number, defined as a difference of the number of events taking place in different directions (later referred to as “forward” and “backward” processes) reaches a defined threshold value. It is shown that for a single-reset systems, i.e. ones in which after every “forward” process the system is reseted to the same state, the subsequent first-passage times are uncorrelated and there exist exact relations

between the cumulants of first-passage time distribution and the long-time full counting statistics, which generalize the ones previously derived for the case of unidirectional processes. When the subsequent first-passage times are correlated these relations do not apply any longer. In such a case full-counting statistics and the first-passage time distribution provide distinct and complementary information; for example, occurrence of the first-passage times correlations may inform about the presence of switching between different dynamical states of the system.

II. METHODS

The study focuses on classical (non-coherent) Markovian systems with a finite numbers of states. To determine the first-passage time distribution I use a modified approach of Saito and Dhar³. Dynamics of the system is described by the counting-field dependent master equation

$$\dot{\mathbf{p}}(z, t) = \mathbf{W}_z \mathbf{p}(z, t), \quad (1)$$

where z is the counting field (here a complex number), $\mathbf{p}(z, t)$ is the counting-field dependent vector of state probabilities and \mathbf{W}_z is the counting-field dependent rate matrix defined as

$$\mathbf{W}_z = \mathbf{W}_0 + z\mathbf{J}_F + \mathbf{J}_B / z, \quad (2)$$

where \mathbf{J}_F and \mathbf{J}_B are operators describing the forward and the backward processes, respectively, \mathbf{W}_0 is z -independent part of the operator (describing uncounted processes). The distribution of first-passage times τ for a defined threshold N is denoted as $F(N|\tau)$. The Laplace transform of this distribution

$$\hat{F}(N|s) = \int_0^{\infty} e^{-s\tau} F(N|\tau) d\tau, \quad (4)$$

can be calculated as¹⁰

$$\hat{F}(N|s) = \text{Tr} \left[\hat{\mathbf{T}}(0|s)^{-1} \hat{\mathbf{T}}(N|s) \mathbf{p}_{\text{in}} \right], \quad (2)$$

where \mathbf{p}_{in} is the vector of the initial state and

$$\hat{\mathbf{T}}(N|s) = \oint \frac{dz}{z^{n+1}} \frac{1}{s - \mathbf{W}_z}, \quad (5)$$

in which integration goes around the unit circle in the complex plane, is the transition matrix.

III. MAIN RESULTS

Main results of this study concern the properties of the first-passage time distribution in single-reset systems, which

are defined as systems in which every forward process reset the system to the same state. Mathematically, this indicates that the matrix \mathbf{J}_F (\mathbf{J}_B) contains non-zero elements only in a single row (column). Examples of such systems are quantum dots in the strong Coulomb blockade regime or simple enzymatic reactions. For such systems Laplace transform of the first passage time distribution is given by the equation¹⁰

$$\hat{F}(N|s) = [z_+(s)]^{-N}, \quad (6)$$

where $z_+(s)$ is larger root of the equation

$$g(z) = s, \quad (7)$$

in which $g(z)$ is the scaled cumulant generating function¹¹ (which is a dominant eigenvalue of the operator \mathbf{W}_z). Equation (6) indicates that the subsequent first-passage times are independent and identically distributed random variables. Moreover, using Eqs. (6) and (7) one can derive exact relations between cumulants (or statistical moments) of the long-time full counting statistics and the first-passage time distributions, such as¹⁰

$$\lim_{t \rightarrow \infty} \frac{\langle [\Delta n(t)]^2 \rangle}{\langle n(t) \rangle} = N \frac{\langle \Delta \tau_N^2 \rangle}{\langle \tau_N \rangle^2}, \quad (8)$$

in which $\langle [\Delta n(t)]^2 \rangle$ and $\langle n(t) \rangle$ are the variance and the mean value of the jump number after a time t , respectively, whereas $\langle \Delta \tau_N^2 \rangle$ and $\langle \tau_N \rangle$ are the variance and the mean value of the first-passage time distribution $F(N|\tau)$. These relations are generalizations of the ones previously derived for the case of unidirectional processes^{4,5}.

In multiple-reset systems, in which forward processes do not reset the system to a single state (such as Coulomb-coupled quantum dots or complex enzymatic reactions, in which one observes switching between different dynamical states of the system) the subsequent first-passage times can be correlated and the aforementioned relations do not longer hold. In this way, analysis of first-passage time distributions can provide information whether the system is a single-reset or a multiple-reset one¹⁰.

IV. UNSOLVED PROBLEMS

One of the newest results of nonequilibrium statistical physics are universal thermodynamic bounds on the minimal value of fluctuations, referred to as the thermodynamics uncertainty relations. For example, for the jump number the following relation holds¹²

$$\frac{\langle [\Delta n(t)]^2 \rangle}{\langle n(t) \rangle^2} \geq \frac{2k_B}{\langle \dot{S}_i \rangle t}, \quad (9)$$

where $\langle \dot{S}_i \rangle$ is the mean entropy production rate (the relation holds for arbitrary time t ¹²). A similar bound has been derived for the first-passage time distribution in the limit of high threshold N ¹³

$$\frac{\langle \Delta \tau_N^2 \rangle}{\langle \tau_N \rangle} \geq \frac{2k_B}{\langle \dot{S}_i \rangle}. \quad (30)$$

As follows from Eqs. (8) and (9), the same relation holds for single-reset systems also for finite (and arbitrarily small) values of the threshold N . The question arises, whether such relation can be generalized also to the case of multiple-reset systems for finite thresholds, for which Eq. (8) is no longer valid. However, due to complexity of the analytic form of the first-passage time distribution for multiple-reset systems (associated with the presence of the complex integrals in Eq. (5)), solution of this problem is a mathematically demanding task.

ACKNOWLEDGEMENTS

I thank B. R. Bułka for the valuable discussion. This work has been supported by the National Science Centre, Poland, under the project 2016/21/B/ST3/02160.

-
- ¹ M. Esposito, K. Lindenberg, I. M. Sokolov, EPL **89**, 10008 (2010).
 - ² D. A. Bagrets, Yu. V. Nazarov, Phys. Rev. B **67**, 085316 (2003).
 - ³ K. Saito, A. Dhar, EPL **114**, 50004 (2016).
 - ⁴ M. Albert, C. Flindt, M. Büttiker, Phys. Rev. Lett. **107**, 086805 (2011).
 - ⁵ A. A. Budini, Phys. Rev. E **84**, 011141 (2011).
 - ⁶ K. Ptasiński, Phys. Rev. B **95**, 045306 (2017).
 - ⁷ K. Ptasiński, Phys. Rev. B **96**, 035409 (2017).
 - ⁸ T. Fujisawa, T. Hayashi, R. Tomita, Y. Hirayama, Science **312**, 1634 (2006).
 - ⁹ M. Nishiyama, H. Higuchi, T. Yanagida, Nat. Cell Biol. **4**, 790 (2002).
 - ¹⁰ K. Ptasiński, Phys. Rev. E **97**, 012127 (2018).
 - ¹¹ H. Touchette, Phys. Rep. **478**, 1 (2009).

¹² J. M. Horowitz, T. R. Gingrich, Phys. Rev. E **96**, 020103(R) (2017).

¹³ T. R. Gingrich, J. M. Horowitz, Phys. Rev. Lett. **119**, 170601 (2017).

Light emission from noise in ac-driven contact

Hongxin Zhan,¹ Gianluca Rastelli¹ and Wolfgang Belzig¹

¹Fachbereich Physik, Universität Konstanz, D-78457 Konstanz, Germany

e-mail address: hongxin.zhan@uni-konstanz.de

e-mail address: gianluca.rastelli@uni-konstanz.de

e-mail address: wolfgang.belzig@uni-konstanz.de

I. INTRODUCTION

Classically, the current noise of a conductor is symmetrized in frequency $S(-\omega) = S(\omega)$. However, for a quantum conductor $S(-\omega) \neq S(\omega)$, which is a manifestation of the quantum nature of the current. On the other hand, light emission is related to the non-symmetrized noise¹. Thus by analyzing the noise spectrum, information about light emission can also be obtained.

II. QUANTUM VS. CLASSICAL NOISE

So far most of the research about noise concern about dc-biased system. While a few concern about zero-frequency noise, there is still a lack of the investigation about finite-frequency noise with ac drive. Here, by using the scattering matrix approach², we derive the finite frequency noise spectrum for arbitrary periodic drive,

$$S(\Omega) = \left(\frac{e}{h}\right)^2 \left\{ 2k_B T \Theta \left(\frac{\hbar\Omega}{2k_B T} \right) \sum_n T_n^2 + \sum_l \left| g_l \left(\frac{eV_{ac}}{\hbar\omega_{ac}} \right) \right|^2 \sum_n T_n (1 - T_n) \right. \\ \left. \times \left[k_B T \Theta \left(\frac{e\bar{V} + \hbar\Omega + l\hbar\omega_{ac}}{2k_B T} \right) + k_B T \Theta \left(\frac{-e\bar{V} + \hbar\Omega - l\hbar\omega_{ac}}{2k_B T} \right) \right] \right\} \quad (1)$$

where T is the temperature, T_n are the transmission coefficients, \bar{V} is the dc voltage (time-averaged), V_{ac} is the amplitude of the ac voltage, ω_{ac} is the frequency of the ac voltage and $\{g_l\}$ are the Fourier coefficients for a certain periodic drive.

For non-symmetrized noise we have

$$\Theta^{NS}(x) = x \exp(x) \operatorname{csch}(x) \quad (2)$$

while for symmetrized noise we have

$$\Theta^S(x) = x \coth(x) \quad (3)$$

In Fig. 1, zero-temperature finite-frequency noise spectra for different shape of ac voltage is plotted. By changing the amplitude or frequency of the ac drive, the noise spectrum is also changed. Unlike the dc-case, where the light emission is limited by $\hbar\Omega > -e\bar{V}$, the noise spectra for ac-case exhibit light emission even for $\hbar\Omega < -e\bar{V}$. To understand this behavior, let us look at the zero-frequency excess noise at zero temperature. For nonzero value of $eV_{ac}/\hbar\omega_{ac}$, there will always be electron-hole pairs created

by the ac pulse^{3,4}, which will contribute to the noise as plotted in Fig.2.

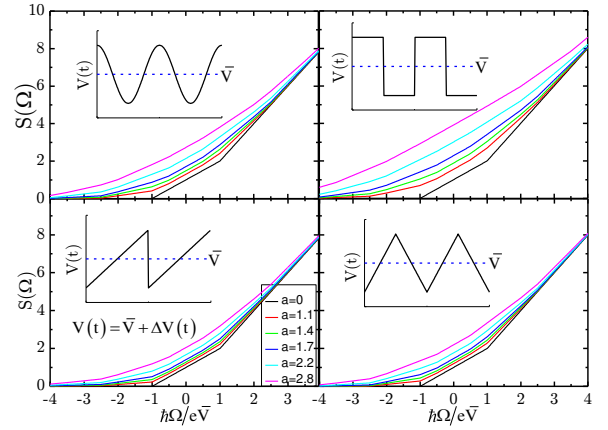


FIG. 1. Non-symmetrized noise spectrum ($T=0$) for different shape of ac voltage. The parameters are chosen as $\hbar\omega_{ac}/e\bar{V} = 1.5$ and in unit of $e\bar{V}$. Here $a = eV_{ac}/\hbar\omega_{ac}$, which is linked to the probability of electron-hole pair creation.

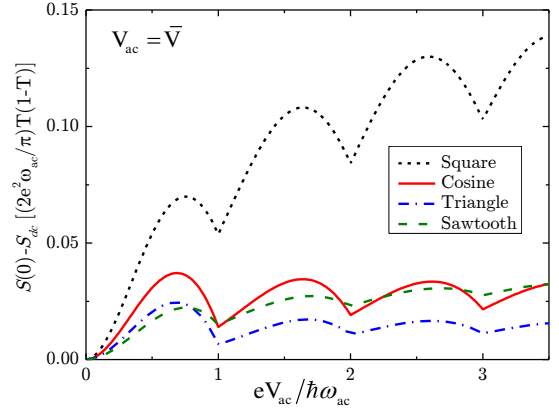


FIG. 2. Zero-frequency excess noise ($T=0$) for different shape of ac voltage. The ac amplitude and the dc offset increase simultaneously, $V_{ac} = \bar{V}$.

III. UNSOLVED PROBLEM

So far we only concern the light emission by single electrons for a coherent conductor without dissipation. One

unsolved problem is that what is the light emission condition if the conductor is coupled to a electronic environment⁵⁻⁷. In this contribution, we will present a solution by using path integrals formalism. Further open problems concern the nature of the emitted light and the effect of correlated electron tunnelin.

ACKNOWLEDGEMENTS

We acknowledges financial support by DFG through SFB 767.

- ¹ R. J. Schoelkopf , A. A. Clerk, S. M. Girvin, K. W. Lehnert and M. H. Devoret, Quantum Noise in Mesoscopic Physics (Nazarov Y.V., Dordrecht, 2003)
- ² M. H. Pedersen and M. Buttiker, Phys. Rev. B **58**, 12993 (1998).
- ³ M. Vanevic, Yu. V. Nazarov and W. Belzig, Phys. Rev. Lett **99**, 076601 (2007).
- ⁴ M. Vanevic, Yu. V. Nazarov and W. Belzig, Phys. Rev. B **78**, 245308 (2008).
- ⁵ J. Tobiska, J. Danon, I. Snyman and Yu. V. Nazarov, Phys. Rev. Lett **96**, 096801 (2006).
- ⁶ F. Xu, C. Holmqvist and W. Belzig, Phys. Rev. Lett **113**, 066801 (2014).
- ⁷ F. Xu, C. Holmqvist, G. Rastelli and W. Belzig, Phys. Rev. B **94**, 245111 (2016).

Characterizing Deviations from Poissonian and IID Statistics with Compressed Exponentials

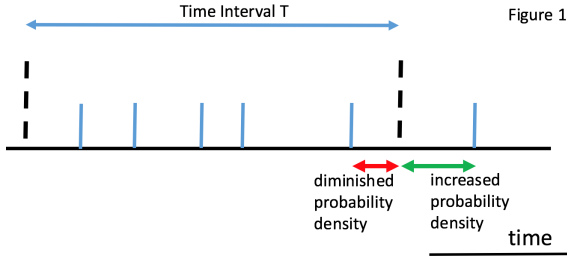
Steven Yuvan¹ and Martin Bier²

Dept. of Physics, East Carolina University, Greenville, NC 27858, USA

¹ yuvans16@students.ecu.edu

² bierm@ecu.edu

Consider a system as in Fig. 1 below. If the probability of a spike to occur in a time interval dt stays constant as time evolves, then we have a Poisson process. We next divide our time axis into subsequent intervals of width T . Here T is much larger than the average interspike time-interval. For a pure Poisson process the number of spikes in subsequent intervals should be a sequence of independent and identically distributed (IID) numbers.



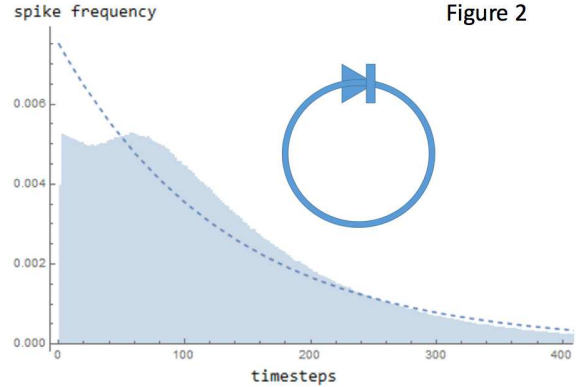
Imagine doing three draws from an IID sequence. The results are n_1 , n_2 , and n_3 . There are six ($3!$) possible ways, i.e. permutations, in which these results can be ordered. The case that $n_3 > n_2 > n_1$, i.e. two subsequent positive increments, is just one of the six possible permutations (ignoring equality) and has a probability of $1/6$. Extending this reasoning, we find that the probability of t or more subsequent increments of the same sign equals $S_p(t) = 1/(t+1)!$. $S_p(t)$ can be thought of as the probability that a sequence of subsequent increases or decreases survives for t or more intervals.

Gosper's Approximation for a factorial¹, $x! \approx \sqrt{\pi} (x/e)^x \sqrt{2x+13}$, is actually more accurate than the well-known Stirling approximation, especially for smaller values of x . In the above expression for $S_p(t)$, we take $\ln t = u$ (and thus $(t+1)! = (e^u + 1)!$). Of $\sigma_p(u) = \ln(-\ln S_p(u))$ we next take the first derivative at $u = \ln t = 0$:

$$\alpha = \sigma'_p(u=0) = \frac{d \ln(-\ln S_p(u=0))}{du} \approx \frac{2(3+13 \ln 2)}{13(\ln(208\pi/3)-4)} \approx 1.33. \quad (1)$$

This means that $S_p(t)$ should be well approximated by the compressed exponential, $S_p(t) = \exp[-(t/\tau)^\alpha]$, where τ is a constant parameter and $\alpha = 1.33$.

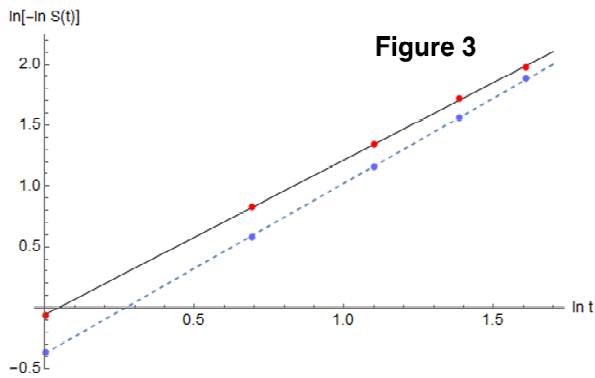
What if we slightly deviate from a Poisson process? Such deviations occur, for instance, for interspike intervals in a neuron². Right after a spike, we then first have a diminished probability (a kind of refractory time). The diminished probability is followed by an augmented probability (compared to a Poisson process) for the next spike to occur. This is indicated in the above Fig. 1 with the red and green double arrows. In this case the spike numbers in the subsequent time intervals are no longer an IID sequence. There is a memory in the sense that probability densities in interval j are affected by how far before the end of the interval $(j-1)$ the last spike occurred.



Consider particles doing 1D diffusion on the loop in Fig. 2. There is a rectifier that allows passage in the clockwise direction and blocks passage in the anticlockwise direction. We count a spike for every time a particle goes through the rectifier. With a finite number of diffusing particles on the loop, the passage of particles across the rectifier is *not* a Poisson process. The histogram in Fig. 2 shows the distribution of interpassage times for 3 particles on a loop with 20 positions where, at each timestep, each particle moves one step to the left or right (both with probability $1/2$). The dashed curve in Figure 2 indicates how the distribution would have looked if the process had been Poisson.

We next take intervals of $T = 10^5$ timesteps (cf. Fig. 1). We performed a simulation of the non-Poisson process shown in Fig. 2 with more than 1.2 billion timesteps. We recorded $S_{NP}(t)$, i.e. the number of sequences of t or more increases. Figure 3 shows the $S_p(t)$ points in blue. The dashed line is the best fit to these points. The slope of this line is 1.40 and close to the Gosper approximation. The red points and the solid line derive from $S_{NP}p(t)$. The slope of the solid line is 1.27, i.e. significantly smaller than for the Poisson case.

UPON 2018, GDANSK, JULY 9-13, 2018



Slopes of around 1.2 have been observed when subsequent increases or decreases of traded stock volumes in subsequent time intervals were followed³. Understanding how these slopes derive from the nature of the underlying nonPoisson process and how they relate to the violation of the IID condition - that is still an unsolved problem.

-
- ¹ R.W. Gosper, *Proc. Natl. Acad. Sci., USA* **75**, 40 (1978).
² G.L. Gerstein and B. Mandelbrot, *Biophys. J.* **4**, 41 (1964).
³ F.R. Brown, D. Pravica, and M. Bier, *Eur. Phys. J. B* **88**, 300 (2015).

Spectral analysis of fluctuations in humans' daily motion using location data

Gergely Vadai¹, András Antal¹ and Zoltán Gingl¹

¹ Department of Technical Informatics, University of Szeged, Szeged 6720, Hungary
e-mail address: vadaig@inf.u-szeged.hu, antal.andras@stud.u-szeged.hu, gingl@inf.u-szeged.hu

I. INTRODUCTION

The spatial and temporal patterns of human dynamics and its scale-free nature are subjects of active research in multidisciplinary fields.

The investigation of human mobility is based on the determination of location using GPS and Wi-Fi signals, phone calls, banknote dispersal or check-ins in web applications¹⁻³. After the animals wandering proved not to be a Brownian motion but Lévy-flight^{4,5}, statistical investigation of individual human trajectories and understanding the underlying dynamics came into the spotlight in the last decade. The displacements and waiting times of human dynamics follow non-Poisson statistics, however several effects like the populations heterogeneity and the motions spatial and temporal regularity make the interpretation and characterization of the observed heavy-tailed distributions more difficult. Numerous measurements and studies led to different conclusions for the scaling laws and models of mobility^{1-3,6}.

The analysis of human dynamics in time domain can be based on the measurement of activity using inertial sensors. The signals of actigraphs mounted on the human body (most often on the wrist) are useful at monitoring rest/activity cycles and in the diagnosis of sleep or several mental disorders⁷. The analysis of the daily activity patterns helped to find universal distribution laws of human behavior; the resting periods follow scale-invariant power law^{7,8}. Furthermore, over the frequency region of circadian rhythm and its harmonics, $1/f$ type noise is observable in the power spectral density of activity signals⁹.

For better understanding of human mobility, instead of the statistical approach, we have examined the temporal patterns of human dynamics and have collected the location data likewise actigraph signals. Based on the measurements we have conducted using smartphones, we have observed $1/f$ type noise over the frequency region of the daily rhythm of motion, however the inevitable measurement errors and the difficulties of the analysis of signals brought up several technical problems. Nevertheless, the scale-free nature of human behavior observed in the frequency region throws new light upon the research of mobility, from which numerous open question emerge.

II. MEASUREMENT OF LOCATION DATA

For the spectral analysis of the temporal patterns observed in humans' daily motion, we studied the displacements between two subsequent measured positions as an activity-like quantity. For this, unlike previous studies, the measurement should be uniformly sampled and its sampling frequency needed to be much higher than the used frequencies in the aforementioned studies. Furthermore, the measurement time period needed to be longer, several days or weeks long. Since the available databases' location data doesn't meet these requirements, we conducted a 3-week long measurement with 40 participants using a smartphone

application specially developed to log the users' location data. This application recorded the GPS and Wi-Fi/mobile internet signals of the user's smartphone with a sample rate of 1 measurement per minute and collected them in a server. The advantage of this solution is that, when the user is in a building or any kind of vehicle, the location data can be recorded through the Wi-Fi or mobile internet signal. However, the optimal energy usage and the operating system's application priority settings caused errors make the measurement procedure's implementation a great challenge due to the used different devices and Android versions.

III. SIGNAL PROCESSING

Because of the mentioned problems, the required long and uniformly sampled measurement is impossible without losing some data points. Furthermore, the location accuracy of the commercially available GPS modules is limited, and the measured data could also contain some false data points.

As a result, the prudent analysis of the measured data and its cleaning is definitely required. Also, the tracking of the effects of these and the exclusion of the possible artefacts is especially important in the appropriate interpretation of the results.

The salient longitude and latitude data points and displacement values, often the effect of using public transportation or travel via car, are being deleted. An important question in the course of analysis is the impact of the intervention, for example a longer travel's deletion can exclude a "big wander" which can damage the motion's Lévy-flight like nature.

Therefore, the motion of different users is being categorized by the amount of missing or deleted data points. In addition, the analysis, that is described below, has been made using different preprocessing methods and the results have been compared.

IV. SPECTRAL ANALYSIS

The Fourier analysis of the measured minutely displacement – otherwise velocity – signals is not possible directly due to the deleted or missing data points. To eliminate the problem of unevenly sampled data, we used Lomb periodogram⁹ for the analysis of the power spectral density (PSD).

In the case of 4 individuals the 3-week long measurement's data can be used in more than 95% and in the case of additional 1 user, it can be used in more than 85%. Regarding these signals, the PSD for the whole time window was similar in shape as can be seen in Fig. (1): peaks can be observed at the frequency belongs to the one-day period ($1,157 \cdot 10^{-5}$ Hz), and at its harmonics. Above this region of daily rhythm of motion, $1/f$ type noise is observable. This nature can be observed more accurately in the averaged PSDs of the three, one-week long periods of the same motion. In case of these signals, the fitting of $1/f^\alpha$ curve's α value is between 0,9 and 1,1 for the whole, weekly or daily averaged spectra and for different fitting parameters, too.

In the case of 12 individuals, data is missing at several, longer time intervals because of measurement errors or deletion of false data points. However, the remaining periods' PSD and shorter – even few-hour long – signal pieces' averaged spectra had shown the same nature in the mentioned frequency domain. The fitting curve's α value varies between 0,8 and 1,3.

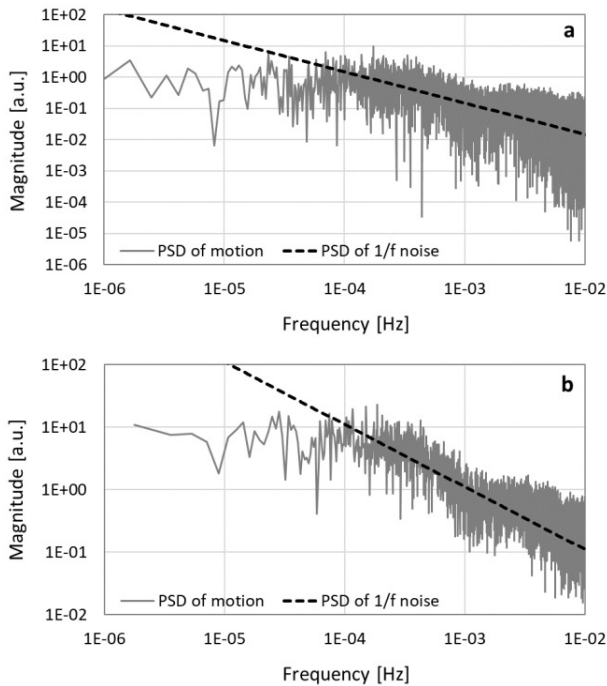


FIG. 1. Lomb periodogram of a participant's motion (displacements per 1 minute) for the whole 3-week long period (a) and averaged spectrum of 1-week long periods (b). PSD of 1/f noise is also depicted for illustration with dashed line.

However, several circumstances made the fitting required to calculate the α value more difficult: we have no information of the breakpoint's accurate value, it has been changing around the 3-hour period's frequency value depending on the user. Furthermore, because of these values and the sampling frequency, which cannot be easily incremented further due to technical issues, the noise can only be examined over 1-2 decades.

For the confirmation that this new result, the 1/f noise's presence, is due to the human behavior and not caused by the measurement process or the preprocessing, we compared the results for every user in several different manners and numerous

time windows. Neither the different deletion rules, nor the signal's under-sampling – namely resampling the signals with a lower sample rate thus eliminating the effect of missing data points – didn't show significant difference.

In the case of the 3-week long signals, "refilling" the missing data points with the last known location or the linear interpolation of the missing periods had shown us same results when we calculated the PSD from the contiguous signal's Fourier-transform. However, this method's reliability and usability brings up additional technical questions when there are several false data points.

V. OPEN PROBLEMS

Through the measurement of humans' location data and the analysis of their minutely displacement, we have observed $1/f^\alpha$ type noise over the frequency region of the daily rhythm of motion. This point of view seems to be useful in the examination of the effects of temporal regularity caused by the circadian rhythm and to characterize the random motion at higher frequencies. On the other hand, as we pointed out in the corresponding chapters, for the characterization and detailed analysis the implementation of the required large, long term, evenly sampled measurements and the appropriate preprocessing of the data remains difficult. For the better understanding of the phenomenon, the determination of the α value and the study of the different circumstances (location, regularity caused by the nature of the user's job, age etc.) more measurements are required.

However, the observed temporal universality could help in the theoretical investigation of the underlying dynamics and in the explanation of scaling laws of human activity and mobility. Our approach opens new perspective in the interpretation of Lévy-flight like motion and opens several theoretical questions in connection with the relationship between the spatial and temporal universality.

ACKNOWLEDGEMENTS

The authors thank Ferenc Lakos and Dániel Vince for their assistance making the smartphone application for the measurements. Discussions with Róbert Mingesz about measurement techniques and spectral analysis are greatly appreciated.

This research was supported by the Hungarian Government and the European Regional Development Fund under the grant number GINOP-2.3.2-15-2016-00037 ("Internet of Living Things").

- ¹ D. Brockmann, L. Hufnagel and T. Geisel, *Nature* **439**, 462–465 (2006).
- ² M. C. González, C. A. Hidalgo and A.-L. Barabási, *Nature* **453**, 779–782 (2008).
- ³ C. M. Song, T. Koren, P. Wang, et al., *Nature Physics* **6**, 818–823 (2010).
- ⁴ G. M. Viswanathan, V. Afanasyev, S. V. Buldyrev, et al., *Nature* **381**, 413–415 (1996).
- ⁵ D. W. Sims, E. J. Southall, N. E. Humphries, et al., *Nature* **451**, 1098–1102 (2008).
- ⁶ L. Alessandretti, P. Sapiezynski, S. Lehmann, et al., *PLoS ONE* **12**, e0171686 (2017).

- ⁷ T. Nakamura, K. Kiyono, K. Yoshiuchi, et al., *Physical Review Letters* **99**, 138103 (2007).
- ⁸ J. K. Ochab, J. Tyburczyk, E. Beldzik, et al *PLoS ONE* **9**, e107542 (2014).
- ⁹ N. R. Lomb, *Astrophysics and Space Science* **39**, 447–462 (1976).

Standalone cold virtual resistor? Can we cool by a linear amplifier without non-linearity, switches, or phase transition?

Jiaao Song and Laszlo B. Kish

Department of Electrical and Computer Engineering, Texas A&M University, TAMUS 3128, College Station, TX 77843-3128, USA
e-mail address: Laszlokish@tamu.edu

The thermal noise (Johnson-Nyquist noise) of resistors is due to the thermal motion of charge carriers in the sample, and it is the manifestation of Boltzmann's energy equipartition theorem. Its existence in the quantum (high-frequency/low-temperature) limit is debated [1,2] however the present paper is about its classical (low-frequency/high-temperature) limit, where there is a common agreement that the voltage noise spectrum $S_u(f)$ of a resistor is correctly given by the Johnson-Nyquist formula:

$$S_u(f) = 4kTR \quad (1)$$

The validity of Equation 1 in thermal equilibrium is guaranteed by the Second Law of Thermodynamics. Conversely, the thermal noise of a resistor at thermal equilibrium cannot be reduced without violating the Second Law, that is, without allowing perpetual motion machines to exist. Such resistor would be a cooler, it would extract heat from the circuitry it is connected to.

However, there is a high technological interest to imitate a resistor with lower absolute temperature than its environment.

This fact is indicated by a fresh patent of Linear Technology Corporation, where they utilize the shot noise of a diode to produce a nonlinear resistor that has $T/2$ noise temperature when its differential resistance is used in Equation 1.

Earlier works [4,5] produced amplifier systems utilizing negative feedback where the virtual noise-contribution of a certain resistor within the circuitry showed lowered noise temperature when the total noise of the amplifier was evaluated. However no system was produced where a standalone resistor with decreased noise temperature was emulated.

Going beyond the efforts of [4,5], we present the following unsolved problems of noise:

1. Can we construct a *linear* circuitry in a black box at physical temperature T , where the black box behaves as a linear resistor with reduced temperature of rT with $r < 1$?
2. In other words: Can we cool by a linear amplifier without non-linearity, switches, or phase transition?
3. If the answer is yes, can we go below $r = 0.5$, which is the lower limit for an ideal diode, a *nonlinear* element [3] ? Can we reach $r \ll 0.5$, and beat the Linear Technology Corporation patent [3] ?

We hope to have some answers at UPoN 2018.

REFERENCES

1. L.B. Kish, G.A. Niklasson, C.G. Granqvist, "Zero-point term and quantum effects in the Johnson noise of resistors: A critical appraisal", *J. Stat. Mech.* (2016) 054006. <http://arxiv.org/abs/1504.08229>
2. L.B. Kish, G.A. Niklasson, C.G. Granqvist, "Zero thermal noise in resistors at zero temperature", *Fluct. Noise. Lett.* **15** (2016) 1640001. Online: http://www.researchgate.net/publication/303959024_Zero_Thermal_Noise_in_Resistors_at_Zero_Temperature
3. M.T. Engelhardt (Linear Technology Corporation), "Active differential resistors with reduced noise", *US patent*, # US9866245B2, January 9, 2018.
4. K. Oide, Y. Ogawa, H. Hirakawa, "Artificial Cold Resistors", *Jpn. J. Appl. Phys.* **17** (1978) 429-432.
5. A. Pullia, R. Bassini, C. Boiano, S. Brambilla, "A "Cold" Discharge Mechanism for Low-Noise Fast Charge Amplifiers", *IEEE Trans. Nucl. Sci.* **48** (2001) 530-534.

Transport Regimes in Tunable Gold Nanoconstrictions: Proposed Solution by Low-Frequency Noise Spectroscopy

V. Handziuk¹, F. Gasparyan^{1,2}, L. Vandamme³, M. Coppola¹, V. Sydoruk¹, M. Petrychuk^{1,4}, D. Mayer¹ and S. Vitusevich^{1*}
¹Forschungszentrum Jülich, Bioelectronics (ICS-8), 52425 Jülich, Germany
e-mail address: v.handziuk@fz-juelich.de, *s.vitusevich@fz-juelich.de
²Yerevan State University, 0025 Yerevan, Armenia
e-mail address: fgaspar@ysu.am
³Eindhoven University of Technology, 5600MB Eindhoven, Netherlands
e-mail address: l.k.j.vandamme@tue.nl
⁴Taras Shevchenko National University of Kyiv, 03127 Kyiv, Ukraine
e-mail address: m.petrychuk@gmail.com

I. INTRODUCTION

Studying of nanoscale structures attracts considerable attention nowadays. The structures possess unique mechanical, chemical and electrical properties which differ from those of bulk materials. Because low-dimensional nanoscale devices are extremely sensitive to surface charges they can be applied in different scientific fields including chemical sensing and biosensing.

In conventional electronics there is a continuous tendency of shrinking down the sizes of active elements in electrical circuits. Cutting-edge technologies allow fabrication of reproducible sub-20 nm devices. However, further scaling down will inevitably lead to a breakdown of the laws of classical physics and to dominant role of quantum effects in charge transport processes. In this respect sub-nanometers objects such as molecular layers or even single molecules have to be considered as candidates for the role of functional elements. A possibility to use a single molecule as a molecular rectifier was first reported by Aviram and Ratner¹ in 1974. Nowadays applications of molecules cover a broad range of similar to semiconductor devices² including diodes, switches, etc. A huge variety of molecules and functional groups allows tailoring the molecular systems with predefined properties. Investigations of electrical properties of functional nanodevices, which could be operated in different transport regimes and whose properties can be modified by molecular layers³ or even single molecules⁴ are therefore especially important for the perspectives of applications in molecular electronics. Up to now, different approaches⁵⁻⁸ are developed for characterization of molecular systems. Techniques, based on investigation of tunable metal nanoconstrictions are essentially important because their electrical properties are mainly determined by covering layers, including molecular ones and binding geometry.

In this contribution, we present analyses of the low-frequency noise behavior of bare-gold and benzene-1,4-dithiol (BDT) modified tunable metallic nanoconstrictions. Altering cross-section of the devices allows their operation in different transport regimes: diffusive, ballistic and tunneling. Changes of the dominant transport regime are revealed to be related with a change of the characteristic power dependence of the normalized flicker noise level S_R/R^2 on the resistance R . Modification of the sample surface by organic molecules results in a decrease of the normalized flicker noise level in the ballistic regime of sample

conductance. We address this effect to an increased impact of the molecular layer to overall conductance of the system.

II. MATERIALS AND METHODS

Samples studied are fabricated on the basis of rectangular shape stainless steel pieces ($W \times L \times h = 1 \text{ cm} \times 5 \text{ cm} \times 0.25 \text{ mm}$). Fabrication procedure is performed as follows. At first substrates are cleaned in acetone and isopropanol to remove organic residuals from the surface. Then two layers of polyimide PI2611 are subsequently spin coated and hard-baked to create a passivation layer. Nanoconstriction pattern and contact pads are defined by means of e-beam lithography. Patterning is followed by metallization (5 nm of Ti and 60 nm of Au) and lift-off processes. Finally, polyimide layer is isotropically etched down to form freestanding gold nanoconstrictions. Characteristic sizes of fabricated devices in the narrowest parts are below 100 nm and can be further decreased in a controlled way.

All measurements are performed under a high vacuum (10^{-5} mbar) in a shielded environment. A homemade three point bending apparatus is used to tune the resistance of the sample in a controlled manner. Bending of the sample results in an elongation of the suspended nanoconstriction, narrowing of its cross-section and subsequent change of the resistance. Stabilization of the resistance is performed by a PC-controlled feedback system. After resistance stabilization, noise measurements are performed using homemade noise measurement setup. This setup⁹ allows precise noise measurement in the frequency range 1 Hz - 100 kHz.

III. RESULTS AND DISCUSSION

Resistance tuning procedures with following noise spectra measurements are performed for a wide range of sample resistances including regions before ($R = 10 \text{ Ohm} - 12.9 \text{ kOhm}$), during and after ($R = 12.9 \text{ kOhm} - 10 \text{ MOhm}$) breaking of the constriction. In the case of bare gold nanoconstrictions noise follows exclusively $1/f$ behavior in all investigated range of sample resistances. Normalized flicker noise power spectral density S_R/R^2 has a power dependence on the resistance, which can be described by:

UPON 2018, GDANSK, JULY 9-13, 2018

$$\frac{S_R}{R^2} \sim R^m \quad (1)$$

During the tuning process several regions with different value of the exponent m can be clearly resolved. At low resistances $m = 2$, while at higher resistances the value of the exponent decreases to $m = 1$. We attribute this effect to a change in the dominant transport regime in the nanoconstriction due to changes of the sample geometry while tuning. In fact, elongation of the gold nanoconstriction leads to shrinking down of its cross-section. When characteristic sizes of the constriction become comparable with the electron mean free path ($\lambda_e \approx 4$ nm for gold at room temperature¹⁰) the dominant mechanism of charge transport changes from diffusive to ballistic. Further elongation of the constriction results in its breaking and therefore transport is then defined by a quantum tunneling regime.

Noise spectra, measured for nanoconstrictions modified with BDT molecules demonstrate that flicker noise still remains a dominant component in noise spectra. However characteristic Lorentzian-shaped components can also be resolved. Noise behavior in diffusion and tunneling regions is similar to the one for samples without molecules. On the other hand, a pronounced difference is registered in the ballistic conductance region, where samples, modified with BDT show around one order of magnitude lower normalized flicker noise level in comparison to bare-gold structures. We explain this effect by an increased impact of the molecular conductance to overall conductance of the system in this regime.

Analytical model can be applied to describe behavior of the flicker noise in the diffusive regime of the sample conductance. For describing the flicker noise behavior of the system in ballistic and tunneling regimes we take into account changes of the nanoconstriction geometry due to elongation and Hooge's relation:

$$\frac{S_R}{R^2} = \frac{S_I}{I^2} = \frac{\alpha_H e}{\tau I} \quad (2)$$

Here α_H is the dimensionless Hooge parameter, e is the elementary charge, τ is the characteristic time and I is the current. Obtained results are summarized in Table 1.

IV. CONCLUSION

Characterization of bare-gold and benzene-1,4-dithiol modified tunable cross-section nanoconstrictions is performed using low-frequency noise spectroscopy. Normalized flicker noise level demonstrates a characteristic power dependence on the nanoconstriction resistance with the exponent reflecting the dominant transport regime in the nanostructure. Noise behavior is well described by phenomenological models, developed considering changes of the system geometry while tuning. Samples modified by BDT molecules demonstrate lower normalized flicker level in comparison to bare gold samples and an additional characteristic Lorentzian noise component. We suggest that this effect takes place due to a significant contribution of molecules to the overall conductance of the system.

Table 1. Noise behavior in tunable gold nanoconstrictions

Dominant transport regime	Approximate resistance range [Ohm]	Characteristic flicker noise behavior
Diffusive	≤ 300	$S_R / R^2 \sim R^2$
Ballistic without molecules (BR1)	3000-12900	$S_R / R^2 \sim \sqrt{R}$
Ballistic with BDT molecules (BR2)	3000-12900	$S_R / R^2 \sim R$, lower amplitude than in BR1 case
Tunneling	> 12900	$S_R / R^2 \sim R / \ln R$

ACKNOWLEDGEMENTS

Nanoconstriction devices were fabricated using the Helmholtz Nanoelectronic Facility of Forschungszentrum Jülich.

¹ A. Aviram, M.A. Ratner *Chem. Phys. Lett.* **29**, 277–283 (1974).
² D. Vuillaume *Proc. IEEE* **98**, 2111–2123 (2010).
³ S. Pud et al. *Small* **9**, 846–852 (2013).
⁴ D. Xiang et al. *Appl. Phys. Lett.* **106**, 63702 (2015).
⁵ G. Binnig and C.F. Quate *Phys. Rev. Lett.* **56**, 930–933 (1986).
⁶ J.C. Cuevas and E. Scheer. *World Scientific*, 3–6 (2010)

⁷ Y. Kim, T. Pietsch, A. Erbe, W. Belzig and Scheer, E. *Nano Lett.* **11**, 3734–3738 (2011).
⁸ C.A. Martin, D. Ding, H.S.J. Van Der Zant and J.M. Van Ruitenbeek *New J. Phys.* **10**, (2008).
⁹ S. Vitusevich et al. *Appl. Phys. Lett.* **80**, 2126 (2002).
¹⁰ Agraït, A.L. Yeyati and van J.M. Ruitenbeek *Phys. Rep.* **377**, 81–279 (2003).

Supercapacitor's temperature fluctuations during charging/discharging processes

Stanisław Galla, Łukasz Lentka, Arkadiusz Szewczyk
Gdańsk University of Technology, Faculty of Electronics, Telecommunications and Informatics,
Department of Metrology and Optoelectronics,
ul. G. Narutowicza 11/12, 80-233, Gdańsk, Poland
e-mail address: galla@eti.pg.edu.pl, lukasz.lentka@gmail.com, szewczyk@eti.pg.edu.pl

I. INTRODUCTION

Characterization of various elements and devices by using thermographic imaging is currently used in many fields. This method is very attractive because of non-destructive character. The method is usually limited to consider temperature distribution in the investigated object. Our experimental studies present measurement results of fluctuations of temperature in supercapacitors cells which should shed light on aging processes in their structures. The specimens were continuously charged and discharged. Their temperature exhibit some distribution over the investigated area. Moreover, their temperature changes when charged or discharge because of energy emission or consumption. Any information about temperature distribution is crucial for their aging pace because even relatively small increase of temperature can accelerate strongly supercapacitors deterioration. Thus, in our studies we focus on accuracy of the measurements and identification of eventual local overheating. The proposed measurement method bases on use of thermographic measurements only. This method is characterized by lower accuracy in determining temperature than the calorimetric methods, described elsewhere [1, 2]. The applied method can be easily used because of application of thermal camera and relatively simple way of temperature stabilization. Moreover, the camera can give accurate information about temperature distribution on the surface of the monitored objects and what is more, by analysing its fluctuations, we can conclude the conditions of the tested specimen. The camera utilizes a phenomenon of electromagnetic waves radiation in infrared region as described, among others, in [3, 4, 5]. Thermographic measurements require considering various factors that may have an impact on the recorded fluctuations which result not only from different types of inhomeogeneities present in the tested structures but also manifest physical properties of the used materials and moreover its encasement. The tested specimens are complex structures, comprising of two metal electrodes of rectangle shape enabling charge flow between the terminals. The electrodes are covered by carbon layer preserving the charge inside the pores. The space between the electrodes is filled with the electrolyte and the separator. Current flowing between the terminals is distributed over the rectangle metal plate and the emitted heat depends on the resistance of the carbon layer and the resistance of the contact between the metal plate and the carbon layer. The structure was sealed in a pouch protecting against humidity interacting with the used electrolyte. In our studies we present a description of the prepared set-up and the algorithm used to estimate statistical parameters of the observed temperature fluctuations in the tested samples.

II. MEASUREMENT SET-UP

Fig. (1) presents a schematic diagram of the applied measurement system [6]. A thermal imaging camera, the model VIGOcam v.50 (1), was used. Basic parameters of this camera are given in [7].

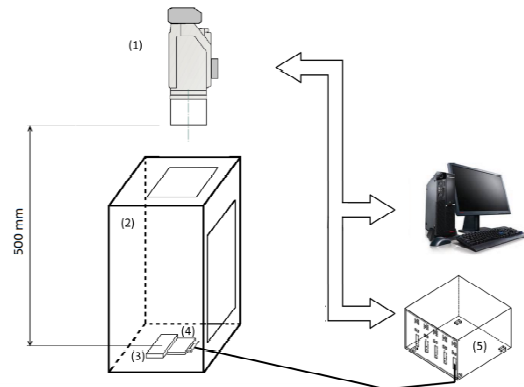


Fig. 1. Schematic diagram of the applied measurement set-up

The samples (4) were protected against eventual influence of external temperature variations by additional enclosure protecting against air flows (2). Repeated charging/discharging of the tested specimen was controlled by the Atlas - Solitech (5) power supply unit. and measurement module was used (performing both the power and measurement functions, allowing for registration of the current conditions of the conducted test.) Additionally, a reference (background) temperature (3) was introduced into the camera observation field (1). The stable object having a background temperature was a ceramic plate of relatively huge volume securing high thermal inertia. That approach, however, does not provide full protection from the changes of temperature induced by external interferences. Additionally, the applied camera has its inherent noise visible as the recorded temperature fluctuations (e.g. about 0.065°C at the temperature of 30°C). Surface of the tested specimen (4) was painted with a graphite painting to avoid any reflections inducing additional errors [8]. The analysis of the recorded data was carried out by using the algorithm presented in [6]. Selected statistical parameters (power spectral density, variance, skewness and kurtosis) were estimated to assess the state of the specimen and its correlation to aging processes.

III. MEASUREMENT RESULTS

Fig.(2) shows a diagram of the recorded temperature changes ΔT during the carried tests, together with a curve of the voltage between the terminals during charging (2.7 V at current

290 mA) and discharging. The temperature increases slowly due to heating up because of repeated charging/discharging. Moreover, we observe some temperature fluctuations because there are different processes during discharging and charging. Some dissipate energy when other take energy. Fig. (3) presents variance of temperature over the scanned area of the discharged specimen at the beginning of the experiment, at time 0 s. Observed noise is uniformly distributed and results mainly from inherent noise of the camera. The picture can't even identify the shape of the investigated pouch.

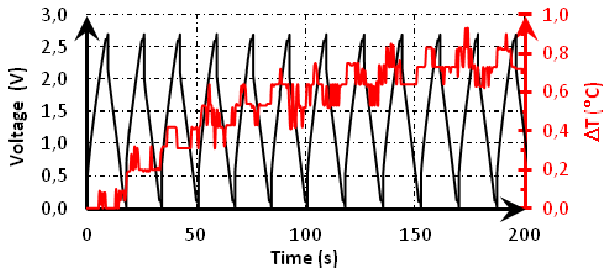


Fig. 2. Temperature changes of the surface of the tested specimen observed during repeated charging/discharging process

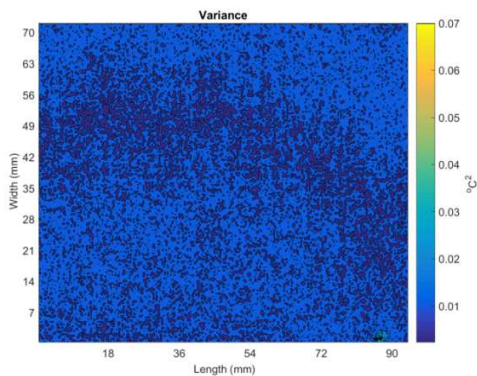


Fig. 3. Variance of temperature across the surface of the tested supercapacitors at the beginning of the experiment before starting charging/discharging process

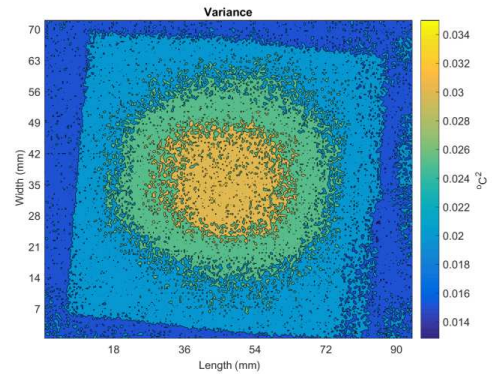


Fig. 4. Variance of temperature across the surface of the tested supercapacitors during the experiment, at 173 s of the experiment, during continuous charging/discharging process

IV. CONCLUSIONS

Observed temperature fluctuations shed light on processes of energy dissipation during discharging and energy consumption during charging of the investigated supercapacitors. We were able to identify eventual inhomogeneity within their structures, especially at vicinity of the specimen's terminals. Some excessive heating was observed within central area of the pouch and resulted in delamination processes of the carbon electrode from the metal collector, when the specimen was dismantled after the experiment. We can claim that intensity of the observed temperature fluctuations is correlated with aging processes and therefore interesting for further and more in-depth analysis. The presented set-up can be used to measure temperature distribution over the specimen area and to evaluate its selected statistical parameters. We may suppose that this method has a strong potential impact when the camera is replaced by temperature sensor monitoring temperature fluctuations in the most fragile parts of the working supercapacitor.

V. REFERENCES

1. Pascot, C.; Dandeville, Y.; Scudeller, Y.; Guillemet, P.; Brousse, T. Calorimetric measurement of the heat generated by a Double-Layer Capacitor cell under cycling. *Thermochim. Acta* **2010**, *510*, 53–60, doi:10.1016/j.tca.2010.06.022.
2. Guillemet, P.; Pascot, C.; Scudeller, Y. Electro-thermal analysis of Electric Double-Layer-Capacitors. In *2008 14th International Workshop on Thermal Investigation of ICs and Systems*; 2008; pp. 224–228.
3. Vollmer, M.; Mollmann, K.-P. *Infrared Thermal Imaging: Fundamentals, Research and Applications*; John Wiley & Sons, 2010; ISBN 978-3-527-40717-0.
4. Živčák, J.; Hudák, R.; Madarász, L.; Rudas, I. J. *Methodology, Models and Algorithms in Thermographic Diagnostics*; Springer Science & Business Media, 2013; ISBN 978-3-642-38379-3.
5. Diakides, M.; Bronzino, J. D.; Peterson, D. R. *Medical Infrared Imaging: Principles and Practices*; CRC Press, 2012; ISBN 978-1-4398-7249-9.
6. Galla, S. A Thermographic Measurement Approach to Assess Supercapacitor Electrical Performances. *Appl. Sci.* **2017**, *7*, 1247, doi:10.3390/app7121247.
7. VIGOCamv50.pdf. Available online <https://www.vigo.com.pl/pub/File/PRODUKTY/Thermal-imaging-system/v50.pdf>
8. Graphit 33.pdf. Available online <https://www.rapidonline.com/pdf/87-0695.pdf>

Effect of intrinsic noise on Chimera states in coupled Kuramoto ensembles: Towards constructing the perturbation theory for the Ott-Antonsen theory

Irina V. Tyulkina¹, Lyudmila S. Klimenko², Denis S. Goldobin³, and Arkady Pikovsky⁴

¹ *Department of Theoretical Physics, Perm State University, Bukireva street 15, 614990 Perm, Russia*
e-mail address: irinatiulkina95@gmail.com

² *Institute of Continuous Media Mechanics UB RAS, Ak. Koroleva street 1, 614013 Perm, Russia*
e-mail address: lyudmilaklimenko@gmail.com

³ *Institute of Continuous Media Mechanics UB RAS, Ak. Koroleva street 1, 614013 Perm, Russia*
e-mail address: denis.goldobin@gmail.com

⁴ *Institute for Physics and Astronomy, University of Potsdam, Karl-Liebknecht-Strasse 24/25, 14476 Potsdam-Golm, Germany*
e-mail address: pikovsky@uni-potsdam.de

I. INTRODUCTION

For ensembles of N phase oscillators obeying equations of the form

$$\dot{\varphi}_k = \Omega(t) + \text{Im}(2h(t)e^{-i\varphi_k}), \quad (1)$$

where φ_k is the phase of the k -th oscillator, instantaneous natural frequency $\Omega(t)$ and $h(t)$ are arbitrary functions of time, the theories of Watanabe-Strogatz and Ott-Antonsen were developed¹⁻⁴. According to the W-S theory, the dynamics of the ensemble possesses $N-3$ integrals of motion, where N is the number of oscillators, and has a very low dimension; it is determined by a single first order ODE for a complex variable. For ensembles of oscillators, such properties of the dynamics allow obtaining a self-contained equation for the dynamics of the order parameter even when the oscillators (their natural frequencies) are nonidentical. In the thermodynamic limit $N \rightarrow \infty$, this integrability of dynamics can be readily shown for the probability density of states $w(\varphi_k, t)$ (O-A theory); in Fourier space,

$$w(\varphi_k, t) = (2\pi)^{-1} [1 + \sum_{n=1}^{\infty} (a_n e^{-in\varphi_k} + c.c.)]$$

and the Fokker-Planck equation yields

$$\dot{a}_n = in\Omega a_n + nh(t)a_{n-1} - nh^*(t)a_{n+1}, \quad (2)$$

where $a_0 = 1$. Eq. (2) admits the particular solutions of the form $a_n = a_1^n$, where $a_1(t)$ obeys

$$\dot{a}_1 = i\Omega a_1 + h(t) - h^*(t)a_1^2. \quad (3)$$

These solutions form so-called Ott-Antonsen manifold; this manifold was demonstrated to be attracting in the realistic case of vanishingly small but nonzero nonidentity of oscillators. Notice, $a_1(t) = \langle \exp(i\varphi_k) \rangle$ is the complex order parameter.

With the model reduction (3), one can rigorously address highly sophisticated and challenging problems and gain deeper insight into some complex phenomena; such as, e.g., interplay of synchronizing effect by common noise and desynchronizing coupling^{5,6}. Employment of W-S and O-A approaches yielded significant advance in understanding many problems in physics and self-organization theory (e.g., Refs.¹⁻⁸).

Construction of the perturbation theory for Watanabe-Strogatz and Ott-Antonsen approaches for ensembles with weak violation

of form (1) is of interest, but turns out to be problematic for the general case⁹. In particular, a straightforward modification of W-S approach yields results which diverges where the basic state is close to the perfect synchrony, while this case is of primary interest for practical problems. Additional essential difficulty is rooted in the fact that the dynamics of the order parameter in system (1) for identical oscillators can be rich, but the mutual positioning of oscillators and their clustering remain frozen. A weak deviation from the form (1) can lead to merging of clusters or self-organized splitting into new clusters. Thus, the dynamics of the ensemble is not merely the dynamics of order parameters for clusters anymore, but also the dynamics of clustering; the number of clusters and their order parameters may vary with time. The reduction of such a dynamics to the unperturbed dynamics described by Ott and Antonsen is impossible.

II. THE CASE OF INTRINSIC NOISE

Particular cases of the deviation from the form (1) can be of interest. Such is the case of the ensemble of oscillators with intrinsic noise:

$$\dot{\varphi}_k = \Omega_k + \text{Im}(2h(t)e^{-i\varphi_k}) + \varepsilon \zeta_k(t), \quad (4)$$

where ε is the intrinsic noise strength, $\zeta_k(t)$ is the normalized individual intrinsic noise signal;

$$\langle \zeta_k(t) \zeta_l(t') \rangle = 2\delta_{kl} \delta(t-t').$$

For the case of small but nonzero intrinsic noise, one can show that the one-cluster solution which is an heir of the Ott-Antonsen solution becomes globally attracting. Thus, one can construct the perturbation theory for the vicinity of the Ott-Antonsen manifold; if the initial state is a multi-cluster one, all clusters merge and one can focus on describing the dynamics of a single-cluster state.

A self-contained description of the dynamics of the order parameter $a_1 = \langle \exp(i\varphi_k) \rangle$ requires accounting for the dynamics of parameter $q = \langle \exp(i2\varphi_k) \rangle - a_1^2$, which turns to zero for the single-cluster states on the O-A manifold and quantifies deviation from this manifold. For a and q , one can derive the reduced equations:

$$\begin{aligned} \dot{a}_1 &= i\Omega a_1 - (\gamma + \varepsilon^2)a_1 + h - h^*(a_1^2 + q), \\ \dot{q} &= (i2\Omega - 2\gamma - 4h^*a_1)q - 2\varepsilon^2 a_1^2 - 4\varepsilon^2 q, \end{aligned} \quad (5)$$

where Ω : mean natural frequency, γ : half-width of the frequency distribution (in the case of the Lorentzian distribution).

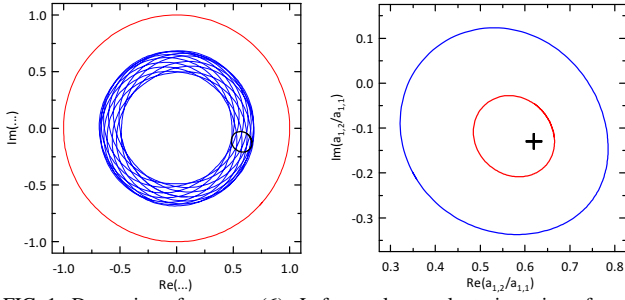


FIG. 1. Dynamics of system (6). Left panel: sample trajectories of $a_{1,1}$ (red), $a_{1,2}$ (blue), $a_{1,2}/a_{1,1}$ (black). Right panel: one-cluster Chimera states for $\alpha = \pi/2 - 0.1$, $A = 0.25$ (black cross), 0.28 (red line), 0.30 (blue line).

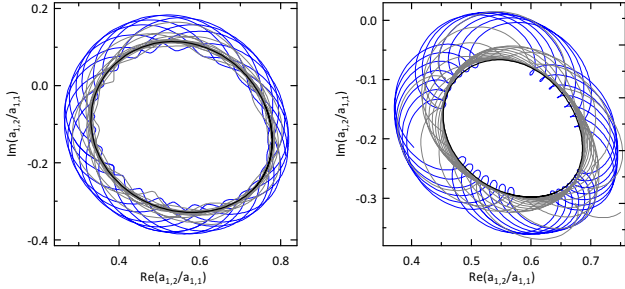


FIG. 2. Dynamics of two-cluster states in system (6) with/w.o. noise for $\varepsilon = 0.01$, $A = 0.3$, $\alpha = \pi/2 - 0.10$ (left) and $\alpha = \pi/2 - 0.15$ (right). Blue: no noise, gray: transient dynamics with noise, black: attractor with noise.

III. CHIMERA STATES IN COUPLED KURAMOTO ENSEMBLES

Eqs. (5) can be utilized for the study of the impact of intrinsic noise on Chimera states in two coupled Kuramoto ensembles:

$$\dot{\varphi}_{s,k} = \omega + \sum_{r=1}^2 K_{sr} N_r^{-1} \sum_{j=1}^{N_r} \sin(\varphi_{r,j} - \varphi_{s,k} - \alpha), \quad (6)$$

where $s = 1, 2$, N_s is the number of oscillators in ensemble s , and coupling coefficients $K_{11} = K_{22} = (1 + A)/2$ and $K_{12} = K_{21} = (1 - A)/2$. Abrams *et al.*⁷ reported for (6) stable Chimera states, where one of the subensembles is perfectly synchronized, $|a_{1,1}| = 1$ (here $a_{1,s} = \langle \exp(i\varphi_{s,k}) \rangle$), while the oscillators of the other subensemble form a breathing cluster—order parameter $a_{1,2}$ oscillates periodically or quasiperiodically (Fig. 1). Later on, regimes with several breathing clusters in the second subensemble were reported⁸, with a higher embedding dimension of dynamics (blue trajectories in Fig. 2).

As expected, intrinsic noise introduces effective dissipation in the system dynamics (Fig. 2). For initial two-cluster states, clusters merge in one, and the dynamics of the resulting cluster is in good agreement with approximation (5), which yields for Eq. (6) with intrinsic noise the following equation system:

$$\begin{aligned} \dot{a}_{1,1} &= (i\Omega - \varepsilon^2)a_{1,1} + h_1 - h_1^*(a_{1,1}^2 + q_1), \\ \dot{q}_1 &= (i2\Omega - 4\varepsilon^2 - 4h_1^*a_{1,1})q_1 - 2\varepsilon^2 a_{1,1}^2, \\ \dot{a}_{1,2} &= (i\Omega - \varepsilon^2)a_{1,2} + h_2 - h_2^*(a_{1,2}^2 + q_2), \\ \dot{q}_2 &= (i2\Omega - 4\varepsilon^2 - 4h_2^*a_{1,2})q_2 - 2\varepsilon^2 a_{1,2}^2, \end{aligned} \quad (7)$$

where $h_s = 0.5(K_{s1}a_{1,1} + K_{s2}a_{1,2})e^{-i\alpha}$.

Consideration of the effect of the intrinsic noise on Chimera states in coupled Kuramoto ensembles suggests that one can introduce an analog of cumulants for phases— κ_m defined as

$$\sum_{m=1}^{\infty} \kappa_m k^m / m! \equiv \Phi(k) = \ln \left(\sum_{m=0}^{\infty} a_m k^m / m! \right)$$

—and reformulate the dynamics of the probability density in terms of these cumulants. Approximation (5) turns out to be the second-term truncation of cumulant expansion. Analysis of the case of intrinsic noise revealed that, in terms of these cumulants, one can construct a perturbation theory with good convergence properties and “transparent” interpretation of results. This theory is not restricted to the case of intrinsic noise.

IV. OPEN QUESTIONS AND UNSOLVED PROBLEMS

- The relationship between the “cumulants” and the Watanabe-Strogatz variables requires further understanding.
- Fruitfulness of the cumulant approach for construction of the perturbation theory for the general case of violation of the equation properties required by the W-S and O-A approaches remains questionable (especially, where clustering dynamics comes into play).
- The cumulant approach turns out to be useful for analytical studies, but numerical simulation requires truncation of expansion. While the second-order truncation (5) is always stable, the plain higher-order truncations result in numerical instability (for some systems this instability appears for any order of truncation above 2). Can it be handled by proper truncation? (Without this instability, one can use 10-order truncation, where Eq. (2) requires several hundreds of terms).

ACKNOWLEDGEMENTS

L.S.K. and D.S.G. were supported by the Russian Science Foundation (Grant No. 14-12-00090).

¹ S. Watanabe and S. H. Strogatz, *Physica* **74D**, 197 (1994).
² E. Ott and T. M. Antonsen, *Chaos* **18**, 037113 (2008).
³ A. Pikovsky and M. Rosenblum, *Phys. Rev. Lett.* **101**, 2264103 (2008).
⁴ S. A. Marvel, R. E. Mirollo, and S. H. Strogatz, *CHAOS* **19**, 043104 (2009).
⁵ A. V. Pimenova, D. S. Goldobin, M. Rosenblum, and A. Pikovsky, *Sci. Rep.* **6**, 38518 (2016).

⁶ D. S. Goldobin, A. V. Pimenova, M. Rosenblum, and A. Pikovsky, *Eur. Phys. J. ST* **226**, 1921 (2017).
⁷ D. M. Abrams, R. Mirollo, S. H. Strogatz, and D. A. Wiley, *Phys. Rev. Lett.* **101**, 084103 (2008).
⁸ A. Pikovsky and M. Rosenblum, *Physica D* **238**, 27 (2009).
⁹ V. Vlasov, M. Rosenblum, and A. Pikovsky, *J. Phys. A: Math. Theor.* **49**, 31LT02 (2016).

White noise as a model of harmonic input for billiard-like systems

Alexander Dubkov¹, Olga Chichigina² and Alexandra Krasnova³

¹ Radiophysical Department, Lobachevsky State University, Russia
e-mail address: dubkov@rf.unn.ru

² Faculty of Physics and International Laser Center, Lomonosov Moscow State University, Russia
e-mail address: chichigina@ilc.edu.ru

³ Institute of Physics of the Earth, Russian Academy of Sciences, Moscow, Russia
e-mail address: krasnova@physics.msu.ru

I. INTRODUCTION

Many dynamical systems have their own chaotic properties; therefore, the result of even a periodical external input can be equivalent to the white noise excitation. Because all correlations of the external signal are destroyed by chaotic dynamics of a system, the periodical input can be modeled as a white noise source of corresponding intensity. The questions arise: (1) how the intensity of the white noise in the model depends on amplitude of periodic input and (2) does the period of input influence the white noise properties?

To answer such fundamental questions the simplest chaotic system is useful. The billiard is a system where non-interacting point particles (or one particle) in free motion undergo elastic collisions with a set of fixed scatterers. Dispersing Sinai billiards (Fig. 1) satisfy the following strong chaotic properties^{1,2,3}: a) the Central Limit Theorem holds; b) correlations decay exponentially; c) the particle flow is ergodic with mixing. We consider billiard with finite space, therefore coordinates distribution is homogeneous and velocity distribution is the same for all regions of billiard.

When the boundary of the scatterers is oscillating, the particle undergoes both head-on and head-tail collisions. The particle gains the velocity ($\Delta v_n > 0$) in the former case, and loses it ($\Delta v_n < 0$) in the latter case. This process is related to the linear increase of mean velocity of a particle in periodically or randomly forced billiards systems and known as Fermi acceleration^{4,5}.

The Fermi acceleration model can be used for an approximate estimation of the diffusion coefficient of adatoms, moving on the surface of fluctuating island⁶. Also the Fermi acceleration mechanism is useful for explanation of extremely fast diffusion of mass-selected golden clusters deposited on graphite⁷. This model gives a resolution of the contradiction between extremely large diffusion coefficient and its dependence on temperature according to Arrhenius law⁸.

The correlations of particle velocity at different collisions are considered for calculation of the kinetic coefficients in Fokker-Planck equation and definition of work in thermodynamic approach.

II. CONDITIONS OF INDEPENDENCE ON PERIOD OF HARMONIC INPUT

We consider billiards with fixed mean free path λ that is given by the expression

$$\lambda = \frac{\pi\Omega}{P},$$

where: Ω is the area of accessible billiard region, and P is the scatterers perimeter.

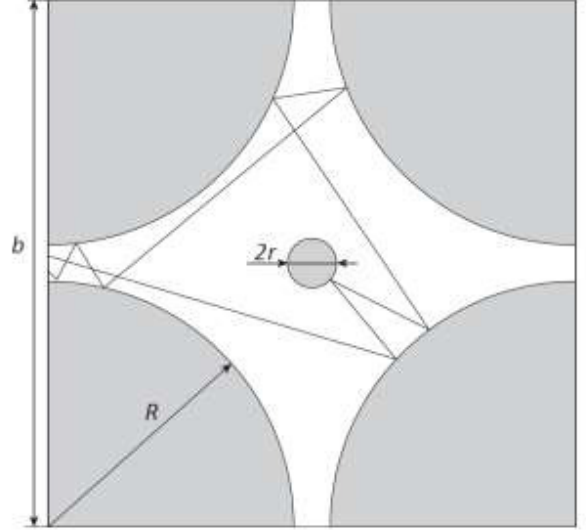


Fig. 1 Sell of Lorentz gas is an example of dispersing billiard

Let the boundary be perturbed by a regular way with the period T ($u(t+T) = u(t)$) and amplitude of velocity u_0 . In general case, Fermi acceleration dependence on T is nontrivial. If $T \ll \lambda/v_0$ (the period is much less than the time of free path) the particle acceleration is exactly the same as it is for the case of stochastic oscillations of scatterers. This case cannot be considered as quasi-stable, because the particle accelerates the time of free path decrease and finally it reaches the value T . If $T \approx \lambda/v_0$, some long-time correlations are possible. If $T \approx \lambda/u_0$ the principle of local equilibrium is broken and the process is not quasi-stable, since the replacement of scatterers boundary is of the same order as the mean free path. As a result,

the thermodynamic interpretation and independence on the period are possible only under condition

$$\frac{\lambda}{v_0} \ll T \ll \frac{\lambda}{u_0}. \quad (1)$$

This approximation of high velocities of the particle means that the mean free time is much less than the period of scatterers oscillations. The correlation time is proved to be less than the period. Therefore the dynamics of particle velocity is Markov process with the step $\tau = T$.

We prove analytically and numerically that coefficients in Fokker-Plank equation and, correspondingly, Fermi acceleration are independent of period under condition (1). Fig. 2 shows Fermi acceleration versus the period of scatterers oscillation for different amplitudes of the oscillations. Horizontal lines represent the analytical calculations and points represent results of numerical calculations. That means precise definition of corresponding white noise intensity in stochastic differential equation following from the Fokker-Plank equation. We also investigate numerically dependence of the acceleration on the period when the last is out of this interval.

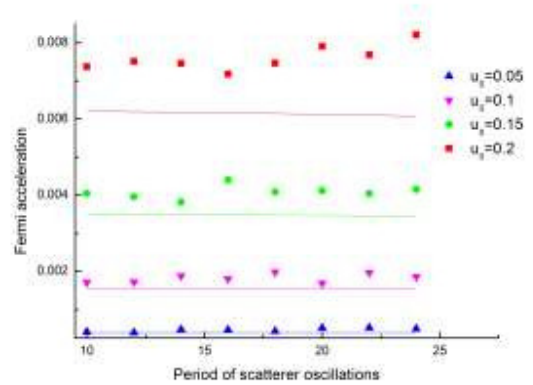


Fig. 2 Dependence of the Fermi acceleration on the period of scatterers oscillation.

Unsolved problems are following:

What kind of analytical mode can present the dependence of noise intensity on the period of harmonic input, when condition (1) is not fulfilled?

How can we generalize the results obtained for billiard-like system for other chaotic systems driven by periodical inputs?

ACKNOWLEDGEMENTS

The authors acknowledge the support of the Russian Science Foundation (Grant No. 16-12-10496).

-
- ¹ L.A. Bunimovich, and Ya.G. Sinai, *Commun. Math. Phys.* **78**, 479 (1981).
 - ² L.A. Bunimovich, *Hard Ball Systems and the Lorentz Gas* (Springer, Berlin, 2000).
 - ³ N. Chernov, *J. Stat. Phys.*, **94**, 513 (1999).
 - ⁴ E. Fermi, *Phys. Rev.*, **75**, 1169 (1949)
 - ⁵ S.M. Ulam, *4th Berkeley Symp. on Math. Stat. and Probability* (University of California Press, 1961)
 - ⁶ L.S. Bulushova, O.A. Chichigina, *Moscow University Physics Bulletin*, **65**, 99 (2010).
 - ⁷ L. Bardotti, F. Tournus, P. Mrelinon, M. Pellarin, and M. Broyer, *Phys. Rev. B*, **83**, 035425 (2011).
 - ⁸ A.K. Krasnova and O.A. Chichigina, *Moscow University Physics Bulletin*, **67**, 48 (2012).

Noise Robustness Analysis and Experimental Implementation of the Coupling Function Secure Communications Protocol

Gorjan Nadzinski^{1,2}, Matej Dobrevski¹, Christopher Anderson³, Peter V. E. McClintock⁴, Aneta Stefanovska⁴, Mile Stankovski¹, Tomislav Stankovski^{4,5}

¹Faculty of Electrical Engineering and IT, Ss. Cyril and Methodius University, Skopje, Macedonia

²e-mail address: gorjan@feit.ukim.edu.mk

³DefiX, Greater Manchester, United Kingdom

⁴Department of Physics, Lancaster University, Lancaster, United Kingdom

⁵Faculty of Medicine, Ss. Cyril and Methodius University, Skopje, Macedonia

I. INTRODUCTION

The increasing need for security and noise robustness of communications has led to new protocols, implementing a variety of different mathematical or logical approaches in order to achieve secure communication. To be useful, such schemes must be resistant to noise and other external perturbations (both malicious and random). Additionally, these protocols must be able to run efficiently in real-time noisy environments, and often on low-cost devices suitable for widespread general use, despite their typical complexity due to the convoluted procedures they employ to achieve security. Thus, not only conceptual and theoretical design, but also practical development and implementation of such communication protocols are necessary.

The hitherto unsolved problem we address in our presentation is whether or not a recently proposed protocol¹, based on the coupling functions² between dynamical systems, works as successfully when implemented in hardware as a real physical system as it does in theory and numerical simulations^{1,3}. We thereby evaluate the robustness and encryption effectiveness of the scheme in the face of actual analog channel noise, thereby testing the potential utility of the new encryption method.

A second question was whether commercially available low-cost devices can support the physical demands of the new communications protocol. Therefore, the transmitter and receiver for communications tests were each implemented on a separate single-board Raspberry Pi 2 computer.

II. EXPERIMENTAL IMPLEMENTATION OF THE COUPLING FUNCTIONS COMMUNICATION PROTOCOL

The experimental implementation of the system is illustrated in Fig. (1). The system first encrypts the information carrying (in this case binary) signals s_i as time-variable parameters of non-linear

coupling functions between two dynamical systems x and y , as shown in Eqs. (1) and (2).

$$\dot{x}_1 = 10x_2 - 10x_1 + s_1(t) \cos(y_1)x_2 + s_2(t)x_1y_2 / y_3 \quad (1)$$

$$\dot{x}_2 = 28x_1 - x_1x_3 - x_2$$

$$\dot{x}_3 = x_1x_2 - 2.67x_3$$

$$\dot{y}_1 = 10y_2 - 10y_1 \quad (2)$$

$$\dot{y}_2 = 28y_1 - y_1y_3 - y_2$$

$$\dot{y}_3 = y_1y_2 - 2.67y_3$$

This process results in a complicated and nonlinear scrambling of the information. The dynamical systems used during the experiment are chaotic Lorenz systems, which are known to be widely used for secure communications⁴ because they provide additional complexity and security for the data encryption process.

One signal from each of the systems is then sent in its analog form (in this case x_1 and y_2). Channel noise is replicated by adding analog white noise to the encrypted signals. The noise is generated in MATLAB and produced with a 100 KHz sampling frequency computer audio card. Since measurement noise and other electronic perturbations and disturbances are inevitable during the experiment, it can be considered that the conditions are close to those of many real world communication applications. During the communication, handshake signals indicating readiness to send/receive data are used to avoid synchronization errors.

These noisy signals are then digitized at the receiver, where they enslave and completely synchronize⁵ two similar coupled systems u and w (Eqs. (3) and (4)), before they are decrypted using dynamical Bayesian inference^{2,6}.

The main advantages of this approach are the unbounded number of possible choices for the forms of the linearly independent coupling functions (which provides a powerful encryption scheme), and the effective separation between the deterministic information and the channel noise perturbations

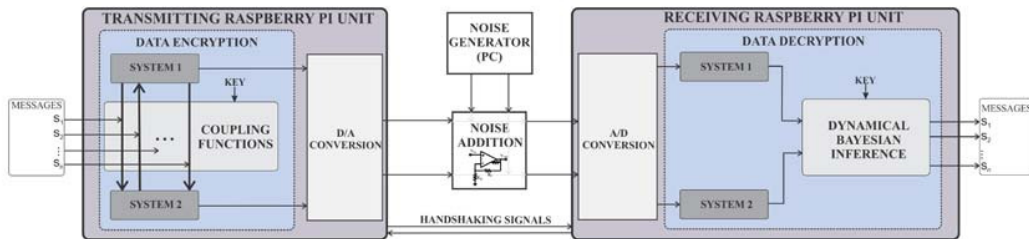


FIG. 1. A schematic diagram showing the experimental implementation of the coupling functions communication protocol.

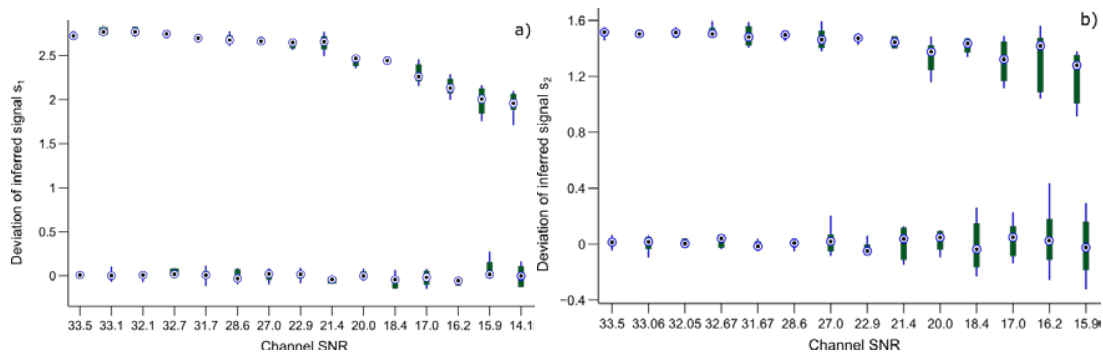


FIG. 2. Deviations of the decrypted signals s_1 (a) and s_2 (b) from their initial binary states shown as functions of the SNR level in the communication channel. Note: Binary {1} for s_1 is 2.7 and binary {1} for s_2 is 1.5.

achieved by the inherently stochastic dynamical Bayesian inference approach (which results in increased noise robustness).

$$u_1 = x_1 \quad (3)$$

$$\dot{u}_2 = 28x_1 - x_1u_3 - u_2$$

$$\dot{u}_3 = x_1u_2 - 2.67u_3$$

$$\dot{w}_1 = 10y_2 - 10w_1 \quad (4)$$

$$w_2 = y_2$$

$$\dot{w}_3 = w_1y_2 - 2.67w_3$$

III. ANALYSIS

The robustness of the protocol was examined for different levels of channel noise by systematically increasing the noise strength while encrypting, sending, and decrypting randomly generated data bits, which resulted in different levels of the signal-to-noise ratio (SNR). The deviations of the binary values of the decrypted signals $s_1(t)$ and $s_2(t)$ as functions of the SNR in the channel are shown in Fig. (2), plotted as compact boxplots which show the median, quartiles, maximum, and minimum. For small noise (higher SNR), the distributions are compressed around their median values for binary ones and zeros. For higher noise (lower SNR), the distributions become wider and even start overlapping, which means that binary one and binary zero cannot be clearly separated and the bit-error-rate (BER) has become nonzero.

The experiment was performed up to values of around 15 dB for the SNR, after which it became impossible because of resolution and precision limitations. While the numerical simulations in theory obtained a much lower threshold of 4 dB², the experimental setup increased it up to a more realistic value: finite BER for $s_2(t)$ appears around SNR = 15 dB. In practice, this

is a relatively high noise level, especially compared to standard SNR thresholds for BER appearance which are around 15 dB for wireless and 40 dB for wireline communication⁷.

Furthermore, the coupling function protocol was also compared with the signal masking protocol⁴, as an example of a well known protocol using complete synchronization of chaotic systems. Without a dynamical Bayesian inference mechanism on the receiving side, this protocol is less complex, but achieves a BER threshold of around SNR = 20 dB under the same experimental conditions, which indicates lower robustness to noise.

IV. CONCLUSION

The coupling function protocol¹ works well in a hardware implementation and remains effective even under conditions of relatively high noise. The results obtained are consistent with previous theoretical findings, and we have demonstrated the protocol's performance on a low-cost and widely used device, thereby helping to bridge the gap between the theoretical development of the protocol and its practical application in the future. In particular, we have shown that the use of dynamical Bayesian inference in the decryption process results in successful decomposition of the noise signal from the deterministic information.

ACKNOWLEDGEMENTS

The work was funded by the EPSRC (UK) through grant EP/I00999X/1 and Lancaster University's Impact Acceleration Account, and by the Faculty of Electrical Engineering and IT in Skopje, Macedonia, through the ERES COP Project.

¹ T. Stankovski, P.V.E. McClintock, and A. Stefanovska, "Coupling functions enable secure communications," *Phys. Rev. X*, vol. 4, pp. 011026, (2014).
² T. Stankovski, T. Pereira, P.V.E. McClintock, and A. Stefanovska, "Coupling functions: Universal insight into dynamical interaction mechanisms," *Rev. Mod. Phys.*, vol. 89, pp. 045001, (2017).
³ G. Nadzinski, M. Dobrevski, C. Anderson, P.V.E. McClintock, A. Stefanovska, M. Stankovski, and T. Stankovski, "Experimental realization of the coupling function secure communications protocol and analysis of its noise robustness," *IEEE Trans. Inf. Forensics Security*, in press, DOI: doi.org/10.1109/TIFS.2018.2825147, (2018).

⁴ K.M. Cuomo and A.V. Oppenheim, "Circuit implementation of synchronized chaos with applications to communications," *Phys. Rev. Lett.*, vol. 71, pp. 65-68, (1993).
⁵ L.M. Pecora and T.L. Carroll, "Synchronization in chaotic systems," *Phys. Rev. Lett.*, vol. 64, pp. 821-824, (1990).
⁶ T. Stankovski, A. Duggento, P.V.E. McClintock, and A. Stefanovska, "Inference of time-evolving coupled dynamical systems in the presence of noise," *Phys. Rev. Lett.*, vol.109, pp.024101, (2012).
⁷ G. Alvarez and S. Li, "Some basic cryptographic requirements for chaos-based cryptosystems," *Intern. J. Bifurc. Chaos*, vol. 16, pp. 2129-2151, (2006).

How to defend against loop current attacks in the KLJN secure key exchange scheme?

Mutaz Melhem and Laszlo B. Kish

Department of Electrical and Computer Engineering, Texas A&M University, TAMUS 3128, College Station, TX 77843-3128, USA
e-mail address: Laszlokish@tamu.edu

The Kirchhoff-law-Johnson-noise (KLJN) offers unconditional (information-theoretic) security [1,2]. However, similarly to quantum communications, potentially non-ideal features in the practical system pose the danger of information leak. Even though the information leak can be reduced by privacy amplification [3], it is desirable to reduce the leak as much as possible.

One of the most dangerous and least explored class of attacks is based on low-frequency or DC current components in the cable and may be caused by a ground loop (leading to a 50/60Hz sinusoidal current), EMI or DC offset. The voltage drop originating from such parasitic currents will introduce a location-dependent bias into the key distributions and quickly uncover the nature of the resistors at the two ends of the wire, as illustrated in Fig. 1.

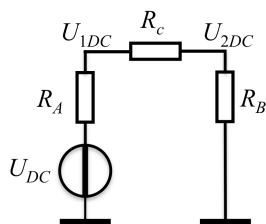


Figure 1. Schematic circuit for illustrating parasitic DC and low-frequency artifacts caused by ground loops [4]. For the sake of simplicity, the parasitic source is assumed to exist solely at Alice's side. Only the parasitic voltage generator is shown, because its impact is additive to the voltages caused by other circuit deficiencies. The parasitic DC or low-frequency components U_{1DC} and U_{2DC} of U_1 and U_2 , respectively, are sensitive to the location of the low/high resistor at Alice's and Bob's side.

Eve can simply measure and compare the DC or 50/60 Hz voltage components of the strongly correlated voltage noises at the two ends of the wire and extract the key or its inverse. Figure 6 shows, as an example, computer simulations of two strongly correlated noises with a small DC shift. In this particular case, a single-time measurement is able to identify the DC voltage shift and uncover the key or its inverse. If the DC shift is greater than the stochastic difference between the time functions, then a single-time measurement is sufficient to distinguish the two noises and the bit-situations in the KLJN scheme.

Obviously, Eve's successful guessing probability in this simple attack, is progressively enhanced by increasing the

cable resistance. However, according to our recent study and new statistical attack, Eve can utilize the loop current even at zero cable resistance. Many unsolved problems emerge; some of them are listed below:

- i) What is the impact of attacks utilizing periodic times function components in the loop currents?
- ii) Is increasing the noise temperature of R_A and R_B beneficial, or not? There are indications of both situations.
- iii) Is there an optimum situation?
- iv) Can we avoid using coax cables or twisted pairs and utilize the economical advantages of ground (single wire correction) ?

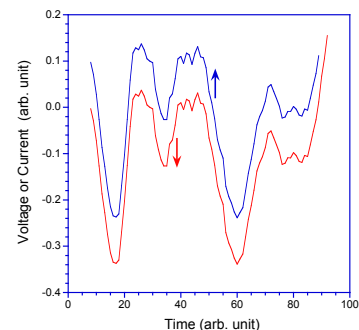


Figure 2. Computer-generated illustration [4] of how a DC shift can distinguish between two strongly correlated noises by comparison at a single moment of time. The arrows indicate the directions of shift.

REFERENCES

1. L.B. Kish, "The Kish Cypher. The story of KLJN for unconditional security". World Scientific 2017.
2. L.B. Kish, C.G. Granqvist, "On the security of the Kirchhoff-law-Johnson-noise (KLJN) communicator", Quantum Information Processing **13** (2014) 2213-2219.
3. T. Horvath, L.B. Kish, J. Scheuer, "Effective Privacy Amplification for Secure Classical Communications", EPL (formerly Europhysics Letters) **94** (2011 April) 28002-p1 - 28002-p6
4. H.P. Chen, L.B. Kish, C.G. Granqvist, G. Schmeta, "On the "cracking" scheme in the paper "A directional coupler attack against the Kish key distribution system" by Gunn, Allison and Abbott". Metrology and Measurement Systems **21** (2014) 389-400.

Signal detection with a noisy nanomechanical bifurcation amplifier

Yukihiro Tadokoro¹, Hiroya Tanaka¹, and M. I. Dykman²

¹TOYOTA Central R&D Labs., Inc., Nagakute, Aichi 480-1192, JAPAN

e-mail address: y.tadokoro@ieee.org, tanak@mosk.tytlabs.co.jp

²Department of Physics and Astronomy, Michigan State University, East Lansing, MI 48824, U.S.A

e-mail address: dykman@pa.msu.edu

I. INTRODUCTION

Nano-mechanical resonators provide a promising platform for mass, charge, and force detection with extremely high sensitivity¹⁻³. The sensitivity is largely limited by the noise, which broadens the spectral response of the vibrational modes. Such broadening is invariably present in all nanomechanical systems. An important and well-established feature of the vibrational modes in nanomechanics, which can also limit their performance as sensors, is the nonlinearity. A consequence of the nonlinearity is that, when a mode is driven close to resonance, the vibrations display bistability: for the same value of the driving force amplitude, the vibration amplitude can take on one of the two values, see Fig.(1).

Here we explore the effect of noise on a bistable driven nanomechanical mode and show that the bistability opens a way for a qualitatively new type of signal processing. It is based on using the driven system as a bi-directional bifurcation amplifier. The sensitivity of this new type of an amplifier depends on the noise parameters. The effect of the noise is qualitatively different from the familiar effects of the noise on mass and force sensing. We reveal a regime of a critical behavior and find the relevant scaling, which bears on the optimal performance of the amplifier.

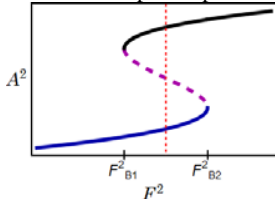


Fig. 1. The squared amplitude of forced vibrations of a nonlinear vibrational mode as a function of the squared amplitude of the driving force. The mode is modeled by a resonantly driven underdamped Duffing oscillator⁴. The stable branches of forced vibrations are shown by solid lines, the dashed line shows the unstable branch. $F_{B1,2}^2$ are the bifurcational values of the force that limit the range of bistability. The vertical line shows the chosen reference value of F^2 in the absence of a signal.

II. BISTABILITY OF DRIVEN NANO-MECHANICAL MODES

We use the standard model, where a nano-mechanical mode is described as a resonantly driven Duffing oscillator⁵ with equation of motion

$$\ddot{q} + 2\Gamma\dot{q} + \omega_0^2 q + \gamma q^3 = F \cos \omega_F t + \xi_0(t), \quad (1)$$

where q is the oscillator coordinate, Γ is the friction coefficient, ω_0 is the eigenfrequency, and γ is the nonlinearity parameter. We assume that, as it is usually the case in the experiment, $\Gamma, |\gamma(q^2)| \ll \omega_0$, and that the drive frequency is close to resonance, $|\omega_F - \omega_0| \ll \omega_0$. Function $\xi_0(t)$ describes noise, which we assume to be δ -correlated with intensity $2D_0$.

It is convenient to write Eq. (1) in dimensionless variables. Then the dynamics in the absence of noise is described by the scaled squared amplitude of the drive $\beta = 3\gamma F^2 / 32 \omega_F^3 (\omega_F - \omega_0)^3$ and $\kappa = \Gamma / |\omega_F - \omega_0|$. The bistability of vibrations occurs in the range $\kappa < \kappa_K = 1 / \sqrt{3}$ and $\beta < \beta_K = 8/27$.

The mode dynamics is simplified in the vicinity of the critical parameter values κ_K, β_K . Here, the two stable vibrational states and the unstable vibrational state shown in Fig.(1) are close to each other in phase space. The motion near these states is described by a ‘‘soft mode’’ $x(t)$, which is a common feature of motion in the vicinity of bifurcation points⁶. The important distinction from the standard bifurcation theory is the presence of the noise, which leads to spontaneous transitions between the coexisting vibrational states⁷. Such transitions have been seen by now in many nano-mechanical systems, starting with Ref.⁸.

III. RESPONSE TO A BIPOLAR SIGNAL

If the amplitude of the driving force F is changed, one of the stable states of forced vibrations can disappear. Such change is of interest for digital detection of modulated signals. These signals are encoded in the discrete values of a phase and can be written as $\delta F_S \cos(\omega_F t + \phi)$ with ϕ being 0 or π . In terms of Eq.(1), the signal modifies the amplitude F and causes it to change between $F + \delta F_S$ and $F - \delta F_S$. Digital detection requires that (i) for a given phase of the signal, the mode has only one stable vibrational state, and (ii) when the phase of the signal changes, the mode switches to another stable vibrational state. Such switching is illustrated in Fig.(2).

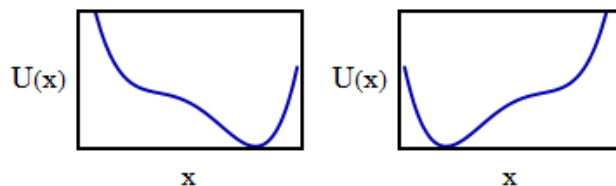


Fig.2. The potential $U(x)$ for the soft-mode variable x of the driven mode, Eq.(2). In the absence of a signal the potential is a symmetric quartic parabola, with the minima corresponding to the two stable vibrational states of the mode. This corresponds to the reference value of the driving amplitude shown by the red vertical line in Fig.(1). The signal, depending on its polarity, tilts the potential to the right or to the left, as shown by the left and right panels. In the absence of noise, the minimal amplitude of the signal is determined by the condition that one of the wells disappears, and the minimal duration of the signal is determined by the condition that, for a given signal amplitude, the mode has time to switch to another minimum.

The evolution of the appropriately scaled soft-mode variable is described by equation, which in dimensionless time $\tau = \Gamma t$ reads

$$\dot{x} = -\partial_x U(x) + \xi(\tau), \quad (2)$$

$$U(x) = -Ax - \frac{1}{2}|\kappa - \kappa_K|x^2 + \frac{1}{3\sqrt{3}}x^4,$$

where $\xi(\tau)$ is white Gaussian noise, $\langle \xi(t)\xi(t') \rangle = 2D\delta(\tau - \tau')$ with $D \propto D_0$. Parameter A is the scaled signal amplitude, $A = (8/27)^{1/2} \delta F_S / F_K$ with F_K given by β_K .

Deterministically, the minimal value δF_{cr} of the signal amplitude $|\delta F_S|$ is given by the condition that a minimum of $U(x)$ merges with its local maximum, which gives $\delta F_{cr}/F_K = (3/4)^{3/4} |\kappa - \kappa_K|^{3/2}$. From this equation it is clear that, by moving closer to the critical value of κ , i.e., by appropriately changing $|\omega_F - \omega_0|$, one can improve the sensitivity. On the other hand, the duration of the pulse needed to switch from one minimum to another when δF_S changes sign increases with decreasing signal amplitude. This time can be shown to be

$$\tau_{min} = (3^{7/8}/2^{5/4})\pi(|\delta F_S|/F_K)^{-1/2} \quad (3)$$

IV. SIGNAL DETECTION ERROR AS A RARE EVENT PROBLEM

The limit on the sensitivity is imposed by noise. For the signal amplitude close to critical, as seen from Fig.(2), there is a region where the potential $U(x)$ is almost flat. It is centered at $-x_{cr} \text{sgn} \delta F_S$, with $x_{cr} = [(\sqrt{3}(\kappa_K - \kappa)/4)]^{1/2}$. The motion here is slowed down, and the effect of fluctuations accumulates. Once the system has moved beyond the critical region, it moves comparatively fast. Near the critical region we introduce a scaled variable $y = (\delta F_S/F_K)^{-1/2}(x + x_{cr})3^{5/8}/2^{1/4}$ (for $\delta F_S > 0$). To the leading order in δF_S , the Fokker-Planck equation for the probability density $\rho(y, \tau')$ in time $\tau' = \pi\tau / \tau_{min}$ reads

$$\partial_{\tau'} \rho = \partial_y (\partial_y \tilde{U} \rho) + \tilde{D} \partial_y^2 \rho, \quad \tilde{U} = -y^3/3 - y, \quad \tilde{D} = (3^{17/8}/2^{7/4})[\delta F_S/F_K]^{-3/2} D. \quad (4)$$

For small δF_S and small \tilde{D} , this equation describes the evolution of the system from $y_i \rightarrow -\infty$ (the state occupied before the signal arrives) to $y_f \rightarrow \infty$ (the state into which the signal drives the system and where it is detected) over time τ_{min} . The evolution of ρ with time τ' is shown in Fig.(3). The maximum of the distribution quickly shifts to positive y and the distribution is broadened because of the ‘‘softness’’ of the potential at small $|y|$.

The noise-induced error is determined by the probability that, by the end of the signal (i.e., of the pulse δF_S), the system is still

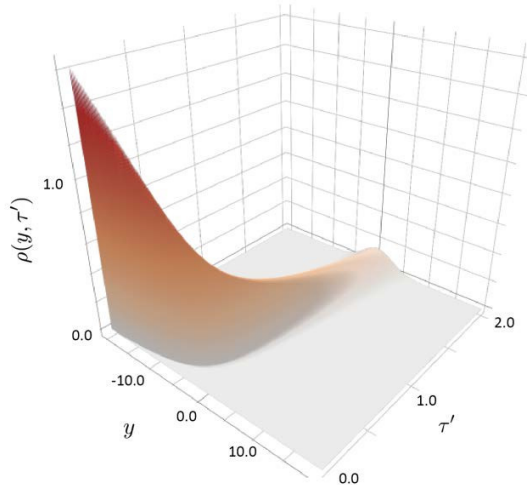


Fig.3. The evolution of the distribution ρ of the scaled vibration quadrature y for a signal with amplitude close to the critical value.

in the region $y \leq 0$, i.e., by the value of $\int_{-\infty}^0 \rho(y) dy$. This value is exponentially small for weak noise. The exponent is determined by the probability density of finding the system at $y = 0$ at the end of the signal, $\tau' = \pi$ (or $\tau = \tau_{min}$).

We find the exponent using the method of optimal fluctuation. As is usually done in this method^{7,9}, we set $\rho(y, \tau') = \exp[-S(y, \tau')/\tilde{D}]$. Function S can be associated with the mechanical action of an auxiliary non-dissipative particle with the coordinate Q , momentum P , and the Hamiltonian $H(Q, P) = P^2 - P\tilde{U}'(Q)$. The problem of finding S turns out to be different from the problems traditionally solved using the method of optimal fluctuation. Nevertheless, we have found a way to solve it. The obtained error rate is

$$p = \rho(0, \pi) = C \exp(-R/\tilde{D}), \quad R = (\pi - 2^{5/2}/3)/4 \quad (5)$$

Here, constant $C \sim 1$ is independent of the noise intensity.

V. DISCUSSION

The condition (5) shows where the proposed here bidirectional amplifier can work reliably for weak signals in the presence of noise. Because \tilde{D} increases as $(\delta F_S)^{-3/2}$ with the decreasing signal amplitude, the error sharply increases with the decreasing $|\delta F_S|$, which imposes a more strict limitation on the minimal signal amplitude than just the condition $|\delta F_S| > \delta F_{cr}$.

This work suggests a new application of nano-mechanical systems, which reveals nontrivial and hitherto unknown aspects of their dynamics in the presence of noise. It describes some of the effects of the noise, but since this is the first work in a new direction, much remains to be learned. One of the major open questions is the effect of frequency fluctuations, which often play an important role in nano-mechanical systems.

ACKNOWLEDGEMENTS

This work was partly supported by JSPS KAKENHI (grant JP17K14690). MID acknowledges partial support from the US National Science Foundation (DMR-1514591 and CMMI-1661618).

- ¹ J. Moser et al., Nat. Nanotech **8**, 493 (2013).
- ² M. S. Hanay et al., Nat. Nanotech. **10**, 339 (2015).
- ³ Y. Tao, A. Eichler, T. Holzherr, and C. L. Degen, Nat. Commun. **7**, 12714 (2016).
- ⁴ L. D. Landau and E. M. Lifshitz, *Mechanics* (Elsevier, Amsterdam, 2004).
- ⁵ I. Kozynsky et al., Phys. Rev. Lett. **99**, 207201 (2008).
- ⁶ J Guckenheimer and P. Holmes, *Nonlinear Oscillators, Dynamical Systems and Bifurcations of Vector Fields* (Springer-Verlag, New York, 1997).
- ⁷ M. I. Dykman and M. A. Krivoglaz, in *Sov. Phys. Reviews*, v. 5, pp. 265-441 (Harwood, New York, 1984)
- ⁸ J. S. Aldridge and A. N. Cleland, Phys. Rev. Lett., **94**, 156403 (2005).
- ⁹ A. Kamenev, *Field theory of non-equilibrium systems* (Cambridge University Press, Cambridge, 2011).

Lorentzians vs global warming hysteria

Michael Levinshtein¹

¹Ioffe Institute, Solid State Department, Politechnicheskaya 26, St. Petersburg 194021, Russia
e-mail address: melev@nimis.ioffe.ru

Valentin Dergachev²

²Ioffe Institute, Astrophysics Department, Politechnicheskaya 26, St. Petersburg 194021, Russia
e-mail address: V.Dergachev@mail.ioffe.ru

Alexander Dmitriev³

³Ioffe Institute, Nanostructure Physics Center, Politechnicheskaya 26, St. Petersburg 194021, Russia
e-mail address: apd1812@gmail.com

Pavel Shmakov⁴

⁴Ioffe Institute, Nanostructure Physics Center, Politechnicheskaya 26, St. Petersburg 194021, Russia

I. INTRODUCTION

Everybody knows that we are living in the era of global warming. However this is not the first, second, third or even the hundredth global warming. Climate fluctuations can be traced throughout the entire history of the Earth. So now the main question is: what role does human activity play in modern warming? The only scientific way to predict the coming future climate changes is to correctly analyze such changes in the past.

Palaeoclimatology, palaeoecology, paleogeography have amassed thousands records of climate changes in time intervals of hundreds, thousands, millions, and even dozens of millions years. These dependencies and the cross-correlation of these parameters are analyzed and continue to be analyzed using highly sophisticated techniques. However for those that are involved in studying noise, these paleodata look often simply as noise

II. PALEODATA AND NOISE ANALYZIS

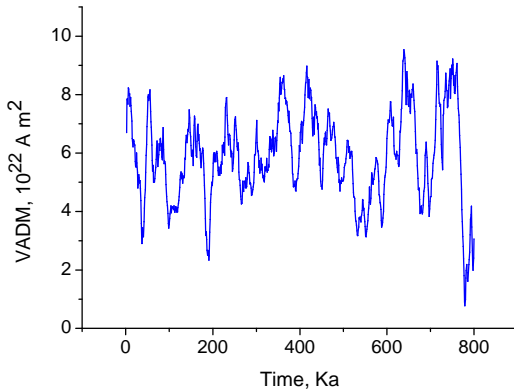


FIG. 1. The time dependence of the virtual axial dipole moment (VADM) for 800 Ka¹. (VADM is very important quantity for sailors, geodesists, cartographers, etc...)

Let's assume that these data represent a random functions, and determine the spectral density of fluctuations for such noise dependences.

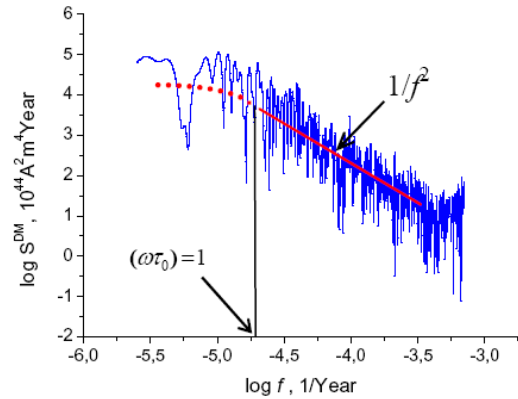


FIG. 2. The frequency dependence of spectral density fluctuations, S^{DM} for the time dependence VADM (Fig. (1)).

Those who do not recognize a Lorentzian can cast the first stone.

$$S \propto \frac{\tau_0}{1 + (2\pi f \tau_0)^2}; \tau_0 \sim (1/2\pi) \times 10^{4.7} \sim \mathbf{8000 \text{ years}}$$

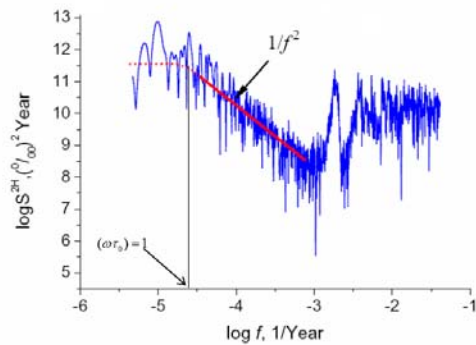


FIG. 3. The frequency dependences of spectral density fluctuations, S^{DH} for the deuterium content (“deuterium thermometer”). Vostok Ice Core Deuterium Data for 420,000 years².

$$S \propto \frac{\tau_0}{1 + (2\pi f \tau_0)^2}; \tau_0 \sim \mathbf{(6-8)000 \text{ years}}$$

Data on average of 57 globally distributed benthic and ice $\delta^{18}\text{O}$ records (“oxygen thermometer”) have been presented for **5.3 million years**³.

The frequency dependence of temperature spectral density fluctuations calculated for these data demonstrates the presence of **two Lorentzians**

1. $\tau_0 \sim (6-8) 000$ years that is close to the corresponding values of τ_0 , found for Antarctic data
2. $\tau_0 > 100 000$ years

Data on fluctuations of solar insolation for **10 million years** have been presented in Ref.⁴

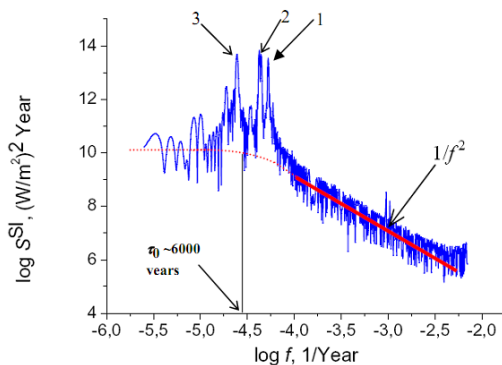


FIG. 4 The frequency dependence of spectral density fluctuations of solar insolation for 10 000 000 years

One can see the Lorentzian (again) with $\tau_0 \sim 6 000$ years.

Peaks 1, 2, and 3 in Fig (5) correlate with well known periodical processes:

3. **41,000-years:** The angle between the axis of rotation of the Earth and the normal to the plane of the orbit oscillates with a period of **41,000-years**;
2. **23,000 years:** The period of the precession of the Earth's orbit is **26,000** years.
1. **18,000 years:** The combination of rotation of the elliptical orbit and precession gives a period of **21,000 years**

Because the Sun is the Master of the Earth, we can assume (just assume) that the temperature (and VIDM) fluctuations with $\tau_0 \sim (6-8)000$ years are caused by fluctuations of the insolation.

The frequency dependence of spectral density fluctuations for the atmospheric radiocarbon $\delta^{14}C = \frac{^{14}C}{^{12}C}$ is Lorentzian with $\tau_0 \approx 300$ years⁵.

An analysis of $C0_2$ fluctuations reveals the frequency dependence characteristic of natural or man-made disasters: floods, crises, stock crashes, etc.

III. PRELIMINARY RESULTS.

1. Interpretation of paleoclimatic data as random functions and calculation their spectral density reveals interesting and previously unknown regularities .

¹ Y. Guyodo and J. Valet, Nature **399**, 249 (1999).

² J. R. Petit, et al., Nature **399**, 429 (1999)

³ L. E. Lisiecki and M. E Raymo, Paleocanography **20**, PA1003 (2005).

⁴ A. Berger and M. F. Loutre, Quaternary Sciences Review **10**, 297 (1991).

⁵ M. Stuiver, et al., Radiocarbon **40**, 1041 (1998)

2. Along with the known periodic and quasiperiodic processes in the formation of many paleoclimatic parameters, an important role play random processes with a single time constant τ_0 .

3. **The nature of such processes is interesting though not clear.** As far as we know, it has never been discussed previously

4. Fluctuations in temperature and solar insolation (and VADM) are characterized by a random process with a single time constant τ_0 on the order of (5-8) thousand years.

We have traced the effect of this process on the time scale of $\sim 10,000,000$ years

Because the Sun is Lord of the Earth it seems plausible that the temperature (and VADM) fluctuations with $\tau_0 \sim (5-8)000$ years are caused by fluctuations of the insolation

5. **The dominant role of the random process with $\tau_0 \sim (6-8)000$ years makes "short-term" (at characteristic times of $\sim 200-500$ years) forecasts of climate change not reliable.**

IV. SOME REMARKS ABOUT GLOBAL WARMING HYSTERIA

Only 20 000 years ago at the location of this Conference lay an ice shield of 2.5-3 km thickness. This monstrous ice shield quickly melted away without any influence of human activity. About $\sim 12,000$ years ago people settled in the territory of modern Scandinavia

Holocene warmings:

1. 6000 BC – 4000 BC. Duration ~ 2000 years.
2. 3000 BC – 1500 BC. Duration ~ 1500 years

"Roman" warming:

~ 200 BC – 200 AC Duration ~ 400 years

"Viking Era"

\sim VIII – XI century AC Duration ~ 300 years

Between 800 and 1200 AC vikings could navigate at latitudes, where floating ice is now encountered. They settled in Greenland which was a **GREEN land** at that time.

In XII-XIII AC on the Baltic coast and in England people grew grapes

V. CONCLUSION

There is a powerful natural random process of unknown nature with a characteristic time of about 5-8 thousand years. It can be traced for at least 10,000,000 years and takes into account glacial periods and periods of intense warming. It seems that modern human activity exerts an incomparably less influence on the climate than this unknown factor.

It appears that an honest scientific answer to the question of whether the observed current warming is a consequence of human activity should be:

"We do not know, but it looks very likely *no.*"

Open problems of utilizing noise in energy harvesting systems

B. Andò¹, S. Baglio¹, A.R. Bulsara², V. Marletta¹

¹University of Catania, Department of Electrical Electronics and Information Engineering (DIEEI)
v.le A. Doria, 6 – 95125 Catania, Italy

e-mail address: bruno.ando@unict.it

²Space and Naval Warfare Systems Center Pacific, Code 71000, San Diego, CA 92152-5000, USA

e-mail address: bulsara@spawar.navy.mil

I. INTRODUCTION

Noisy environmental mechanical vibrations are ubiquitous and in a large variety of forms such as induced oscillations, seismic noise, vehicle motion, acoustic noise, multi-tone vibrating systems, human motion, just to name a few.

A review of common vibrations sources as potential viable power sources was presented by Roundy et al.¹. In last years, the scientific community has focused on the development of solutions for efficiently scavenge energy from vibrations.

Actually, it should be observed that only occasionally, the energy to be collected may be confined to a very specific region of the frequency spectrum but, very often, the available (for harvesting) energy is distributed over a wide frequency spectrum. In such a framework, linear energy harvesters, typically based on oscillators (typically based on cantilever beams) lose their effectiveness. New harvesting configurations based on nonlinear mechanisms², such as bistable systems³, can outperform traditional (linear) energy harvesters under the appropriate operating conditions.

As an example, the fixed-fixed beam in a buckled configuration (also note as “Snap Through Buckling” (STB) configuration) obtained by applying a pre-compression at the beam’s ends, presents a nonlinear bistable behavior in a wide (depending on the geometrical parameters) range of frequencies. The main advantages of the STB configuration are the large displacements of the beam, and the fast switching between the two stable states under external low amplitude wideband mechanical vibrations, which allow to enhance the efficiency of the power conversion mechanism. A drawback of the STB configuration is that to activate the inter-well beam switching and permit the beam to escape from one potential well (stable state) to the other, the input acceleration must overcome a threshold value which is fixed by the inherent potential barrier of the bistable potential energy⁴.

Recently, the authors investigated the mechanical and electrical behavior of buckled beam based nonlinear energy harvesters^{5,6,7,8}. This work deals with a STB harvester to scavenge energy from wideband vibrations, acting along the vertical direction. The system architecture and experimental evidences of its energy conversion performances are addressed.

II. THE NONLINEAR ENERGY HARVESTER

A real view of the device including the experimental setup based on an electromagnetic shaker and the driving electronics is shown in Fig. 1a. It consists of a fixed-fixed flexible PET (TartanTM 801, Hewlett-Packard) cantilever beam in a Snap Through Buckling (STB) configuration, with a pre-compression $\Delta y=1$ mm applied along the main axis. A proof mass is placed in the middle of the beam and two lateral identical piezoelectric

transducers, Midè Volture V21BL, are used to implement the mechanical-to-electrical conversion. The beam dimensions are 6 cm by 1 cm, with a thickness of 140 μm . The proof mass consists of two identical neodymium (NdFeB) disc permanent magnets SN-10-04-N, with an axial (parallel to the height) direction of magnetization. Magnets dimensions are diameter 10 mm, height 4mm. Two hemispherical stainless steel mass, with height 3 mm, diameter 4 mm, and weight of 0.2 g, have been used to maximize the effect of impacts per each switching event. The total mass of the proof-mass is 5.2 g. The beam pre-compression and the proof mass define the switching threshold of the device. In case of a subthreshold signal along the vertical axis, the beam will not exhibit commutations, thus producing intra-well vibrations within one of the two stable states.

A neodymium permanent magnet, S-08-01-N, has been placed underneath the bottom harvester, at the optimal distance $L_m = 29$ mm from the upper state position, to compensate for the effect of the proof mass load. The position of the repulsive magnet has been experimentally fixed by measuring the repulsive magnetic force exerted by the magnet on the proof mass, by using a load cell (Transducer Techniques GSO-10).

An electromagnetic shaker, consisting of two identical electromagnets WF-P34/18 (one facing the other), driven by counter phase current signals through dedicated electronics, has been used for the system characterization. In such a configuration the two electromagnets continuously exert a magnetic force (given by the sum of the two coherent magnetic force components) on the magnetic proof mass of the harvester.

A distance measurement module, QTR-1A by Pololu, including a small reflectance infrared sensor and the conditioning electronics, has been used to continuously monitor the displacement of the proof mass.

III. EXPERIMENTAL CHARACTERIZATION

The experiments were aimed at estimating the response of the harvester to a band limited noise vibration, in a given time interval, by changing the strength of the input signal. More precisely, the device performances were tested in terms of the number of complete commutations of the beam between its stable states, over a set time interval of 20 s, as well as the electrical power and the mechanical to electrical conversion efficiency. The range of frequencies in which the beam can follow the signal dynamics (i.e. the switching rate corresponds to the stimulation frequency) has been observed to be 5 Hz⁷.

Fig. 1b shows an example of the bandwidth limited (at 15 Hz) noise (the magnetic force F_M applied to the beam), used for the sake of harvester characterization, while Fig. 1c shows its frequency spectrum.

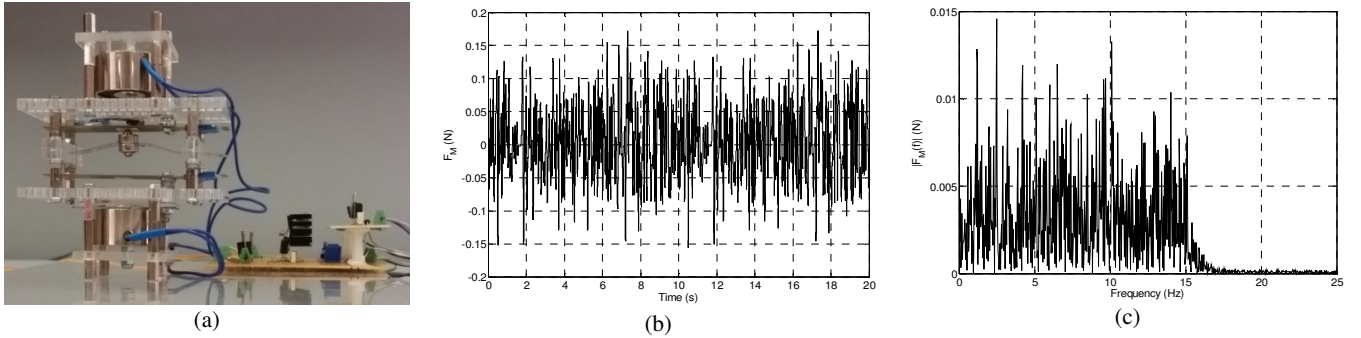


FIG. 1. (a) A real view of the harvester including the electromagnetic shaker and the driving electronics; (b) an example of the input magnetic force used for the harvester characterization; (c) the frequency spectrum of the input magnetic force.

The number of (inter-well) switching events as a function of the noise variance, in the considered observation time, is shown in Fig. 2a. It is readily observed that the number of switching events increases as a function of the noise level. This result can be justified by taking into account that the number of threshold crossing events increases with the noise variance. The number of impacts on the piezoelectric transducers increases consequently, thus improving the electric energy produced.

The observed time domain signals in case of an input acceleration with a variance of $23.38 \text{ m}^2/\text{s}^4$ and $170.26 \text{ m}^2/\text{s}^4$, generating null (sub-threshold) and 74 beam's switching events, are reported in Fig. 2b and 2c, respectively.

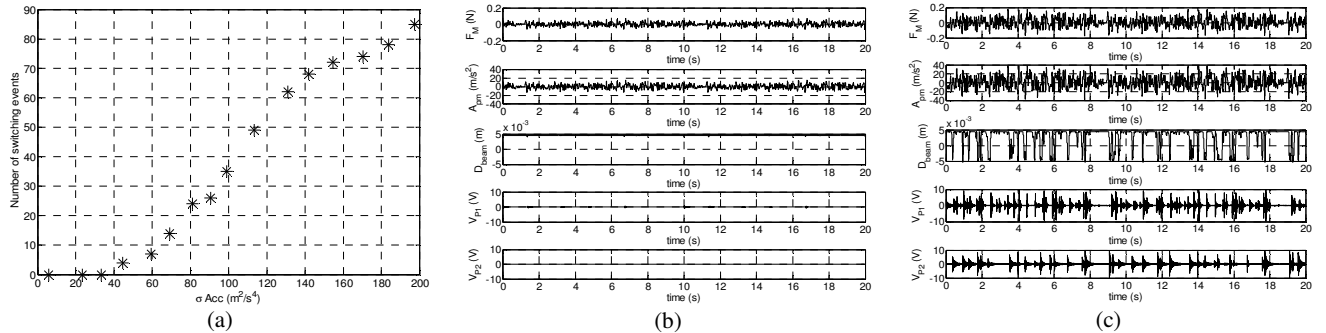


FIG. 2. (a) The number of (inter-well) switching events, in the observation time of 20 s; (b) and (c) the magnetic force F_M , the acceleration A_{pm} , the beam's displacement D_{beam} and the two piezoelectric output voltages V_{p1} and V_{p2} in case of a input noise acceleration with a variance of $23.38 \text{ m}^2/\text{s}^4$ and $170.26 \text{ m}^2/\text{s}^4$, respectively.

ACKNOWLEDGEMENTS

This research activity was carried out under the (Office of Naval Research Global) grant "Advanced nonlinear energy

- 1 S. Roundy et al., A study of low level vibrations as a power source for wireless sensor nodes, Computer Communications, vol. 26, no. 11, pp. 1131–1144, 2003.
- 2 S. Baglio et al., "Exploiting Nonlinear Dynamics in Novel Measurement Strategies and Devices: From Theory to Experiments and Applications, IEEE Trans. Instr. Meas., 60 (3), pp. 667-695, 2011.
- 3 R L Harné, K W Wang, A review of the recent research on vibration energy harvesting via bistable systems, 2013 Smart Mater. Struct. 22 023001.
- 4 R. Masana, M. F. Daqaq, Response of duffing-type harvesters to band-limited noise, Journal of Sound and Vibration 332 (2013) 6755–6767.

Examples of the power conversion efficiency, $\eta\%$, evaluated as the ratio between the average output electrical power, P_e , produced by the piezoelectric transducers and the input mechanical power, P_m , are reported in Tab. 1.

TAB.1. Examples of the power conversion efficiency.

$\sigma_{Acc} \text{ (m}^2/\text{s}^4)$	$P_m \text{ (W)}$	$P_e \text{ (W)}$	$\eta\%$
59.52	8.29e-4	26.17e-6	3.16
113.4	1.15e-3	1.28e-4	11.2
197.3	1.51e-3	2.71e-4	17.88

harvesters in the mesoscale: exploiting a Snap-Through Buckling configuration, for the autonomous powering of electronic devices. ONR N62909-15-1-2015".

- 5 B. Andò et al., "A bistable buckled beam based approach for vibrational energy harvesting", Sensors and Actuators A: Physical, vol. 211, pp. 153-161, 2013.
- 6 B. Andò et al., "A Low-Cost Snap-Through Buckling Inkjet Printed Device for Vibrational Energy Harvesting", IEEE Sensors Journal, vol. 15, n. 6, pp. 3209-3220, 2015.
- 7 B. Andò et al., A. Pistorio, Investigation of a Nonlinear Energy Harvester, IEEE Trans. Instr. Meas., vol. 66 n. 5, pp. 1067-1075, 2017.
- 8 B. Andò et al., Performance Investigation of a Nonlinear Energy Harvester with Random Vibrations and Sub-Threshold Deterministic Signals, IEEE Trans. Instr. Meas., vol. 66 n. 5, pp. 992-1001, 2017.

Fluctuations and time-translation symmetry breaking in vibrational Floquet systems

Niels Lörch¹, Yaxing Zhang², Christoph Bruder¹, and M. I. Dykman³

¹*Department of Physics, University of Basel, CH-4056 Basel, Switzerland*

²*Department of Physics, Yale University, New Haven, Connecticut 06511, USA*

³*Department of Physics and Astronomy, Michigan State University, East Lansing, MI 48824, USA*

I. INTRODUCTION

A periodically driven system has discrete time-translation symmetry with the period of the driving. Its quantum dynamics is described in terms of the Floquet states. Generally, if the system is in a Floquet state, its dynamical variables oscillate with the period of the driving. Recently much interest have attracted systems where the time symmetry is broken, the “time crystal” effect. Nonlinear oscillators provide an ideal platform for studying this effect. A familiar example is parametric resonance: when a dissipative oscillator is modulated close to twice the eigenfrequency, the period of the parametrically excited vibrations is twice the modulation period. For a single classical parametric oscillator, the breaking of the discrete time-translation symmetry has been known already to the ancient Greeks.

The situation becomes far more delicate and interesting when the system is scaled down from the Greek (and modern) swings to a nanomechanical resonator or electromagnetic modes in a microwave cavity. Those are also nonlinear oscillators, and parametric resonance in these systems is well known. However, because the systems are small, classical and quantum fluctuations play a major role in their dynamics. Understanding this role and the possibility of breaking of time-translation symmetry in the presence of fluctuations is the goal of the work to be presented.

II. EFFECT OF QUANTUM TUNNELING AND COUPLING

The major physical effect of fluctuations in the context of the time-symmetry breaking are transitions between the period-two (or period-three, see below) states. These transitions happen at random but, on the time scale long compared to the reciprocal transition rate, the time symmetry is restored. The noise-induced symmetry restoration was first observed in the classical regime for an electron in a modulated Penning trap and for cold atoms in a magneto-optical trap^{1,2}, following the theoretical prediction³.

In the quantum regime, two causes of transitions between period-two states should be considered. One is quantum tunneling between the states and the other is dissipation-induced transitions. Quantum tunneling can be studied using the Hamiltonian⁴ of the parametric oscillator in the rotating-wave approximation $g(Q, P)$, where Q and P are the scaled coordinate and momentum in the rotating frame, $[Q, P] = i\lambda$ (λ is the scaled Planck constant) and

$$g(Q, P) = \frac{1}{4}(Q^2 + P^2 - \mu)^2 + \frac{1}{2}(P^2 - Q^2) - \frac{1}{4}\mu^2 \quad (1)$$

Function $g(Q, P)$ is shown in Fig.1. Parameter μ is determined by the ratio of the detuning of the drive frequency from twice the oscillator frequency to the drive amplitude. The minima of

$g(Q, P)$ correspond, classically, to the stable period-two states. Clearly, there should be tunneling between these minima, and generically it is present. However, it was found⁴ that the tunnel splitting oscillates with the parameters of the system and periodically goes through zero with the varying frequency of the drive, i.e., the states at the bottom of the wells are exactly degenerate. Then the system prepared in one of them will stay there, a quantum coherent breaking of time translation symmetry.

Recently the possibility of eliminating tunneling between the minima of the Hamiltonian in the rotating frame was also found for period tripling⁵. Interestingly, the quantum problem in this

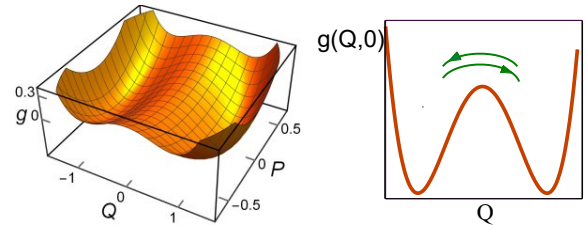


FIG. 1. The effective Hamiltonian of the parametric oscillator in the rotating frame (left panel, $\mu = 0.2$) and its cross-section by the plane $P = 0$ (right panel). The minima of $g(Q, P)$ correspond to the stable period-two states of the oscillator, in the presence of weak dissipation. Fluctuations lead to transitions between the minima and thus restore the discrete time-translation symmetry.

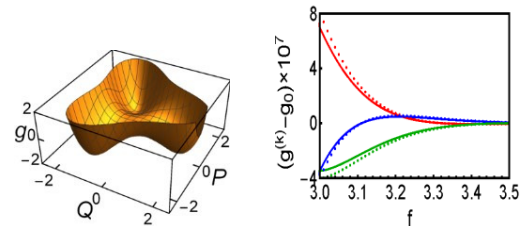


FIG. 2. Left panel: The effective Hamiltonian in the rotating frame for period tripling; the states at the minima of $g(Q, P)$ are the period-three states, classically. Right panel: the positions of the three lowest levels of $g(Q, P)$ as functions of the scaled amplitude of the periodic drive⁵. Where the levels intersect, one can create a coherent quantum period-three state.

case turns out to be far more complicated. The states at the minima of the effective Hamiltonian $g(Q, P)$ are characterized by a nontrivial geometric phase. At the forma level, the elimination of the tunnel splitting in the both cases is a consequence of the oscillations of the wave function in the classically forbidden region.

The coherent multiple-period states survive only for the decay time of the oscillator. A critically important feature is that, in quantum mechanics, decay is invariably accompanied by noise. This is clear already from the very concept of decay as a result of transitions between the oscillator levels due to the coupling to a thermal reservoir. Since the transitions happen at random, relaxation leads to noise. In turn, this noise leads to transitions between the multiple-period states. Remarkably, the rate of transitions between the broken-symmetry states W_{nm} is exponentially larger than the tunneling rate.

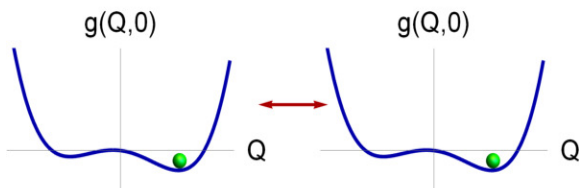


FIG.3 A sketch of the effective Hamiltonian of two coupled parametric oscillators. Because of the coupling, the symmetry of the period-two states of an oscillator is broken if the other oscillator is in a certain state. The sketched regime corresponds to “ferromagnetic” coupling, where the oscillators are occupying the states with the same phase (the same sign of Q).

In the present work it is shown that the rates of dissipation-induced transitions can be exponentially strongly affected by the coupling of different oscillators with each other. This can be understood if one thinks of the oscillators as providing a bias to each other. Indeed, if the oscillators are coupled and one of them is in one of the period-two states, this modifies the Hamiltonian $g(Q,P)$ of the other oscillator, adding a term, the sign of which depends on the sign of the coupling and the state of the oscillator. This is sketched in Fig.3. With this bias, it is exponentially less likely for an oscillator to switch from a “deeper” well than from a more shallow well.

As we will show, the system can be mapped onto a system of Ising spins. The coupling will be described analytically along with the different regimes that occur in the many-oscillator system. Remarkably, in the quantum coherent regime the system of coupled oscillators undergoes a quantum phase transition.

Among the relevant **unsolved problems**, the most important in the context of the present work are the problems of frustration in a noisy set of parametrically coupled oscillators, the multiplicity of the emerging broken –symmetry states, and the fluctuations that accompany the quantum phase transition.

ACKNOWLEDGEMENTS

The research of N.L. and C.B. was supported in part by the Swiss SNF and the NCCR Quantum Science and Technology. Y.Z. was supported by the National Science Foundation (DMR-1609326), M.D. was supported in part by the US National Science Foundation (CMMI-1661618)

- 1 L. J. Lapidus, D. Enzer, and G. Gabrielse, Phys. Rev. Lett. **83**, 899 (1999).
- 2 K. Kim et al., Phys. Rev. Lett. **96**, 150601 (2006).
- 3 M. I. Dykman, C. M. Maloney, V. N. Smelyanskiy, and M. Silverstein, Phys. Rev. E **57**, 5202 (1998).
- 4 M. Marthaler and M. I. Dykman, Phys. Rev. A **76**, 010102R (2007).
- 5 Yaxing Zhang et al., Phys. Rev. A **96**, 052124 (2017).

Unsolved problems in instrumentation for noise measurements

C. Ciofi, G. Scandurra and G. Giusi
University of Messina, Dipartimento di Ingegneria, Messina, Italy
e-mail address: cciofi@unime.it

I. INTRODUCTION

Performing meaningful noise measurements on electron devices require instrumentation with very low level of background noise and strict control of environmental interferences. Especially in the case of Low Frequency Noise Measurements (LFNM), with the minimum frequency of interest that can be as low as a 100 mHz or less and where correlation approaches are not effective because of the very long measurement time required for averaging out the uncorrelated noise, a strict control of the noise contribution coming from each piece of instrumentation is mandatory for obtaining sufficient sensitivity in a number of applications. Depending on the type of application and on the characteristics of the Device Under Test (DUT), it is often the case that the instrumentation available on the market severely limits the sensitivity of the measurement chain. In these cases, resorting to custom instrumentation becomes mandatory for expanding both the frequency range and/or the bias region in which the noise produced by the DUT can be reliably measured. While there are a number of solutions proposed in the literature for the design of voltage or trans-resistance amplifiers with very low background noise¹⁻⁴, this is not the case for the DUT bias systems. Indeed, in most cases, low noise voltages or current sources are obtained starting from batteries and excess noise free resistors with limited, or none at all, provision for programmability and remote control. While working with batteries and manually adjusted resistance networks is usually the best approach for quickly reaching reliable estimates of noise in the characterization of new devices, whenever a systematic investigation is required, lacking a fully automated measurement system may severely limit its scope. The problem, in these situations, is not just the long time and great effort that the investigator need to devote to repeatedly adjust and check the measurement parameters: there are cases in which the characteristics of the DUTs may be subject to drift with time and with environmental exposure. In cases such as these, the availability of an automated system is a necessity rather than just a convenience⁵.

Another aspect that need to be addressed and that is often overlooked is the lack of flexibility in benchtop Dynamic Signal Analyzers (DSA), or even acquisition boards with software that is limited to mimicking the operation of benchtop DSA. Selecting the correct parameters for spectral estimation in LFNMs is often as important as reducing the background noise. Large systematic errors can result in the flicker region because of spectral leakage⁶. Reducing the resolution bandwidth reduces systematic errors in the low frequency region, but this also may result in excessively long measurement time for obtaining sufficient averaging. This issue, together with the lack of programmable bias systems, limits the possibility of automation and deserve to be addressed in the path toward the realization of fully automated noise measurement system.

II. BIAS SOURCES

In most of the few designs proposed in the literature for the realization of low noise bias sources, resorting to conventional DA converters is ruled out because of the large level of low frequency noise that is characteristic of these devices even when they are classified as “low noise”^{7,8}. Effectively filtering out the noise at the lowest frequency of interest (say 100 mHz) without resorting to electrolytic capacitors (that cannot be used in LFNM because of micro-discharge events) is quite difficult. In the last few years, however, supercapacitors have been introduced that couple extremely large capacitance with the absence of the problems affecting electrolytic capacitors. Examples of programmable low noise voltage sources and current sources employing standard solid state DA converters and supercapacitors based filters have been realized^{9,10}. While effective in obtaining a very low level of noise, these realizations all suffer from a significantly long settling time that goes beyond what is strictly required by the setting time of the filtering sections. This has to do with the peculiar behavior of supercapacitors during charging and discharging that is summarized in Fig. 1, where the charging current in the circuit in the inset is reported for two different voltage steps normalized with respect to the ideal current I_M at the beginning of the transient ($I_M = V_M/R$). The dashed line represents the ideal behavior. As it can be noticed, the actual charging curve departs from the ideal

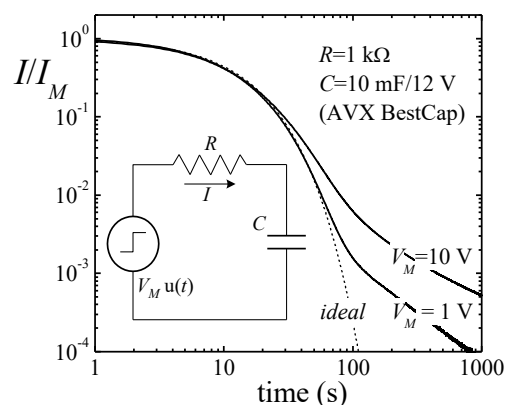


Fig. 1: current in a supercapacitor during charge transients. Large deviations from the ideal behavior are apparent that do not scale linearly with voltage.

behavior and since curves with different V_M do not superimpose, the phenomenon is not linear. Understanding this behavior and designing systems capable of compensating its effects is of great consequence in the path toward the realization of bias system with responses fast enough not to significantly affect the overall measurement time in low frequency noise applications.

III. SPECTRAL ESTIMATION

In conventional DFT spectral analyzers, resolution bandwidth (Δf), record length (N) and acquisition frequency (f_s) are linked together by the equation:

$$\Delta f = \frac{f_s}{N} \quad (1)$$

Typically, at least in benchtop spectrum analyzers, N is in the order of a few thousands, and in setting the analyzer one has to make the choice of sacrificing bandwidth in order to gain in frequency resolution for correctly estimating the low frequency portion of the spectrum. However, the measurement time for obtaining sufficient averaged spectra is inversely proportional to the resolution bandwidth, so that one would like to select the maximum Δf compatible with the minimum frequency of interest not to waste precious measurement time. All the above problems would be ideally solved if one had a large number of spectrum analyzers working in parallel, each one of them set at a

different Δf so that each frequency range could be explored with the proper resolution and the effect of different Δf in terms of systematic errors and averaging time could be constantly monitored. In this way, the measurement could be terminated at the proper time and no beforehand guessing of the correct setting would be required. This very same type of approach was used to demonstrate the feasibility of a spectrum analyzer with a quasi-logarithmic frequency resolution¹¹. Since then, we developed a software library that can be used for easing the development of a multiple channel, real time, cross spectrum analyzers with quasi logarithmic frequency resolution and provision for uninterrupted time domain recording and zoom spectral estimation with adjustable resolution bandwidth. An example of the results that can be obtained is reported in Fig. 2, demonstrating the estimation of the cross spectrum between two channels over 6 decades of frequency while operating with a record length $N=4096$. With regard to the approach we propose, the main issue appears to be the way in which the measurement results (equivalent to those produced by a large number of spectral analyzers working in parallel), are combined together in order to provide the operator with a complete and yet sufficiently clear picture of the evolution of the noise estimation process during measurements.

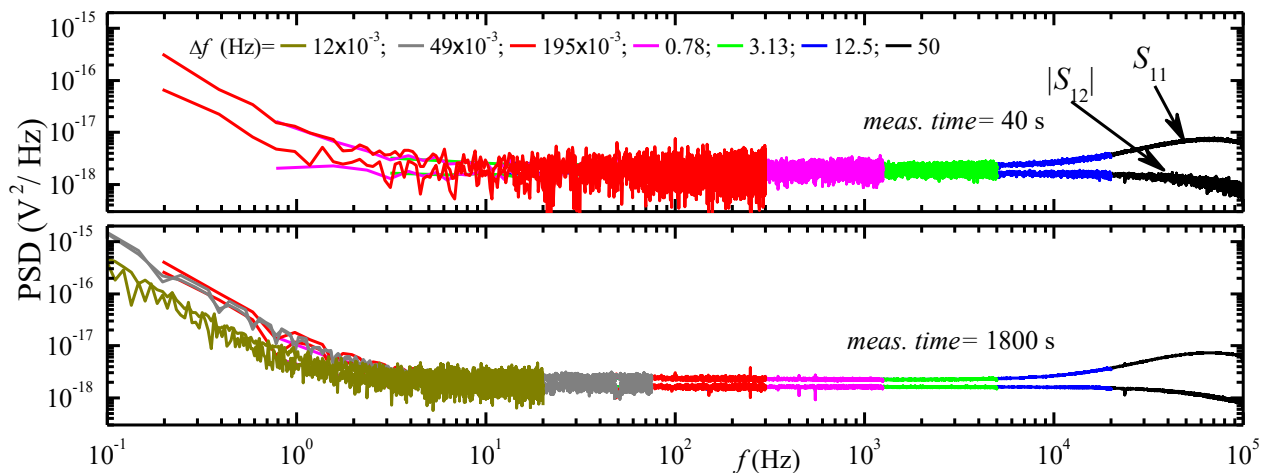


Fig. 2: Evolution of the spectra estimation with the new approach we propose. Plots are relative to cross correlation measurements on a 1 k Ω test resistor and are all shown in real time while the measurement progresses. Errors due to too large values of Δf are clearly noticeable in the lower plot.

¹ G. Scandurra, G. Cannatà, C. Ciofi, AIP Advances, **1**, 022144 (2011).
² V.E. Ivanov, En Un Chye, SIBCON 2017, 7998532 (2017).
³ M. Ferrari et al, ICNF 2015, 7288556 (2015)
⁴ G. Giusi, G. Cannatà, G. Scandurra, C. Ciofi, Int J Circ Theor App, **43**, 1455 (2015).
⁵ G. Giusi et al, Rev Sci Instrum, **87**, 044702 (2016).
⁶ G. Giusi, G. Scandurra, C. Ciofi, Fluct Noise Lett, **12**, 1350007 (2013).

⁷ D. Talukdar, R. K. Chakraborty, S. Bose, K. K. Bardhan, Rev Sci Instrum, **82**, 013906 (2011).
⁸ L. Baracchino, G. Basso, C. Ciofi, B. Neri, IEEE T Instrum Meas, **46**, 1256 (1997).
⁹ G. Scandurra, G. Cannatà, G. Giusi, C. Ciofi, Rev Sci Instr, **85**, 125109 (2014).
¹⁰ G. Scandurra, G. Giusi, C. Ciofi, Rev Sci Instr, **85**, 044702 (2014).
¹¹ C. Ciofi, G. Scandurra, G. Giusi, G. Cannatà, I2MTC 2017, 7969739 (2017).

How fluctuations of membrane permeability parameter influence on subdiffusion in a membrane system

Tadeusz Kosztołowicz

Institute of Physics, Jan Kochanowski University, ul. Świętokrzyska 15, 25-406 Kielce, Poland
e-mail address: tadeusz.kosztołowicz@ujk.edu.pl

Subdiffusion can occur in media, as gels or porous media, in which random walk of particles is significantly hindered by a complex structure of a medium. In a one-dimensional system, subdiffusion is often characterized by a time evolution of mean square displacement of a particle

$$\langle (\Delta x)^2 \rangle = \frac{2Dt^\alpha}{\Gamma(1+\alpha)}, \quad 0 < \alpha < 1,$$

where D denotes a subdiffusion coefficient, α is a subdiffusion parameter and Γ denotes the Gamma function. The case of $\alpha=1$ corresponds to normal diffusion. Subdiffusion is usually described by the following subdiffusion equation with the Riemann-Liouville fractional time derivative¹

$$\frac{\partial P}{\partial t} = D \frac{\partial^{1-\alpha}}{\partial t^{1-\alpha}} \frac{\partial^2 P}{\partial x^2}, \quad (1)$$

where

$$\frac{\partial^{1-\alpha} P(x,t)}{\partial t^{1-\alpha}} = \frac{1}{\Gamma(\alpha)} \frac{\partial}{\partial t} \int_0^t dt' (t-t')^{\alpha-1} P(x,t').$$

The choice of boundary conditions at the membrane is a fundamental problem in the modeling of subdiffusion or normal diffusion in biological systems and in engineering science when the filtration process is considered. We suppose that the thin membrane occupies a region (x_N, x_N+d) , where d is assumed to be very small, the particles move independently and do not clog the membrane. Using the method presented in the papers^{2,3} one can derive the boundary conditions at a thin membrane. The first boundary condition demands the continuity of a subdiffusive flux at the membrane and the second one reads

$$P(x_N^-, t | \rho) = \left(1 + \frac{d}{\rho\sqrt{D}} \frac{\partial^{\alpha/2}}{\partial t^{\alpha/2}} \right) P(x_N^+, t | \rho), \quad (2)$$

where ρ is the probability of stopping a particle by the membrane when it attempts to jump through the membrane, $\rho > 0$, d denotes a membrane thickness, $P(x,t|\rho)$ is a probability of finding the particle at point x and at time t in a system in which the membrane permeability is controlled by the probability ρ . The solutions to Eq. (1) with the boundary conditions described above are shown in the papers^{2,3}. Since Eq. (2) contains the fractional time derivative, a transfer of particles through a thin membrane is a "long-memory process", even for the case of normal diffusion⁴.

In this contribution we consider subdiffusion in a membrane system in which the probability of particles passing through the membrane fluctuates. Let $f(\rho)$ denotes a distribution of the probability ρ and $P(x,t)$ is a solution to Eq. (1) for a system with fluctuating membrane permeability. We will show that the flux is still continuous at the membrane and the boundary condition Eq. (2) should be replaced by the following one

$$P(x_N^-, t) - \frac{d}{\sqrt{D}} \int_0^t dt' \Lambda(t-t') P(x_N^-, t') = P(x_N^+, t) + \frac{d}{\sqrt{D}} \int_0^t dt' \Lambda(t-t') P(x_N^+, t'), \quad (3)$$

where

$$\Lambda(t) = \mathcal{L}^{-1} \left[s^{\alpha/2} \int_0^1 d\rho \frac{f(\rho)}{2\rho + d\sqrt{s^\alpha/D}} \right],$$

\mathcal{L}^{-1} denotes the inverse Laplace transform with respect to the variable s .

We will show that fluctuations of the membrane permeability parameter change the dynamics of the subdiffusion process. As an example, we will consider subdiffusion in a membrane system in which fluctuations are described by the beta distribution

$$f(\rho) = \frac{\Gamma(u+v)}{\Gamma(u)\Gamma(v)} \rho^{u-1} (1-\rho)^{v-1},$$

where u, v are parameters. We will find the exact solutions to Eq. (1) in terms of the Laplace transform and their form in the time domain in the limit of long time. Then, these solutions will be compared with the solutions generated by the boundary condition Eq. (2).

As it was shown in the paper⁵, the occurrence of absorption significantly changes the nature of subdiffusion. As unsolved problem that can be widely used in the description of subdiffusion in biological systems we mention here the problem of including fluctuations of subdiffusion and absorption parameters, together with fluctuations of the membrane parameter, into a subdiffusion-absorption model.

1. R. Metzler and J. Klafter, Phys. Rep. **339**, 1 (2000).
2. T. Kosztołowicz, Phys. Rev. E **91**, 022102 (2015).
3. T. Kosztołowicz, Int. J. Heat Mass Transf. **111**, 1322 (2017).

4. T. Kosztołowicz, S. Wąsik and K.D. Lewandowska, Phys. Rev. E **96**, 010101(R) (2017).
5. T. Kosztołowicz, J. Chem. Phys. **146**, 084114 (2017).

On the design of an automated system for the characterization of the electromigration performance of advanced interconnects by means of low frequency noise measurements

G.Scandurra¹, S. Beyne², G. Cannata¹, G. Giusi¹ and C. Ciofi¹
¹University of Messina, Dept. of Engineering, C.da di Dio, I-98166, Messina, Italy
e-mail: gscandurra@unime.it
²imec, Kapeldreef 75, B-3001 Leuven, Belgium

I. INTRODUCTION

Electromigration (EM) is a mass transport caused by the momentum exchange between the electrons accelerated by an electric field and the metal ions in a conductor. EM is accelerated at high temperatures and high current densities and is a major concern for the reliability of microelectronics interconnects. The continuous downscaling of the interconnect line widths further deteriorates the reliability and at the same time leads to an increase in line resistance. At line widths below 10 nm, the EM performances of Cu based lines will become insufficient and the line resistance unacceptably large^{1,2}. Therefore new materials are being investigated as potential candidates to replace Cu in future generations of interconnection systems. Low Frequency Noise Measurements (LFNM) have been long recognized as a very sensitive tool for the characterization of EM in metal lines^{3,4}. Because of the high sensitivity of LFNM, important information on the EM process can be obtained at much less accelerated stress conditions and in a fraction of the time with respect to conventional MTF (Median Time to Failure) tests. Recently, it has been observed that the temperature dependence of the low frequency noise can be used to directly extract information about the activation energy of the EM process⁵. Such a test method is beneficial to both the semiconductor industry and fundamental EM research. While performing a single LFNM at a given temperature and at a given bias condition does require a few tens of minutes, repeating such measurements for a large number of closely spaced temperatures without sufficient automation can be extremely challenging. In this work we report on the progresses toward the goal of designing a fully automated system.

II. PROPOSED SYSTEM

Obtaining high sensitivity in LFNM requires that: i) instrumentation with very low background noise be employed; ii) interferences coupling with the measurement chain be properly shielded. Test samples for EM testing have resistances in the order of 10 k Ω with a maximum test current in the order of 1 mA and minimum test currents limited by the sensitivity of the measurement chain^{1,2}. Test temperatures should extend up to 300 °C (note that commercially available systems have a maximum operating temperature up to 200 °C). A schematic representation of the test set-up is reported in Fig. (1). Since we are interested in the investigation of the $1/f$ noise produced by the sample, whose level decreases when the test current decreases, we need instrumentation with excellent flicker noise performances. To ensure the lowest level of background noise we can employ battery supplied custom instrumentation for both the amplifier and the current source in the setup in Fig. 1^{6,7}. Batteries with a capacity of 10 Ah are typically sufficient to ensure continuous operation for several hours, so that these pieces of instrumentation

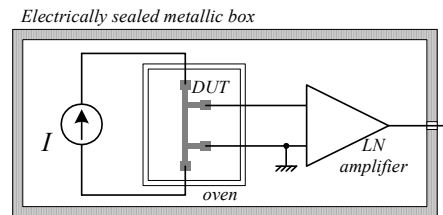


FIG. 1. Simplified diagram of the measurement set-up employed for the characterization of EM by means of LFNM.

can be easily accommodated, together with the batteries, within the very same shielded environment (typically a metallic box) containing the sample, thus insuring rejection of external electromagnetic interferences. Designing a battery supplied oven capable of unattended operation for several hours, as it would be required in an automated system capable of scanning several temperature set points with sufficient resolution, is, however, impractical because of the huge size of the required batteries that would not fit within any reasonably sized shielding box.

The problem to be addressed, therefore, was that of providing power to the heater of the sample holder from outside the shielded box while maintaining a high degree of electromagnetic insulation in order not to degrade the performances of the measurement system. The approach we followed is represented in Fig. (2). The sample holder is made of two cylindrical sections (top and bottom in Fig. (2)). The top section is a solid cinder of aluminum (diameter 10 cm) with a hole in the bottom so that a PT100 sensor can be placed in close proximity to the top surface that is in thermal contact with the sample. An empty volume is present in the bottom section so that a heater can be accommodated (in close contact with the top section). The bottom section has a lateral hole into which a brass pipe is screwed-in that allows for the electrical

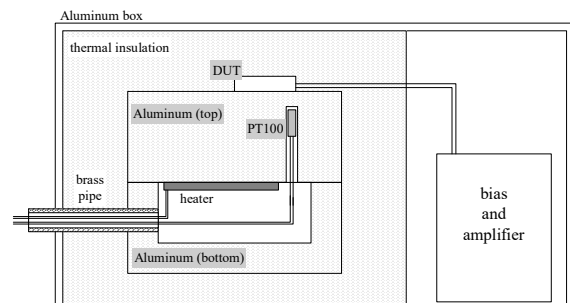


FIG. 2. Structure of the temperature controlled low noise measurement chamber. The heater and sensor cable never cross the metallic EM insulation barrier.

cables (heater and PT100) to be brought outside the shielded box for connection to standard, power line operated instrumentation. As it is apparent from Fig. (2), these cables never cross the shielding surface. In fact, the surface of the void space inside the holder topologically belongs to the outside surface of the shielding box. Clearly, the brass pipe in contact with the sample holder and the shielded box represents a path through which heat is dispersed, thus increasing the power requirements for maintaining the sample holder at the highest temperature. This, however, is not a major concern since, with the approach we propose, a standard programmable power supply can now be used without significant degradation of the background noise. To demonstrate the effectiveness of the approach we propose, we report on the result of noise measurements on one unbiased 10 k Ω resistor as a DUT with the oven maintained at 120 $^{\circ}$ C. In a first case (plot A in Fig. (3)) the top and the bottom sections were maintained 1 cm apart from one another. As it is apparent, no sensible noise estimation

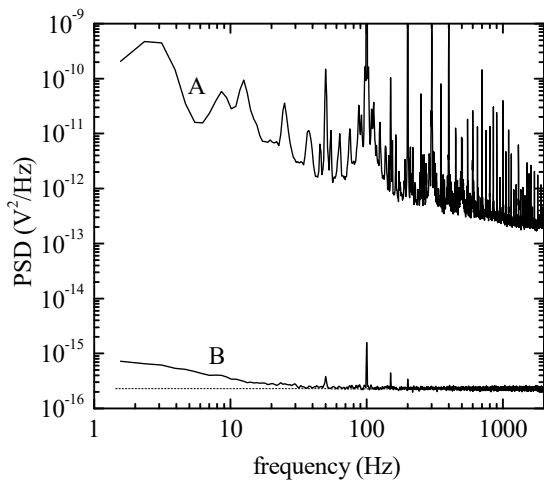


FIG. 3. Test measurements on an unbiased 10 k Ω resistor at 120 $^{\circ}$ C when the top and bottom sections in Fig. (2) are 1 cm apart (A) and when the gap is closed (b). The dotted line is the expected thermal noise of the resistor at 120 $^{\circ}$ C.

result could be obtained in this configuration because of the high level of interferences. However, when complete shielding is obtained by putting in strict contact the top and the bottom sections of the sample holder, interferences from the external power supply are dramatically reduced so that noise measurements with high sensitivity become possible (curve B in Fig. 3; the dotted line is the expected thermal noise of a 10 k Ω resistor at 120 $^{\circ}$ C). Measurements on actual samples (37 nm wide tungsten interconnects) during EM tests have been performed using an automated system based on the approach we have described. Measurements on 22 temperature set-points (ranging from 30 $^{\circ}$ C up to 300 $^{\circ}$ C) can be performed in less than 30 hours with the system unattended, with sufficient averaging on each spectrum to insure a reliable estimate of the frequency noise down to the hundreds of mHz range (Fig. (4)).

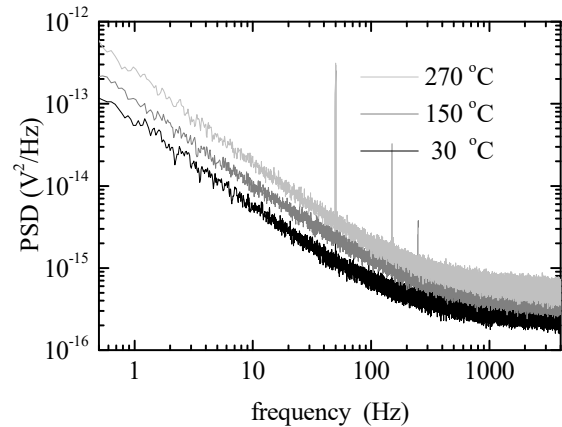


FIG. 4. Three out of 22 spectra obtained in test run on a 37nm wide tungsten single-damascene line from a process aimed at testing alternative interconnect metals; test current was 100 μ A.

III. OPEN ISSUES

While the system in the present configuration represents a significant improvement with respect to more conventional approaches, the fact that we can employ sophisticated control strategies for the temperature control (control system is based on an external computerized system) may allow us to go one step further, namely to perform continuous noise measurements while the test temperature is made to change linearly with time. This would allow to make the most profitable use of the measurement time and come closer to the ideal situation of recording the low frequency noise behavior for continuous temperature values. If the temperature change rate is sufficiently small, this approach has to work. The problem is that, in order to shorten the overall measurement time, one must establish the maximum temperature change rate that can be used. Apart from the problems arising from the fluctuation in the recorded voltage due to thermal stress relaxation that should be recognized and discarded as not directly related to EM noise, there are the following issues that need to be addressed:

- Deterministic temperature changes in a constant current biased resistor result in a deterministic voltage change across its ends because of the temperature dependence of the resistance; the effect of this deterministic change on the low frequency spectra estimation process is not obvious and should be accounted for;
- the problem of the effect of the changing temperature on the flicker noise estimation process needs to be addressed.

Particularly the last listed problem appears to be the most challenging one since, to the best of our knowledge, this is not an issue being dealt with in the literature.

¹ A. F. Mayadas and M. Shatzkes, PhysRevB, 1382, **1** (1970).
² A.S. Oates, ECS J Solid State Sc, N3168, **4**, (2015).
³ B. K. Jones, IET Circ. Device Syst., 149, **13** (2002).
⁴ B. Neri, C. Ciofi, V. Dattilo, IEEE T Electron Dev, 1454, **44** (1997).

⁵ S. Beyne, K. Croes, I. De Wolf, Z. Tókey, J. Appl. Phys., **119**, 184302 (2016).
⁶ G. Scandurra, G. Cannatà, C. Ciofi, AIP Advances, **1**, 022144 (2011).
⁷ G. Scandurra, G. Cannatà, G. Giusi, C. Ciofi, Rev. Sci. Instrum, 125109 (2014).

Mathematical model for the impact of political correctness on science

Laszlo B. Kish

Department of Electrical and Computer Engineering, Texas A&M University, TAMUS 3128, College Station, TX 77843-3128, USA
e-mail address: Laszlokish@tamu.edu

Scientific research can be considered as an information channel, where the incoming message is the science to be discovered. Information theory and the Shannon formula makes it clear that, if the message can be predicted then its surprise factor, that is, its information content (entropy) is reduced or nullified¹.

The maximum of the amount of new information is at the situation where the probabilities are uniformly distributed. Therefore, any deterministic bias reduces the information entropy of the message to be decoded.

Political Correctness in science means that a deterministic bias by pre-set goals, buzzwords, sensationalism, hype and biased reward mechanism influence the scope of research and its achievements.

The biased randomness in Shannon's formula is the result implying strongly reduced new information that the particular research can deliver. In other words, the type of research and achievements that are rewarded under the politically correct bias that impact funding, hiring and promotion, have lower surprise factor and diminished information content, originality and validity.

There is a long list of unsolved problems about this question, for example:

1. How strong is the bias at simple 1-bit (yes/no) questions and what is the implied reduction of information content?

2. How to generalize question for more complex multi-bit situations?

3. The scientific system is dynamic: it involves not only research but its funding, acceptance of papers submitted for publication, and the hiring/firing of scientists. How do dynamically these phenomena are coupled?

4. How do the above system-dynamics under politically correct bias reduce the information content of new research?

5. Particularly, how about originality, validity and importance of new research in the above system-dynamics ?

6. Obviously, anti-political-correctness bias also reduces the scientific information because that is also a deterministic bias. What is the response to questions 1-5 in this case?

7. What happens in a mixed system where both political correctness and anti-political-correctness are present in a polarized fashion?

REFERENCES

1. L.B. Kish, D.K. Ferry, "Information entropy and thermal entropy: apples and oranges", *J. Comp. Electr.* **17** (March 2018) 43–50; <https://arxiv.org/abs/1706.01459>

The problems of finding the steady-state probabilistic characteristics for nonlinear dynamical systems driven by white Poisson noise

Alexander Dubkov

Radiophysical Department, Lobachevsky State University, Russia
e-mail address: dubkov@rf.unn.ru

I. INTRODUCTION

Many stochastic processes occurring in population dynamics, neurodynamics and ecology exhibit instantaneous discrete jumps and therefore can not be provided by excitation in the form of white Gaussian noise. They must be modeled differently in terms of delta-pulse noise which characteristics are determined by the statistics of pulse amplitudes and intervals between stimuli. The nonlinear dynamical systems perturbed by Poisson white noise can be analyzed in the framework of Markovian theory on the basis of integro-differential Kolmogorov-Feller equation. The analytical treatment of such nonlinear dynamical systems poses more difficulties compared to those driven by white Gaussian noise. As a result, the exact expressions for the stationary probability characteristics of these systems have been obtained only for very limited cases, in particular, when the amplitudes of pulses have one-sided exponential probability distribution¹.

II. NONLINEAR DYNAMICAL SYSTEM WITH POISSON WHITE NOISE

In this report we consider a nonlinear dynamical system described by the following Langevin equation

$$\dot{x} = f(x) + g(x)\xi(t) \quad (1)$$

with the multiplicative Poisson white noise

$$\xi(t) = \sum_k a_k \delta(t - t_k), \quad (2)$$

where the moments of pulse appearance t_k form a Poisson flow of events with the mean rate ν and amplitudes a_k are statistically independent and identically distributed with the probability density function $W_a(z)$. The random process $x(t)$ in Eq.(1) is Markovian and its probability distribution is governed by the following integro-differential Kolmogorov-Feller equation

$$\frac{\partial P}{\partial t} = -\frac{\partial}{\partial x} [f(x)P] + \nu \int_{-\infty}^{\infty} W_a(z) \left[\exp\left\{-z \frac{\partial}{\partial x} g(x)\right\} - 1 \right] dz \cdot P(x, t), \quad (3)$$

which represents a particular case of general Kolmogorov equation obtained in the paper² for an arbitrary white non-Gaussian excitation $\xi(t)$. Using the technique of inverse differential operator^{3,4} in the case of one-sided probability distribution of pulse amplitudes $W_a(z) = \lambda e^{-\lambda z}$ ($z > 0$) (pulses of positive polarity in Eq.(2)) we obtain from Eq.(3) the following exact result for the stationary probability density function

$$P_{st}(x) = \frac{1}{f(x)} \exp\left\{-\int \left[\frac{\lambda}{g(x)} + \frac{\nu}{f(x)} \right] dx\right\}. \quad (4)$$

In more interesting, from physical point of view, situation of two-sided exponential probability distribution of pulse amplitudes $W_a(z) = \beta e^{-\beta|z|}/2$ we arrive from Eq.(3) at the following second-order differential equation

$$\left(g(x) \frac{d}{dx}\right)^2 [f(x)P_{st}] + \nu g(x) \frac{d}{dx} [g(x)P_{st}] - \beta^2 f(x)P_{st} = 0, \quad (5)$$

which solution can not be found in quadratures as Eq.(4).

Further we apply the results obtained to two concrete nonlinear systems. Specifically, we examine well-known Verhulst equation for the density of isolated population $x(t)$ with fluctuating saturation parameter

$$\dot{x} = rx - [\beta + \xi(t)]x^2 \quad (6)$$

which is Poisson white noise having pulses of positive polarity with one-sided exponential distribution of amplitudes. Equation (6) can adequately describe the effect of pandemics, natural disasters and other negative phenomena, leading to a significant reduction in the population size within a short time period. Substituting in Eq.(4), in accordance with Eqs.(1) and (6), $f(x) = rx - \beta x^2$ and $g(x) = -x^2$, we arrive at

$$P_{st}(x) = \frac{\lambda^{\nu/r}}{\Gamma(\nu/r) x^{1+\nu/r}} \left(1 - \frac{\beta x}{r}\right)^{\nu/r-1} e^{-\lambda \left(\frac{1-\beta}{x-r}\right)} \quad (0 < x < r/\beta), \quad (7)$$

The stationary probability distribution of the population density corresponding to Eq.(7) for different values of the rate of pulse appearance is depicted in Fig. (1). In the case of rare pulses $\nu/r < 1$ we observe the integrable divergence in the stable point $x=r/\beta$. When the rate of pulse appearance increases the divergence disappears and mostly probable value of the population density shifts to the left.

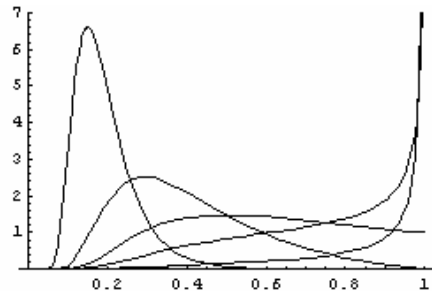


FIG. 1. The stationary probability distribution of the population density versus the rate of pulse appearance ν for fixed values of other parameters: $\lambda=1, \beta=1, r=1$.

Then we consider the stochastic Hongler equation

$$\dot{x} = -\gamma \tanh x + \frac{\xi(t)}{\cosh x} \quad (8)$$

which is a good approximation for the model of genetic selection because it retains some features of the latter⁵. In the case of multiplicative Poisson white noise having bipolar exponentially distributed amplitudes of delta-pulses it is very difficult to find the stationary probability density function directly from Eq.(5). Because of this, we reduce Eq.(8) to linear by changing the variable $y = \sinh x$. As a result, after very complex calculations we get

$$P_{st}(x) = \frac{\beta \cosh x}{\Gamma(\mu)\sqrt{\pi}} \left(\frac{\beta |\sinh x|}{2} \right)^{\mu-1/2} K_{\mu-1/2}(\beta |\sinh x|), \quad (9)$$

where $K_\alpha(z)$ is McDonald function and $\mu = \nu/(2\gamma)$. The plots of the stationary probability distribution are shown in Fig. (2). As can be seen from Fig. (2), we find noise-induced transitions in the behavior of the steady-state probability distribution when changing the noise parameter such as the mean rate of pulse appearance.

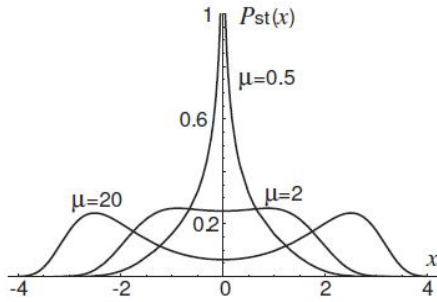


FIG. 2. The plots of stationary probability distribution for different values of the parameter μ and fixed value of $\beta=1$.

Unsolved problems are following:

How can we find the solution of Eq.(5) for the steady-state probability distribution in other situations?

How can we apply our results to more complex nonlinear dynamical systems then (1) driven by Poisson white noise?

ACKNOWLEDGEMENTS

The author acknowledges the support of the Russian Science Foundation (Grant No. 16-12-10496).

- ¹ C. Van den Broeck, *J. Stat. Phys.*, **31**, 467 (1983).
- ² A.A. Dubkov and B. Spagnolo, *Fluct. Noise Lett.*, **5**, L267 (2005).
- ³ A.A. Dubkov, O.V. Rudenko, and S.N. Gurbatov, *Phys. Rev. E*, **93**, 062125 (2016).
- ⁴ O.V. Rudenko, A.A. Dubkov, and S.N. Gurbatov, *Doklady Mathematics*, **94**, 476 (2016).
- ⁵ M.O. Hongler, *Helv. Phys. Acta*, **52**, 280 (1979).

Flicker noise problem

Zenoviy Kolodiy
Institute of Computer Technologies, Automatics and Metrology,
National Lviv Polytechnic University
28a S.Bandery str., 79013, Lviv, Ukraine
e-mail address: kzenoviy@gmail.com

I. INTRODUCTION

Among the unsolved problems of the XX century and the beginning of XXI century particular place possesses the problem of flicker noise (FN): Despite more than 80-year history of studying this noise, there is still no generally accepted hypothesis of its source (or sources), and therefore there are no generally accepted ways of FN reducing. Numerous experimental and theoretical studies of FN only revealed its versatile nature: known experimental results are often in contradiction or remain open to interpretation. This drew FN out of the range of narrowly applied, engineering matters, and made it significant problem of general physics.

An obstacle for creation of the theoretical model of FN is a number of unsolved yet contradictions between theoretical concepts of FN and experimental results. Namely: 1) contradiction between the theoretical model of singular source of FN and the experimental results of FN research, which is that the difference between the energy spectrum of noise at low frequencies in two identical samples is, as a rule, greater than the measurement error, which suggests the different sources of FN; 2) the contradiction between the theoretical models of FN ($S(f) \sim 1/f^\gamma$, where $S(f)$ - is spectral power density (SPD) of fluctuations (noise), f - is frequency), in which the degree of power γ is clearly defined ($\gamma=1$ or $\gamma=2$) and the experimental results showing variance of γ values ($\gamma = 0.8 \div 1.2$); 3) theoretical models, that well enough describe experimental results in the study of FM in electrical systems, do not explain presence of FM in biological, geological and other systems and vice versa. Therefore, the creation of an adequate model of FN, which would be confirmed by experimental results and would be able to explain the mechanisms of FN formation, is an important scientific and applied problem. It enables selection of electronics components with knowingly low level of own noise in low frequency range, and, as a consequence - to increase sensitivity of measuring equipment at low frequencies, which is important in medical, biological, geophysical and other research.

Among the various hypotheses of FN formation of a particular interest is the hypothesis of FN formation in the systems in a nonequilibrium thermodynamic state. This hypothesis lies in the base of the FN model, developed by the author, and verified using computer simulation. This was done assuming the following: 1) all real systems are in a nonequilibrium state; 2) the nonequilibrium state is a particular case of the equilibrium state, since if there are no external influences on the system (system is isolated), after some time it gets into the equilibrium state.

II. CONDUCTED RESEARCHES

Let us introduce the designation P_B for the fluctuations probability of parameters values of a system in an equilibrium state, and P_{NB} for the probability of fluctuations of a system in a nonequilibrium state. Accordingly, the designation of fluctuations SPD in an equilibrium system is $S_B(f)$, and the fluctuations SPD in a nonequilibrium system is $S_{NB}(f)$.

The connection between $S_B(f)$ and $S_{NB}(f)$ for an isolated system, which during certain time passes from nonequilibrium state to equilibrium, can be written as:

$$P_B \cdot S_B(f) = P_{NB} \cdot S_{NB}(f). \quad (1)$$

Expression for P_{NB} from¹:

$$P_{NB} = 1 - e^{-f\tau}. \quad (2)$$

Formula (2) is an expression for the fluctuations probability of a nonequilibrium system, where f - is the fluctuations frequency; τ - is system relaxation time.

As it is known from thermodynamics, the probability of fluctuations appearance in an isolated system in the state of thermodynamic equilibrium $P_B = 1$, and SPD of the equilibrium system is constant $S_B(f) = S_0 = \text{const}$ in the entire frequency range, starting from $f \rightarrow 0$ up to ultrahigh frequencies ($f \rightarrow \infty$), where quantum effects appear².

From (1) and (2):

$$S_{NB}(f) = \frac{e^{f\tau}}{e^{f\tau}-1} \cdot S_B(f). \quad (3)$$

Formula (3) is an expression for the fluctuations SPD in a nonequilibrium system.

From (3) at $\tau \rightarrow \infty$ (system is in equilibrium state) $S_{NB}(f) = S_B(f) = S_0 = \text{const}$. At $\tau < \infty$ and $f \rightarrow 0$ formula (3) takes the form:

$$S_{NB}(f) = \frac{e^{f\tau}}{e^{f\tau}-1} \cdot S_B(f) \approx S_B(f) + \frac{1}{f} \cdot \frac{S_B(f)}{\tau} = S_0 + \frac{1}{f} \cdot \frac{S_0}{\tau}. \quad (4)$$

Formula (4) for $S_{NB}(f)$ contains two components, one of which corresponds to equilibrium fluctuations $S_B(f) = S_0$, and the other corresponds to fluctuations of $1/f$ type (flicker noise), which is consistent with known experimental results.

By the experimentally determined fluctuations spectrum, one can determine the system relaxation time: from (3) at $f_0 = \frac{1}{\tau}$ $S_{NB}(f_0) \approx 1,58 \cdot S_0$, where the value of S_0 corresponds to $S_{NB}(f)$ in

the range of middle frequencies. Here the relaxation time is $\tau = \frac{1}{f_0}$. Analysis of the results of computer modeling shows that the relaxation time τ depends on the characteristics of internal structure of the system³. Therefore, FN can be considered not only as interference, but also as an informative signal that contains information about the features of internal structure of the system.

Analysis of formulae (3) and (4) allows us to solve the above mentioned contradictions between theoretical concepts of FN and experimental results: 1) by the dependence of τ on the internal structure of the system can be explained the difference between the noises energy spectra at low frequencies in two identical samples, since two samples with identical internal structures practically do not exist (or are very rare); 2) from formula (3) it is evident that the dependence of the SPD of FN is exponential and not $\sim 1/f^Y$; 3) formula (3) describes fluctuations SPD in any real (non-equilibrium) system, regardless of its nature.

Hence, flicker noise (or $1/f$ type noise) is not a peculiar noise specified by the particularity of processes occurring in the system (slow relaxation processes, superposition of random processes, abnormal Brownian motion, etc.), but it is of the same

nature as thermal noise. Increase of spectral components at $f \rightarrow 0$ indicates that the system is in a nonequilibrium state and the flicker component of noise occurs due to chaotic motion of the particles from which the system consists (for instance, electrons, ions, etc.) and their interaction with the elements of the system structure (including defects of structure). If the system is in the equilibrium state (theoretical case), the flicker noise component does not appear, and the system has only equilibrium fluctuations.

III. REFERENCES

- ¹ Z. A. Kolodiy, A. Z. Kolodiy Calculation of the noise level in electronic elements, Automatic Control and Computer Sciences, v. **43** (4), p. 179 – 183 (2009).
- ² H. Nyquist, Thermal agitation of electric charge in conductors, Phys. Rev., v. **32** (1), p.110-113, (1928).
- ³ Z. A. Kolodiy, Detection of changes in the structure of a system according to changes of its flicker noise, Ukr. J. Phys., v. **53** (7), p.718-722, (2008) (in Ukrainian).

Subdiffusion via dynamical localization induced by thermal equilibrium fluctuations

Jakub Spiechowicz¹ and Jerzy Luczka¹

¹*Institute of Physics,
Silesian Center for Education and Interdisciplinary Research,
University of Silesia, 41-500 Chorzów, Poland*

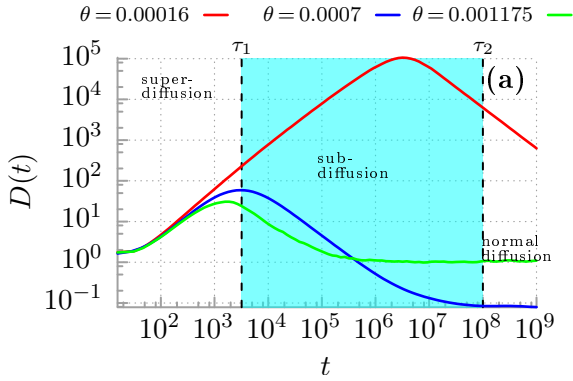


FIG. 1. Diffusion anomalies of an inertial Brownian particle moving in a periodic potential and driven by a unbiased time-periodic force.

We reveal the mechanism of subdiffusion which emerges in a straightforward, one dimensional classical *nonequilibrium* dynamics of a Brownian ratchet driven by both a time-periodic force and Gaussian white noise. In a tailored parameter set for which the deterministic counterpart is in a *non-chaotic* regime, subdiffusion is a long-living transient whose lifetime can be many, many orders of magnitude larger than characteristic time scales of the setup thus being amenable to experimental observations. As a reason for this subdiffusive behaviour in the coordinate space we identify thermal noise induced *dynamical localization* in the velocity (momentum) space¹. This novel idea is distinct from existing knowledge and has never been reported for any classical or quantum systems. It suggests reconsideration of generally accepted opinion that subdiffusion is due to road distributions or

strong correlations which reflect disorder, trapping, viscoelasticity of the medium or geometrical constraints.

The results provide essentially new insight into processes governing transport in complex systems especially of biological origin. Notably, they may explain certain aspects of strange kinetics occurring in living cells, with a particular emphasis on subdiffusive motion of molecular motors which are responsible for the intracellular transport. While we illuminate this phenomenon in the case of the driven Brownian particle moving in the asymmetric (ratchet) potential, in principle there are no restrictions for this *universal* mechanism to be likely observed also for other nonequilibrium setups: driven or non-driven but tilted symmetric periodic systems in strong dissipation regime or in overdamped limit. The latter is especially true due to the fact that in the deterministic limit our setup is in a non-chaotic regime. Therefore complex chaotic dynamics which is characteristic in one dimension for driven inertial systems is not needed for this mechanism to occur. Moreover, due to simplicity and universality of the system with its physical clarity as well as appealing strength of Brownian motion with its intrinsic Gaussian noise propagator our findings can open a wide area of studies and may be corroborated experimentally with a wealth of physical systems. One of the most promising setups for this purpose are optical lattices² and asymmetric SQUID devices^{3,4}.

Yet, a number of open questions of studied system still remain to be answered. Prominent examples of such problems may include the following: What is the mechanism responsible for transition from subdiffusion via thermal noise induced dynamical localization to normal diffusion? What are statistics of thermal fluctuations activated transitions between the observed three states? In particular, can they be of Levy type?..

¹ J. Spiechowicz and J. Luczka, *Nat. Sci. Rep.* **7**, 16451 (2017).

² F. Kindermann *et al.*, *Nat. Phys.* **13**, 137 (2017).

³ J. Spiechowicz, P. Hänggi and J. Luczka, *Phys. Rev. B* **90**,

054520 (2014).

⁴ J. Spiechowicz and J. Luczka, *New J. Phys.* **17**, 023054 (2015).

How to embed the self-assembly dynamics in the Langevin equations with spatio-(temporally) correlated noise?

M. Majka¹

¹Marian Smoluchowski Institute of Physics, Jagiellonian University, ul. *Profesora Stanisława Łojasiewicza 11, 30-348, Kraków, Poland*
e-mail address: maciej.majka@uj.edu.pl

I. INTRODUCTION

Colloidal systems can undergo a variety of transitions such as cluster formation, phase separation, vitrification etc. These phenomena can be simulated e.g. via the molecular dynamic methods, but, in many cases, this is computationally challenging. If we want to model the genuinely complex colloids, with multiple spatial and temporal scales of self-organization (such as e.g. cytoplasm in living cells), a higher-level molecular dynamics is necessary. One needs the effective Langevin equations that can embed various transitions in the properties of noise and friction itself. In this presentation I will describe how such formalism can be build basing on the Spatially Correlated Noise (SCN).

II. SCN AND SELF-ASSEMBLY

The following dynamics will be discussed:

$$\sum_j \Gamma(x_i - x_j) \dot{x}_i = \sum_i F(x_i - x_j) + \xi_i(x_i) \\ \langle \xi_i(x_i) \xi_j(x_j) \rangle \propto H(x_i - x_j)$$

where x_i is the position of i -th particle and $F(r)$ is the inter-particle deterministic force. $\xi(x_i)$ is Gaussian SCN, satisfying the correlation function $H(r)$. $\Gamma(r)$ is the spatially-dependent friction coefficient, which, as I will justify, is required by SCN, so the system is thermodynamically consistent, i.e. it obeys the Boltzmann distribution in equilibrium. The entire approach draws much inspiration from the theory of Generalized Langevin Equations (GLE). However, while GLEs utilize temporal correlations in noise and are well known to describe e.g. the anomalous diffusion, the effects of SCN are incomparably less understood and there are few systematic studies on this problem.

Up to now it was shown that SCN can be related to the effective interactions¹, i.e. the entropic interactions that occur in the averaged-out description of multi-component mixtures, which

very often control the self-assembly². SCN arises as a dynamical counterpart of these effects^{1,3}. Another advancement is the establishing of the fluctuation-dissipation relation for SCN. In the two particle case it predicts the intriguing separation effects in the properties of friction. This result describe the non-equilibrium like-charge attraction in the systems of surface-charged spheres in the solution of counter-ions¹. This approach has been recently extended to the multi-particle case^{3,4}. In this situation, the fluctuation-dissipation relation predicts the molecular arrest and critical slow-down in disordered systems, controlled by the density/temperature and the noise correlation function. These effects share a general similarity to the glass transition⁴. I will discuss all these examples and show that the formalism of SCN allows a significant number of exact, analytical results for arbitrary types of interactions.

III. OPEN PROBLEMS

While all these effects indicate a strong relation between SCN and self-assembly, there are two major problems that remain open. One is the inclusion of a more complex temporal dynamics, i.e. merging the SCN approach with GLEs. The other problem is how to include the non-equilibrium effects in this formalism. The latter is of particular interest, since the knowledge of the proper probability distribution is important in deriving the fluctuation-dissipation relation for SCN. Certain early developments on these two issues will be presented, such as rewriting the system equations as multiple Ornstein-Uhlenbeck processes.

ACKNOWLEDGEMENTS

M. Majka acknowledges the National Science Center, Poland for the grant support (2014/13/B/ST2/02014).

- ¹ M. Majka, P.F. Góra, Thermodynamically consistent Langevin dynamics with spatially correlated noise predicts frictionless regime and transient attraction effect, *Phys. Rev. E*, 94, 4, 042110 (2016).
- ² M. Majka, P. F. Góra, Analytical theory of effective interactions in binary colloidal systems of soft particles, *Phys. Rev. E*, 90, 3, 032303 (2014)
- ³ M. Majka, P. F. Góra, Collectivity in diffusion of colloidal particles: from effective interactions to spatially correlated noise, *J. Phys. A: Math. Theor.*, 50, 5, 054004 (2017)
- ⁴ M. Majka, P. F. Góra, 'Glass transition induced by the spatially correlated stochastic dynamics', <https://arxiv.org/abs/1707.07076> (2017)

Effects of noise-induced coherence on the performance of quantum absorption refrigerators

Viktor Holubec^{1,2} and Tomáš Novotný³

¹*Institut für Theoretische Physik, Universität Leipzig, Postfach 100 920, D-04009 Leipzig, Germany*

²*Department of Macromolecular Physics, Faculty of Mathematics and Physics, Charles University, V Holešovičkách 2, CZ-180 00 Prague, Czech Republic*

e-mail address: viktor.holubec@gmail.com

³*Department of Condensed Matter Physics, Faculty of Mathematics and Physics, Charles University, Ke Karlovu 5, CZ-121 16 Prague, Czech Republic*

e-mail address: tno@karlov.mff.cuni.cz.cz

Recently, it was shown on a simple model^{1,2} that noise-induced coherence can lead to an enhanced output power of heat engines. We study two models of quantum absorption refrigerators with the main focus on discerning the role of noise-induced coherence on their thermodynamic performance.

Analogously to the previous studies on quantum heat engines^{1,2} we find the increase in the cooling power due to the mechanism of noise-induced coherence. We formulate conditions imposed on the microscopic parameters of the models under which they can be equivalently described by classical stochastic processes and compare the performance of the two classes of fridges (effectively classical vs. truly quantum).

We find out that the enhanced performance is observed already for the effectively classical systems with no qualitative change in the quantum cases, which suggests that the noise-induced-coherence enhancement mechanism is caused by static interference phenomena. Nevertheless, there is a puzzling aspect remaining in the observation that a particular enhancement obtained for a *specific* set of classical parameters (all other classical setups perform considerably worse) is reached by virtually *any* truly quantum setup in the limit of maximum coherence. We thus arrive at an unconventional and not understood conclusion: the very best performance, which is achieved by a singular classical setup, can be matched, but not surpassed by a generic quantum system.

¹ M. O. Scully, K. R. Chapin, K. E. Dorfman, M. B. Kim, and A. Svidzinsky, Proceedings of the National Academy of Sciences **108**, 15097 (2011).

² K. E. Dorfman, D. V. Voronine, S. Mukamel, and M. O. Scully, Proceedings of the National Academy of Sciences **110**, 2746 (2013).

A study on simple measurement of mental and physical burden of patients during dental treatment

Hiroataka Asada¹, Kota Akehi, Marzieh Aliabadi Farahani, Naoki Itakura and Tota Mizuno

¹ The University of Electro-Communications, Faculty of Informatics and Engineering, Chofu/Tokyo, Japan
mmpt.hero17@gmail.com

I. INTRODUCTION

Dental treatment has many opportunities to give patients pain, and it is known that patients visit the dental with a sense of uneasiness, fear, and tension. Also, along with pain, you may be nervous about the environment of dental clinics such as sounds and smells. In such a case, using anesthesia or talking to patient is an effective way to decrease the stress. However, it is difficult for the dentist to identify the state of stress of the patient. Therefore, if the state of stress is objectively evaluated and the dentist can identify the patient's condition, there is a possibility to have the progress of smooth treatment according to the condition of the patient.

It has been evaluated in various methods in the measurement and evaluation research of the state of stress in the past, such as subjective evaluation, saliva test, blood test, measurement of brain wave, heart rate, blood pressure, sweating, nasal skin temperature, and sway of center of gravity of body¹. In subjective evaluation, saliva test, blood test, it takes time to evaluate, and in the measurement of brain waves, heart rate, blood pressure, perspiration, nasal skin temperature, restraint of sensor attachment occurs. On that point, measurement of the sway of center of gravity of body is a very useful method because it takes less time to evaluate and there is no restraint such as sensor attachment.

Previous studies on sway of center of gravity of body have shown relevance to visual stimulation, sound stimulation and physical / mental burden². However, there are stimuli and burden which cannot be found in other environments at dental clinic, and there are few reports on the relationship between these and the sway of center of gravity of body. In addition, in the supine position, body motion measurement using a body pressure sensor is common, and there is no example of measuring the sway of center of gravity of body in a situation where the patient is under treatment in a supine position in the dental unit. Furthermore, there is a merit that we can evaluate without consciousness of the patient if measurement is carried out by installing a sensor under a cushion or the like without touching the body.

Therefore, in this study, we assume a situation where a patient is under treatment in a supine position in a dental unit and examine whether it can simply evaluate the mental and physical burden of a patient from the center of gravity sway meter installed under the cushion.

II. EXPERIMENT

In this research, a center of gravity sway meter installed under a cushion was used. The center of gravity sway meter used is a Wii Balance Board (sampling frequency 100 Hz), and it can be handled as a cordless measuring instrument by connecting with PC with Bluetooth. The installation position was set at two parts of the back and buttock which are considered to move during treatment, and the

experiment was conducted with the unit always horizontal. FIG. 1 shows the dental unit used in the experiment.

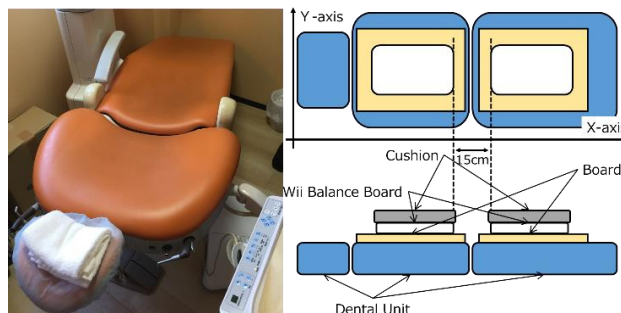


FIG. 1 Dental unit and experiment equipment

In this research, two kinds of experiments were conducted. First, in Experiment 1, three subjects were used, and each subject was measured for 5 minutes by two kinds of methods.

Experiment 1-A Measure in a rest state.

Experiment 1-B The first, third, and fifth minutes are measured in a rest state. Also in the second and fourth minutes as a mental burden, measure with the sound of the mouth washing machine on the mouth.

After the experiment, the x-y coordinates of the center of gravity of body at each sampling time was recorded, and each index was calculated. The outside peripheral area and the locus length per second were calculated every minute, and data was compared between experiment 1-A and experiment 1-B.

In Experiment 2, plaque removal was performed on two subjects as actual treatment. The treatment time was set to 5 minutes, and the rest time was set as 1 minute before and after. In addition, subjects held a mouse on the right hand of them, and asked to click when they felt pain. The indicators are the outside peripheral area, the locus length, and the number of clicks, each of which is calculated every 5 seconds for every 1 second.

Each experiment was carried out at the actual dental clinic in cooperation with a dentist.

III. RESULT AND DISCUSSION

As an example of the result of Experiment 1, the result of Subject A is shown in FIG. 2. In Fig. 2, focusing on the second minute, both the locus length and the outside peripheral area are larger in Experiment 1-B. On the other hand, focusing on the fourth minute, there was hardly any difference in the locus length, and in the outside peripheral area, there was no big difference as compared with the second minute. Because he got accustomed to sound stimulus, it may not have been recognized as a mental burden.

Comparing the position of installation of the center of gravity sway meter, it was confirmed that each subject showed a big

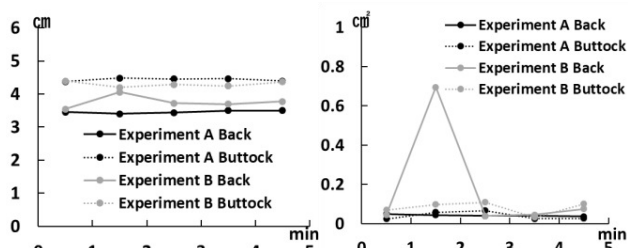


FIG. 2. The locus length per second and the outside peripheral area of subject A

difference in the lower the back than the buttocks. Therefore, it was shown that there is a possibility that the mental burden can be more easily evaluated the back. Also, for each subject, there was a big difference in the outside peripheral area than the locus length in both the second and fourth minutes. Therefore, it was suggested that the evaluation of the outside peripheral area may be easier to evaluate the mental burden.

Next is the result and discussion of Experiment 2. Like Experiment 1, the variation of the outside peripheral area was larger than the locus length. As an example of the outside peripheral area and the number of clicks of pain, the result of subject D is shown in FIG. 3. The black dotted line in FIG. 3 indicates the start and end of dental treatment.

As in the results of Experiment 1, subject D and E showed a large change in outside peripheral area in the back from the buttocks. Therefore, it was shown that mental and physical burden can be evaluated by measuring only the back even under dental treatment. In addition, the outside peripheral area has moved greatly after the finish of treatment, indicating the possibility that the center of gravity may move even when released from mental and physical burden.

Focusing on each subject, from FIG. 3, the subject D showed a larger outside peripheral area during dental treatment than at rest. Changes in the number of clicks and in the outside peripheral area almost agree with each other, so it is suggestion the possibility of measuring the mental and physical burden from the outside peripheral area. Therefore, change in the center of gravity of body is reduced due to power being applied to strong continuous pain, it is thought that change in center of gravity of body became large as a result of release from pain as well as after finish of treatment.

In this experiment, except for subject E, which did not feel pain almost, carried out two additional experiments on Subject D. There was no physical burden in Experiment 1, but Experiment 2 is an experiment accompanied by a physical burden. For comparison between mental burden alone and mental and physical burden, the average of the outside peripheral area when the number of clicks is 0 and the number of clicks is 1 or more is compared with that at rest and is shown in Table 1. Even when each subject did not feel pain, the outside peripheral area moved, and it was shown that the outside peripheral area moves further more with pain. In order to evaluate the mental and physical burden, it is considered that contrivance such as combining with not only the outside peripheral area but also other indicators is necessary.

Therefore, in order to examine the movement of the subject in detail this time, the x coordinate of the back of the subject D and

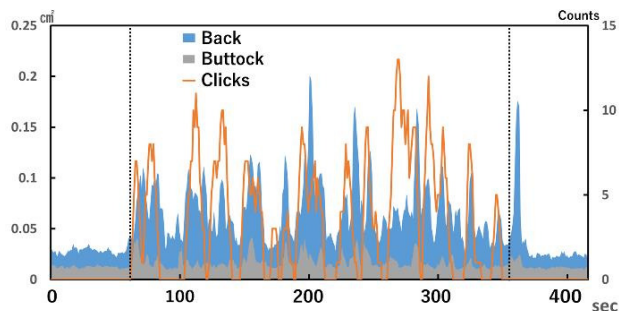


FIG. 3. The outside peripheral area and the number of clicks of the subject D

Table. 1. Increase rate of outside peripheral area of each subject before treatment (%)

	D 1st	D 2nd	D 3rd	E
Click 0 times	142.4	133.9	199.9	106.8
Click one or more times	222.4	217.2	267.3	109.7

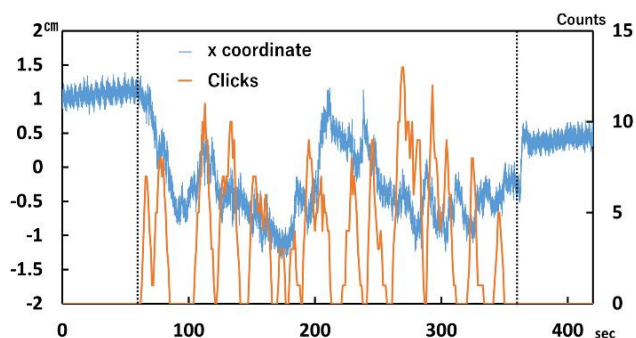


FIG. 4. The x coordinate of the back of subject D and the number of clicks

the number of clicks are shown in FIG. 4. From FIG. 4, it can be seen that the center of gravity of body moves in the head direction before the number of clicks increases, and moves in the foot direction when the number of clicks exceeds the peak. This shows that the center of gravity of body is moving before feeling pain, so it is suggestion that there is a possibility of measuring the mental burden of the patient.

IV. CONCLUSION

It was found that the outside peripheral area of the supine position is easy to move with the back large under dental treatment and the outside peripheral area is more easily changed. In addition, it was suggested that the mental and physical burden of the patient could be measured under dental treatment. The future task is to increase the number of subjects and to consider how to evaluate mental and physical burden.

¹ Yoshihide Tanaka and Shinichi Wakita, Stress and fatigue biomarkers, Journal of Pharmacological Sciences, 137.4: 185-188,2011(in Japanese)

² Shin Murata and Akira Tsuda, Stress and fatigue biomarkers, Journal of Physical Therapy Science, 20.3: 213-217, 2005(in Japanese)

Fluctuations of the red blood cells

Sylwia Babicz¹ and Barbara Stawarz-Graczyk²

¹ Faculty of Electronics, Telecommunications and Informatics, Gdańsk University of Technology, Department of Metrology and Optoelectronics, 11/12 G. Narutowicza Str., 80–233 Gdańsk, Poland
e-mail address: sylwia.babicz@eti.pg.edu.pl

² Faculty of Electronics, Telecommunications and Informatics, Gdańsk University of Technology, Department of Metrology and Optoelectronics, 11/12 G. Narutowicza Str., 80–233 Gdańsk, Poland
e-mail address: bstawarz@eti.pg.edu.pl

I. INTRODUCTION

The problem of fast diagnostics is a matter commonly present in medicine. An important aspect of the treatment process is smooth and clear identification of possible diseases. Early detection of the disease gives an opportunity to take therapy immediately and thus – effectively. As a result, the cure may minimize the effects of the disease. The desire to extend and improve the quality of life is one of the main factors of the progressive development of medical diagnostics. One of the key information about the patient's health is blood which is the basic diagnostic test. Its analysis is needed in the majority of disease cases. Some health problems are detected unambiguously just by analyzing blood. Examples of such diseases can be all kinds of anemia resulting in a deficiency or deformation of the red blood cells (RBCs) - erythrocytes.

Major structural RBCs changes are the result of erythrocytes membrane fluctuations which may be important in the diagnostic process. The vibrations of the cell membrane should be related to the disease process resulting in disintegration or change the shape of the erythrocyte. Some research confirms that vibrations of red blood cells are associated with the metabolic activity controlled by changing the concentration of adenosine-5'-triphosphate (ATP). The nucleotide takes part in important metabolic processes and controls biochemical energy¹. The ATP concentration can be related with the provided and absorbed magnesium ions. The decrease in magnesium is called hypomagnesemia. The disease is usually considered as the main factor of depression, especially in cases refractory to standard treatment.

The complex membrane fluctuations of erythrocytes analysis exacts advanced three dimensions visualization system. As the RBCs do not have organelles and nuclei they can be considered optically homogenous and transparent objects. Consequently, they modify only the phase of the light propagating through from them, little affecting intensity and polarization of the light. From the microscopy point of view, RBCs can be regarded as phase objects. Specialized techniques, such as quantitative phase imaging (QPI) are needed to obtain quantitative information on RBCs. Systems described in literature can provide quantitative information about the structure and size of RBC. The proposed systems use a phase contrast (PC) microscopy technique where the light propagating through the specimen (i.e. an RBC) interferes with a reference beam, forming a fringe field in which the phase is encoded into intensity. Quantitative information about the shape and size of the investigated RBCs can be obtained by processing the fringe pattern using tools routinely employed in the field of optical interferometry. Following, this information can be analyzed in the time domain.

The authors carried out the research in a measurement system which enables the image registration. The investigation system should provide good dimensional resolution in order of tens of nanometers. Such systems are best implemented based on microscope. So that the special measurement system for phase objects fluctuations observation was proposed and described by authors in articles^{2, 3}. The constructed system consists of a laser beam ($\lambda = 532$ nm), which goes first through the microscope objective, having magnification in the range 40x – 60x and next through the investigated object and is reflected by a mirror. Then the beam passes through a shutter, polarizer, the Wollaston prism and analyzer. The final image is created on a CCD/CMOS camera.

The next stage of the research was the image processing which authors carried out in order to know what the shape changes of the RBC. The results are presented in the next chapter.

II. RESULT

The lack of organelles and nuclei as well as uniform structure of RBCs enables treating them as optically homogenous and transparent object. Therefore, the light passing through an RBC undergoes only a phase shift. The fringe spacing depends on the wavelength of light and on the angle between directions of propagation of the interfering beams. Any change in the fringe pattern from the straight parallel form corresponding to the interference of two plane waves is caused by the phase shift introduced by the object, and proportional to its thickness. Therefore, from the shape of the fringes it is possible to find the 2D profile of phase change and estimate the RBC thickness. Flickering can be investigated by recording series of images, calculating the RBC thickness distribution as a function of time and studying selected characteristics of this distribution.

Because of imperfection of measurement system caused by defects of optical elements, pollutants, dust and other light sources, every phase image is burthened by speckles and other distortions. The pattern superinduced with fringe image precludes next proper analysis. To eliminate the adverse effect, the reference image without any object is necessary (Fig. 1). It is used to design the filter eliminating the measurement system distortions. The example of phase image of RBC by differential phase microscope (DPM) is presented in Fig. 2. The image processing based on Fast Fourier Transform enables transform the DPM image into three dimensional representation of RBC (Fig. 3).

It is hard to determine objectively the quality of the RBC image (Fig. 3). On this step of the processing a mathematical procedure based on some objective parameters should be proposed. One of such statistical parameters, which would describe informativeness of the analyzed image and a possibility of its automatic estimation, is the entropy H . The entropy can be viewed as the amount of information provided by the image. Thus, it is

merely a statistical average of uncertainty or information in the analyzed data.

The Shannon entropy is a measure of the uncertainty associated with a random variable. Specifically, the Shannon entropy quantifies the expected value of the information contained in a message. The Shannon entropy $H(X)$ of a random variable X having the values from the set $(x_0, x_1, \dots, x_i, \dots, x_k)$ is defined as:

$$H(X) = -\sum_{x_i=0}^{x_k} p_{x_i} \log_2 p_{x_i} \quad (1)$$

where p_{x_i} denotes the probability of $X = x_i$.

The digital images, of $M \times N$ pixels, can be interpreted as an array of random values of the variable X . By denoting the number of pixels having greyscale intensity i ($0 \leq i \leq 255$) within the analyzed image as d_i , we can estimate their occurrence probability. Therefore, the Shannon entropy H of the image can be calculated as:

$$H(X) = -\sum_{i=0}^{255} p_i \log_2 p_i = -\sum_{i=0}^{255} \frac{d_i}{M \times N} \log_2 \frac{d_i}{M \times N} \quad (2)$$

Authors decided to consider only the RBC area in the image. The procedure is dictated by the different size of RBC in each measurement. Moreover, only the information about the RBC is considered, so the background area should not be taking into account in entropy calculations. Such calculated entropy of the presented image RBC (Fig. 3) is equal 2.1636.

Some diagnostic methods required not only one image of the erythrocyte but complex behavior analysis. To measure up to the expectation, the measurement system enables recording movie of the RBC with proper frame per second. Each movie frame is one image in set of data.

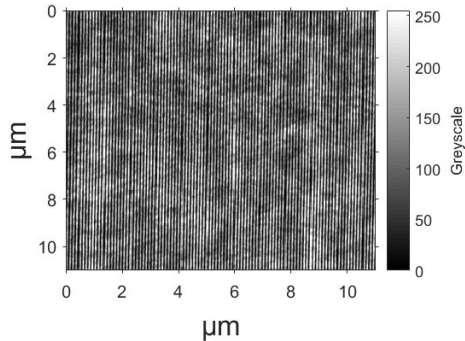


FIG. 1. Reference image.

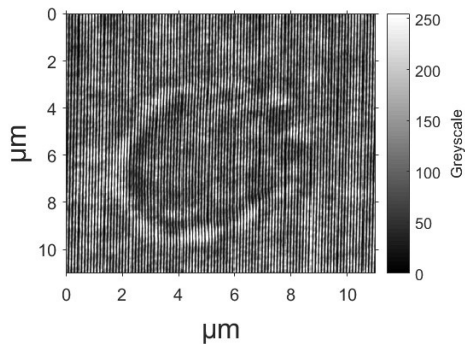


FIG. 2. DPM image of RBC.

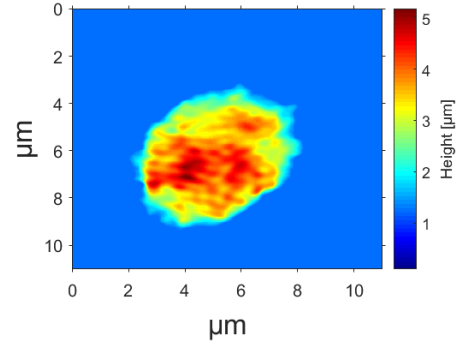


FIG. 3. Processed DPM image of RBC.

It is apparent that the analyzed RBC subtly changes its structure with time. The alterations are clearly visible in movie recorded by measurement system. In order to confirm the hypothesis that the movement depends on diseases, a quantitative study of the flickering and shape changing of the RBCs is needed. In the presented study, the behavior of RBCs from healthy subjects is investigated, in order to establish a comparison baseline and to take into account other factors, such as dehydration or sugar level, that may influence the behavior of RBCs. This part of the study also covers the changes the behavior of RBCs resulting from the standard process of handling the blood samples.

III. CONCLUSIONS

The 2D phase distribution in the RBC can be transformed into thickness map from which quantitative information about the shape and size of the investigated RBCs is obtained and analyzed in the time domain. The results of this analysis, most likely in the form of synthetic parameters, will be correlated with selected diseases and used to detect them at a stage much earlier than possible with conventional techniques.

The proposed project has two main objectives. The first, and most important, objective is performing a quantitative study of the temporal behavior of the RBCs, in order to acquire knowledge about its characteristics in healthy subjects (including natural variability factors) as well as in subjects diagnosed with some diseases, to recognize the modifications specific to particular diseases. The second objective is the development of data processing methods based on temporal data from the QPI microscopy system. As a result of research, a body of knowledge needed for early diagnosis of selected diseases will be developed and applied to further, more application-oriented research.

- ¹ Y. Park, C. A. Best, T. Auth, N. S. Gov, S.A. Safran, G. Popescu, S. Suresh and M. S. Feld, Metabolic remodeling of the human red blood cell membrane. (Proceedings of the National Academy of Sciences, vol. 107, no. 4, 2010).
- ² S. Babicz-Kiewlicz and B. Stawarz-Graczyk, Diffraction Phase Microscopy for observation on red blood cells fluctuation. (Zeszyty Naukowe Wydziału Elektrotechniki i Automatyki Politechniki Gdańskiej Nr 46, XXV Seminarium Zastosowanie Komputerów w Nauce i Technice'2015, Oddział Gdański PTETiS, 2015).
- ³ S. Babicz, B. Stawarz-Graczyk, P. Wierzbą, The observation system for phase objects by diffraction phase microscopy. (Metrology and Measurement Systems, vol. 25, no. 1, 2018).

Is energy conserved when nobody looks?

Adam Bednorz¹, Mateusz Frączak¹, Stanisław Sołtan¹, Wolfgang Belzig²
¹ Faculty of Physics, University of Warsaw, ul. Pasteura 5, PL02-093 Warsaw, Poland
e-mail address: abednorz@fuw.edu.pl
² Fachbereich Physik, Universität Konstanz, D-78457 Konstanz, Germany
e-mail address: wolfgang.belzig@uni-konstanz.de

Conservation principles are essential to describe and quantify macroscopic processes. Classically, they follow from invariance of dynamics under appropriate transformations while quantum mechanics states them for operators in Heisenberg picture. On the other hand quantum measurements, unlike classical, may disturb conserved quantities.

We show that the disturbance is present even in the noninvasive limit of weak measurement, which can be avoided for charge but not for energy, momentum and angular momentum. We exemplify

this effect not only in simple models but also in experimentally feasible setup.

Conservation can be restored by appropriately redefining quantum correlations but they are partly inaccessible by standard detection and violate relativistic objective realism.

Finite-Frequency Noise in a Kondo Quantum Dot with Asymmetric Coupling to the Reservoirs

A. Crépieux¹, S. Sahoo^{2,3}, T.Q. Duong¹, R. Zamoum⁴ and M. Lavagna^{2,5}

¹Aix Marseille Univ, Université de Toulon, CNRS, CPT UMR 7332, 13288 Marseille, France

e-mail address: adeline.crepieux@cpt.univ-mrs.fr

²Univ. Grenoble Alpes, CEA, INAC, PHELIQS, Theory Group, F-38000 Grenoble, France

³Physics Department and Research Center OPTIMAS, University of Kaiserslautern, 67663 Kaiserslautern, Germany

⁴Faculté des sciences et des sciences appliquées, Université de Bouira, rue Drissi Yahia, Bouira 10000, Algeria

⁵Centre National de la Recherche Scientifique - CNRS - 38042 Grenoble, France

I. INTRODUCTION

The understanding of noise in quantum systems is a fundamental issue when one wants to control the transfer of charges in an accurate way. We develop a theory for calculating the noise at finite-frequency in a quantum dot connected to two reservoirs, in the presence of inelastic scattering and asymmetric couplings with the reservoirs. By using the nonequilibrium Keldysh Green function technique, we establish an analytical expression for the noise in terms of the transmission amplitudes between the reservoirs and of some effective transmission coefficients which will be defined. The result that we obtain can be considered as the analog of the Meir-Wingreen formula¹ for the current. Moreover, a physical interpretation is given on the basis of the transmission of one electron-hole pair to one of the reservoirs, where it emits an energy after recombination. The results for the noise derivative versus the voltage V show a zero value until $eV = h\nu$, where ν is the frequency, followed by a Kondo peak when the quantum dot is in the Kondo regime. These findings are in good agreement with measurements recently performed in a carbon nanotube quantum dot².

II. FINITE-FREQUENCY NOISE

When the quantum dot is in a steady state and the flat wideband limit is considered, we show that the finite-frequency noise is given by the following formula³:

$$S_{\alpha\beta}(\nu) = \frac{e^2}{h} \sum_{\gamma\delta} \int_{-\infty}^{\infty} d\varepsilon M_{\alpha\beta}^{\gamma\delta}(\varepsilon, \nu) f_{\gamma}^e(\varepsilon) f_{\delta}^h(\varepsilon - h\nu) \quad (1)$$

where $f_{\gamma}^e(\varepsilon)$ is the distribution function for electrons with energy ε in the γ reservoir, and $f_{\delta}^h(\varepsilon - h\nu)$, the distribution function for holes with energy $\varepsilon - h\nu$ in the δ reservoir. The indices $\alpha, \beta, \gamma, \delta$ can take either the L value when it relates to the left reservoir, or the R value when it relates to the right reservoir. The expressions for the matrix elements, denoted as $M_{\alpha\beta}^{\gamma\delta}(\varepsilon, \nu)$, are given in Ref. 3. They depend on the transmission amplitudes $t_{\alpha\beta}(\varepsilon)$, on the reflexion amplitudes $r_{\alpha\alpha}(\varepsilon)$, on the transmission coefficients $\mathcal{T}_{\alpha\beta}(\varepsilon)$, and on some effective transmission coefficients $\mathcal{T}_{LR}^{\text{eff},\alpha}(\varepsilon)$, which are defined as:

$$t_{\alpha\beta}(\varepsilon) = i\sqrt{\Gamma_{\alpha}\Gamma_{\beta}}G^r(\varepsilon) \quad (2)$$

$$r_{\alpha\alpha}(\varepsilon) = 1 - t_{\alpha\alpha}(\varepsilon) \quad (3)$$

$$\mathcal{T}_{\alpha\beta}(\varepsilon) = |t_{\alpha\beta}(\varepsilon)|^2 \quad (4)$$

$$\mathcal{T}_{LR}^{\text{eff},\alpha}(\varepsilon) = 2\text{Re}\{t_{\alpha\alpha}(\varepsilon)\} - \mathcal{T}_{\alpha\alpha}(\varepsilon) \quad (5)$$

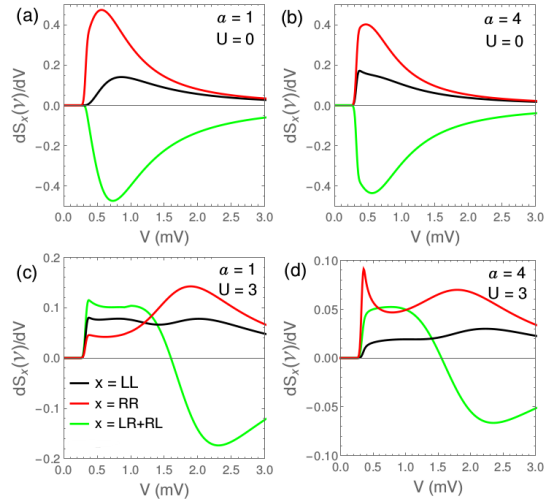
where $G^r(\varepsilon)$ is the retarded Green function in the quantum dot, and Γ_{α} is the coupling strength between the quantum dot and the α reservoir. Eq. (1) is obtained considering the approximation in which the two-particle Green function in the dot is factorized into a product of two single-particle Green functions in the dot. From Eqs. (1) to (5), we see that once $G^r(\varepsilon)$ is known, the transmission amplitudes and coefficients are entirely determined, and consequently, the noise given by Eq. (1) can be calculated explicitly. We want to underline that the effective transmission coefficient given by Eq. (5) takes into account the inelastic scattering contributions^{4,5}. When only elastic scattering is present or/and for a non-interacting system, we underline that $\mathcal{T}_{LR}^{\text{eff},\alpha}(\varepsilon)$ coincides with $\mathcal{T}_{LR}(\varepsilon)$ since in that case, we have: $2\text{Re}\{t_{\alpha\alpha}(\varepsilon)\} = \mathcal{T}_{\alpha\alpha}(\varepsilon) + \mathcal{T}_{LR}(\varepsilon)$, thanks to the optical theorem.

III. INTERPRETATION

According to Eq. (1), $S_{\alpha\beta}(\varepsilon)$ is given by the summation over ε and all possible configurations $\{\gamma, \delta\}$, of the transmission element $M_{\alpha\beta}^{\gamma\delta}(\varepsilon, \nu)$ weighted by the factor $f_{\gamma}^e(\varepsilon)f_{\delta}^h(\varepsilon - h\nu)$ corresponding to the probability of having a pair formed by an electron of energy ε in the γ reservoir and a hole of energy $\varepsilon - h\nu$ in the δ reservoir. Hence we interpret the auto-correlator $S_{\alpha\alpha}(\varepsilon)$ as the probability of transmission of an electron-hole pair from all possible configurations, to the final state for which both electron and hole is in the α reservoir, where by recombining it emits an energy $h\nu$. The additional presence of inelastic scattering does not affect this interpretation³. In the case when there are several possible transmission paths, as happens for $M_{\alpha\alpha}^{\alpha\alpha}(\varepsilon, \nu)$, we point out the importance of considering the quantum superposition of the transmission amplitudes for all possible transmission paths⁶.

IV. KONDO QUANTUM DOT

The retarded Green function for the interacting single level quantum dot is determined numerically by using a self-consistent renormalized equation-of-motion approach^{7,8,9}, which applies to both equilibrium and non-equilibrium situations. When one incorporates the expression of the Green function into Eqs. (1-5), we are able to calculate both the auto-correlators $S_{LL}(\varepsilon)$ and $S_{RR}(\varepsilon)$, and the cross-correlators $S_{LR}(\varepsilon)$ and $S_{RL}(\varepsilon)$. In Fig. (1), we plot the derivatives of $S_{LL}(\varepsilon)$, of $S_{RR}(\varepsilon)$ and of the sum $S_{LR}(\varepsilon) + S_{RL}(\varepsilon)$, which is a real quantity, versus the voltage V . We remark first that at voltage smaller than frequency, the noise derivative is equal to zero in all graphs, as expected at low temperature for the reason that the system does not emit energy at a voltage smaller than the energy provided to it, here $h\nu/e$. Then, we focus on the effect of interactions and on the effect of a coupling asymmetry on the noise profile. We note that the presence of interactions change the sign of the sum of the cross-correlators derivatives (green curves). Indeed, this quantity changes from negative sign at $U = 0$ to positive sign at $U \neq 0$ provided that $eV \lesssim U/2$. This positive sign can thus be seen as the seal of the Coulomb interactions present in the quantum dot. We also note the presence of a Kondo peak close to $eV \approx h\nu$ in the auto-correlator derivatives, together with a broad maximum at $eV \gtrsim U/2$, resulting from the Coulomb blockade which takes place in the system. We underline that with our choice of parameters, the estimation of the Kondo temperature with the help of the Haldane formula gives $T_K \approx 4.38$ K, which is much larger than the temperature in the reservoirs ($T = 80$ mK) and larger than the frequency ($\nu = 78$ GHz ≈ 3.74 K), which ensures the quantum dot to be in the Kondo regime. The profile of the red curve in Fig. (1d) resembles to the profile obtained in the experiments performed in a carbon nanotube Kondo quantum dot². For all the curves, we observe a strong asymmetry between $dS_{LL}(\varepsilon)/dV$ and $dS_{RR}(\varepsilon)/dV$ due to the asymmetric bias profile imposed to the junction. Indeed, we use: $\mu_L = 0$ and $\mu_R = -eV$. It also explains why the noise derivative is larger in the right reservoir than in the left reservoir at $U = 0$, since the latter one is grounded. Finally, we remark that the intensity of the noise derivative is reduced when interactions are present (compare the intensities in graphs (a,b) to the intensities in graphs (c,d)), in full agreement with the fact that the charge is frozen when the quantum dot is in the Kondo regime.



“FIG. 1. Noise derivatives as a function of voltage. The parameters are: $\mu_L = 0$, $\mu_R = -eV$, $T = 80$ mK, $\nu = 78$ GHz. Graphs (a,b) correspond to the noninteracting case: $U = 0$, and graphs (c,d) to the interacting case: $U = 3$ meV. Graphs (a,c) corresponds to the symmetric coupling case where $\Gamma_{L,R} = 0.5$ meV (i.e., $a = \Gamma_L/\Gamma_R = 1$), and graphs (b,d) to the asymmetric coupling case where $\Gamma_L = 0.8$ meV and $\Gamma_R = 0.2$ meV (i.e., $a = 4$). These graphs are extracted from Ref. 3.”

V. CONCLUSION

We have developed a theory to calculate the finite-frequency noise in a non-equilibrium Kondo quantum dot, which allows us to explain most of the features observed in the profile of the noise derivative as a function of bias voltage, i.e., the presence of a Kondo peak close to the frequency value which is the hallmark of the Kondo effect, and the presence of a broad maximum corresponding to the Coulomb blockade structure.

ACKNOWLEDGEMENTS

The authors acknowledge the Indo-French Centre for the Promotion of Advanced Research (IFCPAR); FundRef ID <http://dx.doi.org/10.13039/501100001852> (IN/Republic of India); under Research Project No.4704-02.

¹ Y. Meir and N.S. Wingreen, Phys. Rev. Lett. **68**, 2512 (1992).
² R. Delagrè, J. Basset, H. Bouchiat, and R. Deblock, Phys. Rev. B **97**, 041412(R) (2018).
³ A. Crépieux, S. Sahoo, T.Q. Duong, R. Zamoum, and M. Lavagna, to be published in Phys. Rev. Lett. (2018).
⁴ G. Zarand, L. Borda, J. von Delft, and N. Andrei, Phys. Rev. Lett **93**, 107204 (2004).

⁵ L. Borda, L. Fritz, N. Andrei, and G. Zarand, Phys. Rev. B **75**, 235112 (2007).
⁶ R. Zamoum, M. Lavagna, and A. Crépieux, Phys. Rev. B **93**, 235449 (2016).
⁷ R. Van Roermund, S.Y. Shiau, and M. Lavagna, Phys. Rev. B **81**, 165115 (2010).
⁸ M. Lavagna, J. Phys.: Conf. Ser. **592**, 012141 (2015).
⁹ M. Lavagna, in preparation (2018).

A noise signal generation method for microcontrollers with DACs

Zbigniew Czaja¹, Michał Kowalewski²

¹ Gdansk University of Technology, Faculty of Electronics, Telecommunications and Informatics, Department of Metrology and Optoelectronics, ul. G. Narutowicza 11/12, 80-233 Gdansk, Poland
e-mail address: zbczaja@pg.edu.pl

² Gdansk University of Technology, Faculty of Electronics, Telecommunications and Informatics, Department of Metrology and Optoelectronics, ul. G. Narutowicza 11/12, 80-233 Gdansk, Poland
e-mail address: michal.kowalewski@eti.pg.edu.pl

I. INTRODUCTION

At present, to generate a noise signal in mixed-signal electronic systems, there are used random number generators. In practice, pseudo-random number generators are used due to their simple construction and easy hardware implementation. Especially, well known Linear Feedback Shift Registers (LFSRs)^{1, 2} are easily implemented in hardware^{3, 4, 5} as well as in software^{6, 7, 8, 9}.

LFSRs are used not only in cryptography but also in circuit testing for test-pattern generation and signature analysis, especially in built-in self-test techniques and in digital broadcasting systems. Because LFSRs enable a very fast generation of pseudo-random sequences, they can be applied to generating an approximation of white noise used e.g. in sound generators and in the measurement equipment for digital transmissions.

Often the mixed-signal electronic systems are controlled by microcontrollers. Therefore, to build the noise generators we can use microcontrollers already existing in the system. Thanks to this, we avoid introducing hardware redundancy into the system. Hence, in the paper we propose a new method of noise signal generation based on software implementation of LFSRs for microcontrollers with internal Analog-to-Digital Converters (ADCs) and Digital-to-Analog Converters (DACs). The ADC is used to reseed the LFSR (similarly to that presented in the article⁹), whereas the noise signal is generated by the DAC (Fig. (1)).

The method is presented on an example of an 8-bit ATXmega32A4 microcontroller¹⁰, which is equipped with numerous well-working measurement peripheral devices, e.g.: one 12-bit 4-channel ADC and one 12-bit 2-channel DAC. The structure of the LFSR is based on the common polynomial PRBS7:

$$L(x) = x^7 + x^6 + 1 \quad (1)$$

II. OPERATING PRINCIPLES

In Fig. 1 we can see the hardware structure of the noise signal generator, i.e. only the microcontroller. The ADC of the microcontroller serves as the source of entropy. It samples the voltage at floating pins ADC0, .. ADCn, thus it measures the noise signal; more precisely - interferences from inter alia working digital blocks of the microcontroller. We use a 1 V internal voltage reference¹⁰ to increase the measurement sensitivity of the ADC, which increases the susceptibility of the ADC to noise,

what in our case is preferred. As the reseeding value of the 7-bit LFSR (we base on a polynomial PRBS7) seven lower bits of the 12-bit ADC result are taken. The actual random data from the ADC are used to reseed the LFSR after each its full work cycle consisting of 127 steps (see Fig. 2).

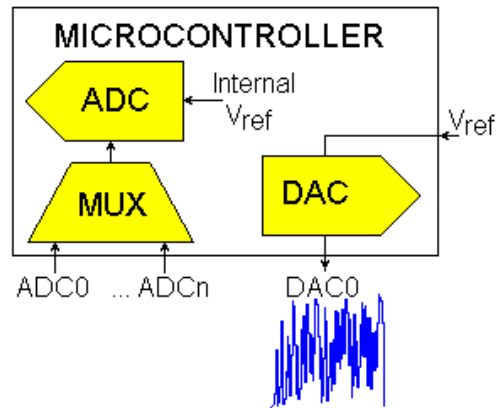


FIG. 1. The hardware structure of the noise signal generator based on a microcontroller with internal ADC and DAC converters.

This solution results from hardware limitations of peripheral devices of an ATXmega32A4 microcontroller¹⁰. The minimum conversion time for 12-bit resolution of the ADC takes 14 μ s, whereas the maximum conversion rate of the DAC is equal to 1000 kps. Therefore, the minimum DAC conversion time is at least 14 times less than that of the ADC (we have to take into account the time needed for servicing the ADC by the software).

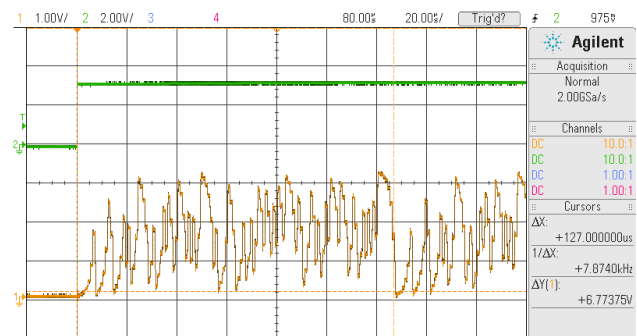


FIG. 2. The noise timing generated at the DAC output of an ATXmega32A4 microcontroller for a polynomial PRBS7.

Low-Frequency Noise in Quasi-1D van der Waals Nanowires Implemented with Transition Metal Trichalcogenides

A. Geremew¹, S. Rumyantsev^{1,2}, M. A. Bloodgood³, T. T. Salguero³ and A. A. Balandin¹

¹Department of Electrical and Computer Engineering, University of California, Riverside, California 92521 USA

e-mail address: balandin@ece.ucr.edu

²Ioffe Physical-Technical Institute, St. Petersburg, 194021 Russia

e-mail address: roumis4@gmail.com

³Department of Chemistry, University of Georgia, Athens, Georgia 30602 USA

e-mail address: salguero@uga.edu

I. INTRODUCTION

A number of transition metal trichalcogenides (TMT) have crystal structures composed of quasi-one-dimensional (1D) atomic threads, i.e. TMT chains, with an individual cross-sectional area on the order of $1 \text{ nm} \times 1 \text{ nm}$. These chains are organized in layers weakly bonded together by van der Waals forces. TMTs can be exfoliated or grown into quasi-1D atomic thread bundles. Furthermore, TMTs can exhibit both metallic and semiconducting behavior. We have recently demonstrated that metallic van der Waals nanowires of TaSe₃ have extremely high breakdown current densities exceeding those of the conventional metals by an order of magnitude¹⁻². Here we report results of the investigation of electrical and low-frequency noise properties of quasi-1D TaSe₃ and ZrTe₃ van der Waals nanowires. The focus of the study is on comparing the noise characteristics of metallic and semiconducting van der Waals nanowires with those of conventional semiconductor nanowires and metals.

II. FABRICATION DETAILS

Bulk TaSe₃ and ZrTe₃ crystals were synthesized by the chemical vapor transport (CVT) method and then mechanically exfoliated onto Si/SiO₂ substrates³⁻⁵. The TaSe₃ devices were fabricated by two different techniques: electron beam lithography (EBL) and the shadow mask method. The device fabricated by EBL utilized h-BN capping layers to protect the TaSe₃ nanowires from oxidation and chemical exposure during the fabrication processes, and from environmental effects during testing. The shadow mask method was used with ZrTe₃ nanowires, which were subject to less degradation. The shadow mask method allowed us to directly deposit metal contacts onto ZrTe₃ channels. This approach reduced the total air exposure time during the fabrication process and avoided chemical contamination associated with the lithographic lift-off processes.

III. RESULTS AND DISCUSSIONS

Figure 1 shows the temperature dependences of the resistance for TaSe₃ and ZrTe₃ devices. TaSe₃ exhibits the temperature dependence of the resistance typical for metals, i.e. resistance increases with increasing temperature. On the contrary, in ZrTe₃ resistance decreases with the temperature increase, which is typical for semiconductors. One should note that both metallic and

semiconducting polymorphs are known for ZrTe₃, which depend on growth and fabrication procedures, although these particular polymorphs are difficult to distinguish by powder X-ray diffraction.

The low frequency noise at room temperature in TaSe₃ has the form of the $1/f^\gamma$ -like noise ($\gamma \approx 1$). With increasing temperature, the γ exponent increased up to $\gamma \approx 1.8$ at $T = 400 \text{ K}$. The amplitude of noise within the temperature range from 300 K to 400 K increases drastically. It was found that these temperature dependencies comply with the Dutta-Horn model, which is often used to describe noise in metals. The activation energy distribution calculated from the noise data in accordance with the Dutta-Horn model was found to have the maximum at $E_p \approx 1 \text{ eV}$. The low frequency noise in ZrTe₃ showed clear signs of the generation recombination (GR) noise typical for semiconductors (see Figure 2).

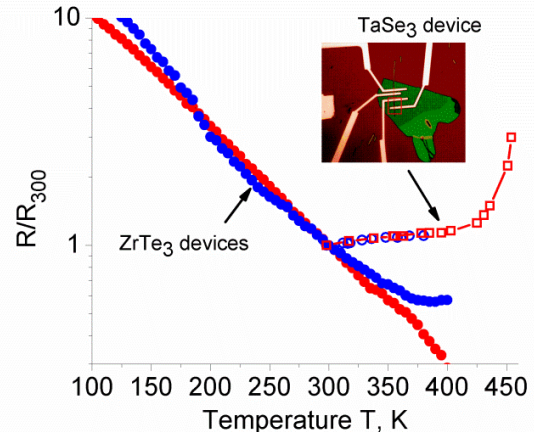


FIG. 1: Temperature dependences of the resistance for TaSe₃ (red and blue open squares and circles) and ZrTe₃ (blue and red filled circles) devices. Insets show the optical microscopy image of the TaSe₃ device capped with h-BN.

The temperature dependence of the resistance and presence of the G-R noise indicate that the studied samples have predominantly semiconductor phase. The activation energy of the dependence of the G-R noise is found to be $\sim 170 \text{ meV}$ (for comparison, the reported band gap of semiconducting ZrTe₃ is $\sim 0.4 \text{ eV}$). The amplitude of noise in both TaSe₃ and ZrTe₃ devices, within the experimental error and dispersion among different samples, can be fitted with the dependence

$S_I/I^2 \times f = 10^{-11}R$, where R is the sample resistance. The measurements at $T \approx 80$ K indicated that the characteristic frequency of the GR noise in $ZrTe_3$ increases with the bias voltage increase (see Figure 2). There might be several reasons for this effect, including the Joule heating. This is the main unsolved problem of noise in the studied devices.

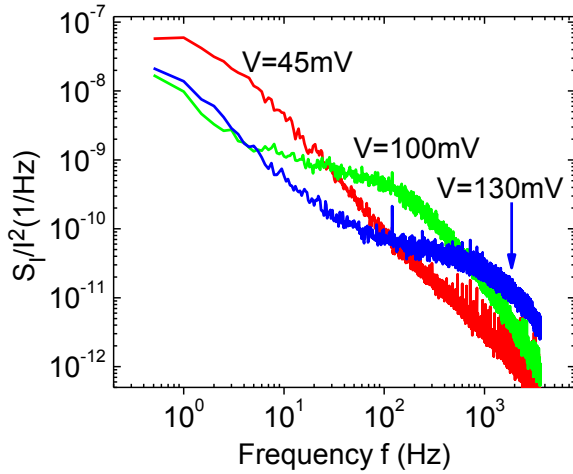


FIG. 2: Noise spectra of current fluctuations and different voltages for $ZrTe_3$. $T=80$ K.

ACKNOWLEDGEMENTS

Device fabrication and testing were supported, in part, by the Semiconductor Research Corporation (SRC) contract 2018-NM-2796: One-Dimensional Single-Crystal van-der-Waals Metals: Ultimately-Downscaled Interconnects with Exceptional Current-Carrying Capacity and Reliability. Materials synthesis and characterization were supported, in part, by the NSF through the Emerging Frontiers of Research Initiative (EFRI) 2-DARE project: Novel Switching Phenomena in Atomic MX₂ Heterostructures for Multifunctional Applications (NSF EFRI-1433395).

1. M. A. Stolyarov, G. Liu, M. A. Bloodgood, E. Aytan, C. Jiang, R. Samnakay, T. T. Salguero, D. L. Nika, S. L. Rumyantsev, M. S. Shur, K. N. Bozhilov, and A. A. Balandin, *Nanoscale*, **8**, pp. 15774–15782 (2016).
2. G. Liu, S. Rumyantsev, M. A. Bloodgood, T. T. Salguero, M. Shur, and A. A. Balandin, *Nano Lett.*, **17**, pp. 377–383 (2017).
3. R. Samnakay, D. Wickramaratne, T. R. Pope, R. K. Lake, T. T. Salguero, and A. A. Balandin, *Nano Lett.*, **15**, pp. 2965–2973 (2015).
4. G. Liu, B. Debnath, T. R. Pope, T. T. Salguero, R. K. Lake, and A. A. Balandin, *Nat Nano*, **11**, pp. 845–850 (2016).
5. G. Liu, E. X. Zhang, C. Liang, M. Bloodgood, T. Salguero, D. Fleetwood, A. A. Balandin, *IEEE Electron Device Lett.*, **38**, pp. 1724–1727, (2017).

The relation between electrical fluctuations and current-voltage characteristics of the mid-IR laser diodes in the subthreshold region

Justinas Glemža, Vilius Palenskis, Sandra Pralgauskaitė and Jonas Matukas

Institute of Applied Electrodynamics and Telecommunications, Vilnius University, Saulėtekio av. 3, LT-10222 Vilnius, Lithuania
e-mail address: justinas.glemza@ff.vu.lt

I. INTRODUCTION

It is well known that the low-frequency noise spectroscopy is a very sensitive diagnostic tool for a variety of optoelectronic devices such as light-emitting diodes (LEDs)^{1,2} and laser diodes (LDs)^{3,4}. The assessment of reliability and quality are especially of high importance for those specimens whose technology of manufacturing is still under improvement, e. g. GaSb-based laser diodes. These LDs emitting in 1.8 – 3.7 μm wavelength region are widely used in medical applications, military, spectroscopy, etc.⁵.

In some cases, the value of the current, which is required for the lasing and to generate enough optical power, is relatively high so there is a demand for a non-destructive testing method in the subthreshold region⁶ in order to avoid the damage of the internal specimen structure. Also, a correct identification of the existing noise sources in the LD can be complicated at higher currents if the contact noise dominates.

As the current-voltage (I-U) characteristic and its derivative IdU/dI , which is called electrical derivative (ED), analysis is widely used for laser diodes investigation^{7,8}, a supplement with the low-frequency noise measurement allows more precise current path determination inside the sample and the origin of the noise evaluation.

In this paper, we present investigation results of the electrical fluctuations of the type-I GaSb-based LDs in order to illustrate the relation between the electrical noise spectral density dependency on the forward current and the current-voltage characteristic. Also, problems concerning the correct interpretation of the noise characteristics, occurring when the noise spectroscopy is desirable to be used as a non-destructive diagnostic tool for the LDs in the subthreshold region, are discussed.

II. DEVICES UNDER INVESTIGATION

Investigated samples radiate at 1.94 μm wavelength at room temperature. They were grown by molecular beam epitaxy. All samples contain doped $\text{Al}_{0.5}\text{Ga}_{0.5}\text{As}_{0.04}\text{Sb}_{0.96}$ claddings and undoped $\text{Al}_{0.25}\text{Ga}_{0.75}\text{As}_{0.02}\text{Sb}_{0.98}$ waveguide layer and barriers, where two $\text{Ga}_{0.73}\text{In}_{0.27}\text{Sb}$ quantum-wells (QWs) are embedded.

III. INVESTIGATION OF ELECTRICAL NOISE SPECTRAL DENSITY

Investigated LDs fluctuations are characterized by 1/f-type electrical noise (Fig. 1), which is due to superposition of many generation-recombination or capture-emission of charge carrier processes with very wide distribution of relaxation times⁹. Experimental and calculated dependencies of electrical noise spectral densities on the forward current of the LD are presented

in Fig. 2. Analysis has shown that such spectral density can be expressed as a sum of two spectral densities of the independent noise sources:

$$S_{U_{\text{out}}} = S_{n1} + S_{n2}. \quad (1)$$

The equivalent electrical circuit of the LD with these voltage noise sources is shown in Fig. 3. The resistance R_1 is a differential resistance R_{dif} of the LD and the resistance R_2 describes serial contacts resistance. As for the 1/f-type electrical fluctuations the current noise, S_I , for a pn junction is proportional to the forward current¹⁰, the differential resistance of the LD is inversely proportional to the current and voltage spectral density of electrical fluctuations $S_{U_{\text{out}}} \sim S_I \cdot R_{\text{dif}}^2$, Eq. (1) can be rewritten as:

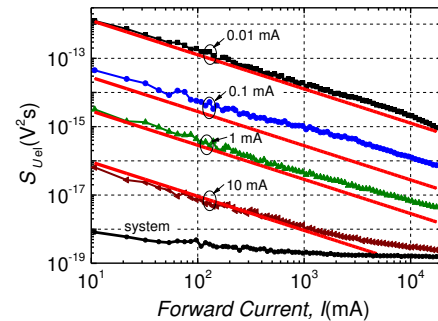


FIG. 1. Electrical noise spectra of the investigated LD at different forward current (“system” represents the measurement system electrical noise floor). Solid red lines represent approximated noise spectra by Eq. (2).

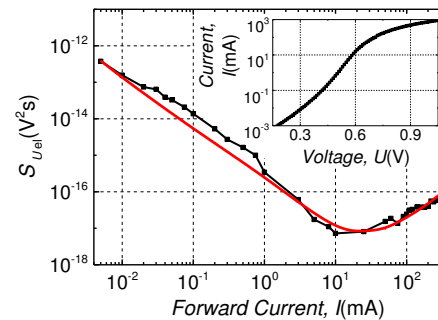


FIG. 2. Experimental (black curve with square symbols) and calculated (red solid curve using Eq. 2) dependencies of the voltage spectral densities of electrical noise on the forward current at 108 Hz frequency. The inset represents I-U characteristic of the sample.

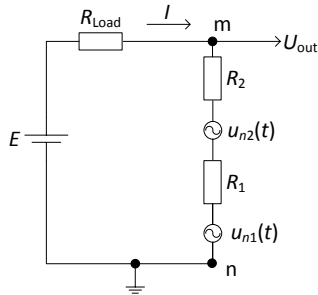


FIG. 3. The equivalent electrical circuit of the LD with the voltage noise sources $u_{n1}(t)$ and $u_{n2}(t)$ (here $R_{Load} \gg R_{mn}$).

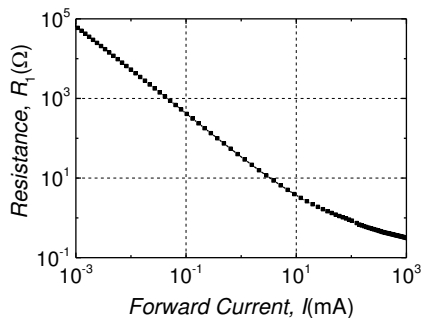


FIG. 4. Dependence of the LD's differential resistance R_1 on the forward current.

$$S_{U_{out}} = \frac{A}{f} I^\gamma R_1^2 + \frac{B}{f} I^2; \quad (2)$$

here index γ is close to 1, quantities A and B define the intensities of the noise sources $u_{n1}(t)$ and $u_{n2}(t)$, respectively. The dependence on the forward current of the differential resistance R_1 , which has been calculated from the experimental I-U characteristic of the LD (the inset in Fig. 2), is presented in Fig. 4.

In the case of the presented LD, noise sources are located in the differential resistance and series resistance of the LD meaning electrical fluctuations arising from the pn junction (main diode, not a parasitic shunt diode) and at higher currents – from the contacts (voltage spectral density for the contact noise⁶ $S_U \sim I^2$). In those cases when various parasitic leakage channels exist, the equivalent electrical circuit should be supplemented by the new noise sources leading to the different dependence of the electrical noise spectral density on the forward current.

IV. LD RELIABILITY AND NOISE CHARACTERISTICS INTERPRETATION

Various defects and imperfections, formed through the manufacturing process of the laser diodes or after, worsen their electrical and optical characteristics, performance and lifetime. There is no doubt that the excess noise is a good reliability indicator for the LDs^{3,4}.

A special attention has to be paid to the interpretation of the results when the low-frequency noise spectroscopy is used for the LDs reliability assessment only from the subthreshold measurements. This is very important when there is a purpose to evaluate noise characteristics changes caused by the technological process variation, not by the induced stress due to the high current flowing through the specimen.

Usually, larger threshold current indicates more defective LD structure, which leads to the more intense 1/f-type electrical fluctuations. This was observed in InGaAsP/InP laser diodes⁴.

However, in some cases, technological variations during the LDs growth lead to the different results. Changes in quantum wells region also determine the threshold current or in a critical case it lead to the situation that there is no laser generation at room temperature. So, such specimens can not be interpreted as reliable LDs despite demonstrating “good” noise characteristics as no additional defects are formed compared to those LDs, which achieve lasing at room temperature.

This is an open problem of our work – to create a reliable unambiguous diagnostic method for the LDs through the low-frequency noise characterization when the measurements are performed only in the subthreshold region.

V. CONCLUSIONS

The presented investigation demonstrates the relation between the I-U characteristic and the spectral density of electrical noise of the 1.94 μm wavelength GaSb-based LD. Also, problems concerning the correct interpretation of the LDs measurement results during the subthreshold electrical noise investigation are discussed.

ACKNOWLEDGEMENTS

The authors would like to thank K. Vizbaras and A. Vizbaras (Brolis Semiconductors UAB, Vilnius, Lithuania) for providing samples, their specifications and valuable consultations.

¹ S. Pralgauskaitė, V. Palenskis, J. Matukas, et al. *Microelectron. Reliab.* **55**, 52-61 (2015).
² V. Palenskis, J. Matukas, S. Pralgauskaitė, *Solid-State Electron.* **54**, 781-786 (2010).
³ B. K. Jones, *IEEE Proc.-Circuits Devices Syst.* **149**, 13-22 (2002).
⁴ S. Pralgauskaitė, V. Palenskis, J. Matukas, *Semiconductor Laser Diode Technology and Applications* (Intech, 2012).
⁵ K. Vizbaras, M.-C. Amann, *Semicond. Sci. Technol.* **27**, 1-4 (2012).

⁶ J. Guan, S. Guo, J. Wang, et al. *Microelectron. Reliab.* **59**, 55-9 (2016).
⁷ J. K. Sheu, Y. K. Su, S. J. Chang, et al. *Solid State Electron.* **42**, 1867-1869 (1998).
⁸ D. Guo, L. Cheng, X. Chen, et al. *J. Appl. Phys.* **109**, 043105 (2011).
⁹ V. Palenskis, K. Maknys, *Scientific Rep.* **5**, 1-7 (2015).
¹⁰ F. N. Hooge, T. G. M. Kleinpenning, L. K. J. Vandamme, *Rep. Prog. Phys.* **44**, 479-532 (1981).

Fluctuation Analysis of Synchronous Repetitive Handwriting

Ryo Kumagai¹ and Masafumi Uchida²

^{1,2}The university of electoro-communications, 1-5-1 Chofugaoka, Chofu, Tokyo, 182-8585 Japan
e-mail address: uchidamasafumi@uec.ac.jp

I. INTRODUCTION

Control of voluntary movement is a dual structure of the cognitive control and kinetic control. Cognitive control involves attentional resources, whereas kinetic control does not. Various voluntary movements can be performed by combining cognitive and kinetic controls. If these two controls could be separated, we could predict the level of acquisition of physical exercise skills from the expenditure of attentional resources. Using a synchronous tapping method, Miyake et al.¹ investigated the relationship between repetitive body movements and attentional resources. For the synchronous tapping task, the action timing needed to be anticipated. We estimated the control system related to the body movements of the synchronization tapping by using the fluctuation features of the synchronization-error time series. Body movements that depended on the attentional resources were performed by the feedback system based on cognitive control, and the synchronous errors fluctuated with the white noise. As the dependence on the attentional resources in the body movement decreased, that is, the human kinetic control decreased, the fluctuations of the synchronous-errors time series gradually shifted to the 1/f fluctuation, that is, to the self-similarity features.

In this study, we evaluate the dependency on attentional resources while learning to perform physical exercises by using the relationship between the attentional resources and fluctuations in body movements. In this study, the physical exercise to be learned was the process of writing certain Chinese characters by hand. We chose to write the Chinese Kanji characters. The slight differences between character shapes were regarded as the difference of difficulty between handwritings; the stroke count of the character is an indicator of the difficulty of writing by hand.

In a previous study, we reported that a handwriting time-element time series contains self-similarity features.^{2,3} In the traditional way of analyzing self-similarities, numerous fractal analysis methods, such as power spectrum analysis, Higuchi method,⁴ and the R/S method, have been proposed to treat a time series.⁵ Detrended fluctuation analysis (DFA)⁶ is an effective method to analyze the physiological signals because it needs only a few rigid assumptions regarding signal stationarity. In this research, it was difficult to ensure the correct stationarity of the handwriting time-element time series; therefore, we used the DFA method. If the time series of the handwriting time element (HTE) had self-similarity, it implied that this time series did not have a fixed timescale. However, in a practical system, we cannot consider that the same self-similarity covers the entire length of the timescale of the time series. Some previous studies^{7, 8} have reported the crossover phenomenon associated with a change in the short- and long-range self-similarity features during the DFA process.

In this study, we investigate the relationship between the scaling index and the differences in the difficulty levels for writing three Kanji characters by hand: “Den,” “Tsu,” and “Dai.” We focused on the self-similarity modality of each timescale.

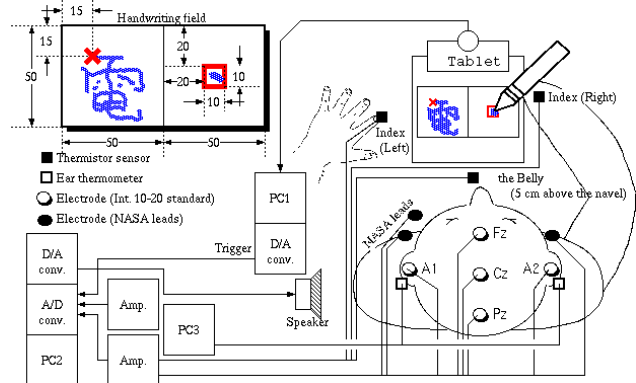


FIG. 1 Experimental system

II. MEASUREMENT AND ANALYSIS

The experimental system is shown in Fig. (1). The system comprised three personal computers: PC1, PC2, and PC3. The coordinates of the pen points were measured by the pen tablet using a 200-Hz sampling frequency and were recorded on PC1. In addition, PC1 applied a trigger signal that indicated the removal and installation of pen points from the tablet to PC2 through a digital-to-analog converter (DAC). PC2 recorded the trigger signal by using an analog-to-digital converter (ADC) with a 1-kHz sampling frequency. A square signal was output to a speaker through a DAC for generating the sound stimulation; this output specified the handwriting time of the subject. The three electrodes measured the electroencephalogram (EEG) signals and were arranged on the Fz, Cz, and Pz electrode sites of the scalp in accordance with the international 10–20 standard. The electrode arrangement of the electrocardiogram (ECG) followed the NASA leads. The EEG and ECG signals were amplified and then recorded in PC2 through an ADC with a 1-kHz sampling frequency. We used a thermistor sensor to measure the temperatures of the peripheral part and the trunk of the body. Each sensor was fixed to the top of the index fingers of both hands and on the belly of the subject. The temperature was recorded in PC2 through an ADC for a 1-kHz sampling frequency. PC3 measured the ear drum temperature using an ear thermometer at a 1-Hz sampling frequency. The experimental protocol was as follows. First, we performed tests comprising POMS and STAI. Then, the subjects were required to close their eyes and rest for 150 s. Finally, the subjects performed the assigned tasks. These tests were repeated after resting for 150 s. This comprised one set of the experimental process. A dual-task method was applied in this experiment, and the method involved the synchronization tapping task and the handwriting task. The handwriting field was set on the pen tablet. This field comprised a square area (H-area) of side 50 mm on the left and a square area (T-area) of side 10 mm on the right. In the T-area, an “x” mark was drawn. The handwriting task is shown in Table 1. Chinese Kanji

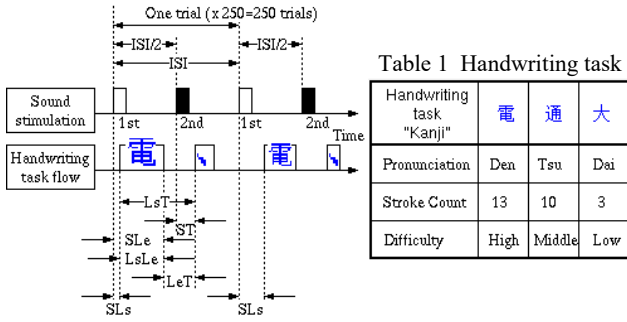


FIG. 2 Time chart of the task

characters were selected for handwriting task. The three letters had slightly different difficulty levels, and their stroke counts were different. Therefore, in this study, the stroke count was chosen as the index of task difficulty.

The time chart of the task is shown in Fig. (2). Based on the repetitive periods that are detected by the preliminary experiment, we maintained the sound stimulation until the end of the task. The subjects were required to start writing with the first sound stimulation. When they finished writing, they tapped the T-area using their pen tips so that they were in synchrony with the second sound stimulation in the best possible manner. The subjects started writing from the "x" mark in the H-area. They were allowed to do 250 trials, which comprised one set. The HTE was divided into six components, "SLs," "SLsLe," "LsT," "LsLe," "LeT," and "ST", and these could be obtained from one trial. One set consisted of 250 trials, and 250 samples were obtained in each HTE. Each time series of an HTE consisted of 250 samples, respectively. Here, the time series of an HTE was represented by x_i ($i = 1, 2, \dots, 250$); then, x_i became the intended signal of the DFA. The time series $y(k)$ ($k = 1, 2, \dots, 250$) of the cumulative sum for x_i was computed as $\sum_{i=1}^k (x_i - \bar{x})$. Here, \bar{x} was a mean value of x_i . The regression line of $y_n^s(k)$ was the time series $\{y(s), y(s+1), \dots, y(s+n-1)\}$ where ($s = 1, 2, \dots, 250 - n + 1$). This time series was to be cut out in the search window of the window of width n , where ($n = 3, 4, \dots, 250$) from the time series $y(k)$.

Then, the slope of the regression line for the relationship between n and $F(n)$ was defined by Eq. (1). Both the logarithmic plots were called the scaling index β , and n was called the timescale. In the application of DFA, we decided to shift the search window by one point time because of the very short time series length of (1).

$$F(n) = \sqrt{\frac{1}{(N-n+1)n} \sum_{s=1}^{N-n+1} \sum_{k=s}^{s+n-1} (y(k) - y_n^s(k))^2} \quad (1)$$

Here, to visualize the local trend of the n vs. $F(n)$ characteristics, the difference in values of $F(n)$ on both logarithmic fields of the n vs. $F(n)$ characteristics was computed as $local\beta_n$. This was called the local scaling parameter.

- 1 Y. Miyake, Y. Onishi, and E. Poppel, Object Recognition, Attention, and Action, Part III, pp. 231-244 (2007)
- 2 A. Maleki, Y. Oshima, A. Nozawa, T. Mizuno, and M. Uchida, 7th Int. Conf. on Unsolved Problems on Noise, 21 (2015)
- 3 R. Kumagai and M. Uchida, 2017 Int. Conf. on Noise and Fluctuations, pp. 350-353 (2017)
- 4 T. Higuchi, Proc. of the institute of Statistical Mathematics, vol. 37, no. 2, pp. 209-233 (1989)

The subjects were 10 healthy males (21–25 years old), and we conducted six sets of experiments for each writing task.

III. RESULTS AND DISCUSSION

Our focus in this experiment was on what the subjects were paying attention to during the handwriting task, for example, the sound stimulus, drawing of the Kanji shape, or tapping to draw a point. We evaluated the destinations of the subjects' attentional resources during the handwriting task execution by using the fluctuation modality of each HTE. To estimate the fluctuation modality, we used the relationship between the timescales n and the local scaling parameter $local\beta_n$.

Fig. 3(a) shows the frequency distribution of six kinds of HTEs in a subject (ISI = 1450 ms). Fig. 3(b) shows the n vs. $local\beta_n$ characteristics of the measured LsLe time series. We confirmed the differences between the Kanji characters in a specific timescale on the n vs. $local\beta_n$ characteristics (e.g., $n > 85$). Using the n vs. $local\beta_n$ characteristics, it is possible to estimate the timescale to which the subject is paying attention during the task execution.

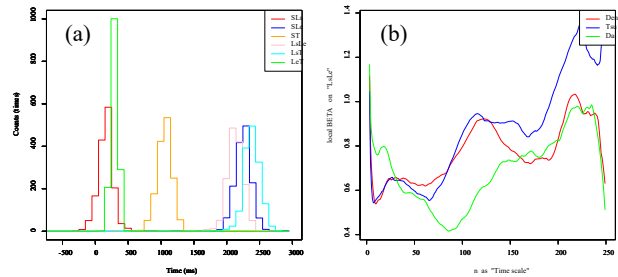


FIG. 3 Results of analysis (a)Histogram of HTE (b) n vs. $local\beta_n$ characteristics on LsLe

IV. CONCLUSION

In this study, we investigated the relationship between the characteristics of the scaling index and the differences in the difficulty levels for writing Kanji characters by hand. We used the DFA method to analyze the physiological signals. The crossover phenomenon of the DFA process was considered to be a local tendency of the self-similarity modality for each timescale n . We also proposed a new evaluation index $local\beta_n$. These investigations enabled us to visualize the relationship between the handwriting task difficulty and the self-similarity modality in each timescale by using the n vs. $local\beta_n$ characteristics.

ACKNOWLEDGMENTS

This is research is supported by JSPS KAKENHI 25330406.

- 5 B. B. Mandelbrot and J.R. Wallis, Water Resources Research, vol. 5, no. 2, pp. 321-341 (1969)
- 6 R. Hardstone, S-S. Poil, G. Schiavone, R. Jansen, V.V. Nikulin, H.D. Mansvelder, and K.L-Hansen, Frontiers in Physiology, vol. 3, no. 450, pp. 1-13 (2012)
- 7 C. K. Peng, S. Havlin, H. E. Stanley, and A. L. Goldberger, CHAOS, vol. 5, no. 1, pp. 82-87 (1995)
- 8 T. Komatsu and Y. Miyake, SICE, vol. 41, no. 6, pp. 518-526 (2005)

Simplified method of trend removal to determine noise observed during supercapacitor's discharging

Łukasz Lentka and Janusz Smulko

Gdańsk University of Technology, Department of Metrology and Optoelectronics, Gabriela Narutowicza 11/12, 80-233 Gdańsk, Poland
e-mail address: lukasz.lentka@pg.edu.pl

I. INTRODUCTION

In this paper a simplified method of trend removal to determine random component generated in supercapacitor structure during discharging is proposed. Voltage fluctuations, observed across the loading resistance connected to the terminals of the supercapacitor, are superimposed on slowly decaying trend component. The trend function is not exactly an exponential function, as it is in a case of a pure capacitor, because supercapacitor equivalent circuit model consist of many RC branches with successively increasing time constants¹. It is possible to stand out at least two the most significant branches with the lowest time constants. In Fig. (1) we can see an exemplary discharging curve of supercapacitor having two visible time constants (the first one is dominant to about 6000 s and the second one is dominant after 10000 s) and the transient region where both time constants are taking part in discharging process.

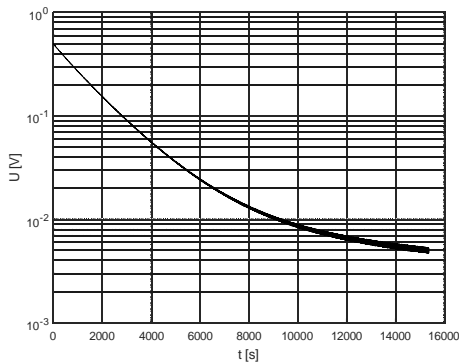


FIG. 1. Voltage between the terminals of supercapacitor $C = 8 \text{ F}$ when discharged by loading resistance $R = 200 \Omega$ with visible two time constants; the OY axis has logarithmic scale for better visualization of time constants.

After effective detrending the recorded noise component can be used to investigate degradation mechanisms in supercapacitor structure. Former investigations² showed that adequate trend removal method was crucial to evaluate noise statistical parameters. The main problem is to determine trend component and, after necessary subtraction, to determine fluctuations. We have observed that voltage fluctuations can exhibit some fast changes in intensity as presented at Fig. (2), e.g. at the moments around 5700 s or 6100 s. These abrupt changes may result from charge redistribution mechanisms or exclusion of some regions of porous carbon electrodes from further charging/discharging ability

because of pores clogging or corrosion reactions. In our paper we propose a simplified method for fast and computationally simple trend determination which takes into account additive noise component having properties as presented at Fig. (2).

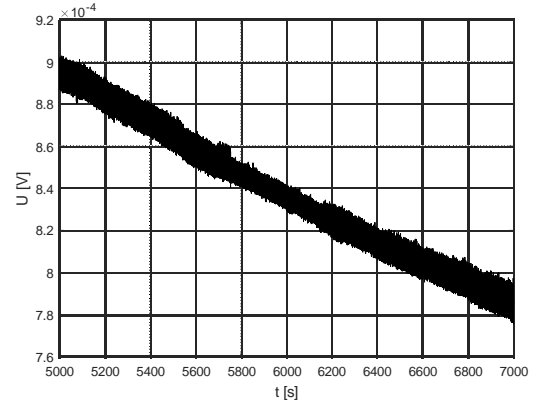


FIG. 2. Voltage fluctuations superimposed on the discharging voltage curve observed between the terminals of the supercapacitor at selected time interval.

II. THE PROPOSED METHOD

The proposed method applies the EMD decomposition³, but is much less computationally expensive and therefore it should be much faster. The EMD decomposition of the exemplary signal comprising of 8 million samples can take tens of minutes using Matlab software installed on contemporary personal computer. Then it is another difficulty how to establish trend, which should be removed, from the intrinsic mode functions (IMFs). There are some approaches to do that³, but they are not easily implemented. Human decision is needed to run the algorithm. Therefore, we try to optimize the method for trends function similar to the observed during supercapacitor's discharging, as presented in Fig. (1). In the proposed method the trend is determined by the formula:

$$m(t) = \frac{e_u(t) + e_l(t)}{2}, \quad (1)$$

where: $m(t)$ is the determined trend component, $e_u(t)$ and $e_l(t)$ are upper and lower envelopes of the measured discharging curve. The resulting trend component determined for the exemplary supercapacitor's discharging curve, shown in Fig. (1), is presented in Fig. (3).

We have calculated the upper and lower envelopes, marked as black solid lines on Fig. (3), by using MATLAB function *envelope* with the specified *peak* parameter. The envelopes are

determined using a spline interpolation over local maxima separated by at least n samples⁴. The spline function⁵ is a function defined piecewise by polynomials of relatively low degree. It is preferred in interpolation problems, because it gives relatively small interpolation error by using low degree polynomials for the spline. It avoids Runge's phenomenon⁵ when too high degrees of polynomials are used. Runge's phenomenon concerns possible oscillations between the measurement points. Thus, the proposed spline interpolation seems to be a better choice.

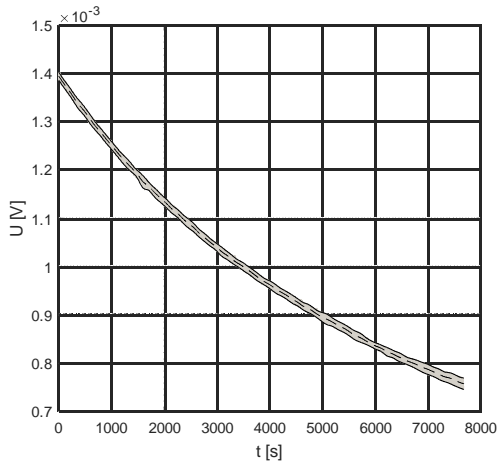


FIG. 3. Idea of the proposed method – the trend function (dashed line) was determined as the mean value of the envelopes marked by solid lines.

III. RESULTS

We have applied the proposed method for an exemplary discharging curve presented in Fig. (2). The parameter n of the function *envelope* available in MATLAB software was set to $n = 100\,000$ to get the most accurate trend approximation. Its value cannot be too small because low frequency component will be attenuated. It cannot be too high at the same time because trend component won't be determined accurately. We can identify in Fig. (4) the differences in time records of the identified trends by both proposed methods (e.g., at $t = 1700$ s, $t = 2500$ s). Power spectral densities $S_u(f)$ of the determined voltage fluctuations after trend removal exhibit the main difference at low frequencies range, as presented in Fig. (5). Polynomial approximation attenuates these low frequency components and therefore the proposed method is more relevant to identify noise generated in supercapacitors and to consider its correlation with supercapacitors aging.

IV. CONCLUSIONS

The considered discharging voltage curve in supercapacitors needs a new methods of detrending to determine additive noise component. The proposed method is more efficient in establishing noise component which gives information about aging processes in the investigated supercapacitors. The proposed method identified low frequency component in a better way than the method based on polynomial approximation.

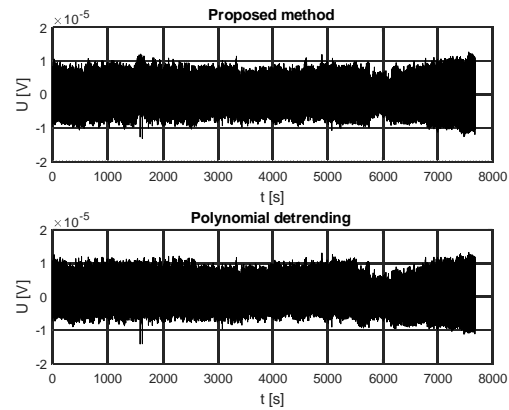


FIG. 4. Voltage fluctuations obtained using different detrending methods.

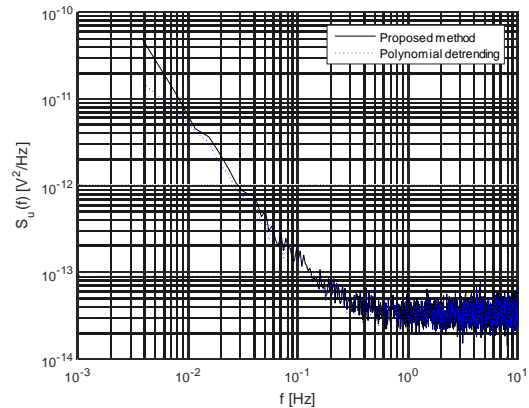


FIG. 5. Comparison of power spectral densities of signals presented in the Fig. (4).

ACKNOWLEDGEMENTS

This research was financed by the National Science Center, Poland, project No. DEC-2014/15/B/ST4/04957, "Charging/discharging mechanism at the electrode/electrolyte interface of supercapacitors".

¹ S. Fletcher, V.J. Black and I. Kirkpatrick, A universal equivalent circuit for carbon-based supercapacitors *Journal of Solid State Electrochemistry* **18.5**, 1377-1387 (2014).
² Ł. Lentka and J. Smulko, Analysis of effectiveness and computational complexity of trend removal methods *Zeszyty Naukowe Wydziału Elektrotechniki i Automatyki Politechniki Gdańskiej* **51**, 111-114(2016).

³ A. Moghtaderi, P. Flandrin and P. Borgnat. Trend filtering via empirical mode decompositions *Computational Statistics & Data Analysis* **58**, 114-126(2013).
⁴ C. De Boor, Spline toolbox for use with MATLAB: user's guide, version 3. MathWorks, (2005).
⁵ C. De Boor, A practical guide to splines, New York: Springer-Verlag, (1978).

Effect of analyte flow on the voltage fluctuations of gas chemiresistors

Filip Mívalt¹, Jiří Majzner¹, Vlasta Sedláková¹, Petr Kuberský², Janusz Smulko³ and Petr Sedlák¹

¹Brno University of Technology, Faculty of Electrical Engineering and Communications
Technická 10, Brno 616 00, Czech Republic
e-mail address: sedlakp@feec.vutbr.cz

²University of West Bohemia, Faculty of Electrical Engineering,
Univerzitní 26, Plzeň 301 00, Czech Republic

³Gdańsk University of Technology, Department of Metrology and Optoelectronics
ul. G. Narutowicza 11/12 80-233 Gdansk Poland

I. INTRODUCTION

Understanding of sensor mechanisms and their properties is tightly bounded with characterization of electric charge transport and its fluctuations at/in active electrochemical interfaces.

Stochastic behavior becomes an increasingly dominant characteristic of electrochemical systems as we probe them on the smaller scales^{1,2}. This stochasticity is completely hidden from the observer due to massive averaging – so many charge carriers (electron, ions or molecules) are involved that only their mean behavior is observable and a probabilistic description is unnecessary. Nevertheless, the effect of randomness may show significance in some systems, especially very small ones in comparison to the macroscopic world but larger than microscopic scale of molecules, as the averaging of the random particle motion is not so effective^{1,3,4}. For example, the kinetics of many physico-chemical, electrochemical, and bioelectrochemical processes is known to be accompanied by noise generation, which virtually represents the dynamic fluctuations of electric potential or current². Even though not every sensor system is considered as a small - mesoscopic, several authors showed that fluctuation analyses represent the approach of extracting more selective response from macroscopic chemical sensors, e.g. chemiresistors⁵⁻⁸, surface acoustic wave sensors, and resonant sensors⁹. In conductometric sensors the observed fluctuations give more information than a single DC resistance value and therefore obtained results lead to the reduction of the number of gas sensors necessary for the detection of different gas mixtures by sensor arrays^{7,10}. The high-order statistics enables the extraction of non-conventional features and leads to significant improvements in selectivity and sensitivity^{7,8} of sensors.

Another way to improve selectivity and sensitivity of conductometric sensors is targeted change of their operating conditions, such as temperature modulation^{8,11}, light exposure of sensitive layer with various intensity¹², sampling-and-hold method¹³, transient flow modulation^{14,15}, etc.

Our motivation aims on possibility of improved selectivity by modulation of analyte flow rate around conductometric sensors at equilibrium conditions by studying voltage fluctuations. By setting different flowrate, the concentration of analytes at the surface of sensors is modulated, and the specific response patterns, which are characteristic of the analytes present, develop. The method could be adapted to both static and dynamic headspace sampling strategies. However, this contribution aims to present how the flow rate of analyte affects the voltage fluctuation of the resistive gas sensor, which has not yet been sufficiently presented.

II. EXPERIMENTAL SETUP

The experimental study was carried out on two commercially available gas resistive sensors: metal-oxide-based sensor MICS5524 (SGX sensortech) and TGS2600 (Figaro sensors), both types of sensors target on multiple application (e.g. indoor quality monitor or breath analysis), i.e. they are sensitive to a wide range of gases and a humidity but often with various sensitivity. To study effect of cover, the metal cover was removed from the one of TGS2600 sensor.

Each sensor was put to the same position at gas-tight chamber to be under almost the same fluidic condition. The flow rate of analyte through the chamber was set by two manual flow controllers. As the analyte was used the air with relative humidity 40%. All noise measurements were done under equilibrium conditions.

The noise measurement setup consisted of a low-noise preamplifier PA15 (3S Sedlak, Ltd), an amplifier with highly selective filters AM22 (3S Sedlak, Ltd) which covered the selected frequency range, 12-bit AD convertor HS3 (TiePie Engineering), and a notebook. To minimize external disturbances, the whole system was powered from battery. The test chamber with gas resistive sensor and preamplifier were electrically and magnetically shielded.

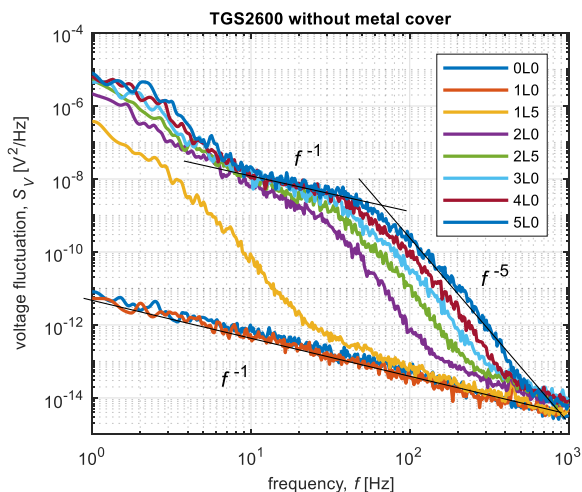


FIG. 1. Spectral density of voltage fluctuations via TGS2600 for analyte flow from 0 L/min to 5 L/min ($T = 298$ K, $RH = 50\%$). The cover of the sensor was taken out and only structure of sensor was exposed to ambient environment.

III. RESULTS AND DISCUSSION

The fluctuation phenomena in every chemical sensor are connected to intrinsic sources (sensor structure, contacts, etc.) and to chemical processes in/on a sensing layer. The additional noise sources connected to the second group are considered to be associated with fluctuations of charge carrier mobility and density (concentration fluctuation and motion of chemical fragments) originating from the chemical environment, and are supposed to be^{16,17}: (i) adsorption-desorption process of gas molecule on the active layer, (ii) diffusion of the adsorbed molecules or molecule fragments on the sensor surface. The measured spectral density of current or voltage fluctuations is assumed to result from the superposition of the contributions of these two noise sources as well as inherent noise sources.

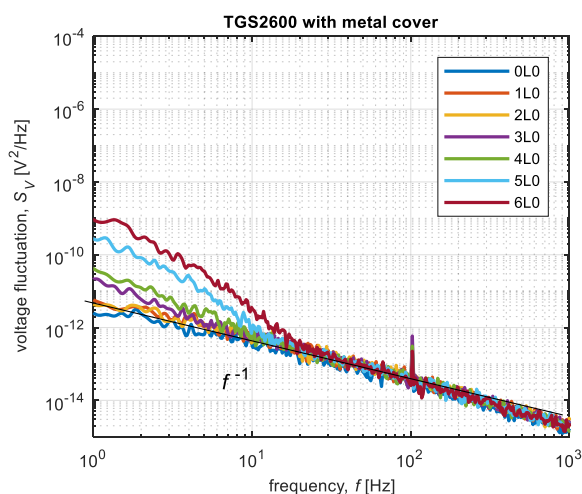


FIG. 2. Spectral density of voltage fluctuations via TGS2600 for analyte flow from 0 L/min to 6 L/min ($T = 298$ K, $RH = 50\%$).

Both types of studied gas resistive sensors exhibit the presence of significant $1/f$ noise at low flowrates from 0 L/min to 1 L/min as shown in Figs. 1 and 3. Fig. 2 shows significant $1/f$ noise component till 4 L/min for sensor TGS2600 with cover. Remove of the metal cover results in a rise of noise voltage and a change of the cut-off frequency of the unexpected noise component. The difference in the spectrum of these TGS2600 sensors indicates and confirms the effect of the cover on the sensor properties (such as

response kinematics, sensitivity, selectivity and stability). As flowrate increases, unexpected noise component of Lorentzian-like spectra with f^α ($\alpha = -4$ for MICS, $\alpha = -5$ for TGS2600) become more significant and spectra of voltage fluctuations evolve as illustrated by Fig. 1 and Fig. 3. The cut off frequency of this noise shifts to higher values as flowrates increases. None of detrending techniques (linear and polynomial detrending, empirical mode decomposition etc.) was able to suppress this behavior. Further, the acquired time series of voltage fluctuations are of Gaussian distribution. We suppose that this noise component is a result of two mutual influencing stochastic processes: adsorption-desorption noise and noise arising from turbulent/laminar flow around the sensor (partial pressure fluctuations). This noise component is strongly dependent on the sensitive layer and its reachability for wide spectrum of chemical particles (cover construction/membrane layer of each sensor).

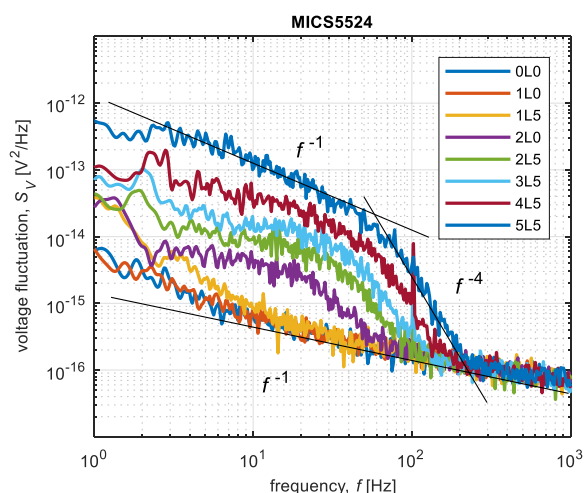


FIG. 3. Spectral density of voltage fluctuations via MISC5524 for analyte flow from 0 L/min to 5.5 L/min ($T = 298$ K, $RH = 50\%$).

ACKNOWLEDGEMENTS

Research described in this paper was financed by the National Sustainability Program under grant LO1401, by the grant 18-19104S of the Czech Science Foundation (GACR) and also partially financed by the Czech-Polish project 7AMB16PL039.

- ¹ P. S. Singh and S. G. Lemay, *Anal. Chem.*, **88**, 5017–5027 (2016).
- ² S. F. TIMASHEV and Y. S. POLYAKOV, *Fluct. Noise Lett.*, **7**, R15–R47 (2007).
- ³ S. Vitusevich and I. Zadorozhnyi, *Semicond. Sci. Technol.*, **32**, 43002 (2017).
- ⁴ B. M. Grafov, *Russ. J. Electrochem.*, **50**, 92–94 (2014).
- ⁵ L. B. Kish, R. Vajtai, and C. G. Granqvist, *Sensors Actuators B Chem.*, **71**, 55–59 (2000).
- ⁶ T. Contaret, J.-L. Seguin, K. Aguir, and P. Menini, in 2013 22nd International Conference on Noise and Fluctuations (ICNF), p. 1–4, IEEE (2013).
- ⁷ B. Ayhan et al., *Sensors Actuators B Chem.*, **188**, 651–660 (2013).
- ⁸ R. Macku, J. Smulko, P. Koktavy, M. Trawka, and P. Sedlak,

- Sensors Actuators, B Chem.*, **213** (2015).
- ⁹ P. Sedlak et al., *Sensors Actuators, B Chem.*, **166–167** (2012).
- ¹⁰ J. M. Smulko et al., *Sensors Actuators B Chem.*, **106**, 708–712 (2005).
- ¹¹ A. Vergara, E. Martinelli, E. Llobet, A. D’Amico, and C. Di Natale, *J. Sensors*, **2009**, 1–10 (2009).
- ¹² M. Trawka et al., *Sensors Actuators B Chem.*, **234**, 453–461 (2016).
- ¹³ J. Smulko and M. Trawka, *Sensors Actuators B Chem.*, **219**, 17–21 (2015).
- ¹⁴ N. El Barbri et al., *Sensors*, **8**, 7369–7379 (2008).
- ¹⁵ M.-D. Zhou et al., *Microsystems Nanoeng.*, **3**, 17062 (2017).
- ¹⁶ L. B. Kish et al., *IEEE Sens. J.*, **5**, 671–676 (2005).
- ¹⁷ S. Gomri, J.-L. Seguin, J. Guerin, and K. Aguir, *J. Phys. D: Appl. Phys.*, **41**, 65501 (2008).

Investigate of feeling estimation for content viewer focusing on skin surface temperature distribution using facial thermal images

Tomoyuki Murata, Marzieh Aliabadi Farahani, Kota Akehi,
Kazuyuki Mito, Naoaki Italura and Tota Mizuno
The University of Electro-Communication, Japan
e-mail address: m1730105@edu.cc.uec.ac.jp

I. INTRODUCTION

Due to the advanced information society, the variation of content has been increased. As the amount of information increases, it is difficult to select content that matches the user's preference. Therefore, recommendation system of contents matching the user's preference has attracted attention. In order to construct this recommendation system, it needs using information relating to user's favorite. In previous study, users' preference is estimated and evaluated by analyzing user's requests and impressions based on a subjective evaluation such as a questionnaire. However, the user's direct input method is burdensome to the user. In order to solve this problem, there are some researches to minimizing restraint of a subject to users by using objective evaluation such as physiological and behavior evaluation.

In previous research, we investigated the estimation method of autonomic nervous activity by using facial skin temperature. The skin temperature depends on the blood flow, and the blood flow volume changes due to the vasoconstriction action of the sympathetic and parasympathetic nervous systems of autonomic nervous system activity¹. Psychological state affects autonomic nervous activity, so it appears remarkably in facial skin temperature. Therefore, previous research have evaluated emotional and stress from facial skin temperature change². However, in conventional method, the influence of change of maximum and minimum nasal skin temperature and the fluctuation of the nasal skin temperature is not considered.

In this study, we aimed for more detailed emotion estimation other than pleasant feelings, detailed analysis of nasal skin temperature distribution, and comparative evaluation of each evaluation value. In order to examine experiments to remind the axes of various emotions, we measured the facial skin temperature of the viewer who read manga using infrared thermography.

II. EXPERIMENT

Experiments were carried out to acquire facial thermal images (FTIs) of the different psychological states. In order to measure biological information on preferences of content viewers, using silent cartoons without letters applying a passive stimulation to the user.

Fig.1 shows the experimental system. An infrared thermography (View Ohre IMAGING XA0350) was placed at a distance of 0.5 m horizontally from the nose of the subject. The thermal image size was 320×256 pixels, and the sampling period was 1 sec. A PC display were placed upon the desk.

Fig.1 shows the experimental protocol. Subjects was asked to rest for another 30 seconds, in a sitting position. After this initial rest period, subjects began reading manga task.

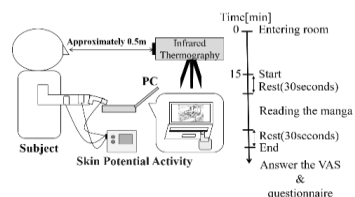


FIG. 1. Measurement environment and protocol.

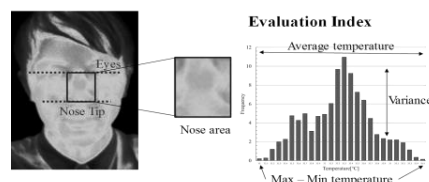


FIG. 2. Analysis area.

The subject read the manga without letter of about 10 to 30 pages per trial. For each subject, 27 works (about 5 works per day, different manga every time) were imposed. In order to avoid sudden temperature fluctuation, the subjects were allowed to enter the laboratory 15 minutes before measuring in the room. It was seated in front of the measuring device 15 minutes after entering the room, and it was measured for 30 seconds before and after resting and at the time of viewing comic books.

In addition, Visual Analogue Scale (VAS) was used as psychological indices. In this experiment, five pairs of one apace "Pleasant - Unpleasant", "Joy - Sadness", "Anger - Fear" "Trust-Disgust", "Anticipation-Surprise" words were employed for VAS. The subjects were four healthy adults from 22 to 28 years old who were well rested the night before the experiment. VAS was written before and after the task.

III. EVALUATION

In this research we measured the psychological state of subjects and their changes in mental and physical condition. We measured the psychological state of the subject and the change of psychosomatic state. Difference value of psychological state before and after task was standardized for each subject. In this research, we investigated the influence of nasal skin temperature distribution when the arousal of emotions by reading manga. The analysis area are shown in Fig.2. In previous research, it is possible that the differential value between the cheek and nose is effective for detecting emotions of joy. However, it has been clarified in previous studies that the edge portion of the face, where there is no angle between the thermography and the object to be photographed, has been decreased in consequence of reflections estimation accuracy was also increased.

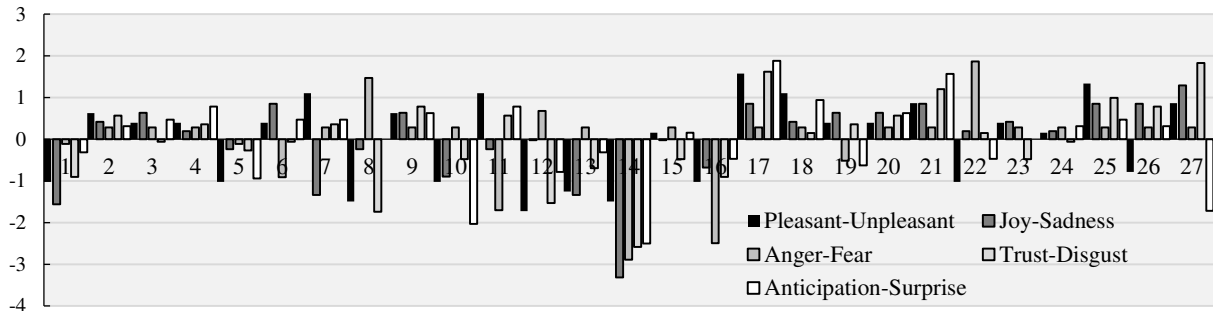


FIG. 3. III. Score of VAS (Sub.A).

Therefore, we defined analysis area as the area from the nose root to the tip of the nose excluding mouth area, because there is a possibility the mouth area was influenced by action such as respiration. We compared among the average temperature of the nose area to the difference the high and the low temperature pixel in the nose area, and the variance value of the nose area as evaluation value. In addition, we compared between the results of the questionnaire as psychological indices and nasal skin temperature as physiological indices. We measured influence of temperature distribution by use of an evaluation value calculating the difference and the dispersion value between the highest temperature and the lowest temperature within the defined area

IV. RESULT AND DISCUSSION

Fig.3 shows the results of psychological data standardized for each subject. According to the Fig3, it is speculated that the task of this experiment have plurality of feeling variations depending on the contents of the manga and was not able to be evaluated with a simple index like "pleasant-unpleasant". Some manga have increased negative evaluation values such as unpleasant, sadness, fear and dislike like no1, 14 and 16, others have increased positive evaluation values such as pleasant, joy and trust like no.17, 18 and 21. Some manga feel close to others feeling about content of manga. Focusing on the questionnaire about manga after experiments, there were some manga that manga expressions were commonplace and boring. Therefore, it is suggested that the feeling was weakened when reading the work. There were some subjects reporting that the manga was interesting but disliked.

Fig.4 and 5 show the results of evaluation values of nasal skin temperature of subA when reading manga. Focusing on the manga, the score of pleasant - unpleasant was the highest, we analyzed. In addition, we examined the influence of the evaluation value of nasal skin temperature of the subject. Fig. 4 shows a manga whose value of pleasant state has increased. In the state of pleasant after reading manga, it is suggested that the average temperature of the nose area is increasing. On the other hand, In Fig.5, unpleasant index is high about the score of manga. As for the manga which became unpleasant after reading, the average temperature of nose area have been decreasing slightly. Next, the average temperature and the difference between the maximum and minimum temperature and the variance value were compared with each other. Next, the difference between the average temperature and the maximum and minimum temperature and the dispersion value were compared. In Fig. 5(a), peaks were confirmed with variance values and difference

values at about 100s after the beginning to read manga. On the other hand, the average temperature has been increased at about 110s after the beginning to read manga. There is possibility that some kind feelings was aroused at 100s after the beginning to read manga. There is a possibility that estimation of emotion other than "pleasant-unpleasant" is measured by variance value and difference value However, In Fig 4,5(b,d), there were some cases where temperature have not been decreased. There are several possible reasons for this. In some subjects, there were individual differences in the influence of the situation resulting from the task, and the differences in the temperature exposed on the face caused by these individual differences prevented the appropriate evaluate. There were individual differences in the areas of the nose where the low temperature occurred. Emotion different for every individual.

Therefore, it is need to rethink health, emotion, intellect, mental state, desire, human relations of the person, and corresponding there to individually.

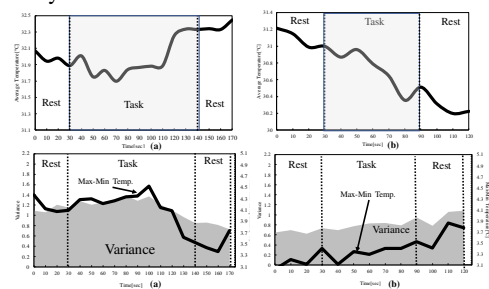


FIG.4 Nasal Skin Temperature evaluation value (pleasant).

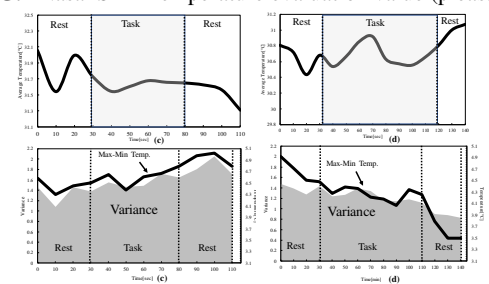


FIG. 5. Nasal Skin Temperature evaluation value (unpleasant).

ACKNOWLEDGEMENTS

This work was supported by JSPS KAKENHI Grant Number15H05323.

- 1 T. Mizuno, S. Kawazura, H. Asano, K. Mito, Y. Kume and N. Itakura (2015), Evaluation of the autonomic nerve activity using facial thermal image, Proceedings of the International Symposium on Artificial Life and Robotics (AROB 20th), Japan, 2015, pp.512-514.
- 2 T. Mizuno, T. Sakai, S. Kawazura, H. Asano, K. Akehi, S. Matsuno, K. Mito, Y. Kume and N. Itakura (2016), Measuring Facial Skin Temperature Fluctuation Caused by Mental Work-Load with Infrared Thermography", Institute of Electrical Engineers of Japan, Transactions on Electronics, Information and Systems, 136(11):1581-1585.

Application of the correlation methods to measurement of the IR detectors noise spectral density

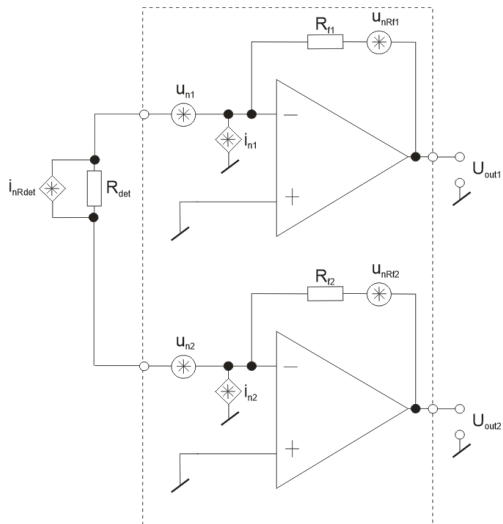
Małgorzata Panek

Military University of Technology, gen. Witolda Urbanowicza 2, 00-908 Warsaw
e-mail: malgorzata.panek@wat.edu.pl

The infrared (IR) detectors are used in many applications, such as e.g.: telecommunication (free space optics, fiber optics), spectroscopy, thermography, medicine, industry and many others. That is why, this technology is being developed in several directions: high detectivity, low time constant, size, cooling requirements, spectral range with multicolor option, and readout capability. The observed progress in construction of modern IR photodetectors causes the need to design a new diagnostic tool [1]. The parameters of these detectors can be varied within the broad values range and a conventional measurement technique are becoming less effective. One of the most important detector parameter is noise spectral density (NSD). It is usually specified in terms of noise current spectra and/or related wideband measures [2-3]. The most often, the noise characteristics is measured by a direct method using a low-noise signal conditioning unit (preamplifier) and spectrum analyzer (lock-in, FFT digital analyzer). The main limitations of this measurements are noises of the first stage of amplifiers. However, photodetectors development characterized by low noise and different resistances makes it necessary to develop advanced measuring techniques. Nowadays, some techniques have been used to measure noise of other electronic devices such as resistors and transistors. In these cases, the signal correlation methods have been applied to minimize influence of read-out electronics noise [4].

The work presents a concept of two read-out electronic units (ROU). The units provides to applied cross-correlation method (CCM) [5-7]. In comparison to autocorrelation method (ACM), the correlation between two-time series (from two-channel signal readout) is performed. In CCM-ROU setup, two preamp configurations can be implemented (Fig. 1).

a)



b)

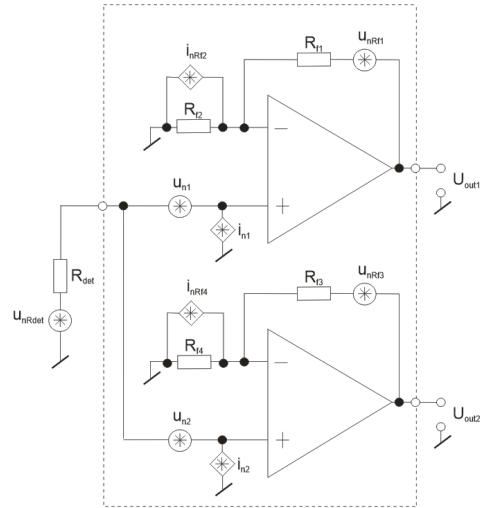


Fig. 1. Scheme of ROU with transimpedance amplifiers (a) and voltage amplifier (b) - (u_{nx} – noise voltage sources, i_{nx} – current noise sources, R_n – resistors, R_{det} – device under test).

In practice, the autocorrelation spectrum is determined using registered signal from a single channel (U_{out1}). For CCM method, the spectral characteristics is obtained by analyzing signals from both channels (U_{out1} and U_{out2}) at the same time. These presented operations determine formulas to calculate output noise signals. For ROU with transimpedance preamp (TIA), the voltage output noises equal

$$U_{nTIA(ACM)}^2 = i_{n1}^2 R_f^2 + u_{n1}^2 \left(1 + \frac{R_{f1}}{R_{det}}\right)^2 + u_{n2}^2 \left(\frac{R_f}{R_{det}}\right)^2 + u_{nRf1}^2 + i_{nRdet}^2 R_f^2, \quad (1)$$

$$U_{nTIA(CCM)}^2 = 2u_n^2 \left(1 + \frac{R_f}{R_{det}}\right) \left(\frac{R_f}{R_{dut}}\right) + i_{nRdet}^2 R_f^2. \quad (2)$$

In the case of voltage preamp (VA), the signals are described by

$$U_{nVA(ACM)}^2 = u_{nRdet}^2 \left(1 + \frac{R_{f1}}{R_{f2}}\right)^2 + u_n^2 \left(1 + \frac{R_{f1}}{R_{f2}}\right)^2 + 2i_n^2 R_{det}^2 \left(1 + \frac{R_{f1}}{R_{f2}}\right)^2 + u_{n1}^2 + i_{nRf2}^2 R_{f1}^2, \quad (3)$$

$$U_{nVA(CCM)}^2 = u_{nRdet}^2 \left(1 + \frac{R_{f1}}{R_{f2}}\right)^2 + 2i_n^2 R_{det}^2 \left(1 + \frac{R_{f1}}{R_{f2}}\right)^2. \quad (4)$$

In Eq. (2) and Eq. (4), there is assumed: $u_{n1} = u_{n2} = u_n$, $i_{n1} = i_{n2} = i_n$, $R_{f1} = R_{f3}$ and $R_{f2} = R_{f4}$. The described relations make it possible to calculate the noise figure (NF) of different ROU configurations (Fig. 3). The NF was determined depending on the DUT resistance and TIA or VA gains (R_f and G). Comparing, some results obtained using ACM method are also presented. The setup configuration of ROU-TIA provides to minimize influence

of its current noise. In the case of ROU-VA, the voltage noise has been minimized.

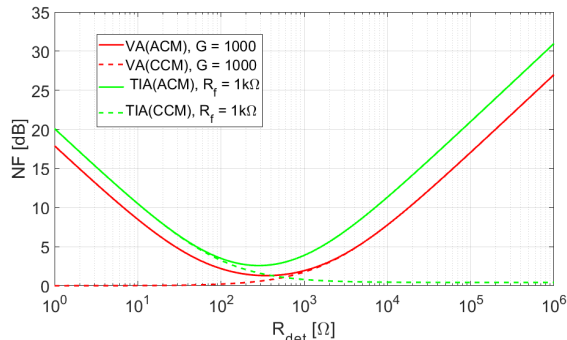


Fig. 3. Calculated NF for ACM (solid lines) and CCM setups (dashed line).

Based on performed analyses, ROU-TIA setup was constructed (Fig. 4). In this setup, low-noise preamps with AD797 op-amp were applied. The developed construction provides to register signals that can be processed in ACM and CCM procedures.

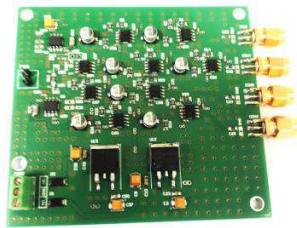


Fig. 4. The constructed ROU-TIA setup

The setup was tested during measurement of the noise density of resistors (noise sources) with well-defined noise characteristics. The spectrum analyzes was performed using the TiePie HS4 data acquisition card and own-developed MATLAB software. The NF of this setup for different resistors values was determined and compared with theoretical values (Fig. 5).

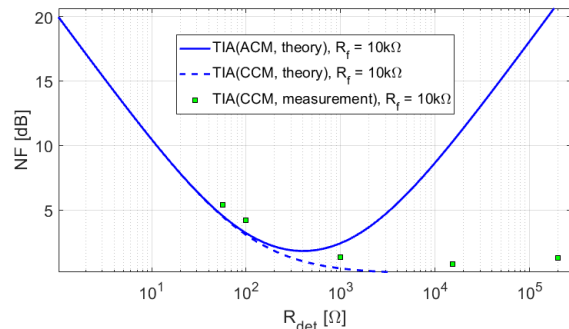


Fig. 5. NF of ROU-TIA for different values of the noise source resistances

The tests results confirmed reduction of ROU-TIA current noise influence.

Finally, the noise measurement of an IR photodetector was made (Fig. 6). The results have been compared with data obtained using ACM techniques with a commercial low-noise current amplifier (model SR570) and with designed single-channel ROU-TIA (with AD797 op-amp). There is observed $1/f$ noise suppression.

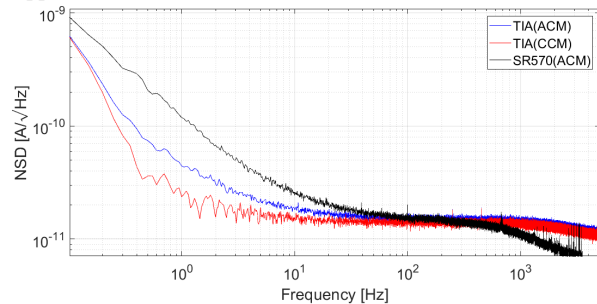


Fig. 6. Characteristics of photodetector noise spectral density of the photodetector (NSD).

ACKNOWLEDGEMENTS

I would like to express my sincere thanks to Krzysztof Achtenberg for technical support in developing the ROU setup. I would also like to thank Dr Janusz Mikołajczyk for their scientific support. This research was supported by The Polish National Centre for Research and Development grant DOB-BIO8/01/01/2016.

-
- [1] A. Rogalski, Z. Bielecki, and J. Mikołajczyk, "Detection of optical radiation," in *Handbook of Optoelectronics*, CRC Press. Taylor & Francis Group, 2018, pp. 65–125.
 - [2] Ł. Ciura, A. Kolek, W. Gawron, A. Kowalewski, and D. Staszek, "Measurements of low frequency noise of infrared photodetectors with transimpedance detection system," *Metrol. Meas. Syst.*, vol. 21, no. 3, pp. 461–472, 2014.
 - [3] J. Smulko, *Szumy czujników metody pomiarów i analizy*. Wydawnictwo Politechniki Gdańskiej, 2014.
 - [4] M. Sampietro, L. Fasoli, and G. Ferrari, "Spectrum analyzer with noise reduction by cross-correlation technique on two channels," *Rev. Sci. Instrum.*, vol. 70, no. 5, pp. 2520–2525, 1999.
 - [5] A. Konczakowska, J. Cichosz, A. Szewczyk, and B. Stawarz, "Systemy do pomiaru szumów własnych przyrządów półprzewodnikowych w zakresie małych częstotliwości."
 - [6] F. Crupi, G. Giusi, C. Ciofi, and C. Pace, "A novel ultra sensitive method for voltage noise measurements," *2005 IEEE Instrumentation and Meas. Technol. Conf. Proc.*, vol. 2, no. May, pp. 17–19, 2005.
 - [7] C. Ciofi, G. Scandurra, R. Merlino, G. Cannatà, and G. Giusi, "A new correlation method for high sensitivity current noise measurements," *Rev. Sci. Instrum.*, vol. 78, no. 2007, p. 114702, 2007.

Study on mental load measurement of center of gravity fluctuation in sitting position

Shuhei Sakamoto¹, Kota Akehi, Marzieh, Aliabadi Farahani, Naoki Itakura, Tota Mizuno

The University of Electro-Communications, Graduate school of Informatics and Engineering, Chofu/Tokyo, Japan

e-mail address: fctamagawa@yahoo.co.jp

I. INTRODUCTION

With the recent advanced information society, so-called VDT work using computers has been increasing and diseases such as VDT syndrome are concerned.

Therefore, various prior studies on mental burden in VDT work are carried out¹. These are evaluated by methods such as subjective evaluation, saliva test, blood test, brain waves, heart rate, blood pressure, perspiration, nose skin temperature etc.

Subjective evaluation, saliva / blood test etc. require time for evaluation. Measurement of brain waves, heart beat, blood pressure, sweating, nasal skin temperature, etc. involves restraint of sensor attachment and long restraint. Therefore, it is difficult to reflect it in actual work, and it is not practical. If evaluation of mental burden / burden of workers can be evaluated unconstrained while involving actual work, it becomes one index to relieve stress.

On the other hand, considering ordinary VDT work, it is often done in sitting position. Furthermore, there are many works in the sitting position in desk work and daily life in the workplace.

Based on the above points, this study examines a method that can evaluate the mental burden in the sitting state simply and nonconstrainingly. If mental burden / burden in the sitting state can be evaluated, it is beneficial for workers to grasp the mental state by sitting on a chair regardless of VDT work, desk work and daily life.

A method using images and centroid shaking can be cited as a mental evaluation performed by a simple and unconstrained measurement method.

Many previous studies on the former evaluated the mental state from real and thermal images. However, since this method is evaluated while photographing with a camera, it is applicable for VDT work but it is difficult to evaluate everyday life.

On the other hand, in the previous studies on the center of gravity fluctuation, the relation with vision / sound stimulation, physical / mental load, fatigue is shown². Many of the previous studies have been evaluated in the standing position, but the evaluation in the sitting position is small. Measurement of the center of gravity fluctuation in the sitting position has an advantage that it can be easily measured by incorporating a pressure sensor in the chair.

Therefore, in this research, we investigate whether the mental load of subjects can be evaluated simply by measuring the center of gravity fluctuation in the sitting state.

II. PROPOSAL METHOD

In this research, two centroid motion sensors were used to measure the center of gravity sway of the buttocks and feet. The center of gravity swing meter used was set to a sampling frequency of 100 Hz on a balance Wii board (hereinafter referred to as Wii board). The Wii board can be handled as a cordless measuring instrument by connecting with a PC with Bluetooth. The

installation position was assumed to be the sitting position and it was set at the bottom two parts of the buttocks and feet. Experiments were conducted with the unit tilted always horizontal. The Wii board can not be measured properly unless it is supported only by the strain gauge type force sensor built in the four corners. For that reason, the chair adopted a flat seating surface and laid a cushion on the center of gravity swaymeter. On the foot part, we did not put the cushion on the floor assuming the Wii board directly in contact with the floor.

For the measurement, the method shown below was performed for each subject for 30 minutes. We evaluated the effects on body and mind every 5 minutes together with the physiology and psychological index described later.

Subjects were seven healthy adults (average age 23.8 ± 4.1 , male 6, female 1) without severe neurological, academic, or orthopedic diseases that had a clear influence on task performance.

The contents of the experiment were VDT worked in the chair sitting position and the x - y coordinates of the center of gravity at each sampling time were recorded.

VAS (Virtual Analogue Scale) was used as an indicator of mental load. Since the VAS can quantitatively evaluate the sensory measure of the subject, we measured changes in the psychological state and mental and physical condition of the subjects.

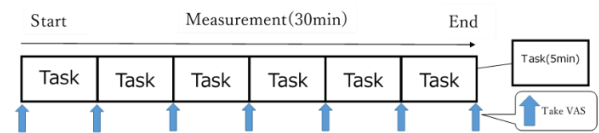


Fig1 Experiment procedure

III. REFERENCES

In previous studies in the past, research has been conducted to calculate the outer circumference area per minute and the track length per second and compare the data for each subject. Experiments were also conducted in this research, in the same procedure as in the previous study³. However, it was not possible to obtain significant results in the outer circumference area and total travel distance.

Therefore, in this research, we focused on the vector formed by the center of gravity fluctuation and evaluated it. The vector is an angle to the next acquired coordinates with the origin acquired from the coordinates acquired every sampling time. We divided the vector of the center of gravity fluctuation by 15 degrees, and focused on the average moving distance, the maximum moving distance and the number of times of movement, respectively. As a result, the center of gravity fluctuation during the VDT operation in the sitting state concentrated in the anteroposterior direction and was not seen in the lateral direction much. In all subjects, there was a correlation of 0.9 or more between the average movement distance and the movement frequency. Therefore, in this research, we focus on the average moving distance and show the maximum

and minimum transition of the average moving distance throughout the experiment as follows.

Table 1 The maximum and minimum angle at which the average moving distance at the foot portion

Subjects	A	B	C	D	E	F
Max	-90 ~-75	-90 ~-75	-90 ~-75	-90 ~-75	-90 ~-75	-90 ~-75
Min	165 ~180	-180 ~-165	-180 ~-165	165 ~180	165 ~180	165 ~180

The angle is set to 0 degree on the right side, positive angle on the front side and negative angle on the back side. From the results in Table 1, it was confirmed that all the subjects were in common and the foot moved the most to the right rearward, but not moved to the left most. When attention was paid to other angles, it was found that the foot part moves much in the anteroposterior direction and is small in the lateral direction.

Also, it was confirmed that the buttocks are moving most to the right side of the right side, but not moved to the left front most. From Table 1, it was found that the concentration was concentrated in one direction. Even though attention was paid to other angles, there was no significant difference from the feet.

It was found that there are many movements in the anteroposterior direction in common with the feet and buttocks and it is found to be small in the lateral direction.

As for VAS, negative correlation was observed with concentration and fatigue degree, so we attention on concentrating ability and evaluate. Table 2 shows the VAS for each subject.

Figures 2 and 3 show the transition of the maximum average travel distance at the above angle.

Table2 VAS of each section of each subject

Time	~ 5min	~ 10min	~ 15min	~ 20min	~ 25min	~ 30min
A	8	7	6	4	3	2
B	7	7	6	4	4	3
C	8	7	7	6	6	5
D	8	7	6	4	3	2
E	10	9	7	4	2	3
F	9	8	6	4	2	2

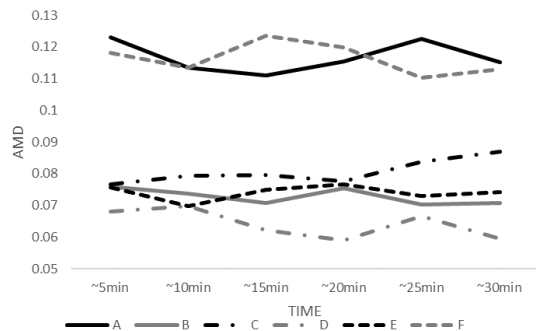


Fig2 Transition at an angle at which the average moving distance of the foot portion is the maximum

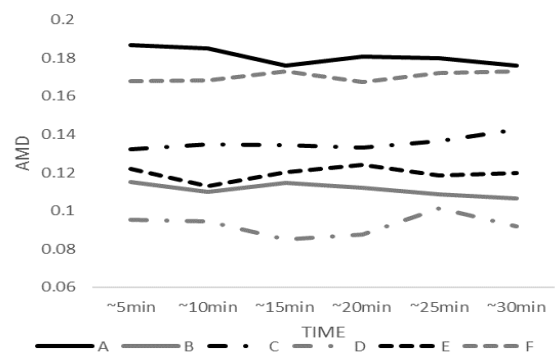


Fig3 Transition at an angle at which the average moving distance of the foot portion becomes the minimum

IV. CONSIDERATION

When the angle is not limited, a correlation of 0.9 or more was found between VAS and average moving distance. In other words, it turns out that when the person is not concentrating, the movement of the center of gravity of the foot part is seen more often. However, the value of the correlation between VAS and average moving distance varied among subjects when limiting the angle with the largest mean moving distance. Some subjects moved many centers of gravity in one direction but some subjects are not always so. As for the cause this time, we tried the experiment with fixed attitude to sit on the subject but the possibility of experimenting with the posture different from usual. From now on, subject information such as attitude and body weight in the state of the sitting position of each subject is further refined and applied to the results obtained in this research so as to obtain meaningful results.

¹ Rin Kosaka and Hiroshi Iwasaki, Fundamental study on fatigue mitigation effect during VDT work by installing plants, Japan Greening Engineering Journal 40(1), 254-256, (2014)
² Fumiya Kinoshita, Hiroki Takada and Yuki Mori, A study of stabilometry in sitting position with alcoholic intake, Bulletin of Social Medicine, Vol.33(1)2016.

³ Yoshiyuki MIYAZAWA, Tomoyuki ASAKURA, Shigeru USUDA, Validity of Postural Sway Measurements during Static Standing Made by Accelerometers Placed on Different Body Segments, Physical Therapy Science 923-927, 2017.

Hyaluronic acid dynamics and its interaction with synovial fluid components as a source of the color noise

Jacek Siódmiak and Piotr Beldowski

Department of Physics, Institute of Mathematics and Physics,
UTP University of Science and Technology, 85-796 Bydgoszcz, Poland
e-mail addresses: jacek.siodmiak@utp.edu.pl; piotr.beldowski@utp.edu.pl

I. INTRODUCTION

Synovial fluid that fills the joints is a very dynamical multicomponent system. Most abundant in synovial fluid hyaluronic acid (HA) and phospholipids (PL) are key constituents of the lubricating molecular layer in synovial joint organ systems¹. Long hyaluronic acid chains (in contrast to the short fraction characteristic for osteoarthritis) in combination with phospholipids has a tendency to cross-link through the formation of intra- and inter-chain hydrogen bonds, Fig. (1), as well as through hydrophobic interactions between polar residues. The formation and breaking of hydrogen bonds between elements of hyaluronic acid can be a source of noise at the molecular level^{2,3}.

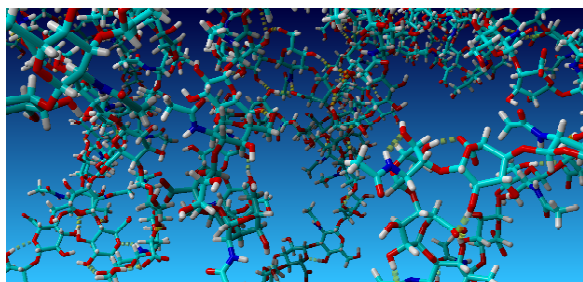


FIG. 1. Simulation snapshot showing HA chain with indicated hydrogen bonds marked with a yellow dotted cylindrical lines. Atoms are colored as follows: light blue - carbon, dark blue - nitrogen, red – oxygen and white - hydrogens.

II. METHODS AND RESULTS

Using Molecular Dynamics simulations we show that in contrast to the macroscopic thermal (white) noise^{2,3} the short-time noise on the molecular scale has the properties of color noise⁴ with the power spectrum distribution (PSD) proportional to the inverse of frequency:

$$S(f) \sim \frac{1}{f^\alpha}, \quad (1)$$

¹ J. Siódmiak, P. Beldowski, W. K. Augé II, D. Ledziński, S. Śmigiel, A. Gadomski, *Molecules* 22/9, 1436 (2017).
² N. Wax, Ed., *Selected Papers on Noise and Stochastic Processes*, Dover Publications, New York 1954.
³ P. Hänggi, P. Jung, *Adv. Chem. Phys.* 89, 239 (1995).

where f is frequency and α is power spectrum exponent, Fig. (2).

We also show that the long-time simulations are characterized by a power spectrum similar to that of white noise.

The simulations were carried out for long and short chains of hyaluronic acid in the presence and absence of phospholipids. Because in the biological system the temperature is a very important factor that affects many biological processes we also examine the influence of the temperature on the PSD in all mentioned scenarios.

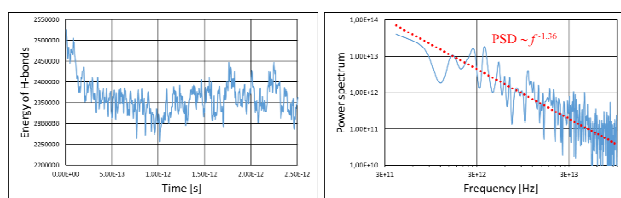


FIG. 2. An example results obtained for short-time simulation of HA-PL system for temperature equal 310 K. The summary energy change in time of H-bonds (left) and power spectrum of the energy change (right). Red dotted line represents fitting function of the PSD.

III. SUMMARY

Modern techniques of measurement allow to tracking of individual molecules, e.g. single molecular tracking, which are very sensitive to any fluctuations of the measured parameters^{5,6}.

The question is whether these methods will be able to record energy changes with frequencies characteristic of the formation and breaking of hydrogen bonds. If so, the presented analyzes may be useful in the removal of noise and interpretation of measurement results.

ACKNOWLEDGEMENTS

This work was supported by an internal Grant No. BS39/14 of the Institute of Mathematics and Physics of the UTP University of Science and Technology in Bydgoszcz.

⁴ Z. Zhi, S. Nan, F. Haiping, W. Rongzheng, *Phys. Chem. Chem. Phys.*, 18, 30189 (2016).

⁵ C. Zhou, X. Li, Z. Gong, C. Jia, Y. Lin, C. Gu, G. He, Y. Zhong, J. Yang, X. Guo, *Nature Commun.*, 9, 807 (2018).

⁶ C. Manzo, M. F. Garcia-Paraj, *Rep. Prog. Phys.* 78, 124601 (2015).

Noise measurements in supercapacitors at selected floating voltages

Arkadiusz Szewczyk, Łukasz Lentka, Janusz Smulko
Gdańsk University of Technology, Faculty of Electronics, Telecommunications and Informatics,
Department of Metrology and Optoelectronics,
80-233 Gdańsk, ul Narutowicza 11-12
szewczyk@eti.pg.edu.pl

I. INTRODUCTION

Supercapacitors are devices that are capable to store relatively high amount of energy in comparison with its mass. On a Ragone plot, where the power density versus energy density of devices is presented, supercapacitors are placed between classical capacitors and batteries¹. Due to low equivalent series resistance (ESR) the supercapacitor could be charged/discharged with high current, even of hundreds of Amperes.

Increasing market of supercapacitors and growing number of applications requires control of its electrical parameters and quality. Supercapacitor's quality is usually derived from its capacitance C , resistance ESR, equivalent distributed resistance EDR, and impedance. Commonly used methods of supercapacitors' testing are: cycling voltammetry (CV), galvanostatic cycling with potential limitations (GCPL), impedance spectroscopy. These parameters are observed at accelerated aging²⁻⁶. All those methods are based on observation of current and voltage during forced charging/discharging of the supercapacitor at selected polarization conditions.

Very sensitive and promising method of quality and reliability assessment is based on low frequency noise (flicker noise) measurements. It's widely used for semiconductor devices, sensors of various characters, electrochemical units, chemical reactions as corrosion, and other random phenomena⁷⁻¹². It's sensitive to structure impurities, any defects or even tiny degradations. The detailed procedure is not obvious, as those devices have huge capacitance and therefore flicker noise can be dominant at very low frequency range only.

II. NOISE MEASUREMENT SET-UP

Noise measurements require stable conditions and low inherent noise of the measurement set-up. In a case of supercapacitor the relatively high capacitance results in a very low frequency of low pass filter formed by its capacitance and loading resistance connected to the supercapacitor's terminals. Thus, only very low frequency noise generated inside supercapacitor may be observed and measurement time have to be relatively long, up to a few hours to estimate power spectral density at limited random error.

To ensure stable conditions of noise measurements, we decided to measure noise during supercapacitor's discharging through the selected loading resistance. The measurement set-up is shown in Fig. (1).

As a source of voltage and current for polarizing the specimen a computer controlled by potentiostat/galvanostat was used. The tested supercapacitor (DUT) is connected to the measurement set-up through a switching unit. This unit can disconnect the sample from current/voltage source during noise measurements.

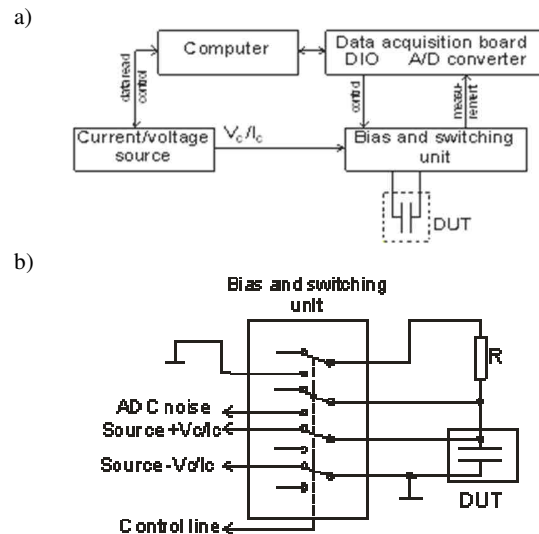


FIG. 1. Measurement set-up of noise recording: a – block diagram, b – schematic of polarizing and switching unit.

Measurement procedure starts with charging the specimen to the selected voltage. Then, the DUT is kept at this voltage for 2 h to charge the structure. Next, the specimen is disconnected from a voltage/current unit and the loading resistor is connected and next voltage across the supercapacitor is recorded by data acquisition board. The capacitance and equivalent series resistance ESR of specimen were also measured.

In the experiment two types of supercapacitor's samples were used. The samples differ in a composition of active carbon electrodes used for their fabrication.

III. MEASUREMENTS RESULTS

In the experiment noise was measured at selected floating voltages. The voltages were: 0.5 V, 1.0 V, 1.5 V, 2.0 V, 2.5 V and next 2.0 V, 1.5 V, 1.0 V, 0.5 V. For each voltage, the samples were floated for 2 h and noise was recorded across the loading resistor of 200 Ω . After each run, the specimen was refreshed by applying the procedure of discharging by short circuiting and next slightly negative polarization.

The recorded data consists of a strong component decaying close to exponential function and corresponding to capacitor discharge voltage and less intense additive noise component.

The main component was removed by applying trend removal procedure¹³ and power spectral density of the identified additive

noise was estimated. Exemplary spectrum is shown in Fig. (2). Spectrum exhibits $1/f$ –like noise component at very low frequency range, below 3 Hz, and white noise component above this point. To compare noise level for different polarizing voltages the mean value of $1/f$ component and mean value of white-noise component was calculated. Results for PB11 samples are shown in Fig. (3) and Fig. (4).

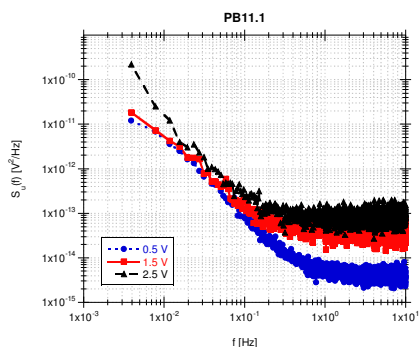


FIG. 2. Power spectral density of additive noise voltage of the specimen PB11 observed at different polarizing voltages

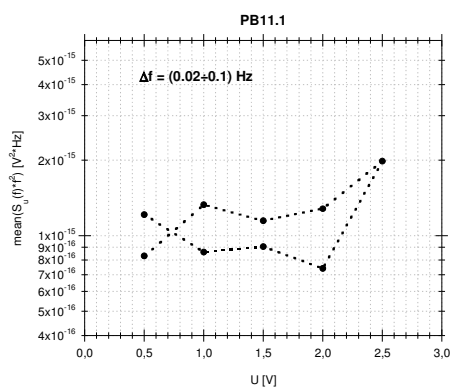


FIG. 3. Mean value of the product of power spectral density multiplied by frequency f^2 of discharge voltage of PB11 sample at the frequencies when $1/f$ noise dominates

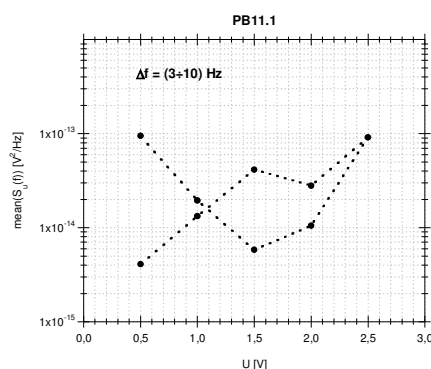


FIG. 4. Mean value of power spectral density of discharge voltage of PB11 sample for white-noise region

A small increase in intensity of noise is observed for both, $1/f$ and white noise region.

IV. CONCLUSIONS

Presented results of low frequency noise measurements in supercapacitors confirmed that the developed measurement set-up and methodology of low frequency noise measurements enable identification of $1/f$ -like noise component. Flicker noise was observed at frequencies below 1 Hz.

The investigated devices increased noise intensity when high polarizing voltages was applied (e.g., 2.5 V). At lower voltages flicker noise remains almost unchanged, although for the second part of the experiment (voltages from 2.0 V to 0.5 V) noise intensity is slightly higher. It could be caused by either the memory effects in the structure of the specimen or by device degradation. More experiments are required to investigate this issue and to give conclusive remarks.

ACKNOWLEDGEMENTS

This research was financed by the National Science Center, Poland, project No. DEC-2014/15/B/ST4/04957, “Charging/discharging mechanism at the electrode/electrolyte interface of supercapacitors”.

- 1 R. Kötz and M. Carlen, *Electrochimica Acta* 45, 2483–98, (2000).
- 2 F. Beguin and E. Frackowiak, *Supercapacitors: Materials, Systems and Applications* (Weinheim, Germany, Wiley-VCH Verlag GmbH & Co. KGaA 2013).
- 3 V. Sedlakova, J. Sikula, J. Majzner, P. Sedlak, T. Kuparowitz, B. Buergler and P. Vasina, *Metrology and Measurement Systems* 23, 345–58, (2016.)
- 4 A.M. Bittner, M. Zhu, Y. Yang, H. F. Waibel, M. Konuma, U. Starke and C.J. Weber, *Journal of Power Sources* 203, 262–273, (2012).
- 5 M. Zhu, C.J. Weber, Y. Yang, M. Konuma, U. Starke, K. Kern and A.M. Bittner, *Carbon* 46, 1829–1840, (2008).
- 6 O. Bohlen, J. Kowal and D.U. Sauer, *Journal of Power Sources* 172, 468–475, (2007).
- 7 J. Smulko, K. Darowicki and A. Zieliński, *Electrochimica acta*, 47(8), 1297-1303, (2002).
- 8 M. Kiwilszo and J. Smulko, *Journal of Solid State Electrochemistry* 13(11), 1681-1686, (2009).
- 9 J. Smulko, *Fluctuation and Noise Letters* 6 (2), R1-R9, (2006).
- 10 J. Smulko, B. Kish and G. Granqvist, *Ionics* 13 (3), 179–182, (2007).
- 11 L.K.J. Vandamme, *IEEE Transactions On Electron Devices* 41 (11), 2116-2187, (1994).
- 12 A. Konczakowska, *Quality and Reliability Engineering International* 14, 83-85, (1998).
- 13 Ł. Lentka, J. Smulko, *Zeszyty Naukowe Wydziału Elektrotechniki i Automatyki Politechniki Gdańskiej* 51, 111-114, (2016).

Low frequency noise and resistivity characteristics of epoxy composites with onion-like carbon and multi-walled carbon nanotubes

Marina Tretjak, Sandra Pralgauskaitė, Jonas Matukas, Jan Macutkevič, and Jūras Banys
Institute of Applied Electrodynamics and Telecommunications, Vilnius University, Sauletekio 3, 10257 Vilnius, Lithuania
e-mail address: marina.tretjak@ff.vu.lt

I. INTRODUCTION

Composite materials with carbon nanoparticles are widely used in various modern electronic and bioelectronic devices¹⁻⁴. The electromagnetic properties of composites strongly depend on the features of conductive particles, their density, distribution, etc. Therefore, varying the nanoparticles and their properties, materials with desired characteristics can be fabricated. In addition to the mentioned, the composites with carbon nanoparticles have the immunity to the excess electrical noise that, in general, tends to increase as dimensions of the structure decrease. Carbon nanoparticles behaving as covalently bonded metallic wires are less susceptible to such fluctuations. This aspect enables composites with carbon nanoparticles widely employ in nanoelectronics.

One of the important features of the isolator/conductor composite material is the percolation threshold. It is aimed to obtain a low percolation threshold with the minimal density of expensive fillers (as carbon nanotubes are). Usage of more than one type of carbon nanoparticles in one material makes possible electrical transport in different fillers' percolation networks together, what decreases the percolation threshold⁵. Therefore, polyphase composites even more enlarges opportunities to fabricate materials with wanted characteristics.

Comprehensive characterization of new materials is of high importance before employing them for devices' fabrication. The noise characteristics are very sensitive to the physical processes that take place in various materials and structures. Their analysis helps to clear up the charge carrier transport and conduction mechanisms in disordered materials (as the composite materials are).

The purpose of this work was to investigate the low frequency noise and resistivity characteristics of polyphase composites with onion like carbon (OLC) and multi-walled carbon nanotubes (MWCNTs) in order to clear up the influence of the density of different carbon nanoparticles to the electrical characteristics of the composite.

II. MATERIALS

The investigated materials are polyurethane composites with various density of carbon nanotubes and onion like carbon particles. The materials are polyphase composites – contain both OLC and MWCNTs⁵. In this work there are presented results for materials with:

- 5 wt% OLC and 0.5 wt% MWCNT;
- 7 wt% OLC and 0.5 wt% MWCNT;
- 7 wt% OLC and 1 wt% MWCNT;
- 7 wt% OLC.

Polyurethane, manufactured using the Clear Gloss MINWAX1 technology, was used as a bonding matrix. Multi-walled carbon nanotubes with a diameter about 20 nm and a length 5-10 μm and onion like carbon nanoparticles with diameter about 100 nm were used as nanofillers. MWCNTs were purchased from Amorphous Carbon Materials Inc., while OLC was manufactured using

vacuum heating from exploded nano diamonds⁵⁻⁸. The investigated composite materials distinguish by semiconductor's properties and are above the percolation threshold.

III. MEASUREMENT TECHNIQUE

Comprehensive measurement of resistivity and low frequency noise in a wide range of temperature (75 K - 365 K) have been performed. The measurement of the resistivity characteristics was carried out by a digital analyzer "Keysight Technologies B1500A". The noise measurements were performed in a specially shielded laboratory to avoid interference from electrical network and communication systems. Noise spectra were measured in the frequency range from 10 Hz to 20 kHz.

The measured noise signal was processed by a low-noise amplifier, a filter system, and an analogue digital converter (National InstrumentsTM PCI 6115board)⁹. The measuring scheme is presented in Fig. (2). The load resistance, R_{load} , was at least 10 times smaller than the resistance of the sample under test. These conditions were chosen to guarantee the constant voltage operation – current fluctuations were measured.

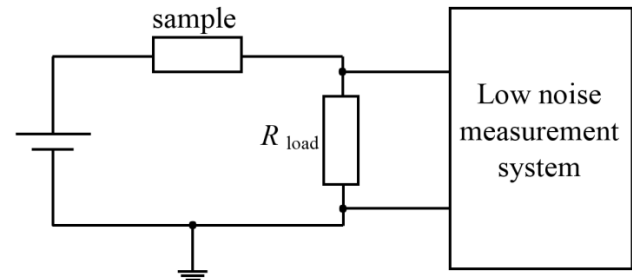


FIG. 1. Scheme of the measuring system.

The noise spectral density was calculated using the standard Cooley–Tukey Fast Fourier Transform algorithm and evaluated by comparison with the thermal noise of the standard resistor (described by Nyquist's theorem), which was at the room temperature, and also used as a load resistor. The voltage noise spectral density was evaluated according:

$$S_U = 4kTR_{load} \frac{S - S_{load}}{S_{load}} \left(\frac{R_{load} + R}{R_{load}} \right), \quad (1)$$

where S and S_{load} are the noise variances of the sample and the standard resistor, respectively, in the narrow frequency band Δf ; T is the absolute temperature of the standard resistor, R is the sample resistance, R_{load} is the standard resistor resistance and k is the Boltzmann constant.

IV. RESULTS AND DISCUSSION

The resistivity values of the investigated materials differ depending on the type and density of the carbon nano particles. Up to a voltage of 1 V the resistivity is constant apart for the material without MWCNTs (with 7 wt % OLC fillers) (Fig. 2). At higher voltage the resistance of the investigated materials decreases (Fig.

2), what is typical for composites with conductive fillers (carbon nanoparticles can be treated as having the metallic conductance).

The composite with 5 wt % OLC, 0.5 wt % MWCNT fillers have the largest resistance and the composite with 7 wt % OLC, 1 wt % MWCNT fillers distinguish by the smallest resistance comparing the investigated materials (Fig. 2). The density of the OLC fillers has greater influence to the composite's conductivity comparing to the MWCNTs. If 7 wt % of OLC fillers are present in the material, its resistivity is comparably low (about 1-100 k Ω m). The MWCNTs addition to the composite slightly decreases the resistivity, but it does not have a strong effect.

The resistivity dependencies on temperature are presented in Fig. 3. At low temperatures (up to 172 K) the resistivity decreases when the temperature increases. At these temperatures the

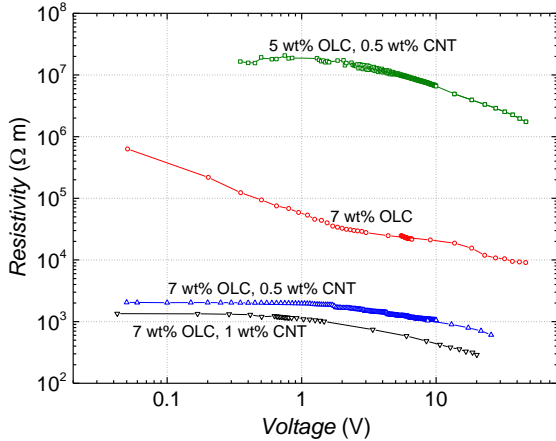


FIG. 2. Resistivity dependence on voltage at 290 K.

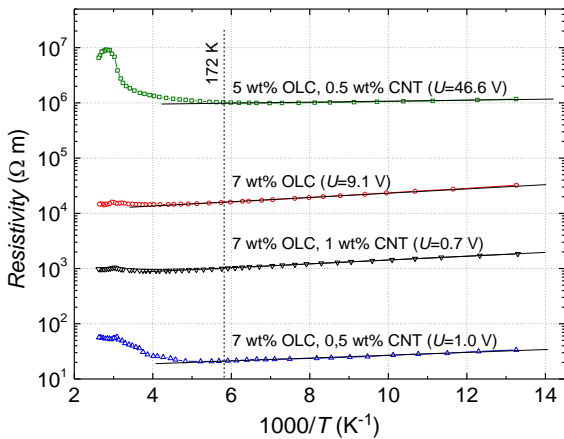


FIG. 3. Resistivity dependence on temperature at fixed voltage.

resistivity can be well approximated as $1/T$ (Fig. 3), what suggest that fluctuation induced tunneling dominates in the charge carrier transport¹⁰. At higher temperature the resistivity starts to increase due to polyurethane matrix expanding; and above 357 K the resistivity decreases as conductivity in the matrix starts.

The low frequency fluctuations of the investigated materials distinguish by $1/f^\alpha$ -type and Lorentzian-type spectra (Fig. 4). $1/f^\alpha$ -type fluctuations are an outcome of the superposition of many generation and recombination processes of similar intensity and with widely distributed characteristic times. At particular temperatures Lorentzian-type spectra are observed what indicates intensive generation and recombination processes with characteristic times ranging from 0.1 μ s to 1 μ s (e. g., curves at 85 K and 93 K in Fig. 4).

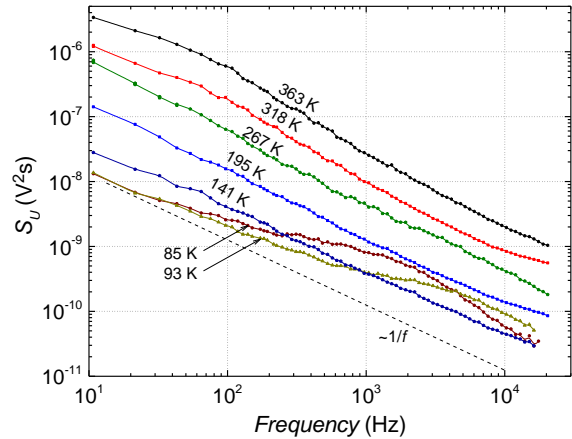


FIG. 4. Voltage fluctuation spectra at different temperatures for composite with 7 wt % OLC fillers at 9.1 V.

The noise spectral density is proportional to the voltage square. Therefore, the observed voltage noise is caused by the resistance fluctuations that originate from the random charge carrier capture and release processes in defects' formed centers.

V. CONCLUSIONS

The low frequency noise and resistivity characteristics of polyphase composite materials with onion like carbon and multi-walled carbon nanotubes were investigated. The low frequency noise spectra comprise of $1/f^\alpha$ -type and Lorentzian-type components.

The predominant charge carrier transport mechanism in the investigated materials is tunneling controlled by the charge carrier capture and release processes in defects' formed centers. And it does not depend on the density of the carbon nanofillers (for the investigated ranges).

¹ С. Н. Колокольцев, Углеродные материалы: свойства, технологии, применения. (Интеллект, Долгопрудный, 2012).
² B.S. Sreeja, S.Radha, *Microelectronics J.* **43**, 1 – 12 (2012)
³ T. Li, X. Liu, C. Dong, L. Yin, *Microelectronics J.* **119**, 155 – 158 (2014)
⁴ П. Н. Дьячков, Электронные свойства и применение нанотрубок (Бином Лаборатория знаний, Москва, 2012).
⁵ I. Kranauskaite, J. Macutkevicius, J. Banys, E. Talik, V. Kuznetsov, N. Nunn, and Olga Shenderova, *Phys. Status Solidi B*, **252**, 1799–1803 (2015).
⁶ V. L. Kuznetsov, Yu. V. Butenko, A. L. Chuvilin, A. I. Romanenko, and A. V. Okotrub, *Chem. Phys. Lett.* **336**, 397-404 (2001).

⁷ J. Macutkevicius, I. Kranauskaite, J. Banys, S. Moseenkov, V. Kuznetsov, and O. Shenderova, *J. Appl. Phys.* **115**, 213702, (2014).
⁸ J. Macutkevicius, D. Seliuta, G. Valusis, J. Banys, V. Kuznetsov, S. Moseenkov, and O. Shenderova, *Appl. Phys. Lett.* **95**, 112901 (2009).
⁹ S. Pralgauskaitė, J. Matukas, M. Tretjak, J. Macutkevicius, J. Banys, A. Selskis, A. Cataldo, F. Micciulla, S. Bellucci, V. Fierro, and A. Celzard, *J. Appl. Phys.*, **121**, 114303 (2017).
¹⁰ P. Sheng, *Phys. Rev. B* **21**, 2180 (1980).

Determination of Low Frequency Noise in Polycrystalline ZnO Layers

Virt I.S.^{1,3}, Bester M.², Didowska O.³

¹Centre for Innovation and Transfer of Natural Sciences and Engineering Knowledge, University of Rzeszow, 1, Pigionia Str., 35959 Rzeszow, Poland: ivirt@ur.edu.pl

²Centre for Innovation and Transfer of Natural Sciences and Engineering Knowledge, University of Rzeszow, 1, Pigionia Str., 35959 Rzeszow, Poland: mbester@ur.edu.pl

³Ivan Franko Drohobych State Pedagogical University, 24, I. Franko Str., 82100 Drohobych, Ukraine: olga-aspir@ukr.net

I. INTRODUCTION

There is a lot of interest in the study of nanostructured composite materials, especially ZnO, due to the possibility of obtaining ultraviolet sensors - photodetectors (PD). Measurements of the spectral density of present noise were made in the form of nanomaterial layers - ZnCoO. Low frequency noise measurement is also widely used as a powerful tool to study the distribution of traps and defects in semiconductors. It has been found that in comparison with other spatially disordered materials, these samples show a low degree of resistance changes which changes with ultraviolet (UV) blooming.

As a broadband semiconductor ($E_g = 3.3\text{eV}$), the easily produced semiconductor, zinc oxide (ZnO) has a lot of interest due to the potential for a wide range of optoelectronic applications and is a functional material. One of the important applications is based on ZnO UV light sensor [1]. ZnO can also be used in photovoltaic devices, light emitting diodes, solar cells and gas sensors. In addition to the two-dimensional (2D) ZnO layers, it is also possible to increase 1-dimensional (1D) ZnO nanostructures, such as nanowires and nanotubes. This photoconductive gain depends strongly on the interfacial properties of the nanostructures. Compared to 2D thin-film PDs, it has been shown that PD with 1D nanostructures can provide large internal reinforcement due to the high efficiency of hole and electron separation on the surface. Doping can also significantly improve both the optical and electrical properties of 2D ZnO thin films. In this work we present the results of low frequency noise measurements from polycrystalline Zn-based polycrystalline layers in the dark as well as under UV radiation under normal conditions.

II. EXPERIMENTAL PROCEDURE

In this study, polycrystalline layers were used in ZnO-cobalt-doped layer synthesized on Al_2O_3 substrate by pulsed laser deposition. The samples were made by the laser spraying the target at 30°C for 30 minutes. A rectangular sample measuring 7.0×3.0 mm was made to test the electrical conductivity of the material. Metallic Ag contacts were then made. Photoelectronic and noise properties will also be discussed. ZnO photoconductance is often dominated by surface-mediated phenomena, and oxygen chemisorptions always play a key role in photosensitivity regulation. A high-quality ceramic ZnO disk was used as the target source. The pressure in the chamber was maintained at 10^{-6} Pa during the sputtering process. The thickness of the films ZnO was about 300 nm. The sample was placed in a shielded kilt. Amplifier was 100 by UNIPAN amp. The noise

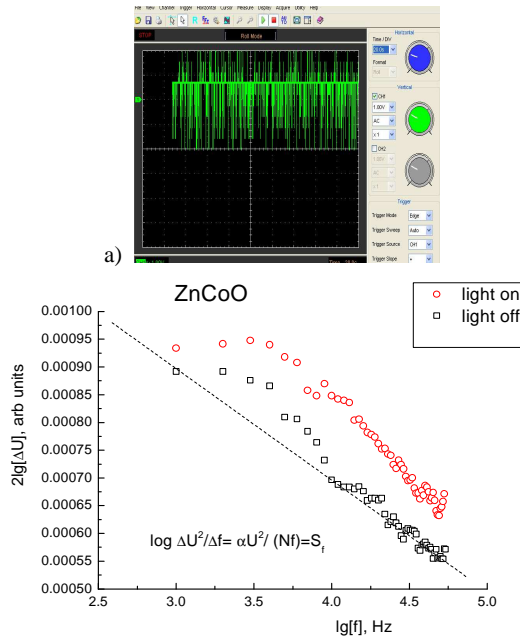
current was fed to the low level amplifier and the output signals were analyzed using a DSO oscilloscope (Fig. 1a). The current intensity has been set by the maximum allowable input voltage applied to 1 mA. The observation time was set at sampling rates of 4096/s and 256/s, which corresponds to two spectra from 10 to 10^6 1/s, obtained in the fast Fourier transformation of the DSO oscilloscope. The frequency range of 10 Hz ÷ 1 MHz was selected for noise measurements. To determine the frequency content of the sampled signal, the discrete Fourier transform – DFT was used. The resolution that is obtained in the frequency domain depends on the time at which N samples of the input signal were collected. This time was related to the sampling frequency f_s and the length of the recorded record N as $t = N/f_s$. Then the number of collected samples required to obtain the appropriate resolution Δf is $N = f_s/\Delta f$. The measurements were carried out in non-equilibrium conditions: the sample was polarized with a constant voltage. Both the voltage on the sample and the voltage on the low noise (wire) series resistor with known resistance R_s were monitored.

III. RESULTS AND DISCUSSION

The figure that shows the noise spectrum measured at approximately 30°C . The spectral power density of the measured Sv voltage fluctuations is presented. The spectral shape has also been corrected due to the amplifier transition function for the used amplifier. The power density DFT PD in Fig. 1b. The sample shows the typical fluctuation characteristics of the time constraints and the frequency of ZnO photoconductive detectors. It is noted that the noise curve ZnO w is linear. While the ZnO layer is UV-exposed, the electric current increases significantly. The characteristic frequency dependence has the form $1/f^\alpha$, (alpha parameter ≈ 1). In this case, the spectral density of the fluctuations, for example the voltage, can be shown in the $S_V(f)$ form, and for the relative S_N fluctuations (f) we have $S_N(f) = G_V(f)/V^2 = G_R(f)/R^2$, where V, R are the average voltage and resistance of the test sample, and $G_V(f)$, $G_R(f)$ are the voltage and noise resistance spectra respectively [3].

Low-frequency noise, measured by UV radiation, is an order of magnitude higher in the dark. In the samples, the dependence of the spectral noise characteristic as $1/f$ was observed as well as the square dependence of its intensity on the average voltage. $1/f$ low frequency noise behaviour is observed on ZnO layers both in the dark and under UV illumination. The shape of the image of the excited noise shows that oscillations from the processes are observed, delaying the capture of oxygen by states with a broad continuous distribution of the energy level. Thus, the samples of nanostructured ZnCoO under investigation show a very low level of excess noise $1/f$, which apparently results from very small spatial dimensions of material inhomogeneities.

The increase is related to the photo-induced noise component, which results from the oxygen-related random processes associated with the holes, the trapped members are at the



b) Fig. 1. The time domain of the stress for the ZnCoO layer – (a) i log–log plot of the voltage dependence of the noise power spectral density both in the dark and under UV illumination – (b). The solid lines are linear fits $1/f$ to the data.

interface. It is assumed that this is due to the uneven distribution of the interstitial barrier. Holes migrate at the grain boundaries and recombine negative oxygen ions, which can cause uneven state of traps associated with oxygen or uneven grain barrier distributions in ZnO polycrystals. After lighting with the energy of the photon around the energy reserve, photogeneration is partly electron-hole. The holes migrate to the interface along the potential slope, appear when the strip is bent, and the negative oxygen ions are unloaded, which leads to the holes being trapped. Collection of negatively charged oxygen ions at the grain boundary reduces the height of the intergranular barrier, which leads to an increase in conductivity with the participation of photogenerated electrons. The low frequency noise of the ZnO layers shows the proportionality $f^{-\alpha}$ similar behavior in both

darkness and under lighting, where there is the frequency indicator. As you can see, the spectrum of measured fluctuations differs significantly from the $1/f$ ratio. The $f:S$ from f plot has a maximum for the frequency $f_{\max} = 3$ kHz. The time scale of changes is shown in Figure 1a. As to other semiconductors, point defects also play an important role in the electrical and noise properties of the ZnO layers. To determine if the noise of the ZnO layer is derived from point defects, a measurement of noise in UV light was performed, which gives a higher conductivity. In the presence of UV light, the measured noise is usually one level of magnitude higher than the dark noise. Of course, the increased density of carriers caused by UV illumination and the higher spectral power density of the noise can not be interpreted by G-R activity, which is caused by defects in electron trapping. ZnO polycrystalline wastes were prepared in PLD methods; Oxygen molecules were absorbed at the ZnO grain boundary and captured free electrons from n-grains. As a result, negatively charged oxygen ions arose around the ZnO grain boundaries that act as trapped oxygen-associated states. A series of stochastic processes (trapping electrons) occurs, causing fluctuations in the dark current. After lighting with photon energy above E_g , there are photogenerated electron-hole pairs. Annihilation of holes with negatively charged oxygen ions at the grain boundaries reduces the height of the inter-spherical barrier, which leads to increased conductivity with the participation of photogenerated electrons [4].

The indexed noise component contributes to an increase in the noise level in UV illumination by one order of magnitude. The superposition of kinetics of cargo trapping and migration has a continuous distribution of relaxation times. Distribution of activation energy would be almost constant in a sufficiently wide range to show $1/f$ noise. Some holes migrate to the grain boundaries and discharge negatively charged oxygen ions, which has a non-uniform distribution of oxygen-bound trap states or uneven distribution of intergranular barriers in the ZnO layer.

IV. CONCLUSIONS

The current level of noise in ZnCoO nanostructural layers was investigated. Based on experimental research, it has been shown that the normalized spectral power density characteristic of disordered systems has an excessive $1/f$ -type noise. Excessive low frequency noise is usually a decisive factor in the spatial heterogeneity of semiconductor materials. It has been found that in comparison with other spatially unordered materials, these samples show a low degree of resistance changes which changes with ultraviolet (UV) lighting.

- ¹ S.J. Chang, B.G. Duan, C.H. Hsiao, S.J. Young, B.C. Wang, T.-H. Kao, K.S. Tsai, and S.L. Wu IEEE Photonics Technology Letters, **volume 25**, 2043, (2013).
- ² W.C. Lai, J.T. Chen, Y.Y. Yang, Optics Express, **volume 21**(8), 9643-9651(2013).
- ³ O.V. Gerashchenko Technical Physics Letters, **volume 34**, pp 124–125, (2008).
- ⁴ D. Li, Y. Meng, P. Zhang, Z. Liu, and H. Zhao Japanese Journal of Applied Physics, **volume 52**, 084101, (2013)

ALPHABETICAL LIST OF AUTHORS

Akehi K.	71, 117, 136, 140
Anderson C.	93
Andò B.	100
Antal A.	82
Asada H.	117
Babicz S.	119
Baglio S.	100
Balandin A. A.	126
Banys J.	29, 145
Barabash M. L.	33, 65
Barkai E.	47
Bednorz A.	57, 121
Bełdowski P.	142
Bellon L.	27, 59
Belzig W.	57, 78, 121
Bester M.	147
Beyne S.	107
Bezrukov S. M.	12
Bialas P.	73
Bier M.	80
Bloodgood M. A.	126
Bruder C.	57, 102
Bulsara A. R.	100
Bülte J.	57
But D.	41
Cagnetta F.	17
Cagnoli G.	27
Cannatà G.	107
Cappy A.	45
Celi A.	67
Chevalier P.	55
Chialvo D. R.	31
Chichigina O.	91
Ciofi C.	104, 107
Colomé E.	49, 51
Coppola M.	85
Corberi F.	17
Crépieux A.	122
Cywiński G.	41
Czaja Z.	124
Danneville F.	45
Dergachev V.	98
Didovska O.	147
Dmitriev A.	98
Dobrevski M.	93

Dolique V.	27
Dubkov A.	91, 110
Duong T. Q.	122
Dybiec B.	61
Dykman M. I.	96, 102
El-Beyrouthy J.	55
Farahani M. A.	71, 117, 136, 140
Farrer I.	74
Fedorenko O. F.	65
Feigel'man M. V.	48
Fontana A.	59
Frączak M.	121
Galla S.	87
Garcia-March M. A.	67
Gasparyan F.	85
Geremew A.	126
Gibby W. A. T.	33, 65
Gingl Z.	82
Giusi G.	104, 107
Glattli D. C.	74
Glemža J.	128
Gloria G.	55
Goldobin D. S.	89
Gonnella G.	17
González T.	49
Gori M.	19
Goychuk I.	15
Grabowski M.	41
Graff B.	21
Guardiani C.	33, 65
Gudowska-Nowak E.	61
Haendler S.	55
Hakonen P.	13
Handziuk V.	35, 85
Hansali G.	27
Hedayat S.	45
Hlukhova H.	35
Hoel V.	45
Hoffmann A.	55
Holubec V.	116
Itakura N.	71, 117, 140
Italura N.	136
Jung G.	23, 43

Kapfer M.	74
Karg S.	53
Kenyon A. J.	39
Khovanov I. A.	33, 63
Kish L. B.	11, 32, 84, 95, 109
Klimenko L. S.	89
Knap W.	41
Kolodiy Z.	112
Kosztolowicz T.	106
Kowalewski M.	124
Krasnova A.	91
Kruszewski P.	41
Kuberský P.	134
Kumagai R.	130
Kutovyi Y.	35, 53
Lavagna M.	122
Lechelon M.	19
Lentka Ł.	87, 132, 143
Levinshtein M.	98
Lewenstein M.	67
Lörch N.	102
Loyez C.	45
Luchinsky D. G.	33, 65
Łuczka J.	73, 114
Macutkevič J.	29, 145
Majka M.	115
Majzner J.	134
Makowiec D.	21
Manzo C.	67
Marletta V.	100
Mateos J.	49
Matukas J.	29, 128, 145
Mayer D.	85
McClintock P. V. E.	33, 65, 93
Mehonic A.	39
Melhem M.	95
Meriguet Y.	19
Miranda E. A.	39
Mito K.	71, 136
Mívald F.	134
Mizuno T.	71, 117, 136, 140
Müller J.	25
Muñoz-Gil G.	67
Murata T.	136
Nadzinski G.	93
Ng W. H.	39
Novotný T.	116

Nowakowski-Szkudlarek K.	41
Oriols X.	49, 51
Palenskis V.	128
Pandey D.	51
Panek M.	138
Pascal F.	55
Pedurand R.	27, 59
Petrychuk M.	35, 53, 85
Pettini M.	19
Pikovskiy A.	89
Pralgauskaitė S.	29, 128, 145
Prystawko P.	41
Przybytek J.	41, 43
Ptaszyński K.	76
Rastelli G.	78
Reulet B.	57
Riel H.	53
Ritchie D. A.	74
Roberts S. K.	65
Rouleau P.	74
Rumyantsev S. L.	41, 126
Sagnes B.	55
Sahoo S.	122
Sai P.	41
Sakamoto S.	140
Salguero T. T.	126
Sasaki K.	69
Scandurra G.	104, 107
Sedlák P.	134
Sedláková V.	134
Seif M.	55
Shinagawa R.	69
Shmakov P.	98
Simin G. S.	41
Siódmiak J.	142
Smulko J.	132, 134, 143
Sokolov I. M.	61
Sołtan S.	121
Song J.	84
Sourikopoulos I.	45
Spiechowicz J.	114
Stankovski M.	93
Stankovski T.	93
Stawarz-Graczyk B.	119
Stefanovska A.	37, 93
Struzik Z. R.	21
Suma A.	17

Suñé J.	39
Suprunenko Y. F.	37
Sydoruk V.	85
Szewczyk A.	87, 143
Tadokoro Y.	96
Takagi M.	71
Tanaka H.	96
Torres J.	19
Tretjak M.	29, 145
Tyulkina I. V.	89
Uchida M.	130
Vadai G.	82
Vandamme L.	85
Varani L.	19
Virt I. S.	147
Vitusevich S.	35, 53, 85
Wejer D.	21
Yahniuk I.	41
Yuvan S.	80
Zadorozhnyi I.	35, 53
Zamoum R.	122
Zhan H.	78
Zhan Z.	51
Zhang Y.	102

SIGHTSEEING GDAŃSK 12TH JULY 2018

Bus departure: 16:00 (meeting at the front of the Main Building, Gdańsk University of Technology).

Gdańsk Main Town:

- Green Gate, The Long Warf and the Motława river
- Mariacka Gate
- The Old Crane
- Mariacka Street, St. Mary's Basilica
- Royal Chapel
- Beer Street and The Great Armory
- Golden Gate, Prison Tower, Long Street and The Long Market, Main City Hall, Artus Court, Golden House, Neptune's Fountain
- Piwnica Rajców from 6.00 pm - regional beer tasting, dinner (address: Długi Targ 44, 80-980 Gdańsk, in front of the Neptune's Fountain).

Return to the hotels/dorms on your own.

